

#### 4. Mössbauer Backscattering Spectra

As shown in the two preceding Chapters, Mössbauer backscattering spectroscopy allows studies to be conducted in situ on both thin and bulk samples, i.e. on scatterers in which the thickness considerably exceeds the absorption length  $l$  of the radiation to be detected [see (2.34)]. In such a case the Mössbauer spectra convey information on a layer which is as thick as  $l$ . If the linear absorption coefficient for the detected radiation is much greater than  $(\mu_r + \mu_a)$ , the re-scattering process results in the Mössbauer spectrum being contributed to by a part of the sample which is deeper than  $l$ . Mössbauer backscattering spectroscopy has been used so far for semiquantitative evaluations despite the considerable potential of the method for the surface analysis of industrial materials [4.1]. As a rule, rather complicated preliminary calculations have to be made of intensities for different scattering channels [4.2-5].

Phase analysis studies assume that, for polycrystalline samples at poor collimation (large values of the parameter  $D$  (2.65)), the Mössbauer lines will be symmetric since interference effects may be completely neglected. As seen in Sect.2.3 interference between Mössbauer and Rayleigh scattering occurs on scattering even by an atom. If an approximate compensation can be obtained of the intensities of the  $\gamma$ -quanta which are resonantly and non-resonantly scattered, then the line asymmetry due to the interference effect might be observed experimentally [4.2,4]. More detailed studies on small effects of line asymmetry in transmission and scattering experiments have been reported in [4.6]. However, at present these effects are usually discounted in applied research, since a simpler theory of quantitative spectral analysis has not yet been developed.

Generally, the properties of the sample such as the phase and elemental composition and structure are depth-dependent. This considerably complicates the interpretation of experimental spectra if the sample is a multilayer one. The energy distribution of radiation reaching each of the layers is determined by resonant scattering from the upper layers. The deeper a layer, the more its Mössbauer spectrum differs from the reference Mössbauer spectrum of the substance. Moreover, the deeper the layer, the more affected is the spectrum shape by non-resonant scattering. The quantitative interpretation of experimental data also requires that the effects of granularity should be taken into account [4.7,8].

Some of the problems related to the interpretation of scattering spectra will be discussed in this Chapter. First, the problems connected with resonant re-scattering process which have been neglected so far will be considered. Then, we shall evaluate the intensities of radiations produced by scattering of monochromatic  $\gamma$ -rays and the effect on the spectrum shape of resonant and non-resonant scattering. Some problems will also be discussed which arise from spectral analysis of multilayer samples. Most attention will be given to backscattering Mössbauer spectroscopy.

#### 4.1. Weight Functions and Re-scattering

Let  $\gamma$ -rays from a Mössbauer source be normally incident to the surface of a uniform bulk sample and the scattered  $\gamma$ -radiation escape at any angles to the surface. Only the fraction of resonant radiation  $f$  will be taken into account since non-resonant fraction contributes only to the background. The scattered  $\gamma$ -radiation will be detected with the 100 % efficiency. Assuming that both the source and scatterer are characterized by a narrow single Lorentzian line, the beam of scattered  $\gamma$ -quanta is described by

$$I(\varepsilon) = f \int_0^\infty dx \int_{-\infty}^\infty L(E - \varepsilon) e^{-\mu_a(E)x} \left\{ \frac{\mu_r(E)}{1 + \alpha} \left[ f' T_r(x, E) + (1 - f') T_n(x) \right] + \mu_R f_R T_r(x, E) + \left[ (1 - f_R) \mu_R + \mu_C \right] T_n(x) \right\} dE, \quad (4.1)$$

where  $T_r(x, E)$  and  $T_n(x)$  are the probabilities of the elastically and inelastically scattered radiation escaping from the depth  $x$  to the sample surface. They are dependent on both the probability of the radiation to directly escape from the depth  $x$  to the surface, and the probability of the quanta re-scattering in the vicinity of a certain point at depth  $y$  and the subsequent generation of a resonant or non-resonant quantum which escapes to the sample surface. For example, if a resonant quantum is re-scattered, the probability of the process is proportional to the quantity

$$C_r \mu_a(E) T_r(y, E) \exp [-\mu_a(E) |x - y| / \cos \theta] \frac{dy}{|\cos \theta|},$$

where  $C_r = f / (1 + \alpha)$ . Integrating over the angle, an integral equation is obtained which enables the  $T_n(x)$  and  $T_r(x, E)$  probabilities to be found [4.9,10]:

$$T_n(x) = \frac{1}{2} E_2(\mu_a x) + \frac{1}{2} (\mu_R + \mu_C) \int_0^\infty E_1(\mu_a |x - y|) T_n(y) dy, \quad (4.2)$$

$$T_r(x, E) = \frac{1}{2} \left\{ E_2(\mu_a(E) x) + \left[ \frac{1 - f'}{1 + \alpha} \mu_r(E) + (1 - f_R) \mu_R + \mu_C \right] \int_0^\infty E_1(\mu_a(E) |x - y|) T_n(y) dy + \left[ \frac{f' \mu_r(E)}{1 + \alpha} + f_R \mu_R \right] \int_0^\infty E_1(\mu_a(E) |x - y|) T_r(y) dy \right\}. \quad (4.3)$$

In (4.3)  $T_n(y)$  is the function obtained by means of (4.2). The first term in the braces in (4.3) gives the probability of an elastically scattered resonant  $\gamma$ -quantum at a depth  $x$  escaping the surface without any intermediate interactions. The second and third terms account for the fact that this quantum may be inelastically or elastically re-scattered at a depth  $y$  and then may escape. A conventional detector, due to a poor energy resolution, will also detect the Compton-scattered  $\gamma$ -quanta. In (4.2) and (4.3), the scattering was assumed to be isotropic. This assumption is not strictly true but in the absence of level splitting it is justified for most applications.

Equation (4.2) represents the classical problem of Milne involving radiation leaving the solid. The problem considers the transmission of radiation from a certain depth to the sample surface [4.11-13]. This problem was originally formulated for the radiation from stars reaching the surface of the Earth but it has subsequently found application for a number of other phenomena. Similar problems exist in studies of the escape of neutrons from the object under investigation. In classical Milne's problem it is assumed that there is one scattering channel. Hence the weight function  $T(x)$  of radiation from depth  $x$  can be described by the Fredholm integral equation of the second kind. Equation (4.3) is a generalization of the classical Milne's problem for the case of Mössbauer radiation. The problem can be formulated as follows. In a certain point in the scatterer, a resonant quantum has been produced. What is the probability of a  $\gamma$ -quantum leaving the surface of the scatterer? The intensity of scattered radiation has been calculated by several authors [2.5,41,42,49, 4.2] without taking into account the re-scattering processes. The problem of multiple Mössbauer scattering has been investigated by MKRTCHYAN et al.[4.14,15].

The authors have considered the problem of Mössbauer radiation scattering at the angle  $\theta$  inside a sample of thickness  $d$ . It has been shown that when the reemission probability (the internal conversion coefficient  $\alpha < 1$ ) is large or the sample represents a large effective thickness, the problem cannot be limited only to the single scattering. An essential simplification has been made in [4.14]. The re-scattering processes have been considered for the elastic resonant channel of scattering with  $f' = 1$  and  $\mu_a = 0$ . To calculate the weight functions, the authors have used the solution of the integral equation calculated using tabulated Ambartsumyan's functions [4.13]. In this case the weight functions are found by numerical integration. In the model one-dimensional case it is possible to find the exact expression for the weight function.

The problem is difficult to solve in the general case. A simplification is possible for the samples that are highly enriched in the resonant isotope, i.e. for cases where  $\mu_r \gg \mu_a$ , introducing the function

$$T^\gamma(x, E) = f' T_r(x, E) + (1 - f') T_n(x),$$

which determines the probability for the recoil- and recoilless  $\gamma$ -quanta to return to the sample surface. The scattered intensity (4.1) may be transformed into

$$I(\varepsilon) = \frac{f}{1 + \alpha} \int_0^\infty dx \int_{-\infty}^\infty L(E - \varepsilon) e^{-\mu_a(E)x} \mu_r(E) T^\gamma(x, E) dE. \quad (4.4)$$

The probability for a  $\gamma$ -quantum escaping the surface  $T^\gamma(x, E)$  satisfies the equation

$$\begin{aligned} T^\gamma(x, E) = & \frac{1 - f'}{2} E_2(\mu_a x) + \frac{f'}{2} E_2(\mu_a(E) x) \\ & + \kappa \int_0^\infty E_1(\mu_a(E) |x - y|) T^\gamma(y, E) dy. \end{aligned} \quad (4.5)$$

To obtain the integral exponents (see e.g.(2.104)) the change of variables has been made  $t = 1/\cos\theta$ . The  $\kappa$  parameter is

$$\kappa = \frac{f' \mu_r(E)}{2(1 + \alpha)}. \quad (4.6)$$

The inhomogeneous second order Fredholm equations (4.2), (4.3) and (4.5) are of the same type. For simplicity, only (4.5) will be discussed here.

The exact solution of the integral equation (4.5) has not yet been obtained due to mathematical difficulties. An approximate solution can be obtained by means of an iterative procedure

$$T_{k+1}^{\gamma}(x, E) = T_1^{\gamma}(x, E) + \kappa \int_0^{\infty} E_1(\mu_a(E) |x - y|) T_k^{\gamma}(y, E) dy \quad (4.7)$$

under a natural assumption that

$$T_1^{\gamma}(x, E) = \frac{1 - f'}{2} E_2(\mu_a x) + \frac{f'}{2} E_2(\mu_a(E) x) \quad (4.8)$$

If all the  $T_k$  ( $k = 1, 2, \dots$ ) are subsequently substituted into (4.7) and all the  $T_k^{\gamma}(y, E)$  values of the resulting equation are replaced with the maximal values (equal to unity), the power

series is produced for the parameter  $\kappa \int_0^{\infty} E_1(\mu_a(E) |x - y|) dy$ .  
The iterative process is convergent if the relation is satisfied

Hence, the estimate follows

$$\kappa \int_0^{\infty} E_1(\mu_a(E) |x - y|) dy < 1 \quad .$$

Hence, the estimate follows

$$T_1(x, E) < T_{k+1}(x, E) < T_1(x, E) + \max T_1(x, E) \sum_{l=0}^k (2\lambda_r)^l$$

where

$$\lambda_r = \frac{c_r \mu_r(E)}{\mu_a(E)} \quad (4.9)$$

The relation  $2\lambda_r < 1$  is the condition for the iterative process to converge. Since  $\mu_r(E)$  is always less than  $\mu_a(E)$  and  $f / (1 + \alpha) < 1$ , the relation above is fulfilled.

The convergence parameter  $f/(1 + \alpha)$  which is derived for  $^{57}\text{Fe}$  is 0.08. This means that for the  $^{57}\text{Fe}$  Mössbauer effect the role of multiple re-scattering should not be great. If only single re-scatterings are taken into account the weight function can be written in the form

$$T_2^{\gamma}(x, E) = T_1^{\gamma}(x, E) = \kappa \int_0^{\infty} E_1(\mu_a(E) |x - y|) T_1^{\gamma}(y, E) dy \quad (4.10)$$

There are two ways to evaluate the  $T_2^{\gamma}(x, E)$  weight function. The first way is related to direct calculations and gives the following result

$$T_2^{\gamma}(x, E) = T_1^{\gamma}(x, E) + a \left[ \frac{1 - f'}{2} F_0 + \frac{f'}{2} F_1 - \frac{E_2(\mu_a(E)x)}{2\mu_a(E)} \right]_1,$$

where C is the constant

$$F_i = \frac{1}{\mu_i} \int_1^{\infty} e^{-\mu_i x t} \ln \left| \frac{\mu_i t + \mu_a(E)}{\mu_i t - \mu_a(E)} \right| \frac{dt}{t^3} \\ - \frac{\mu_i}{(\mu_a(E))^2} \int_1^{\infty} e^{-\mu_a(E) x t} \ln \left| \frac{\mu_a(E)}{\mu_i} t - 1 \right| \frac{dt}{t^3} \\ i = 0, 1; \quad \mu_0 = \mu_a; \quad \mu_1 = \mu_a(E).$$

The integrals contained in the  $F_0$  and  $F_1$  functions can be easily tabulated.

Another way to evaluate the weight functions when single re-scatterings are taken into account is connected with a series expansion of the  $T_1^{\gamma}(y, E)$  function (see (4.10)) in the vicinity of  $y = x$ , where  $E_1(x - y)$  changes sharply:

$$T_1(y, E) = T_1(x, E) + T_1'(x, E)(y - x) + \frac{1}{2} T_1''(x, E)(y - x)^2 + \dots$$

Restricting ourselves to the first term of the series, we have

$$T_2(x, E) < T_1(x, E)(1 + 2\lambda_r) \quad (4.11)$$

Using the procedure (4.7), the contribution can be evaluated into the weight function from other subsequent re- scattering processes.

The exact solution of (4.5) can be obtained only in a hypothetical one-dimensional case, i.e. considering  $\gamma$ -quanta being back-scattered along the surface normal ( $\theta = \pi/2$ ). Although this situation is not realized in practice, it is very instructive and an expression for the weight function, which is the probability that a  $\gamma$ -quantum will escape the surface in this one-dimensional case, can be written as

$$T^{\gamma}(x, E) = a_1 e^{-\mu_a x} + a_2 e^{-\beta x}, \quad (4.12)$$

where

$$a_1 = \frac{1 - f'}{2} \frac{\mu_a^2(E) - \mu_a^2}{\beta^2 - \mu_a^2}, \quad (4.13)$$

$$a_2 = \frac{f' \mu_a(E)}{\beta + \mu_a(E)} - \frac{1 - f'}{2} \frac{[\mu_a(E) + \mu_a][\mu_a(E) - \beta]}{\beta^2 - \mu_a^2},$$

$$\beta = \mu_a(E) \sqrt{1 - \frac{f'}{1 + \alpha} \frac{\mu_r(E)}{\mu_a(E)}}.$$

Numerical calculations performed using (4.8), (4.10) and (4.12), have shown that the contribution of re-scattering increases with increasing depth of the layer where scattering occurs, and with the increase of the  $\mu_r(E)$  value. In the essential range of changes in  $x$ , i.e. where  $T(x, E) > 0.1$ , the contribution of re-scattering processes does not exceed 10 % and double re-scattering should be accounted for only when the accuracy required for the solution exceeds 1 %.

In a three-dimensional case, an exact analytical expression for the weight functions is not obtainable even for  $\mu_r \gg \mu_a$  and simplifying assumptions are required. Results of the numerical calculations are presented in Fig.4.1. The data in Table 4.1 show the difference in the  $T_1(x)$  and  $T_2(x)$  functions. If the accuracy required is to be better than 1 %, the contribution of double re-scattering should be taken into account.

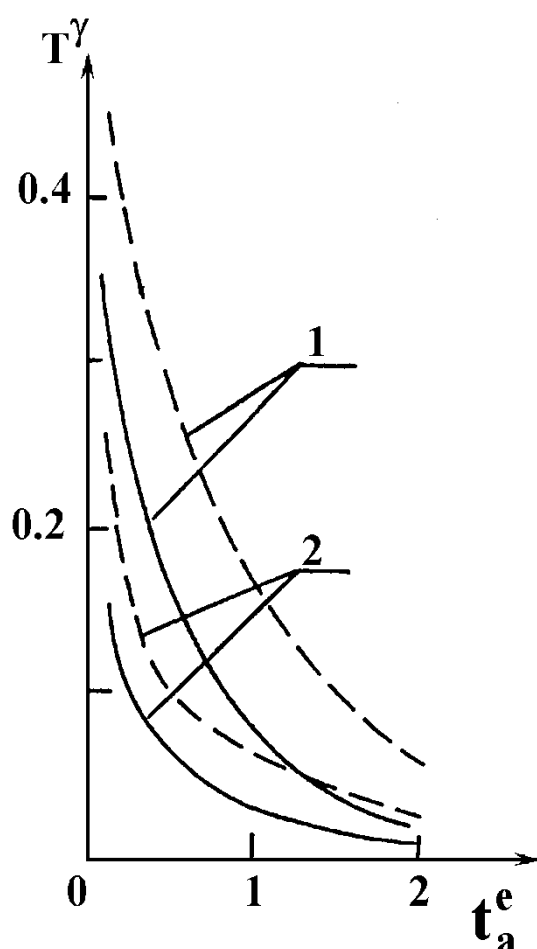


Fig.4.1. Weight functions  $T(t_a^e, E)$  for a sample of non-magnetic iron. The incident radiation is at resonance. The values of  $\mu_r/\mu_a = 0.1$  (curves 1) and 10 (curves 2) correspond to different enrichment in the resonant isotope. The solid lines give the calculated results for the 3D case, when re-scattering is accounted for. The dashed lines give exact calculated results for the one-dimensional case. ( $t_a^e = \mu_a x$ ).

## 4.2. Evaluation of the Intensity of Scattered $\gamma$ -Radiation

The direct calculation of the scattered intensity is made possible using the evaluations derived in the preceding Section [4.9]. To do this it is necessary to consider the response of the scatterer to the incident monochromatic radiation. Quantities that are proportional to the probability of the scattered radiation escaping the surface as a result of only one resonant scattering event for a  $\gamma$ -quantum of energy  $E$  will be denoted as  $P_i^{\prime}(E)$ , where subscript  $i = r, rn, x, K, L, A$  refer to recoil- and recoilless  $\gamma$ -quanta, characteristic X-rays, K- and L-conversion electrons, or to Auger electrons, respectively. The corresponding quantities for resonant re-scattering are denoted by  $P_i^{\prime\prime}(E)$ .



Table 4.1

The results of the numerical calculations of the  $T^Y(t_a^e)$ ,  $T_1^Y(t_a^e)$  and  $T_2^Y(t_a^e)$  functions in hypothetical one-dimensional and three- dimensional (3D) cases,  $\xi = \mu_r/\mu_a$ ,  $t_a^e = \mu_a x$ .

Dimension	$\xi$	0.1			11		
	$t_a^e$	0.1	0.5	1	0.1	0.5	1
1D	$T^Y(t_a^e)$	0.4502	0.2940	0.1726	0.2670	0.0995	0.0593
	$T_2^Y(t_a^e)$	0.4502	0.2940	0.1726	0.2662	0.0990	0.0590
	$T_1^Y(t_a^e)$	0.4493	0.2929	0.1717	0.2522	0.0924	0.0552
3D	$T_2^Y(t_a^e)$	0.3561	0.1549	0.0677	0.1636	0.0526	0.0237
	$T_1^Y(t_a^e)$	0.3550	0.1540	0.0672	0.1533	0.0492	0.0223

Notes:  $T^Y(t_a^e)$  - the weight function, when multiple re-scattering are taken into account;  
 $T_1^Y(t_a^e)$  - the weight function, when re-scatterings are not taken into account;  
 $T_2^Y(t_a^e)$  - the weight function, when single re-scatterings are taken into account.

The total probability is proportional to  $P_i(E)$ :

$$P_i(E) = P_i'(E) + P_i''(E) . \quad (4.14)$$

The  $P_i(E)$  function is determined by the properties of the scatterer and does not depend on the relative velocity  $v$ .

Let a beam of monochromatic  $\gamma$ -quanta be incident onto the sample with energy  $E$  equal, for example, exactly to the resonance energy, and the radiation resonantly scattered isotropically from a layer  $dx$  be not able to re-scatterer more than once. The  $P_i(E)$  function then be presented in the form:

$$P_i(E) = \frac{C_i}{2} \int_0^\infty \int_0^{\pi/2} W(E, x) \exp(-\nu_i x / \cos\theta) \sin\theta \, d\theta \, dx , \quad (4.15)$$

where  $C_i$  - the weight factor for the scattering channel where radiation of the  $i$ -th type is produced.  $W(E,x)dx$  is the total probability of resonant scattering and single re-scattering for monochromatic radiation in a layer  $dx$  at depth  $x$ . Equation (4.15) may be rewritten in a more compact form. Thus, on detection of inelastically scattered  $\gamma$ -rays ( $\nu_i = \mu_a$ ):

$$P_{rn}(E) = \frac{C_{rn}}{2} \int_0^{\infty} W(E,x) E_2(\mu_a x) dx. \quad (4.16)$$

In this approach the function  $E_2(\nu_i x)$  is similar to the weight function. Taking into account the above the  $W(E,x)$  function is written as

$$W(E,x) = W_1(E,x) + W_2(E,x) = \mu_r(E) e^{-\mu_a(E)x} + \mu_r(E) \kappa \int_0^{\infty} dy \int_1^{\infty} \exp[-\mu_a(E)|x-y|t - \mu_a(E)x] \frac{dt}{t}. \quad (4.17)$$

The  $W_2(E,x)$  term refers to the process in which a  $\gamma$ -quantum is resonantly scattered in a layer  $dy/\cos\theta$  at a depth  $y$ , and is then resonantly scattered in a layer  $dx$  at a depth  $x$ . After integrating over  $y$  and changing the variable  $t = 1/\cos\theta - 1$ , we obtain

$$W_2(E,x) = \mu_r(E) e^{-\mu_a(E)x} \lambda_r \left\{ \ln 2 + \int_0^{\infty} \left[ 1 - \exp[-\mu_a(E)xt] \right] \frac{dt}{t(t+1)} \right\}. \quad (4.18)$$

A feature of this approach for the evaluation of re-scattering is that the type of detected radiation only determines the value of the  $\nu_i$  parameter in the integral exponent of (4.16). This allows an approach to be developed for evaluating the probabilities of photons (as well as electrons) escaping the surface due to both resonant scattering and re-scattering events. Expression (4.15) with (2.97), (2.98) and (4.17) can be transformed into

$$P_i(E) = P'_i(E) [1 + \lambda_r(\ln 2 + B(a(E), \nu_i d))] , \quad (4.19)$$

$$B(a(E), \nu_i d) = J(a(E)) / \hat{E}_2(a(E), \nu_i d) , \quad (4.20)$$

where

$$P'_i(E) = \lambda_i \hat{E}_2(a(E), \nu_i d) / 2 , \quad (4.21)$$

where  $\lambda_i$  is the parameter analogous to  $\lambda_r$  (4.9). For example, on detection of recoilless  $\gamma$ -rays after resonant scattering

$$P'_r(E) = \lambda_r \hat{E}_2(1, \mu_a(E) d) / 2 . \quad (4.22)$$

The probability for a photon or electron escaping the surface after resonant scattering is determined by the energy dependence of the linear resonant scattering coefficient. The probability value is determined by the ratios:  $\mu_a(E)/\nu_i$  and  $\mu_r(E)/\nu_i$ . Formula (4.21) remains valid for any other scattering channels if  $\mu_a(E)$  and  $\mu_r(E)$  are replaced by the values of the linear scattering coefficients which correspond to these channels. Of course,  $P_i$  is then energy independent in the energy interval of interest ( $E = E_0 \pm 1000 \Gamma$ ).

To obtain  $P'_i(E)$  requires the evaluation of the  $K(a(E), d)$  integral and also  $J(a(E))$

$$J(a(E)) = \int_0^\infty \int_0^\infty [e^{-az} - e^{az(t+1)}] \frac{dz dt}{t(t+1)} , \quad (4.23)$$

This is because the contribution of resonant re-scattering is determined by the ratio of the two integrals. It is possible to make simple estimates for the different parameter  $a(E)$  values:

$$\begin{aligned} \text{for } a > 1 \quad B(a) &= 1 - \frac{0.5 \ln a - 0.39}{a - \ln a} \rightarrow 1 , \\ \text{for } a = 1 \quad B(a) &= 0.57 , \\ \text{for } a < 1 \quad B(a) &= \frac{2}{3} a \ln \frac{1}{a} - 0.24 a \rightarrow 0 . \end{aligned} \quad (4.24)$$

Thus, the contribution of resonant re-scattering

$$P_1''(E) = \lambda_r P_1'(E) [\ln 2 + B(a)] \quad (4.25)$$

can be easily estimated from (4.24). The value changes from  $0.69 \lambda_r P_1'$  to  $1.69 \lambda_r P_1'$ .

Let us use the approach developed above for evaluating the scattered intensity. On detection of recoilless scattered  $\gamma$ -quanta  $\nu_i = \mu_a(E)$  and consequently for any Mössbauer nuclide,  $K_2(a, \infty) = K_2(1, \infty) = 0.307$ . In accordance with (4.21) and (4.25),  $P_r'(E)$  and  $P_r''(E)$  are a function of the  $\lambda_r$  parameter only

$$P_r'(E) \approx 0.154 \lambda_r \quad ; \quad P_r''(E) \approx 0.194 \lambda_r^2 \quad . \quad (4.26)$$

The scattered intensity is not solely determined by resonant scattering the probability of which  $P_v'(E)$  may be written as

$$P_\gamma'(E) = f [P_r'(E) + P_{rn}'(E)] \quad .$$

$$P_v'(E) = f [P_r'(E) + P_{rn}'(E)] \quad .$$

when re-scattering processes are not taken into account.

There are two more groups of contributions to the total intensity. For the first group the intensity depends on the source velocity whilst for the second one the intensity is velocity-independent. Let  $Q_v(E)$  be the probability determining the total scattered intensity. The scattered intensity being caused by resonant scattering is maximized on resonance. Non-resonant scattering channels, for which the scattered intensity is also velocity-dependent, make a minimal contribution to the total intensity on resonance but off resonance they determine the  $Q_v(E)$  value which will be denoted by  $Q_v(\infty)$ . It is evident that on resonance, i.e. at  $E_0$ , the  $Q_v(E_0)$  value may be either greater than the  $Q_v(\infty)$  value - and we have a peak on resonance - or less than  $Q_v(\infty)$ , when the Mössbauer spectrum will show a dip on resonance.

Taking all the above into account, the  $Q_v(E)$  value can be found. It is known that non-resonant scattering channels are Rayleigh scattering and the Compton effect characterized by  $\mu_R$ ,  $f_R$  and  $\mu_C$ .

$$Q_\gamma(E) = \frac{1 - f}{2} \frac{\mu_R + \mu_C}{\mu_a} \hat{E}_2(1, \infty) + P_\gamma'(E) +$$

$$\begin{aligned}
& + f \left\{ \frac{\mu_C}{2\mu_a} \hat{E}_2 \left[ \frac{\mu_a(E)}{\mu_a}, \infty \right] + \frac{\mu_R}{2} \left[ \frac{f_R}{\mu_a(E)} \hat{E}_2(1, \infty) \right. \right. \\
& \left. \left. + \frac{1 - f_R}{\mu_a} \hat{E}_2 \left[ \frac{\mu_a(E)}{\mu_a}, \infty \right] \right] \right\} . \quad (4.27)
\end{aligned}$$

The first term in the right-hand part of (4.27) accounts for the escape from the sample surface of  $\gamma$ -radiation emitted with recoil which then suffers Rayleigh or Compton scattering. This term contributes only to the background. The second and third terms account for the escape of  $\gamma$ -rays which are recoillessly emitted and then elastically or inelastically scattered in the sample. All these  $\gamma$ -quanta are supposed to be detected with equal probability. The intensity of  $\gamma$ -rays emitted without recoil and backscattered due to the Compton effect which escape from the bulk sample surface is determined by the first term in braces. Of these  $\gamma$ -rays, those backscattered due to Rayleigh scattering are determined by the second term in braces in (4.27). Off resonance, the intensity of  $\gamma$ -radiation returning to the bulk scatterer surface is

$$Q_\gamma(\infty) \approx 0.154 \frac{\mu_C + \mu_R}{\mu_a} . \quad (4.28)$$

For phase analysis it is useful to consider the following quantity:

$$\begin{aligned}
R_\gamma(E) = Q_\gamma(E) - Q_\gamma(\infty) = P'_\gamma(E) + \frac{f}{2} \left\{ \frac{C}{\mu_a} \left[ \hat{E}_2(a(E), \infty) \right. \right. \\
\left. \left. - \hat{E}_2(1, \infty) \right] + (1 - f_R) \frac{\mu_R}{\mu_a} \left[ \hat{E}_2(a(E), \infty) - \hat{E}_2(1, \infty) \right] \right. \\
\left. + f_R \hat{E}_2(1, \infty) \left[ \frac{\mu_R}{\mu_a(E)} - \frac{\mu_R}{\mu_a} \right] \right\} . \quad (4.29)
\end{aligned}$$

This determines the absolute value of the observed effect for monochromatic  $\gamma$ -radiation. Irrespective of the type of the detected radiation,  $R_i(E)$  is always less than  $P_i(E)$ .  $R_i(E)$  may be positive or negative. Moreover, it may be zero at an appreciable intensity in resonant scattering channels.

This occurs if the  $\gamma$ -quanta with a certain energy  $E$   $Q_i(E) = Q_i(\infty)$  and arises from a specific relation between the  $\mu_i$ ,  $v_i$ ,  $C_i$  parameters which characterize the scattering in partial channels. It should be recalled that on resonance the  $a(E)$  parameter has its maximal value and the  $K_2(a(E), \infty)$  function reaches its minimal value (see Fig.2.28).

Off resonance, the intensity of  $\gamma$ -rays which are scattered due to the Compton effect and Rayleigh scattering increases. This is shown by the term in braces in (4.29). Indeed, all three expressions in square brackets are always less than zero. The larger the total linear absorption coefficient, the greater the absolute values of those expressions. The less the contribution of the photoelectric effect to the total interaction cross section, the less the amplitude of the Mössbauer lines.

The main quantities used to characterize the escape of monochromatic  $\gamma$ -rays to the bulk sample surface in  $^{57}\text{Fe}$ . Mössbauer spectroscopy are presented in Table 4.2. Values of the main parameter  $\mu_r(E)$  may refer to different iron compounds which depend on the hyperfine interaction parameter values and isotopic abundance (see, e.g. Table 2.3). The effect of non- resonant scattering channels on the line shape and intensity is demonstrated by the parameter  $\xi = |P_V'(E) - R_V(E)|/P_V'(E)$ . This describes the percentage of the experimental intensity as compared to the situation where the observed intensity is determined by resonant scattering channels only.

It follows from Table 4.2 that resonant scattering from a bulk sample containing  $^{57}\text{Fe}$  in backscattering geometry is governed by several factors: (i) For a sample of  $\alpha$ -Fe the resonantly scattered radiation intensity cannot exceed 0.42 % of the incident beam intensity when the energy of the monochromatic radiation coincides with the centroid of line 3 (4) of the . Mössbauer spectrum of ordinary iron, and cannot reach even 2 % for a hypothetical scatterer with  $a = 90\%$   $^{57}\text{Fe}$  and  $H_{\text{eff}} = 0$ . The intensity increase by a factor of 4.6 when  $\mu_r$  increases by a factor of 500 is caused by a relatively small  $\mu_a$  value. (ii) A significant dilution of the sample with low  $Z$  elements (1 : 100 for beryllium) will not change the absolute contribution of resonant scattering channels to the  $\gamma$ -rays intensity. A sharp increase of the contribution of Rayleigh and Compton scattering results in a considerable rise in the non- resonant scattering intensity and, thereby in an increase in the  $Q_V(E)$  and  $\xi$  values. The effect value is reduced considerably and, from a certain concentration of . Mössbauer atoms, a dip is observed on resonance.

It is more difficult to calculate  $P_i'(E)$  for a sample of a finite thickness. In the limiting case of an infinitely thin sample we have considerable rise in the non-resonant scattering intensity and, thereby in an increase in the  $Q_V(E)$  and  $\xi$  values. The effect value is reduced considerably and, from a certain concentration of . Mössbauer atoms, a dip is observed on resonance.



Table 4.2 (continued)

Notes:  $P_r'(E)$  and  $P_m'(E)$  are the corresponding probabilities of elastic and inelastic resonantly scattered  $\gamma$ -quanta\* escaping the surface as a result of one resonant scattering event;  $P_r''(E)$  and  $P_m''(E)$  are the corresponding quantities for resonant re-scattering;  $P_v(E)$  is the probability of resonant scattering (elastic plus inelastic) of  $\gamma$ -quanta if re-scattering is not taken into account;  $Q_v(\infty)$  is the probability for  $\gamma$ -quanta to return to the bulk scatterer's surface off resonance;  $R_v(E)$  is the quantity determining the intensity at resonance;  $\xi$  is the intensity of non-resonantly scattered  $\gamma$ -quanta as a percentage of the resonantly scattered  $\gamma$ -quanta intensity.

---

\* monochromatic radiation,  $f = 0.7$

It is more difficult to calculate  $P_i'(E)$  for a sample of a finite thickness. In the limiting case of an infinitely thin sample we have

$$\lim_{d \rightarrow 0} P_i'(E) = C_i \mu_r(E) d \quad (4.30)$$

and the scattered intensity is determined only by the  $C_i$  value. The effect value at  $d \rightarrow 0$  on detecting  $\gamma$ -quanta is

$$\varepsilon(E) = \frac{R_\gamma(E)}{Q_\gamma(\infty)} = \frac{f}{1 + \alpha} \frac{\mu_r(E)}{\mu_R + \mu_C} \quad (4.31)$$

The effect value for thin non-enriched samples is only slightly greater than the corresponding value for the bulk sample (cf.  $\varepsilon_3 = 300$  % on line 3(4) for a thin sample of ordinary  $\alpha$ -Fe and  $\varepsilon_3 = 210$  % for a bulk sample). However, if the enrichment is as high as 90 %, the effect value for a thin sample increases by the same factor i.e. for  $\alpha$ -Fe  $\varepsilon_3 = 1.2 \cdot 10^4$  %.

### 4.3. Evaluation of the Intensity of X-Rays and Electrons

To evaluate the line intensities when X-rays or electrons are detected it is necessary to consider the situation involving bulk samples. Assume that the detector is set to register K-X-rays and is not capable of detecting the  $\gamma$ -rays from the source or the  $\gamma$ -quanta produced as a result of Compton scattering. Let the Mössbauer spectrum be determined only by scattering channels related to resonant scattering and by the photoelectric effect.



The intensity scattered from a bulk sample of  $\alpha$ -Fe is proportional to the quantity

$$Q_x(E) = \frac{1-f}{2} \frac{\mu_{ph}}{\nu_x} \omega_K C'_K \hat{E}_2(\mu_a/\nu_x, \infty) + \frac{f}{2} \hat{E}_2(\mu_a(E)/\nu_x, \infty) \left[ \frac{\mu_r(E)}{\nu_x} \frac{\alpha_K \omega_K}{1+\alpha} + \frac{\mu_{ph}}{\nu_x} \omega_K C'_K \right] \quad (4.32)$$

$C'_i$  means that the corresponding electron ( $i = K, L, A$ ) has been produced by the photoelectric effect. If resonant  $\gamma$ -rays are photoelectrically absorbed by Mössbauer atoms, then  $C_K = C'_K$ .  $\omega_K C'_K$  is the probability of the photoeffect in the K-shell producing characteristic X-rays. If the sample contains several medium-Z elements whose characteristic X-rays have energies close to 6.5 keV, it may be assumed that the calculation of  $Q_x(E)$  requires one  $\nu_x$  value to be used and that all K-X-rays will be detected with equal probability. Each of the elements in the sample will be characterized by the linear coefficients  $\mu_{ph}$  and  $\mu_a^K$  and also the  $\omega_K C'_K$  factor. If low-Z or high-Z elements are present then the problem is more complicated. If the scatterer contains heavy elements, for example, uranium, the K- and L-X-rays will not be detected directly but will lead to the photoelectric effect on iron and its neighbour elements, and the detection of the corresponding K-X-rays. Another term must then be added then to (4.32). If the scatterer is, for example, beryllium with an iron admixture the calculation of  $Q_x(E)$  requires that only the photoelectric absorption of iron should be taken into account. Hence, in this simple case of evaluating the effect by detecting K-X-rays it is necessary to calculate the following:

$$Q_x(\infty) = \frac{\omega_K C'_K \mu_{ph}}{2 \nu_x} \hat{E}_2 \left[ \sum_{k=1}^2 \mu_a^K / \nu_x, \infty \right] \quad \text{and}$$

$$R_x(E) = f \left\{ P'_x(E) + \frac{\mu_{ph} \omega_K C'_K}{2 \nu_x} \left[ \hat{E}_2(\mu_a(E) / \nu_x, \infty) \right. \right.$$

$$- \hat{E}_2 \left\{ \left[ \sum_{k=1}^2 \mu_a^K / \nu_{X,\infty} \right] \right\} .$$

The  $\mu_{ph}$  value is determined by the photoeffect on iron and is just proportional to its content in the sample (see Table 4.3). The  $\mu_a$  coefficient is a sum of two terms: one is determined by the beryllium matrix whilst the other is determined by the admixture iron atoms.

The quantities characterizing the K-X-ray intensity of iron and of other X-rays which are indistinguishable by the energy are shown in Table 4.3. Since the photoelectric absorption cross section is considerably larger than the sum value of the Rayleigh scattering and the Compton scattering cross section, the  $Q_x(\infty)$  value turns out to be more, and the expected effect less, than on detecting  $\gamma$ -quanta (cf. the data of Table 4.1). The  $\xi$  parameter is prevented from increasing considerably because of competing non-resonant processes. This is true even when the scatterer is mainly of a substance capable of producing characteristic X-rays together with the K-X-rays of iron. This has been demonstrated by a hypothetical example of iron in samarium. It may seem somewhat unexpected that the effect is increased due to the strong dilution of the scattering substance by the light element. However, it follows from Table 4.3, that the effect value on line 3(4) of  $\alpha$ -Fe increases from 19 % to 22 % and 29 %, depending on the composition of technical beryllium.

Consider now the escape of electrons to the surface of a bulk sample. The photoeffect on K- and L-shells of Mössbauer atoms leads to the emergence of electrons with an energy equal to the energy of electrons produced by conversion electrons from these same shells.

The photoelectric effect on any atoms produces electrons that can be detected in CEMS. An expression similar to (4.32) is needed for quantitative evaluations. Let us analyze the escape of three groups of electrons, assuming that their attenuation follows the exponential law. The first two groups are directly generated by  $\gamma$ -quanta due to K- or L-shell electron conversion and to the photoelectric effect producing electrons of the same energy. The third group of electrons are the Auger electrons which follow the K-conversion, and electrons which are photoelectrically produced by the characteristic K-X-rays. The calculated results for  $^{57}\text{Fe}$  are presented in Tables 4.4 - 4.6.

Re-emission processes in CEMS are more difficult to account for. Recalling that  $\mu_R \ll \mu_r$ , an evaluation of the intensity of  $\gamma$ -quanta shows that it is sufficient to be restricted by  $P(E)$  (see (4.14)). The detection of electrons requires that the  $\mu_{ph}$  value be commensurable with  $\mu_r$ , and any of the  $\gamma$ -quanta produced in the first scattering event be photoelectrically absorbed with an appreciable probability.

Table 4.3

Parameters characterizing K-X-rays escaping the surface of bulk samples. K-X-rays are produced by resonant scattering and by the photoelectric effect (at resonance).

Table 4.3

Parameters characterizing K-X-rays escaping the surface of bulk samples. K-X-rays are produced by resonant scattering and by the photoelectric effect (at resonance).

Para- Units	meters	Scatterer																																																																																																																																																																																																																																																																																																																
-------------	--------	-----------	--	--	--	--	--	--	--	--	--	--	--	--	--	--	--	--	--	--	--	--	--	--	--	--	--	--	--	--	--	--	--	--	--	--	--	--	--	--	--	--	--	--	--	--	--	--	--	--	--	--	--	--	--	--	--	--	--	--	--	--	--	--	--	--	--	--	--	--	--	--	--	--	--	--	--	--	--	--	--	--	--	--	--	--	--	--	--	--	--	--	--	--	--	--	--	--	--	--	--	--	--	--	--	--	--	--	--	--	--	--	--	--	--	--	--	--	--	--	--	--	--	--	--	--	--	--	--	--	--	--	--	--	--	--	--	--	--	--	--	--	--	--	--	--	--	--	--	--	--	--	--	--	--	--	--	--	--	--	--	--	--	--	--	--	--	--	--	--	--	--	--	--	--	--	--	--	--	--	--	--	--	--	--	--	--	--	--	--	--	--	--	--	--	--	--	--	--	--	--	--	--	--	--	--	--	--	--	--	--	--	--	--	--	--	--	--	--	--	--	--	--	--	--	--	--	--	--	--	--	--	--	--	--	--	--	--	--	--	--	--	--	--	--	--	--	--	--	--	--	--	--	--	--	--	--	--	--	--	--	--	--	--	--	--	--	--	--	--	--	--	--	--	--	--	--	--	--	--	--	--	--	--	--	--	--	--	--	--	--	--	--	--	--	--	--	--	--	--	--	--	--	--	--	--

Table 4.3 (continued)

Notes:  $P_x'(E)$  is the probability of characteristic X-rays escaping the surface as a result of one resonant scattering\* event;  $P_x''(E)$  is the corresponding quantity for resonant re-scattering;  $Q_x(\infty)$  is the probability for K-X-rays to return to the bulk scatterer's surface off resonance;  $R_x(E)$  is the quantity determining the intensity at resonance;  $\xi$  is the intensity of non-resonantly scattered K-X-rays as a percentage of the resonantly scattered K-X-ray intensity.

\* monochromatic radiation,  $f = 0.7$ .

Table 4.4

Parameters characterizing electrons escaping the surface of bulk samples. The electrons are produced by K-shell conversion that follows the resonant scattering and by the K-shell photoelectric absorption - ( $\mu_{ph}(E)$ ) ( $\nu_K = 17.5 \mu\text{m}^{-1}$ ).

Parameters	Units	A scatterer of iron				
		$(\mu_a = 0.0504 \mu\text{m}^{-1}, \mu_{ph} = 0.0498 \mu\text{m}^{-1})$				
$\mu_r$	$\mu\text{m}^{-1}$	0.026	0.079	0.316	3.28	13.1
$fP_K'(E) \times 100$		0.02	0.06	0.24	2.2	6.8
$P_K''(E)$	% of $fP_K'$	0.9	-	2.3	-	2.6
$P_K(E)$	% of $fP_K'$	2.5	2	1.2	0.3	0.09
$\xi(E)$	%	0.22	0.22	0.21	0.21	0.20
$Q_K(\infty) \times 100$				0.063		
$\epsilon(E)$	%	32	96	380	3650	10 900

$P_K'(E)$  is the probability of K-conversion electrons escaping the surface as a result of one resonant scattering\* event;  $P_K''(E)$  is the corresponding quantity for resonant rescattering;  $P_K(E)$  is the probability of a re-scattered  $\gamma$ -quantum producing a photoelectron;  $Q_K(\infty)$  is the probability of the photoelectrons escaping the surface off resonance;  $\xi$  is the intensity of electrons produced in non-resonant channels relative to that of electrons produced in resonant channels when re-scattering is neglected.

\* monochromatic radiation,  $f = 0.7$ .

This will lead to the appearance on the surface of additional electrons or X-rays. The probability of such a process will be

Table 4.5

Parameters characterizing electrons escaping the surface of bulk samples. the electrons are generated by L-shell conversion following the resonant scattering and by the photoelectric effect producing electrons of approximately the same energy (monochromatic radiation ( $f = 0.7$ ) at resonance)

Para- meters	Units	Scatterer									
		Iron					Beryllium +1 at.% Fe				
a	%	2.14	2.14	2.14	2.14	2.14	2.14	2.14	90	90	90
$\mu_r$	$\mu\text{m}^{-1}$	0.026	0.079	0.316	3.28	13.1	0.00026	0.01	0.001		
$\nu_L$	$\mu\text{m}^{-1}$			6.9				1.6			
$\mu_{ph}$	$\mu\text{m}^{-1}$			0.0498				$5.2 \cdot 10^{-4}$			$6.9 \cdot 10^{-5}$
$fP'_L(E) \times 100$		0.007	0.021	0.083	0.68	1.65	0.0006	0.012	0.0025		
$P''_L(E)$	% of $fP'_L(E)$	0.9	1.7	2.6	3.0	3.2	-	-	-		
$P_L(E)$	% of $fP'_L$	17	14	8.4	1.9	0.6	-	-	-		
$\xi$	%	17.6	14.4	8.5	1.9	0.6	-	-	-		
$Q_L(\infty) \times 100$				0.022			0.002		0.00026		
$\varepsilon(E)$	%	32	95	375	3090	7500	30	610	9		

Table 4.5 (continued)

$P_L'(E)$  is the probability of L-conversion electrons escaping the surface as a result of one resonant scattering\* event;  $P_L''(E)$  is the corresponding quantity for resonant rescattering;  $P_L(E)$  is the probability of a re-scattered  $\gamma$ -quantum producing a photoelectron;  $Q_L(\infty)$  is the probability of the photoelectrons escaping the surface off resonance;  $\xi(E)$  is the intensity of electrons produced in non-resonant channels relative to that of electrons produced in resonant channels when re-scattering is neglected.

---

\* monochromatic radiation,  $f = 0.7$ .

denoted by  $P_i(E)$ , where  $i = K, L, A, x$ . Moreover, X-rays produced as a result of the first scattering event (the number of these being  $\alpha_K \omega$  times the number of  $\gamma$ -quanta) with a certain probability  $P_i'(E)$  may also lead to the appearance of photoelectrically produced electrons on the surface. For the Mössbauer effect in  $^{57}\text{Fe}$  these will be the Auger electrons and probability of such a process is  $P_i'(E) = P_A'(E)$ . All the three contributions of K, L or Auger electrons:  $P''(E)$ ,  $P_i(E)$  and  $P_i'(E)$  are mainly determined by the phase composition of the bulk and not by the surface layer of the sample.

The probability of the escape of electrons belonging to the first two groups is determined by the following equation:

$$\begin{aligned}
 P_i(E) = & \frac{f}{4(1 + \alpha)} c_i' \mu_{ph} \int_0^{\infty} \mu_r(E) e^{-\mu_a(E)x} dx \\
 & \left\{ \int_0^x dy \int_0^{\pi/2} \int_0^{\pi/2} \frac{\sin\theta \sin\theta_1}{\cos\theta} \exp \left[ -\mu_a y / \cos\theta \right. \right. \\
 & \left. \left. - \mu_i (x - y) / \cos\theta_1 \right] d\theta d\theta_1 + \int_0^{\infty} dy \int_0^{\pi/2} \sin\theta_1 d\theta_1 \right. \\
 & \left. \right\} \quad (4.33)
 \end{aligned}$$

$$\int_{\pi/2}^{\pi} \frac{\sin\theta \, d\theta}{|\cos\theta|} \exp\left[-\mu_a y / |\cos\theta| - \nu_i (x + y) / \cos\theta_1\right] \Bigg\} ,$$

$i = K, L.$

Table 4.6

Parameters characterizing a sample of iron ( $\mu_a = 0.0504 \, \mu\text{m}^{-1}$ ;  $\mu_{ph} = 0.0498 \, \mu\text{m}^{-1}$ ;  $\nu_A = 27 \, \mu\text{m}^{-1}$ ;  $\mu_r$  is variable) and the escape of electrons (whose energy is close originally to the  $\sim 5.5 \, \text{keV}$  Auger-electrons) from the surface of the bulk sample. The electrons are produced as a result of K-shell conversion following resonant scattering\*, by subsequent K-shell photoelectric absorption of re-scattered  $\gamma$ -quanta ( $P_A(E)$ ) and by L-shell photoelectric absorption of X-rays ( $P_A'(E)$ ) produced by resonant scattering.

Parameters	Units	Scatterer				
$\mu_r$	$\mu\text{m}^{-1}$	0.026	0.079	0.316	3.28	13.1
$fP_A'(E) \times 100$		0.0086	0.026	0.1	1.0	3.3
$P_A''(E)$	% of $fP_A'$	0.9	—	—	—	3.1
$P_A(E)$	% of $fP_A'$	3.4	2.7	1.8	0.4	0.13
$P_A'(E)$	% of $fP_A'$	18.8	13.5	9	2	0.7
$\xi(E)$	%	20.8	16.1	10.8	2.4	0.8
$Q_A(\infty) \times 100$		0.023	0.023	0.023	0.023	0.023
$\varepsilon(E)$	%	36	109	420	4200	13 900

$P_A'(E)$  is the probability of Auger- electrons escaping the surface as a result of one resonant scattering\* event;  $P_A''(E)$  is the corresponding quantity for resonant re-scattering;  $P_A(E)$  is the probability of a re-scattered  $\gamma$ -quantum producing a K- shell photoelectron;  $P_A'(E)$  is the probability of an X-ray following resonant scattering producing an L-shell photoelectron;  $Q_A(\infty)$  is the probability of the photoelectrons escaping the surface off resonance;  $\xi(E)$  is the intensity of electrons produced in non-resonant channels relative to that of electrons produced in resonant channels when re-scattering is neglected.

\* monochromatic radiation,  $f = 0.7$ .

The probability of interest, i.e. the probability of re-scattering, is determined by the product of the following probabilities. First, that a resonant  $\gamma$ -quantum will be scattered in a layer  $dx$  at depth  $x$ , and this probability is proportional to  $\mu_r(E) \exp[-\mu_a(E)x] dx$ . Second, that the photon produced by scattering, will travel a distance  $y/\cos\theta$  and will cause the photoelectric effect with a probability proportional to  $\mu_{ph} \exp(-\mu_a y/\cos\theta) dy/\cos\theta$ . If this is an X-ray quantum,  $\mu_a$  and  $\mu_{ph}$  should be replaced by  $\nu_x$  and  $\nu_{ph}$  respectively. Third, the probability that the electron produced reaches the surface by moving toward it at a certain angle  $\theta_1$ . Since the characteristic absorption length for  $\gamma$ -rays or X-rays ( $l_x = \nu_x^{-1}$ ; for  $^{57}\text{Fe}$   $l_x \sim 15 \mu\text{m}$ ) is much greater than the corresponding value for electrons ( $l_L = \nu_L^{-1}$ ; for  $^{57}\text{Fe}$   $l_L \approx 0.01 l_x$ ), the second integral in braces in (4.34) may be neglected since its contribution is proportional to the  $l_L/l_x$  ratio.

The intensity of Auger electrons produced by the secondary effects is determined by the photoelectric absorption of both  $\gamma$ -quanta  $P_A(E)$  and of X-rays -  $P_A'(E)$ , and may be evaluated using the following equation:

$$\begin{aligned}
 P_A(E) + P_A'(E) = & \frac{f}{4} \frac{(1 - \omega)}{(1 + \alpha)} C_K \mu_{ph} \int_0^\infty \mu_r(E) e^{-\mu_a(E)x} dx \\
 & \left\{ \int_0^x dy \int_0^{\pi/2} \int_0^{\pi/2} \frac{\sin\theta d\theta}{\cos\theta} \exp \left[ - \frac{\mu_a y}{\cos\theta} - \right. \right. \\
 & \left. \left. - \frac{\nu_A(x - y)}{\cos\theta_1} \right] \sin\theta_1 d\theta_1 + \frac{f}{4} \frac{\alpha_K \omega}{1 + \alpha} C_A' \nu_{ph} \right. \\
 & \left. \int_0^\infty \mu_r(E) e^{-\mu_a(E)x} dx \int_0^x dy \int_0^{\pi/2} \int_0^{\pi/2} \frac{\sin\theta d\theta}{\cos\theta} \right. \\
 & \left. \exp \left[ - \frac{\nu_x y}{\cos\theta} - \frac{\nu_A(x - y)}{\cos\theta_1} \right] \sin\theta_1 d\theta_1 \right. . \quad (4.34)
 \end{aligned}$$



On deriving (4.34) it was assumed that the non-resonant part of  $\mu_a(E)$  includes the interaction of the  $\gamma$ -quantum with all atoms in the scatterer. The photoelectric absorption is calculated for those atoms producing photoelectrons with an energy close to that of the Auger electron from iron. The absorption of all these electrons is characterized by the same total linear absorption coefficient  $\nu_A$ . The quantities  $\mu_{ph}$  and  $\nu_{ph}$  contain weighted contributions from all the processes which lead to the appearance of photoelectrons with similar energies. The rather complicated equation (4.34) may be considerably reduced and be written in the form:

$$\mathcal{P}_A(E) + \mathcal{P}'_A(E) = \frac{f}{4} \frac{\mu_r(E)}{\mu_a(E)} a(E) \hat{E}_2(a(E), \infty) \left\{ \frac{1 - \omega}{1 + \alpha} c_K \mathcal{F}(\beta(E)) + \frac{\alpha_K \omega}{1 + \alpha} c'_A \mathcal{F}(\beta'(E)) \right\},$$

where  $\mathcal{F}(\beta) = 1 - \beta(E) \hat{E}_2(\beta(E), \infty)$ ;  $\beta(E) = \mu_a(E)/\mu_{ph}$ ;  $\beta'(E) = \mu_a(E)/\nu_{ph}$ ;  $a(E) = \mu_a(E)/\nu_A$ . For non-resonant interaction

where  $F(\beta) = 1 - \beta(E) K_2(\beta(E), \infty)$ ;  $\beta(E) = \mu_a(E)/\mu_{ph}$ ;  $\beta'(E) = \mu_a(E)/\nu_{ph}$ ;  $a(E) = \mu_a(E)/\nu_A$ . For non-resonant interaction processes, following resonant scattering, one can speak of two subsequent scattering channels. One of them, as before, is characterized by the  $a(E)$  parameter and the other one is characterized by the  $\beta(E)$  (or  $\beta'(E)$ ) parameter which is essentially analogous to the  $a(E)$  parameter.

As it has been noted in Sect.3.2, the exponential attenuation of electrons is a fairly good approximation. Hence, the calculated results of Tables 4.4-6 are also approximate. Nevertheless, a comparison with the results from Monte Carlo simulations (see, e.g. [3.38]) shows a good agreement between the results obtained by the two methods. Effective procedures and the results of numerical calculations of the Mössbauer effect value have been given in [3.6,163]. The calculated areas under the spectra and intensities of electrons produced by resonant and non-resonant scattering were also detailed.

#### 4.4. Line Shapes and Intensity Ratios

In general, the intensity of radiation scattered at a relative velocity  $v$  is given by

$$I_1(\varepsilon) = I \int_{-\infty}^{\infty} J_M(E', \varepsilon) Q_1(E') dE'. \quad (4.35)$$

For monochromatic radiation  $J_M(E', E)$  should be replaced with  $f \delta(E')$  and the scattered intensity is then proportional to the probability of the radiation emerging from the surface. If this radiation has a Lorentzian distribution, the spectrum shape and line intensity analysis becomes considerably more complicated, since it results in saturation effects and in a change of the energy distribution of the incident radiation as it penetrates into the sample [4.9,16,17].

For incident monochromatic and Lorentzian distributed radiation, the intensity relations for elastically scattered  $\gamma$ -rays scattered from a bulk sample are:

$$I_r(\varepsilon) = \frac{\sqrt{1 + \mu_r/\mu_a}}{1 + \sqrt{1 + \mu_r/\mu_a}} P_r(E)$$

The left-hand and right-hand parts of the formula contain the formally different variables. However, these are one-to-one related - the maximum of the  $J_M(E', E)$  function on the energy scale corresponds to monochromatic radiation of energy  $E$ . For inelastically scattered  $\gamma$ -rays

$$I_{rn}(\varepsilon) = \frac{\sqrt{1 + \hat{E}_2(1) \mu_r/\mu_a}}{1 + \sqrt{1 + \hat{E}_2(1) \mu_r/\mu_a}} P_{rn}(E)$$

Thus, the intensities become equal only at  $\mu_r \gg \mu_a$ . When the enrichment in the resonant isotope is low ( $\mu_r \ll \mu_a$ ) the intensity of the resonantly scattered  $\gamma$ -quanta will be twice as large if the incident resonant radiation is monochromatic.

Let us discuss the general features of Mössbauer spectra obtained by the detection of  $\gamma$ -quanta assuming that the radiation is scattered isotropically. The spectrum  $I(E)$  from a bulk sample when only single scattering occurs and when interference effects are neglected may be considered as a sum of partial spectra due to resonant scattering channels and scattering from electrons. The partial spectrum  $I_r(E)$  corresponding to elastic resonant scattering is described by the expression

$$I_r(\varepsilon) = \frac{f'}{2(1 + \alpha)} \frac{\mu_r}{\mu_a} \hat{E}_2(1, \infty) \int_{-\infty}^{\infty} \frac{L(E - \varepsilon) dE}{1 + \mu_r/\mu_a + E^2}, \quad (4.36)$$

which is a convolution of two Lorentzians with widths  $\Gamma$  and  $\Gamma\sqrt{1 + \mu_r/\mu_a}$ . The result may also be considered as Lorentzian but the width is summary. The contribution to the total spectrum is positive, i.e. it corresponds to a peak.

$\gamma$ -Rays may also be elastically scattered by electrons and the line shape of the corresponding partial spectra is then determined by the expression:

$$I_{Rr}(\varepsilon) = \frac{f_R}{2} \frac{\mu_R}{\mu_a} \hat{E}_2(1, \infty) \int_{-\infty}^{\infty} L(E - \varepsilon) \left[ 1 - \frac{\mu_r/\mu_a}{1 + \mu_r/\mu_a + E^2} \right] dE. \quad (4.37)$$

The right-hand part of (4.37) consists of two summands. The first contributing only to the background. The second describing the partial spectrum similar to the elastic resonant scattering spectrum (see (4.36)), but has a dip on resonance as in transmission experiments.

To consider the partial spectra from inelastic scattering channels the  $K_2(a(E), \infty)$  function should be analyzed as a function of energy (Fig.2.28). On detecting  $\gamma$ -quanta,  $a(E) > 1$  and may be written

$$\hat{E}_2(\mu_a(E)/\mu_a, \infty) = \hat{E}_2(1, \infty) [1 - f(E)], \quad (4.38)$$

where  $f(E)$  is a positive centrally symmetric function, decreasing as the distance from the symmetry centre  $E_a$  increases,  $0 < f(E) < 1$ . As a first approximation, the  $f(E)$  function may be assumed to be Lorentzian.

The inelastic resonant scattering spectrum is the difference of the two subspectra:

$$I_{rn}(\varepsilon) = \frac{1 - f'}{2(1 + \alpha)} \frac{\mu_r}{\mu_a} \hat{E}_2(1, \infty) \int_{-\infty}^{\infty} \frac{L(E - \varepsilon) [1 - f(E)]}{1 + E^2} dE. \quad (4.39)$$

The first subspectrum is described by a convolution of two Lorentzians and the second subspectrum by three Lorentzians, the  $f(E)$  function being the third Lorentzian. The convolution of the three Lorentzians produces a line with a shape similar to that of the Lorentzian of width  $1.4 \Gamma$ . Subtraction of a narrower line from a wider one, when the centres of gravity coincide, leads to a broadening of the resulting line. Since  $f(E) < 1$ , the resulting spectrum has a peak.

The partial spectrum corresponding to inelastic scattering by electrons is given by the following equation:

$$I_{Rn+C}(\varepsilon) = \frac{(1 - f_R)\mu_R + \mu_C}{2\mu_a} \hat{E}_2(1, \infty) \int_{-\infty}^{\infty} L(E - \varepsilon) [1 - f(E)] dE, \quad (4.40)$$

which is similar in structure to (4.37). This means that the shape of the spectrum is also similar to the spectrum shape obtained from transmission experiments.

Addition of the four partial spectra, three of which are different in their shape, may produce an unusual spectrum. Calculations have shown that for bulk scatterers of iron with abundances ranging between 2.14 % and 90 %, the line shape departures from Lorentzian are not large for inelastic scattering channels. To a first approximation these lines may be extrapolated by the same Lorentzian with a width which is less than that of the line corresponding to elastic scattering channels. At certain relations between  $\mu_r$ ,  $\mu_R$ ,  $\mu_a$ ,  $\mu_C$ ,  $f$ ,  $f'$  and  $f_R$  parameters, the resonant and non-resonant contributions may compensate one another. On scanning the spectra there will be no change of the scattered intensity observed.

The evolution of the resulting spectra may be observed during studies of spectra recorded from bulk scatterers with a low abundance of the resonant isotope ( $\mu_r/\mu_a \ll 1$ ). The detection of  $\gamma$ -quanta from these scatterers characterized by different  $\mu_r/\mu_a$  ratios enables the line shape evolution from the spectral shape typical of scattering experiments to that typical of transmission ones to be examined. The  $K_2(a(E), \infty)$  function may now be expanded into the series, where only the first two terms are left

$$\hat{E}_2(a(E), \infty) = \hat{E}_2(1, \infty) + \hat{E}_2'(1, \infty) \frac{\mu_r}{\mu_a(1 + E^2)}.$$

Under these conditions the  $f(E)$  function in (4.38) has an exactly Lorentzian shape and it is possible to perform integration in the corresponding equations for the partial spectra. Restricting ourselves to the main contribution to the spectrum we have:

$$I(\varepsilon) = \frac{\mu_r}{\mu_a} \frac{\hat{E}_2(1, \infty)}{4 + \varepsilon^2} \left[ \frac{1}{1 + \alpha} - \left\{ \frac{f_R \mu_R}{\mu_a} + \frac{(1 - f_R)\mu_R + \mu_C}{\mu_a} \right. \right. \\ \left. \left. \frac{\hat{E}_2'(1, \infty)}{\hat{E}_2(1, \infty)} \right\} \right] + \text{Const} + o \left( \left[ \frac{\mu_r}{\mu_a} \right]^2 \right).$$

The main part of the spectrum is a Lorentzian of doubled width. At a certain relation between the linear coefficients, non- resonant scattering channels may determine the line shape. Thus, for iron-bearing compounds, when the condition  $\mu_C + \mu_R > 0.15 \mu_a$  is satisfied the spectral shape is similar to that of transmission spectra. This is the case, for example, for beryllium, where iron is an admixture.

In reality, the angular distribution of the scattered  $\gamma$ -radiation is not isotropic, since each of the partial scattering channels has an angular distribution of its own. Expression (2.81) for the intensity of the scattered radiation becomes more complicated [4.18,19]. Let us neglect the interference effects considered in Chapter 2. For a substance characterized by the isotropic Lamb- Mössbauer factor and in the absence of texture, the  $I_r(v)$  and  $I_m(v)$  terms are proportional to the  $W(\theta)$  directional correlation function (see (2.50)). As already noted in Chapter 2, the angular dependence of  $\gamma$ -radiation due to Rayleigh scattering when the incident radiation is not polarized may be written as a product of the atomic form factor and the polarization factor

$$w(\theta) = F^2(\theta)(1 + \cos^2\theta) .$$

The atomic form factor is known from the X-ray scattering literature and gives the scattering amplitude relative to that of the single-electron scattering [1.10,11]. Furthermore, even for an isotropic crystal the Debye-Waller factor  $f_R$  is angular dependent, and, if the sample consists mainly of Mössbauer atoms, it can be shown [4.19] that

$$f_R = \exp(4 \sin^2(\theta/2) \ln f) .$$

For the sample where there is no level splitting due to hyperfine interactions, the intensity of radiation resulting from Mössbauer and Rayleigh scattering may be written in the form:

$$\begin{aligned} I(v) &= w(\theta) [ I_r(v) + I_{rn}(v) ] + w(\theta) [ I_R(v) + I_{Rn}(v) ] \\ &= C_1 [ 1 + 0.125 G_2(3 \cos^2\theta - 1) + C_2 F^2(\theta) (1 + \cos^2\theta) \\ &\quad \exp(4 \sin^2(\theta/2) \ln f) + C_3 F^2(\theta) (1 + \cos^2\theta) ] , \end{aligned}$$

where  $C_1$ ,  $C_2$  and  $C_3$  are constants. The calculated functions are presented determining the angular dependences:  $w'(\theta)$  (see (2.37));  $w(\theta)$  and  $v(\theta) = f_{RW}(\theta)$  in Fig.4.2 on a semilogarithmic plot. For comparison, in the same Figure in the linear scale, the plot is given of the  $W(\theta)$  function.

The calculations are made for a Ni-Cr stainless steel for which  $C_2 = 0.5$  and  $f' = 0.74$ . Thus, unlike Mössbauer scattering which is symmetric relative to  $\theta = 90^\circ$ , Rayleigh scattering makes the greatest contribution to forward-scattering by the angle  $\theta < \theta_0$  (see (2.36)). However, even on scattering at large angles the contribution of Rayleigh scattering to the Mössbauer spectra cannot be neglected.

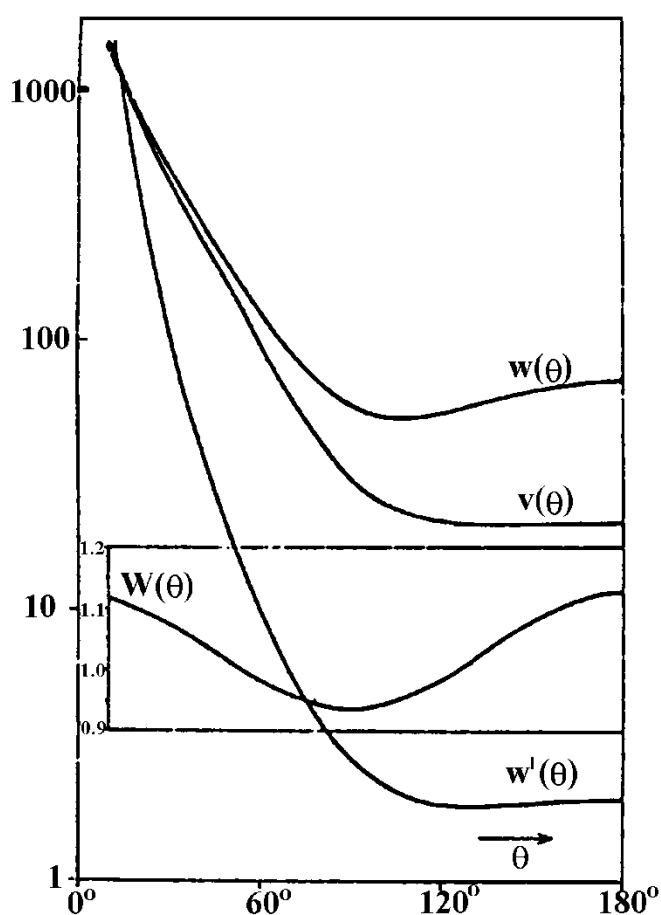


Fig.4.2 Angular dependences characterizing Rayleigh scattering:  $w'(\theta)$ ,  $w(\theta)$  and  $v(\theta)$  (the semilogarithmic plot), and Mössbauer scattering  $W(\theta)$  (the linear plot, inserted) (from [4.19]).

Thus, it is only in transmission Mössbauer spectroscopy that the effect value, if the proper corrections are made, is a monotonously increasing function of the sample thickness and approaches saturation. In scattering experiments the competition of resonant and non-resonant scattering channels results in a reduction of the observed effect value as the sample thickness increases. The greater the conversion coefficient and the larger the number of "non-resonant" atoms in the sample, the more "efficient" appear the non-resonant scattering channels and this leads to the emergence of  $\gamma$ -quanta. As a consequence, the effect value may even change its sign.

On detecting characteristic X-rays a similar effect takes place but it is less strongly manifested and does not result in such a sharp change of the line shape. This is illustrated by the spectra shown in Fig.4.3 [4.2]. Beryllium scatterers

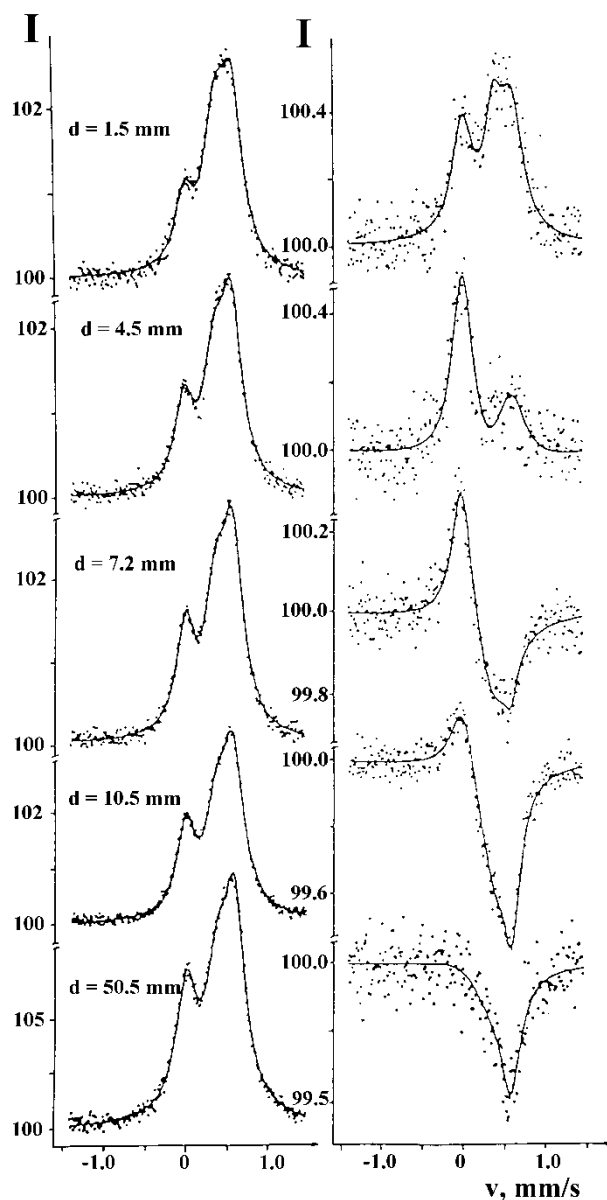


Fig.4.3 Mössbauer spectra of iron impurities in beryllium plates, recorded simultaneously in the same geometry and by the same detector. a - X-ray detection; b -  $\gamma$ -ray detection (from [4.2]).

containing iron impurities were used which gave transmission spectrum showing an asymmetric doublet. Spectra of beryllium plates were recorded at a scattering angle of  $130^\circ$ . A pulse shape discriminator [4.2] was used to separate the signals corresponding to the K-X-rays of iron and the Mössbauer

radiation enabled two spectra to be recorded simultaneously with the same detector. The spectra recorded by X-ray detection are shown in Fig.4.3a, and those by  $\gamma$ -ray detection in Fig.4.3b. Whereas the shapes of the scattering spectra in Fig.4.3a are independent of the scatterer thickness, the line shape of Fig.4.3a changes drastically according to sample thickness. These changes depend both on the scatterer thickness and the  $\mu_r/\mu_a$  ratio. The change is larger for the right hand side line of the spectrum for which  $\mu_r$  is greater. For the observed effect value to become zero on detecting X-rays or electrons, quite specific conditions should be fulfilled. Thus, if X-rays are detected, the condition is

$$\frac{\mu_a}{\nu_x} \frac{\hat{E}'_2(a, \infty)}{\hat{E}_2(a, \infty)} > \frac{\alpha}{1 + \alpha}.$$

For  $^{57}\text{Fe}$  it is equivalent to the requirement  $\mu_a/\nu_x > 20$ . A similar condition appears when electrons are detected. It is evident that there are no Mössbauer isotopes for which such conditions could be fulfilled. On detecting electrons, the above effect may be neglected due to the small depth of the analyzed layer, but quite a specific circumstance should be taken into account since there is a substantial contribution from the signal from the bulk of the sample to the signal from the surface layer. The lower the  $\mu_r(E)$  value, the greater the role of this effect.

For a non-enriched bulk iron-bearing sample  $a(E) \ll 1$  and  $\hat{E}_2(a(E), \infty) \approx 0.5$ . This allows the equation for the total beam of electrons produced by a monochromatic radiation to be written in the simple form

$$\sum_i^{K,L,A} P'_i(E) = \frac{\mu_r(E)}{4} f \left[ \frac{c_K}{\nu_K} + \frac{c_L}{\nu_L} + \frac{c_A}{\nu_A} \right] \approx 0.0279 \mu_r(E),$$

where  $\mu_r(E)$  is given in  $\mu\text{m}^{-1}$ . For an enriched sample, e.g.  $\alpha\text{-}^{57}\text{Fe}$ , the electron beam intensity produced due to resonant scattering in the bulk with an accuracy better than  $\approx 5\%$  may also be written in a fairly simple form

$$I_i = I_0 \frac{c_i}{8} \frac{\mu_r}{\nu_i} \left[ 1 - 0.3 \frac{\mu_r}{\nu_i} - 0.4 \frac{\mu_a}{\nu_i} \right]. \quad 2.$$

The intensities are given of X-rays and K- and L- conversion and KLM- and KLL-Auger electrons produced as a result of resonant scattering in a bulk sample of



non-magnetic iron in Table 4.7. The incident radiation is monochromatic or has a Lorentzian energy distribution. Similar to the detection of  $\gamma$ -quanta, the intensity ratio  $\eta_i$  changes from unity at  $\mu_r \gg \nu_i$  to 0.5 if  $\mu_r \ll \nu_i$ .

Table 4.7

The relative intensities of X-rays, K- and L-conversion and KLM- and KLL-Auger electrons produced as a result of resonant scattering in a bulk sample of non-magnetic Fe

The energy distribution of the incident radiation	<sup>57</sup> Fe abundance %	The relative intensities			
		K X-rays	K-conversion electrons	L-conversion electrons	KLM and KLL-Auger electrons
Monochromatic	2.2	0.052	0.0024	0.00083	0.001
	90	0.091	0.068	0.0165	0.033
Lorentzian	2.2	0.03264	0.0012	0.000415	0.0005
	90	0.079	0.0375	0.00975	0.017

#### 4.5. The Quality of a Mössbauer Spectrum

In Mössbauer spectroscopy, especially in surface studies, a single technique either scattering or transmission one should be chosen. The reason is that the amplitude of Mössbauer lines in scattering experiments can often be greater than in a transmission geometry ( $\epsilon < f'$ ). However, the intensity loss of the scattered radiation of about two orders of magnitude makes it necessary to compare both the sensitivity of the two methods and the quality of the two spectra obtained.

The quality of a spectrum is directly related to the quantity of information contained in the spectra. If a thin sample ( $t \ll 1$ ) is under investigation the quality of the spectra is initially related to the thickness of the sample. This can be illustrated by transmission experiments. For the thin absorber described by (1.36) we have

$$I_i = I(\infty) (1 - p_i t_a),$$

where  $p_i = \epsilon_i/t_a$  - is the observed effect magnitude in an  $i$ -th channel of a storage device (MCA) for this particular sample normalized to the sample of a unit effective thickness. By definition, the information matrix element of interest,  $J$ , may be written as:

$$[\hat{J}]_{t_a, t_a} = \frac{1}{I(\infty)} \sum_{i=1}^N \left[ \frac{\partial I_i}{\partial t_a} \right]^2 = I(\infty) \sum_{i=1}^N p_i^2. \quad (4.41)$$

For real samples, the accuracy of determining the effective thickness is proportional to the quantity

$$\varphi^{-1/2} = \left[ I(\infty) \sum_{i=1}^N \varepsilon_i^2 \right]^{-1/2}. \quad (4.42)$$

For a thin sample characterized by a single Lorentzian with a full width at half maximum  $\Gamma$ , the summation in (4.42) is easy to make, and turns out to be

$$[\hat{J}]_{t_a, t_a} = \frac{\pi}{4} \varepsilon^2(0) I(\infty) \Gamma, \quad (4.43)$$

where  $\Gamma$  is given by the number of channels of the MCA used to obtain the spectrum. Thus, the quality of the spectrum in relation to the quantity of information on the  $t_a$  parameter given by (4.41) may be described by fairly simple expressions. In practice, the quality of the spectrum must be related to several parameters simultaneously. In addition, for scattering experiments which are of prime interest, the effect magnitude is related to the  $t_a$  parameter by a more complex dependence as compared with that in transmission experiments. Nevertheless, expressions like (4.42) and (4.43) are often used for such evaluations.

In order to increase the effect, the experimentalist needs to decrease the solid angle towards the detector and sample to prevent the source radiation from reaching the detector as a result of multiple non-resonant scattering in collimators and surrounding materials. This always gives a greater  $\varepsilon_i$  value, but the  $I(\infty)$  is decreased. Expression (4.43) allows the evaluation of the limit when a further increase of  $\varepsilon_i$  values is no longer reasonable. After the optimal experimental conditions are chosen for the particular series of samples, the  $\varepsilon^2(0)$  values are fixed for each sample under investigation. The quality of the spectrum is determined by the product  $I(\infty)\Gamma$  and, as well as  $I(\infty)$ , is also proportional to the measuring time.

In practice, the evaluation of the effect magnitude is of prime interest. For a spectrum which is a single Lorentzian line, the corresponding element of the information matrix is written in the form

$$[\hat{J}]_{\varepsilon, \varepsilon} = \frac{\pi}{4} I(\infty) \Gamma.$$

The standard deviation in evaluations of  $\varepsilon$  (defined as a square root of the variance) is  $\sigma_\varepsilon = 2 / \sqrt{\pi I(\infty) \Gamma}$  and the relative standard deviation is

$$\delta_\varepsilon = \frac{2}{\sqrt{\pi \Gamma}} \frac{1}{\varepsilon \sqrt{I(\infty)}}. \quad (4.44)$$

This deviation can also be found directly from (1.36):

$$\Delta = \frac{\Delta \varepsilon}{\varepsilon} = \frac{\sqrt{I(\infty) + I(0)}}{\varepsilon I(\infty)} + \frac{1}{\sqrt{I(\infty)}} \approx \frac{\sqrt{2}}{\varepsilon \sqrt{I(\infty)}} \quad (4.45)$$

(for  $\varepsilon \ll 1$ ).

Thus, the two expressions obtained via the information matrix (4.44) and directly (4.45) coincide within the accuracy of the constant. They determine the signal-to-noise ratio but (4.44) does it by taking the whole spectrum into account whilst (4.45) derives the ratio from the amplitude of the signal (see (4.29)).

The effectiveness of fitting criteria often involves a consideration of the quantity  $S$  (see (4.42)) as a measure of the quality of the spectrum, and the error in its determination is  $\Delta S = 2\sqrt{S}/4$ . The less the relative standard deviation in determining  $\varepsilon$ , the greater the signal-to-noise ratio and the higher the quality of the spectrum. A similar approach has been developed in [2.45, 4.20, 21]. At  $\varepsilon \ll 1$  the standard deviations are proportional to  $\delta_\varepsilon$ , and the quality of the spectrum is inversely proportional to  $S$ . If, as suggested in [3.29], the relative standard deviations in transmission experiments be  $\Delta_a$ , and those in scattering experiments be with the upper indices  $\Delta^{e,x,\gamma}$ , where  $e$ ,  $x$ , and  $\gamma$  stand for the detection of electrons, X-rays and  $\gamma$ -quanta, respectively, and  $\Delta_a^2 = 2/(\varepsilon^2 I(\infty))$  (if  $\varepsilon < 0.2$ ), and  $(\Delta^{e,x,\gamma})^2 = 1/I(0)$  (if  $\varepsilon > 5$ ). The question often arises as to whether transmission experiments or CEMS are most expedient for obtaining a spectrum of a given quality. The ratio of the relative standard deviations may be written as:

$$\left[ \frac{\Delta_a}{\Delta^e} \right]^2 = \frac{4 \Omega \alpha}{f' t_a (1 + \alpha)}, \quad (5.6)$$

where  $\Omega$  is the solid angle normalized to  $4\pi$  within which the backscattered radiation is detected. CEMS appears to be preferable if the electrons are collected within a solid angle satisfying the condition

$$\Omega > \frac{f' t_a (1 + \alpha)}{4 \alpha}.$$

Even at  $f' = 1$ , this condition is equivalent to the solid angle being greater than  $\pi$ , since  $t_a < 1$  when electrons are detected. The condition  $\Omega > \pi$  is easily attained in practice. In practice the requirements are much less rigid.

The advantages of CEMS (at  $\varepsilon \gg 1$ ) over transmission spectroscopy are demonstrated in Fig.4.4 which corresponds to single lines in both the source and sample using the same source-detector distance and measuring time. The hatched area

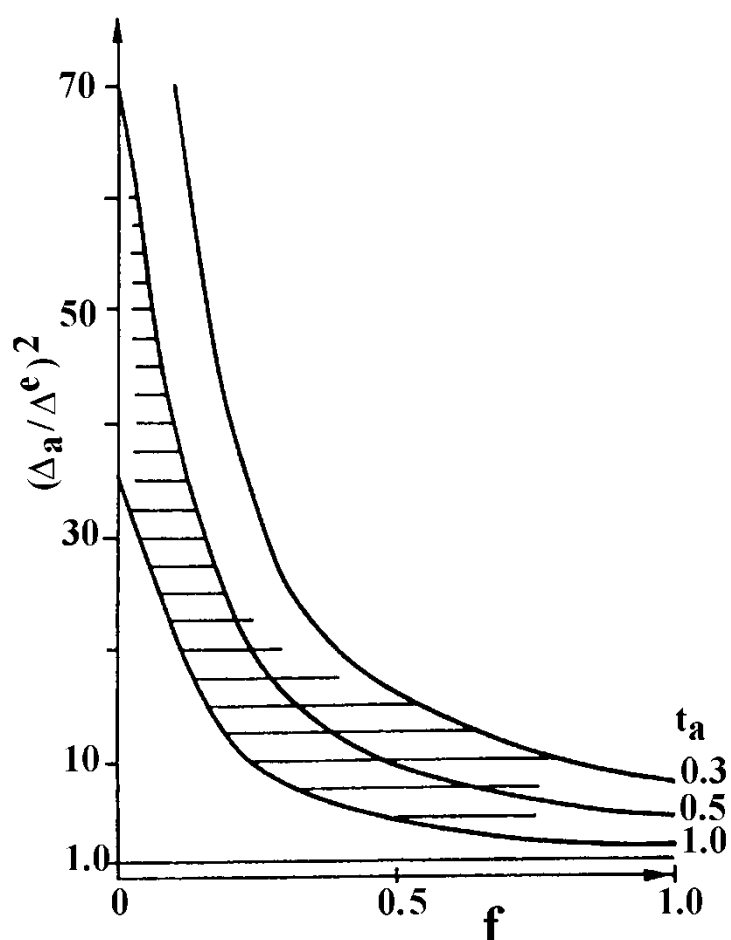


Fig.4.4 Relative standard deviations in transmission experiments and in CEMS for  $^{119}\text{Sn}$  as a function of the factor  $f$  of the source (from [3.29]).

shows the interesting values of the Lamb-Mössbauer factor of the source:  $f = 0.05 - 0.8$  for relatively thin samples ( $0.3 < t_a < 1.0$ ), where line broadening may be neglected.

Since the time required to achieve a given statistical accuracy is proportional to  $\Delta^2$  then, in accordance with Fig.4.4, the advantages of CEMS are evident. This is of practical significance in emission Mössbauer spectroscopy where the  $f$  factor may be small, especially, in experiments on ion implantation. That is why resonance detectors are widely used in emission Mössbauer spectroscopy.

If a spectrum consists of two closely positioned lines, so as  $I_1 \gg I_2$ , then for the resolution of the lines CEMS or resonance detectors are most convenient. Indeed,

$$\left( \frac{\Delta_a}{\Delta_e} \right)_2 = \sqrt{\frac{I_1}{I_2}} \left( \frac{\Delta_a}{\Delta_e} \right)_1 ,$$

i.e. the accuracy of determining the second line increases by a factor of  $\sqrt{I_1/I_2}$ .

The detection of electromagnetic radiation gives rise to a different situation. The detection of characteristic X-rays requires the solid angle to be  $\Omega > f t_a (1 + \alpha)/4 \alpha \omega$ , whilst that for the detection of  $\gamma$ -quanta is  $\Omega > f' t_a (1 + \alpha)/4$ . It can be seen that, starting from not very large values of  $f'$  and  $t_a$  parameters, the right-hand parts of the relations become greater than 0.5 such that the relative standard deviation of transmission experiments are less. This is because the solid angle  $\Omega$  cannot exceed  $2\pi$ .

For the experimental geometry shown Fig.2.7, the ratio of the quality parameters  $S_a/S^y$  of the first lines of the  $\alpha$ -Fe and haematite sextets in transmission and scattering experiments are presented in Fig.4.5 [2.45]. This situation is unfavourable for scattering experiments (due to the small  $\Omega$  values), and  $S^y > S_a$  only for thin ( $\sim 0.4 \mu\text{m}$ ) and very thick ( $> 100 \mu\text{m}$ ) samples. On increasing the solid angle for the scattered radiation or decreasing the  $f$  and  $f'$  values, the area where  $S_a > S^y$  narrows sharply and then disappears.

The problem of separating signals of interest from the spectrum and problems of statistical accuracy are very important in Mössbauer spectroscopy. This is partly due to the limited strength of Mössbauer sources and the fact that the intensity of the detected scattered radiation is generally only a small fraction of the incident intensity. At the same time, great care should be taken in attempting to diminish the source - sample distance which enhances the statistical accuracy. This can be considered in terms of a source whose radius is  $R$  allowed to move at a velocity  $v$  and emitting monochromatic  $\gamma$ -quanta. Let the source - sample distance be  $d$ . Radiation emitted within the solid angle  $\Omega$  specified by the directions at

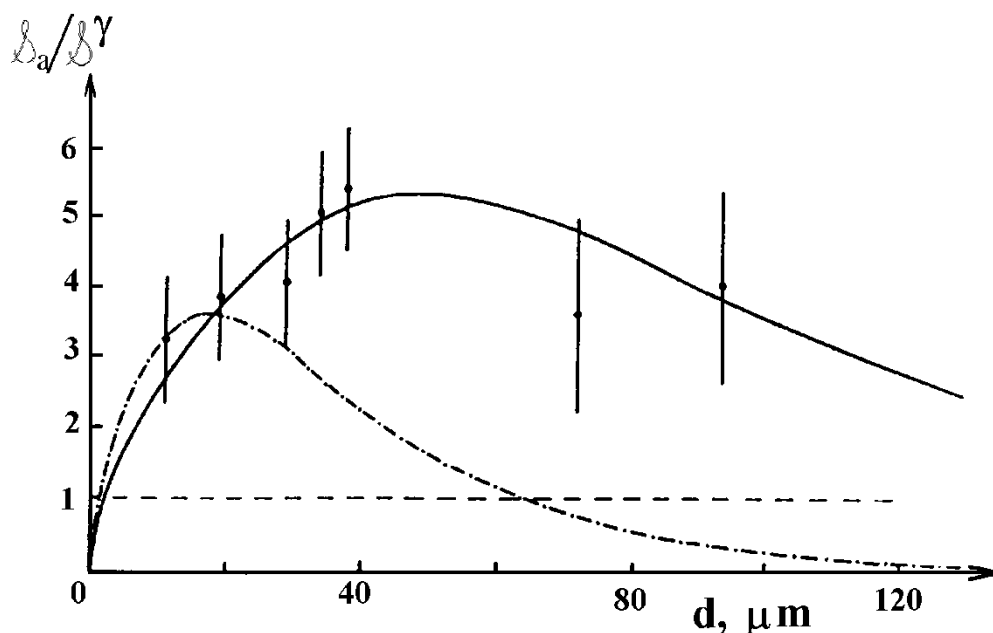


Fig.4.5 The ratios of the line quality parameters  $S_a/S^\gamma$  for the first lines of the Mössbauer spectrum of iron and haematite ( $a = 2.14\%$ ) of various thicknesses using the experimental geometry of Fig.2.7: solid line - haematite; dot-dashed line corresponds to calculations for  $\alpha\text{-Fe}$ ; dots are experimental data. Above the dashed line the transmission geometry is preferable. (from [2.45]).

an angle  $\theta$  to the source surface normal, may reach the surface of the sample. However, in reality the sample will be irradiated by a beam smeared by an amount  $\Delta E = Ev(1 - \cos\theta)/c$ . The result is a broadening of the lines, a deviation of their shape from Lorentzians and a shift of the line positions towards the spectrum centre and a decrease of the effect. Further increases in the  $\Omega$  value result in the lines becoming asymmetric. In transmission spectroscopy the solid angle is actually specified not by the source - sample distance but by the source - detector distance. In scattering spectroscopy everything is determined by the source - sample distance. For a source and sample of the same size, the Mössbauer spectra distortions become significant at  $d < 20 R$ .

#### 4.6. Quantitative Information from Mössbauer Spectra

In spectroscopy, the intensity of the detected radiation may be written in the form:

$$I(E) = C \int_{-\infty}^{\infty} L(E - E') \phi(E') dE' + \xi(E) \quad (4.46)$$

where  $E$  is an energy parameter depending on the experimental set-up,  $E$  is the current energy value,  $L(E - E)$  is the instrumental line,  $\varphi(E)$  is a function describing the response of the substance under investigation to monochromatic radiation, and  $\xi(E)$  is the noise due to the stochastic nature of radioactive decay and the interaction of the radiation with matter.

In Mössbauer spectroscopy, any sample is characterized by a unique function  $\mu_a(E)$ . Each i-phase or each j-non-equivalent position of resonant atoms within a given phase are characterized by their own total linear absorption coefficient  $\mu_{ai}(E)$ . The sum of these coefficients is the  $\mu_a(E)$  function. The simplest situation for recovering the  $\mu_a(E)$  function from experimental data is in transmission spectroscopy if all the phases are homogeneously distributed within the homogeneous sample volume. On evaluating the contribution of each phase to the total spectrum, the same instrumental line may be used.

In scattering spectroscopy the phase composition may often vary with the distance from the surface and  $\mu_a(E) = \mu_a(E, x)$ . If within a layer  $dx$  there is one only phase then

$$\mu_a(E, x) = \mu_a(x) + \mu_r(E, x) .$$

Let the chemical composition of the sample under investigation be known and the  $\mu_a(x)$  values be obtained from tables (e.g. [1.17, 2.1]).

The experimentalist is interested in depth-phase analysis with the first step being the recovery of the  $\mu_r(E, x)$  function from the spectra. The instrumental line in Mössbauer spectroscopy may be assumed to be Lorentzian. However, the energy distribution of the incident radiation is depth-dependent.

At present, techniques have been developed for the analysis of Mössbauer spectra making use of iterative procedures. Generally they refer to Mössbauer transmission spectra and there is a large body of literature in this field (e.g. [1.13-18, 4.22-26]). An experimentally observed spectrum may be described by the function:

$$I'(\varepsilon) = C_1 \int_{-\infty}^{\infty} L(E - \varepsilon) \exp[-\mu_a(E)d] dE + C_2 ,$$

$$C_1 = \frac{2f}{\pi\Gamma} I_0 , \quad C_2 = (1 - f) I_0 \exp(-\mu_a d) .$$

The constant  $C_1$  is determined by the  $\gamma$ -quanta incident on the sample and by the factor  $f$ ; the constant  $C_2$  is determined by the fraction of  $\gamma$ -quanta emitted with recoil. The two constants can be found from ancillary experiments, and the line shape may be written as

$$I(\varepsilon) = \frac{I'(\varepsilon) - c_2}{c_1} = \int_{-\infty}^{\infty} L(E - \varepsilon) \exp[-\mu_a(E)d] dE . \quad (4.47)$$

There are two ways to find the  $\mu_a(E)$  function. The first involves a hypothesis concerning the nature of this function. Analysis of an experimental spectrum amounts to the determination of the parameters characterizing the  $\mu_a(E)$  function in accordance with the hypothesis. The second way is connected with natural assumptions only on the nature of the  $\mu_a(E)$  functions, for example, on their smoothness. Although this way does not require any hypothesis, some additional physical information and/or assumptions on relations between hyperfine interaction parameters are required.

Using the first way it is desirable to use sufficiently thin sample. Neglecting re-scattering effects, equation (4.47) may be written in the form:

$$I(\varepsilon) = A_0 - d \int_{-\infty}^{\infty} L(E - \varepsilon) \mu_a(E) dE , \quad (4.48)$$

where the series expansion is used (see (2.9) and (2.14)) with all terms, except the first two, neglected. The line width appears to be a function of the sample thickness. If the  $\mu_a(E)$  function is presented as a sum of two Lorentzians then, after integration over  $E$  in (4.48),  $I(E)$  may be written as a sum of Lorentzian peaks:

$$I(\varepsilon) = A_0 - \sum_{i=1}^m \frac{A_i \Gamma_i^2 / 4}{(E_i - \varepsilon)^2 + \Gamma_i^2 / 4} ,$$

where  $m$  is the total number of lines. The parameters to be evaluated are:  $A_i$ , the line amplitudes;  $\Gamma_i$ , the observed line widths;  $E_i$ , the line positions. The approach whereby hyperfine interaction parameters are varied and physically motivated constraints are imposed on the amplitudes, positions and line widths is more generally used.

For a thick absorber ( $\mu_a(E)d > 1$ ) equation (4.47) should be used. The required parameters are in the integrand and their change gives rise to certain problems [1.16,18]. Thus, the parameter values obtained may depend for example, on the method used to compute the integral. This approach allows the  $\mu_a(E)$  function to be recovered and simultaneously the effective thickness of the sample determined (which includes the  $f'$ -factor).



There are simple expansions of the transmission integral. The approximation presented e.g. in [4.27] is model independent and would be applied to accurate, quantitative analysis of Mössbauer spectra, affected by the thickness effect. Simultaneous fitting of complementary Mössbauer spectra to the exact line shape has been shown [4.28] to be most useful method for directly extracting the values of basic physical parameters associated with the Mössbauer line shape. This representation of the line shape in terms of fundamental physical parameters produces physical values directly and without approximation.

The second approach usually involves the following principles. If there are no grounds for choosing a hypothesis, a certain initial assumption is made as to the nature of the required function. This often amounts to a search for an expression describing the response of the medium to monochromatic radiation, and sometimes "an enhanced resolution of the method" is spoken of. The idea is that the best quality of the spectrum is attained using a source with a line shape described by the  $\delta$ -function. Recently, a new method of "restoration and enhancement of the image quality" has been developed [4.29,30]. This approach is analogous to the method of solution of incorrect problems [4.31] and allows a diminution of the distortions brought in by the measuring instrument.

It should always be born in mind that a reduction of the observed line width (even in simple spectra) by an amount close to the instrumental line width is accompanied by increased noise and distortions in the transformed spectrum. If the transform operator is correctly chosen and low-pass filters are applied, the loss of information amounts to a two-fold increase of the standard deviation [4.32] in every point of the spectrum described by equation (4.46). A thorough analysis of the situation in Mössbauer spectroscopy has shown [4.33,34] that the formalism of [4.29,30] allows a significant advancement in the analysis of experimental spectra. As a result, a new technique has been developed which allows the resolution to be enhanced at a controlled noise level in the transformed spectrum, though at the price of giving up the restrictions imposed on the line shape of the source.

Within the framework of the second approach the presentation of the information contained in Mössbauer spectra is given in a form which is convenient for checking the structure of the sample. An example is a distribution diagram for some parameters of hyperfine interactions ( $H_{\text{eff}}$ ,  $\phi_{\text{zz}}$  and  $\delta$ ) obtained from the experimental spectra and used to find the configuration of the environment of the Mössbauer atoms in the object under study and the relative probabilities of the configurations occurring.

Most often it is assumed that one of the distributions, as a rule  $P(H_{\text{eff}})$ , is predominant and the function required is presented as a series of trigonometric [4.35] or step functions [4.36]. Following [4.35,36], a number of reports have been published which suggest various approaches to obtain distributions of the required parameters. The first examples were related to studies of amorphous alloys. The main problem here involves the avoidance of a strong correlation between the hyperfine parameters obtained.

Reviews of this field are given in [4.37-41]. In [4.42] it has been shown that the consistent use of a method based on the principle of maxi-entropy which is well known from information theory, results in a more unambiguous determination of hyperfine parameter distributions from Mössbauer spectra. Apart from studies of amorphous alloys similar problems have been dealt with in studies of ferrites (see, e.g. [4.34]) and of multicomponent alloys, for example the distribution of Cr in ternary Fe-Cr-Ni alloys [4.43].

The Fourier transform method used in Mössbauer spectroscopy has been initially applied to the enhancement of resolution [4.44]. The method involves the application of the direct and inverse Fourier transforms to both part of (4.47):

$$\mathcal{D} \left\{ I(\varepsilon) \right\} = \exp \left[ -\mu_a(E) d \right] - 1 ,$$

where  $\mathcal{D}$  stands for an operator that represents the whole process of deconvolution. The function required is determined by the following equation:

$$\mu_a(E) = - \frac{1}{d} \ln \left[ \mathcal{D} \left\{ I(\varepsilon) \right\} + 1 \right] .$$

8

Formally, this way is simple, but it has not been realized in practical applications. Even for a spectrum consisting of only two lines, unwanted oscillations appear in the line wings. In practice, this may lead to distortions of the lines in low intensity partial spectra or even to the appearance of "false" lines. In spite of these problems the authors of this approach believe that the formal application of the Fourier transform technique allows the elimination of the instrumental line, a calculation of the response of the medium to monochromatic radiation, and then an evaluation of the distribution of hyperfine parameters of interest [4.45]. Further developments of the technique are described in [4.46-48].

The clarification of the initial hypothesis and specification of the parameter values may be obtained by simpler differential methods [4.49]. The idea is that the plot of a derivative of the symmetric line is two peaks of the same shape and area but in opposite directions. If a slightly shifted line is added to a symmetric line, a strong asymmetry of the peaks on the differential curve results. The differentiated spectra are easily obtained by simple procedures in data accumulation devices. Such a procedure does not replace the conventional data treatment but facilitates the choice of a hypothesis for poorly resolved spectra. At present, various modified techniques are used to obtain the differentiated spectra where the statistical scatterer of experimental data is reduced. After a hypothesis is chosen, numerical values of its characteristic parameters may be obtained directly from the differentiated spectra. Least-squares fitting procedures allow a more rapidly converging iterative process for the differentiated spectra than for the conventional ones. The methods considered above often find application in

backscattering spectroscopy, especially when X-rays or electrons are detected. Some difficulties arise if quantitative relations concerning the phase composition are required. The analysis of complex Mössbauer spectra by stripping techniques [4.50] developed in transmission spectroscopy is not appropriate in scattering spectroscopy.

It is useful to compare the line shape of scattering and transmission spectra of the same sample. After substitution of  $x$  into (4.44) and differentiation with respect to  $x$ , an expression is obtained for the line shape of a hypothetical transmission spectrum  $I'(E, x)$  of a layer  $dx$  at depth  $x$

$$\begin{aligned} I'(\varepsilon, x) &= \frac{d}{dx} I(\varepsilon, x) \quad dx = \\ &= dx e^{-\mu_a x} c \int_{-\infty}^{\infty} L(E - \varepsilon) \exp[-\mu_r(E)x] \mu_a(E) dE. \end{aligned} \quad (4.49)$$

Let there be no split lines both in the source and in the sample. Compare the line shape of transmission spectra from a sample  $(x + dx)$  thick and a layer between  $x$  and  $x + dx$ . If  $(\mu_r + \mu_a)x \ll 1$ , the spectrum is considered as a Lorentzian of width  $\Gamma_a = 2 \Gamma_{nat}$  and integrating (4.49) over energy gives:

$$\begin{aligned} I'(\varepsilon, x) &= c_1 \frac{\Gamma_{nat}^2 \mu_a dx}{(\varepsilon - \delta)^2 + \Gamma_a^2} \left\{ \left[ \frac{\Gamma_a}{\Gamma_{nat}} + \frac{(\mu_a + \mu_r)x}{4} \right] \right. \\ &\quad \left. - \frac{1}{2} \frac{\Gamma_a^2 (\mu_a + \mu_r)x}{(\varepsilon - \delta)^2 + \Gamma_a^2} \right\}. \end{aligned}$$

The second term in braces shows that resonant scattering by the layer preceding the layer  $dx$  leads to a broadening of the spectrum. The expression for the line shape of the spectrum from a layer  $dx$  explicitly accounts for the spectral broadening, whereas the spectrum from the entire sample (including the layer  $dx$ ) does not reveal this broadening. Since (4.49) and the expression for the volumetric source strength  $S(E, x)$  for the same  $dx$  layer (see (2.94)) are identical, then any radiation from the layer  $dx$  in transmission experiments reaching the detector gives similar line shapes in transmission and scattering Mössbauer spectra.

In practice, the radiation scattered from the layer  $dx$  escapes the sample surface with a probability given by the weight function. Since the weight functions are always less than modulo 1, this results in a greater value of  $x$  (and the more distorted the spectrum of resonant radiation reaching  $dx$ ) being associated with a smaller contribution of  $dx$  layer to the total scattering spectrum, as compared to the hypothetical transmission experiment with the same sample. On detecting elastically scattered  $\gamma$ -quanta such unambiguous conclusions cannot be drawn since the effects of resonant self-absorption may considerably distort the spectrum of the backscattered radiation.

Various theoretical and experimental techniques used to obtain the weight functions have been discussed. One more method must now be considered which is based on the analysis of Mössbauer spectra. The weight functions obtained are related to the experimental arrangement used. Let us have a bulk scatterer characterized by a single Lorentzian line (the total linear absorption coefficient being known). The scattered intensity is related to the required weight function  $T_i(x)$  by the following expression

$$I(\varepsilon) = \frac{fC_i}{\pi\Gamma} \int_{-\infty}^{\infty} \int_0^{\infty} L(E - \varepsilon) e^{-\mu_a(E)x} \mu_a(E) T_i(x) dx dE. \quad (4.50)$$

By means of Fourier transform or some other method the convolution with the instrumental line (i.e. the energy convolution) can be eliminated, and only the integration over coordinates will be left.

Applying the Fourier transform  $F$ , we have:

$$\mathcal{F}I(p) = \frac{fC_i}{2} e^{-|p|\Gamma/2} \int_{-\infty}^{\infty} \int_0^{\infty} e^{ipE} e^{-\mu_a(E)x} \mu_a(E) T_i(x) dx dE. \quad (4.51)$$

Multiplying the both parts by  $9 \exp(|p|\Gamma/2)$  and applying the inverse transform, we obtain:

$$I'(E) = \frac{1}{\pi f C_i} \int_{-\infty}^{\infty} e^{-ipE} \mathcal{F}I(p) e^{|p|\Gamma/2} dp$$

$$= \mu_a(E) \int_0^{\infty} e^{-\mu_a(E)x} T_i(x) dx, \quad (4.52)$$

where the  $T(x)$  function is the only unknown.

Thus, the response of the medium is obtained to monochromatic radiation and since the linear coefficient  $\mu_a(E)$  is known, the  $T(x)$  function can be recovered from the experimental Mössbauer spectra.

Equation (4.52) may be considered as an integral equation with the weight function as the kernel. There are two evident ways to solve it. Since  $\mu_a(E)$ , and consequently,  $I'(E)$ , are even functions of energy, it allows the  $E$  variable to approach  $\mu(E)$ . The right-hand part of (4.52) is the Laplace transform LT of the function  $T$ , depending on the new variable  $\mu$ :

$$(\mathcal{L} T)(\mu) = I' [E(\mu)] \mu^{-1}.$$

To find the weight function from Mössbauer spectra, the transform should be inverted. This can be easily done if  $I'(E(\mu))$  has an analytical continuation into the complex plane. It can be also changed by an appropriate rational function. Then

$$T(x) = \frac{1}{2\pi i} \int_{C-\infty}^{C+\infty} e^{\mu x} I'(E(\mu)) \mu^{-1} d\mu, \quad (4.53)$$

where  $C$  is determined from the condition that all the singularities of the  $I'(E(\mu))\mu^{-1}$  function lie to the left of the line  $\text{Re } \mu = C$ .

Another way to obtain the weight function is to reduce it to the problem of moments assuming that all the moments of the  $T(x)$  function exist. Then the integrand of (4.52) should be expanded into the power  $\mu$  series with a sufficiently large number of terms:

$$\begin{aligned} \mu \int_0^{\infty} T(x) e^{-\mu x} dx &= \mu \int_0^{\infty} T(x) dx - \frac{\mu^2}{1!} \int_0^{\infty} x T(x) dx \\ &+ \frac{\mu^3}{2!} \int_0^{\infty} x^2 T(x) dx - \dots \end{aligned}$$

Expand the  $I'(E)$  function into the Taylor series:

$$I'(E) = C_0\mu - C_1\mu^2 + C_2\mu^3 - C_3\mu^4 + \dots \quad (4.54)$$

Comparing the two equations, we have

$$C_0 = \int_0^{\infty} T(x) dx, \quad C_1 = \int_0^{\infty} x T(x) dx \dots$$

The problem of recovering  $T(x)$  is therefore reduced to the problem of moments that has an extensively developed theory. Thus, each of the ways mentioned above allows the weight function  $T(x)$  to be obtained from experimental data and used to analyze the data under more complicated conditions when the function  $\mu_a(E)$  is not known.

#### 4.7. Layer-by-layer Analysis

So far, non-destructive methods of analysis have been considered which are based on the dependence of the energy of electrons escaping the surface from their depth of origin. Such analysis may also be performed by recording the spectra obtained by detecting radiation that is quite different in range.

To analyze multilayer samples one can apply a stripping technique for the removal of layers. The technique has been used in Mössbauer spectroscopy [4.51,52]. The treatment of experimental data has been suggested in a simple case assuming that Mössbauer spectra do not significantly overlap [4.53-55]. The progress of this destructive method is hindered by the absence of a sufficiently general theory to interpret the set of spectra required to recover the  $\mu_{ai}(E)$  functions. Spectra from individual phases may overlap and the thickness of the layers (as well as their order) may be arbitrary. Such a theory can be developed if the weight functions are assumed to be known, i.e. either there are analytical expressions, or the functions are obtained by one of the methods discussed in Sect.3.7 or 4.6.

Let us deal with CEMS measuring the thickness of stripped layers in mass/area. Assume that the  $T(x)$  function is known and smoothly dependent on the variable  $x$ ; this is a convenient method for the analysis of multilayer samples. Based on these assumptions, the problem of phase identification is reduced to the solution of an integral equation with the weight function as the kernel. The following model is assumed. There are  $N$  layers, each one being related to a definite phase and characterized by its own  $\mu_{ai}(E)$  function. The thickness of the  $i$ -th layer is  $d_i = x_i - x_{i-1}$ , and  $x$  is measured from the sample surface. The coordinate of the boundary between the first layer and the substrate is

$$x_0 = \sum_{i=1}^N d_i = \sum_{i=1}^N (x_i - x_{i-1}) .$$

The function  $\mu_a(E, x)$  must be obtained completely since it characterizes the phase composition of the sample and the order of the layers. The layered structure of the sample causes the  $\mu_a(E, x)$  function to be a piece-wise constant function of  $x$ . For the substrate  $x > x_0$ ,  $\mu_a(E, x) = \mu_a(E)$ . For the 1-st layer  $x_1 < x < x_0$  and  $\mu_a(E, x) = \mu_{a1}(E)$ . Let a layer be removed of thickness  $y$ , and the position in the original sample be between  $x = 0$  and  $x = y$ . The line shape of the Mössbauer spectrum from the new sample can be written as:

$$I(\varepsilon, y) = \int_{-\infty}^{\infty} \int_y^{\infty} L(E - \varepsilon) e^{-\int_y^x \mu_a(E, l) dl} \mu_r(E, x) T(x - y) dx dE .$$

The response of such a sample to monochromatic radiation is described by the following equation

$$I'(E, y) = \int_y^{\infty} \mu_r(E, x) e^{-\int_y^x \mu_a(E, l) dl} T(x - y) dx , \quad (4.55)$$

which differs from (4.52) which was derived for the monophasic sample.

To recover the  $\mu_a(E, x)$  function a new function must be introduced

$$\varphi(E, x) = \exp \left\{ - \int_0^x \mu_a(E, l) dl \right\} . \quad (4.56)$$

The required  $\mu_a(E, x)$  function is the logarithmic derivative of the above function

$$\mu_a(E, x) = \varphi'(E, x) / \varphi(E, x) . \quad (4.57)$$

The introduced function  $\varphi(E, x)$  gives the probability for monochromatic radiation to reach a depth  $x$  in the original sample.

The equation of interest, by substitution of (4.56) and (4.57) into (4.55), is written in the form:

$$\left\{ I'(E, y) - T(0) \right\} \varphi(E, y) = \int_y^{\infty} T(x - y) \varphi(E, x) dx. \quad (4.58)$$

The  $\varphi(E, x)$  function has discontinuities at  $x = x_i$ . The derivative of the weight function is a smooth function and since the smoothness is enhanced on integrating, the right-hand part of (4.58) has no breaks. Hence, the breaks of the  $I'(E, y)$  and  $\varphi(E, y)$  functions in the left-hand part of (4.58) compensate each other. Let us differentiate (4.58) with respect to  $y$  and denote by  $[\ ]_i$ . The jumps of derivatives of the  $I'(E, y)$  spectrum recalculated for monochromatic radiation (e.g. by Fourier transform) and of the  $\mu_a(E)$  function correspond to the boundaries between  $i$  and  $i-1$  layers. The  $\varphi(E, x_i)$  function appears as a factor in both parts of the equation and may be cancelled. Finally, we have:

$$[\mu_a(E)]_i = \frac{\left[ \frac{d}{dy} I'(E, y) \right]_i}{I'(E, x_i) - T(0)}. \quad (4.59)$$

This relation is valid for all energy values. By the jumps of the derivative of the  $I'(E, y)$  function evaluated for any energy values, jumps are found in the  $\mu_a(E)$  values for the same points and energies. Hence, the  $\mu_{ai}(E)$  values for each layer are obtained by summation, starting from the layer on the substrate boundary. The  $\mu_{ai}(E)$  functions are recovered in the order that is opposite to the order of stripping

$$\begin{aligned} \mu_{a1}(E_j) &= \mu_a(E_j) + [\mu_a(E_j)]_1, \\ \mu_{aN}(E_j) &= \mu_a(E_j) + [\mu_a(E_j)]_1 + \dots + [\mu_a(E_j)]_N. \end{aligned} \quad (4.60)$$

The  $j$  index runs upon the values  $j = 1, 2 \dots k$ , where  $k$  is the number of points (i.e. of energy values), where the experimental spectrum is recalculated to  $I'(E, x)$ .

Assume that the layers are thin (the change of curvature for the  $I'(E, x)$  function may be neglected within the layer) and we can strip one layer at a time. Then  $[\mu_a(E_j)]_i$  may be calculated approximately by the formula:



$$[\mu_a(E_j)]_i = \frac{I'(E, x_{i+1}) + I'(E, x_{i-1}) - 2I'(E, x_i)}{2[I'(E, x_i) - T(0)]} . \quad (4.61)$$

This simplifies substantially the calculations of the resonant absorption cross section in separate layers. It should be noted that in CEMS  $T(0) \approx 0.75$ , and on detection of X-rays  $T(0) \approx 0.5$ . To find the  $\mu_{ai}(E)$  functions, no other information on the  $T(x)$  function shape is required if the above assumptions are true. Moreover, even if the  $T(x)$  function has breaks, all the considerations above are valid.

Suppose now that there are no sharp boundaries between phases or that the sample is a monophasic one, and that the hyperfine interaction parameters change with distance from the surface. This is realized, for example, on implantation of the bulk samples of semiconductors or alloys, and  $\mu_a(E, x)$  is a continuous function of  $x$ . This can be recovered even in a complicated case providing that the weight function is known.

Let us demonstrate the solution of this problem by assuming three different (often used) hypotheses about the  $T(x)$  function. Assume at first, that the weight function is just an exponential function (see Sect.3.2)

$$T(x) = \exp(-\nu x) ,$$

where  $x$  expressed in mass/area. Equation (4.58) remains valid. It should be noted that the  $d/dy$  operation corresponds to the process of etching. The differential operation  $d/dy - \nu I$  may be applied to both parts of (4.58) ( $I$ , the identity operator) to eventually cancel the corresponding exponential function (i.e., the weight function). It yields

$$\begin{aligned} \left[ \frac{d}{dy} - \nu I \right] \left\{ I'(E, y) - T(0) \right\} \varphi(E, y) + T(0) \varphi(E, y) \\ = - \int_y^\infty \left[ \frac{d}{dx} + \nu I \right] T(x, y) \varphi(E, x) dx . \end{aligned} \quad (4.62)$$

The right-hand part of this equation is zero, and for the introduced function  $\varphi(E, y)$  a normal differential equation is obtained:

$$\varphi(E, y) = \exp[-\mu_a(E)(y - x_0)] \quad \text{at} \quad y > x_0 .$$

Thus, our approach proves to be consistent, and a trivial result has been obtained, i.e. resonant scattering in the bulk is determined only by the  $\mu_a(E)$  coefficient. Equation (4.62) allows the  $\varphi(E,y)$  function to be obtained explicitly although it is unnecessary to do so here. Indeed, using relation (4.57), equation (4.62) may be rewritten as:

$$\left\{ I'(E,y) - T(0) \right\} \mu_a(E,y) + \frac{d}{dy} I'(E,y) + T(0) - \nu I'(E,y) + \nu T(0) = 0. \quad (4.63)$$

For the unknown function  $\mu_a(E,y)$  we have:

$$\mu_a(E,y) = - \frac{\frac{d}{dy} I'(E,y) + T(0) - \nu I'(E,y) + \nu T(0)}{I'(E,y) - T(0)}. \quad (4.64)$$

If the weight function is a sum of exponents [3.39], for example:

$$T(x) = \sum_{i=1}^p h_i e^{-\nu_i x}, \quad (4.65)$$

the corresponding differential operations must be successively applied to (4.62). Thus, if there are only two exponents in (4.65), then applying the differential operation  $(d/dy - \nu_i)$  to (4.62), we obtain the integral in the right-hand part to become zero, and a second order linear differential equation is obtained for the  $\varphi(E,x)$  function. This equation must be solved numerically. In the general case, a  $p$ -th order linear equation is obtained for the  $\varphi(E,x)$  function. The initial condition, as before, is the  $\varphi(E,x)$  function for the bulk. It should be stressed that a correct investigation of multilayer sample is labourous and time-consuming. It requires a number of strippings to be made, the thicknesses  $\Delta x$  of the stripped layers being sufficiently small so as to satisfy the relation  $h_i \nu_i \Delta x \ll 1$ .

Let us consider now the most interesting case where the weight function is given by the equation:

$$T(x,y) = 2\pi \int_0^{\pi/2} e^{-\int_Y^x \nu(s) ds / \cos \theta} \sin \theta d\theta.$$

This allows a similar interpretation to be made of the spectra obtained from a given sample by detecting both electrons and characteristic X-rays, if the detector is adapted to detect the two types of radiation. As before, we assume the properties of the sample to vary smoothly with depth down to the bulk boundary whose coordinate is  $x_0$ .

Recall now (4.55) which describes the response of the medium to monochromatic radiation. Multiplying both parts of this equation with  $\varphi(E, y)$  and integrating by parts we have:

$$\begin{aligned}
 I'(E, y) \varphi(E, y) = & -2\pi \varphi(E, x) \left[ \int_y^\infty \int_1^\infty e^{-t \int_y^x \nu(s) ds} t^{-2} dt \right. \\
 & \left. + 2\pi \int_y^\infty \varphi(E, x) [-\nu(x)] \left\{ \int_1^\infty e^{-t \int_y^x \nu(s) ds} t^{-1} dt \right\} dx \right] .
 \end{aligned} \tag{4.66}$$

Introducing new variables  $p$  and  $q$ , which describe the dimensionless layer thickness for absorption of the detected radiation  $p = 10 \int \nu(s) ds$ , instead of (4.66) we have:

$$\begin{aligned}
 \left\{ 2\pi - \hat{I}(E, q) \right\} \hat{\varphi}(E, q) &= 2\pi \int_q^\infty \hat{\varphi}(E, p) K(p - q) dp ; \\
 K(p - q) &= \int_1^\infty e^{-t(p-q)} t^{-1} dt ,
 \end{aligned} \tag{4.67}$$

where the functions used before, have been redesignated as follows:

$$\begin{aligned}
 \varphi(E, x) &= \hat{\varphi}(E, p) ; & \varphi(E, y) &= \hat{\varphi}(E, q) , \\
 I'(E, y) &= \hat{I}(E, q) , & dp &= \nu(x) dx ,
 \end{aligned}$$

and the  $K(p - q)$  function is energy-independent. Thus, an integral equation for the  $\hat{\varphi}(E, q)$  function has been obtained which does not contain the absorption coefficient  $\nu(x)$  for the detected radiation. If (4.67) can be solved, the obtained function  $\hat{\varphi}(E, q)$  can be used to recover  $\hat{\varphi}(E, x)$ . The subsequent recovery of the  $\mu_a(E, x)$  function requires a knowledge of  $\nu(x)$ .

To solve (4.67) we replace the integral representing the  $K(p - q)$  function, by the Riemann sum

$$\left\{ 2\pi - \hat{I}'(E, q) \right\} \hat{\phi}(E, q) = 2\pi \int_q^\infty \sum_{s=1}^N e^{-t_s(p-q)} (\Delta_s/t_s) \hat{\phi}(E, p) dp, \quad (4.68)$$

where  $t_s$  are the break points of the interval  $(1, \infty)$ ;  $\Delta_s = t_s - t_{s-1}$ . This equation is similar to (4.58) and may be solved using a differential operator with constant coefficients. Applying the operator

$$Q = \prod_{s=1}^N \left[ \frac{d}{dr} + t_s \right] \quad 11$$

to the both parts of (4.68) gives a differential equation, but with variable coefficients. Each differentiation leads to the appearance of an extra term outside the integral due to differentiation of the integral in (4.68) with respect to the lower limit. Applying the  $Q$  operator to the left-hand- and the right-hand parts of (4.68) means that all the terms outside the integral are collected in a new differential operator  $Q'$  of the  $(N - 1)$  order with constant coefficients. Applying the  $Q'$  operator to the kernel  $K(p - q)$  we get zero and have:

$$Q \left\{ \left[ \hat{I}'(E, q) - 2\pi \right] \hat{\phi}(E, q) \right\} - Q' \hat{\phi}(E, q) = 0. \quad (4.69)$$

Of all solutions (4.69), one should be chosen, giving at  $x \rightarrow \infty$  ( $p \rightarrow \infty$ ) the probability for monochromatic radiation reaching a depth  $x$  in the bulk when only resonant interaction is taken into account. For the bulk itself we have:

$$\phi(E, x) = C \exp[-\mu_a(E, x_0) x(p)].$$

Thus, to solve the problem of recovering the  $\mu_a(E, x)$  function from experimental data one should recalculate  $p$  in  $x(p)$ . Then, from the set of solutions (4.69), those solutions are chosen that are proper at  $p \rightarrow \infty$ . The numerical coefficient should be selected from the condition  $\phi(E, 0) = 1$  and, thereby, the  $\phi(E, x)$  function can be explicitly determined. The required linear resonant absorption coefficients at a depth  $x$  are found through the logarithmic derivatives of the  $\phi(E, x)$  function:

$$\mu_a(E, x) = - \frac{\varphi'(E, x)}{\varphi(E, x)} . \quad (4.70)$$

Thus, a model of layer-by-layer analysis may be developed even when the hyperfine interaction parameters depend on the distance from the surface.

## References

- 4.1 Y. Ujihira, Proc. Intern. Conf. Appl. of the Moessb. Effect, Jaipur, India (December 1981), New Delhi, 1982, pp. 166-170.
- 4.2 J.J. Bara and B.F. Bogacz, Nucl. Instr. Meth., 186 (1981) 561-568.
- 4.3 N.K. Jaggi and K.R.P.M. Rao, Proc. Intern. Conf. Appl. of the Moessb. Effect, Jaipur, India (December 1981), New Delhi, 1982, pp. 268-270.
- 4.4 J.J. Bara and B.F. Bogacz, Proc. Intern. Conf. Appl. of the Moessb. Effect, Jaipur, India (December 1981), New Delhi, 1982, pp. 950-952.
- 4.5 A. Kumar, M.R. Singh and K.C. Tripathi, Nucl. Instr. Meth. Phys. Res., B36 (1989) 189-193.
- 4.6 J.G. Mullen, A. Djedid, B. Bullard, G. Schupp, D. Cowan, Y. Cao, M.L. Crow and W. Yelon, Hyperfine Interactions, 40 (1988) 123-134.
- 4.7 J.D. Bowman, E. Kankeleit, E.N. Kaufmann and B. Persson, Nucl. Instr. Meth., 50 (1967) 13-21.
- 4.8 Ts. Bonchev and S.S. Amin, Compt. Rend. Acad. Bulgar Science., 38, No. 3 (1985) 307-310.
- 4.9 G.N. Belozerskii, A.E. Dozorov and B.S. Pavlov, Izv. Vyssh. Uchebn. Zaved., Fiz., No.8 (1989) 23-29.
- 4.10 G.N. Belozerskii and A.E. Dozorov, Nucl. Instr. Meth. Phys. Res., B44 (1989) 211-215.
- 4.11 P.M. Morse and H. Feshbach, Methods of Theoretical Physics, McGraw-Hill Book Company, New York, 1953.
- 4.12 B. Noble, Methods based on the Wiener-Hopf Technique, Pergamon Press, London, New York, 1958.
- 4.13 V.V. Sobolev, Kurs Teoreticheskoi Astrofiziki, Nauka, Moskva, 1985.
- 4.14 A.R. Mkrtchyan and R.G. Gabrielyan, Astrofizika, 20 (1984) 607.
- 4.15 A.R. Mkrtchyan, R.G. Gabrielyan, A.H. Martirosyan and A.Sh. Grigoryan, Phys. Stat. Sol. (b), 139 (1987) 583.
- 4.16 B. Fultz and J.W. Morris Jr., Nucl Instr. Meth., 188 (1981) 197-201.
- 4.17 B. Fultz and J.W. Morris Jr., Nucl. Instr. Meth. 211 (1983) 569-570.
- 4.18 W. Meisel, Proc. Int. Conf. Mössbauer Spectr., Bucharest, 1977, pp. 71-94.
- 4.19 W. Meisel, Hyperfine Interactions, 3 (1977) 413-422.
- 4.20 E. Kankeleit, in Proc. Int. Conf. on Mössbauer Spectr. ed. by A.Z. Hryniewicz and J.A.

- Sawicki, Cracow, 1975, Vol. 2, p.43.
- 4.21 M. Seberini, in Proc. 5-th Intern. Conf. Mossb. Spectr., Bratislava, Czechoslovakia, September 3-7, 1973.
  - 4.22 S. Margulies and J.R. Ehrman, Nucl. Instr. Meth., 12 (1961) 131-137.
  - 4.23 D.A. O'Connor, Nucl. Instr. Meth., 21 (1963) 318-322.
  - 4.24 R.L. Collins, J. de Physiq. C2, Suppl. No.3, 40 (1979) 36- 38.
  - 4.25 T. Mukoyama and J. Vegh, Nucl. Instr. Meth., 173 (1980) 345-346.
  - 4.26 T. Kobayashi and K. Fukumura, Nucl. Instr. Meth., 173 (1980) 363-369.
  - 4.27 K. Szymanski and L. Dobrzynski, Nucl. Instr. Meth. Phys. Res., B51 (1990) 192-195.
  - 4.28 B.R. Bullard, J.G. Mullen and G. Schupp, Physical Review B., B43, (1991) 7405.
  - 4.29 Yu.P. Pyt'ev, Dokl. Akad. Nauk SSSR, 245 (1979) 42-46.
  - 4.30 Yu.P. Pyt'ev, Dokl. Akad. Nauk SSSR, 255 (1980) 540-544.
  - 4.31 A.N. Tikhonov and V.Ya. Arsenin, Metodi recshenija nekorrektnih zadach, Nauka, Moskva, 1979.
  - 4.32 P.N. Zaikin and A.S. Mechenov, in Nekotorie Voprosi Avtomatizirovannoy Obrabotky i Interpretazii Fizicheskikh Eksperimentov, vip. 1, ed. by A.N. Tihonov, MGU, Moskva, 1975, pp. 202-211.
  - 4.33 V.I. Nikolaev, Yu.P. Pyt'ev, V.S. Rusakov, A.G. Svecshnikov and E.N. Terent'ev: Dokl. Akad. Nauk SSSR, 260 (1981) 848-852.
  - 4.34 V.I. Nikolaev and V.S. Rusakov, Messbauerovskie Issledovaniya Ferritov, MGU, Moskva, 1985.
  - 4.35 B. Window, J. Phys. E. Sci. Instr., 4, No. 5 (1971) 401- 402.
  - 4.36 J. Hesse and A. R bartsch, J. Phys. E. Sci. Instr., 7, No. 7 (1974) 526-532.
  - 4.37 O. Le Gaer and J.M. Dubois, J. Phys. E. Sci. Instr., 12 (1979) 1081.
  - 4.38 J. Keller, J. Appl. Phys., 52 (1981) 5268.
  - 4.39 F. Varret, J.M. Greneche and J. Teillet, in Trends in M ssbauer Spectroscopy, ed. by P. G tlich and G.M. Kalvius, Johannes-Gutenberg-Universitaet Mainz/FRG, 1983, p.105.
  - 4.40 S.J. Campbell, in Trends in M ssbauer Spectroscopy, ed. by P. G tlich and G.M. Kalvius, Johannes-Gutenberg-Universitaet Mainz/FRG, 1983, pp. 117-130.
  - 4.41 S.V. Pridvzhkin, B.V. Ryzhenko and O.V. Gel'd, Nucl. Instr. Meth. Phys. Res., B51 (1990) 288-293.
  - 4.42 R.A. Brand and G. Le Caer, Nucl. Instr. Meth. Phys. Res., B34 (1988) 272-284.
  - 4.43 S. Nagy, E. Kuzmann, A. Vertes, G. Szabo and G. Konczos, Nucl. Instr. Meth. Phys. Res., B34 (1988) 217-223.
  - 4.44 M. Celia Dibar Ure and P.A. Flinn, in M ssbauer Effect Methodology, ed. by I.J. Gruverman and C.W. Seidel, Vol. 7, Plenum Press, New York, 1971, pp.245-362.
  - 4.45 I. Vincze, Nucl. Instr. Meth., 199 (1982) 247-262.
  - 4.46 J.G. Mullen, A. Djedid, G. Schupp, D. Cowan, Y. Cao, M.L. Crow and W.B. Yelon, Phys. Rev., B37, No. 7 (1988) 3226- 3245 ; Errata: Phys. Rev., B39 (1989) 753.
  - 4.47 J.G. Mullen, A. Djedid, D.Cowan, G. Schupp, M.L. Crow, Y. Cao and W.B. Yelon, Phys. Lett., A127, No. 4 (1988) 242- 246.
  - 4.48 J.G. Mullen, B.R. Bullard and G. Schupp, Condensed matter studies by nuclear methods, in Proceedings XXV Zakopane School on Physics, Zakopane, Poland, 1990.
  - 4.49 E. Ratner and M. Ron, Nucl. Instr. Meth., 188 (1981) 191- 196.
  - 4.50 A.H. Muir,Jr, in M ssbauer Effect Methodology, ed. by I.J. Gruverman and C.W. Seidel, Vol.5, Plenum Press, New York, 1969, pp. 75-101.
  - 4.51 V.A. Bychkov, P.L. Gruzin, Yu.V. Petrikin and L.A. Sharova, Zavodskaja Laborotorija, 44,

No. 8 (1978) 970- 973.

- 4.52 Yu.F. Babikova, A.B. Bateev, V.P. Filippov and A.V. Stoljarevich, Vsesojuznoe Soveschanie po Prikladnoi Messbauerovskoi Spectroscopii "Volga". Sept. 2-7, 1988, Moskovskii Injenerno-fizicheskii Institut, Moskov. Gosud. Universitet, p.80.
- 4.53 P.H. Smit, H.A. Algra and J.M. Robertson, Appl. Phys., 22 (1980) 299-302.
- 4.54 P.H. Smit and R.P. van Stapele, Appl. Phys., A28 (1982) 113-117.
- 4.55 A.A. Kiselev, R.N. Kuz'min and A.A. Novakova, Pis'ma Zh. Tekhn. Fiz., 12 (1986) 32-36; Sov.Tech. Phys.Lett (Engl. Transl) 12 (1986) 14-15.

## 5. Practical Aspects of Surface Layer Analysis

The techniques of surface layer analysis discussed above find extensive applications in science and industry. In addition to the International Conferences on the Applications of the Mössbauer Effect there have also been a number of conferences devoted to industrial applications of Mössbauer spectroscopy, e.g. [5.1] or specific problems of material science. The scope of problems addressed is extremely wide and ranges from studies of the electronic structure and magnetic properties of surface layers; structural studies of these layers and their modification by various means; phase analysis; the monitoring of the surface of finished products and technologically important equipment. These studies are often in fields of electrochemical processes, corrosion and the oxidation of metals and alloys; surface modifications by thermal treatments, ion implantation, laser processing; noncrystalline materials; superconductivity; surface magnetism and superparamagnetism; catalysis and solid-state reactions on solid surface. In this Chapter some of the problems will be considered. The interested reader is referred to the Proceedings of International and National Conferences on the Applications of the Mössbauer Effect first published as supplements to *Journal de Physique* and more recently as separate editions, and subsequently for example in *Hyperfine Interactions* e.g. volumes 27-29, 40-42, 45-47, 53-57.

The problem of spin texture is essential for analysis of surface layers and for the interpretation of Mössbauer spectra in phase analysis. Section 5.3 is devoted to this problem. It should be noted that a preferred spin orientation occurs not only in cold-rolled foils or epitaxial layers but also in powders. This effect should be taken into account for example, in studies of the high-temperature conductivity of ceramics otherwise it may result in an inadequate interpretation of the Mössbauer spectra.

### 5.1. Corrosion Studies of Metals and Alloys

The first studies by Mössbauer spectroscopy showed that the spectral shapes recorded from iron oxides are quite different from those of metallic iron and its alloys. Moreover, the spectra recorded from a series of ferric oxides and hydroxides were found to differ especially when the samples were prepared under different conditions. The chemical degradation of iron and iron-based materials shows a very broad variety of phenomena. In most cases the overall effect is an oxidation process. The resulting products however are very different in their composition and morphology and hence they may slow down or accelerate the process. Since 1967 a number of papers have appeared which demonstrate that Mössbauer spectroscopy is an efficient tool for studies of the phase composition of corrosion products of iron and its alloys [5.2- 9]. Transmission Mössbauer spectroscopy has been used to study the corrosion of thin foils;  $^{57}\text{Fe}$  was electrodeposited on the total surface to increase the sensitivity. For studies of corrosion of bulk samples a technique involving the preliminary removal of the oxide films by stripping the films from the substrate was suggested [5.10,11]. The



progress in scattering techniques, especially in CEMS, has stimulated the use of Mössbauer spectroscopy for studies of corrosion.

Iron and steel can be passivated by anodic oxidation. This behaviour is of both practical and scientific interest and Mössbauer spectroscopy seems to be one of the best physical methods for the studies. It is important to conduct *in situ* the corrosion studies by electrochemical investigations because oxidation under potentiostatic control may form a rather closed layer tight enough to inhibit subsequent corrosion. Such passivating layers are found to be very thin and, therefore, their thorough analysis needs some experimental effort.

For *in situ* measurements, one must consider which detection mode can best be adapted to an electrochemical arrangement which optimizes the current distribution. In principle, this consideration favours transmission spectroscopy for uncompromised *in situ* measurements. This is due to the relatively small absorption by water of 14.4 keV  $\gamma$ -rays compared to the increased absorption of the 6.4 keV X-rays and 5 - 7 keV electrons. A good cell design would be difficult for X-ray or electron detection. Only with the detection of the 14.4 keV  $\gamma$ -rays is the attenuation length in water consistent with a reasonable electrochemical cell dimension. At the same time there is a problem of separating the weak useful signal from the total spectrum of the sample in transmission spectra which may be of rather poor quality in such experiments. Both the iron substrate and the passive film contribute to the Mössbauer spectra; the iron substrate should be as thin as possible while preserving the electrochemical behaviour of bulk iron.

Indeed, the transmission technique has been shown to be convenient for investigations *in situ*, of corrosion processes, passivation and corrosion inhibition. In the first work of the series O'GRADY [5.12] studied the passivation of iron in a buffered borate solution. For this purpose radiation of a Mössbauer source was made to pass through the 2 mm thick electrolyte layer and fall onto the multilayer sample under investigation. The most important elements of both this and similar subsequent investigations [5.13-23] were the cell design and preparation of the sample under study (i.e. the working electrode). O'GRADY used a fairly complex sample consisting of a 25 nm thick layer of gold vacuum deposited onto a mylar backing; a 25 - 30 nm thick  $^{57}\text{Fe}$  layer was then electrodeposited onto the gold layer. The passivation resulted in 10 to 20%  $^{57}\text{Fe}$  being in the passive layer and the Mössbauer signal from the layer being relatively easy to detect.

This first investigation of the passive film in situ showed it to consist of an amorphous ferric oxide and a polymeric iron-containing coating. Drying the sample caused the compound to transform to  $\gamma\text{-Fe}_2\text{O}_3$ . It was possible to associate the results with a 40 - 60 Å thick layer and the study shows that many problems of electrochemistry can be in fact examined by transmission Mössbauer spectroscopy. Thus, for example, by a similar technique, the nature of oxidation products was studied for iron under conditions of pitting corrosion in the presence of Cl ions [5.13].

A multilayer structure on a mylar backing which was used in [5.12] for corrosion studies is quite different in its properties from real samples for which the corrosion studies are of most interest. The studies of formation of passive iron films on bulk iron or, at least, on iron foils are interesting. In order to simulate the real situation ESIPENKO and SUKHOTIN [5.14-16] used metal foils as substrates. The studies were possible because thin cold-rolled foils of  $\alpha\text{-}^{56}\text{Fe}$  were used with the  $^{57}\text{Fe}$  abundance of less than 0.05 % in an electrolytic cell which is shown in Fig.5.1. The entrance and exit windows of the cell are made of polymethylmethacrylate 0.3 mm thick. The electrolyte layer between the cell windows is not thicker than 2 mm which results in not a very strong attenuation of the Mössbauer  $\gamma$ -rays in the cell. The design of the cell provides

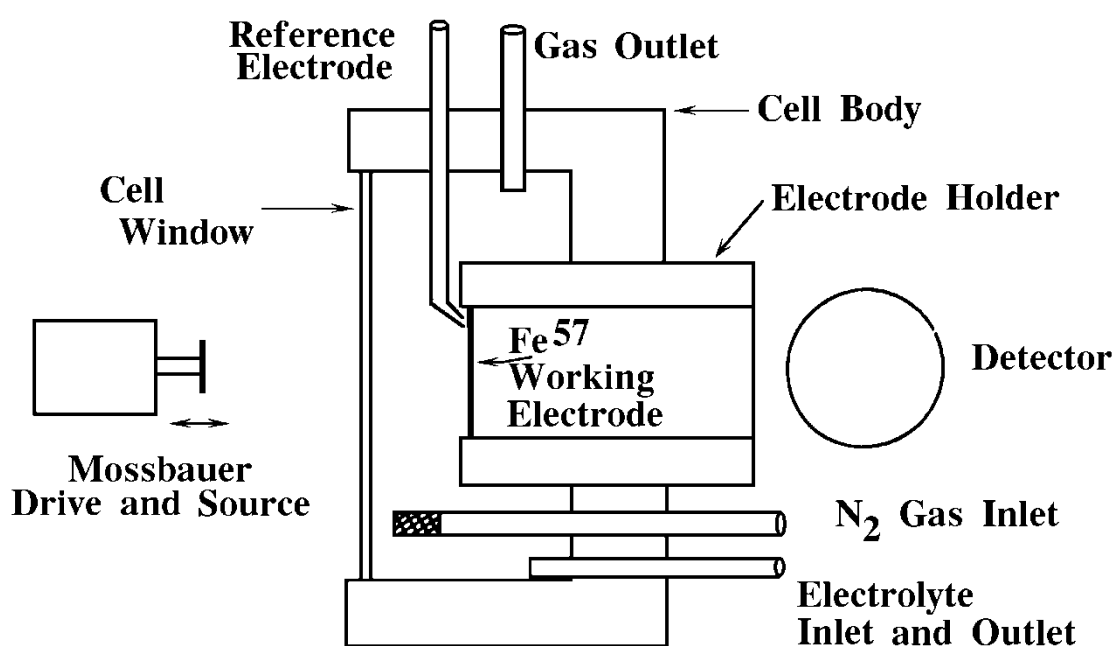
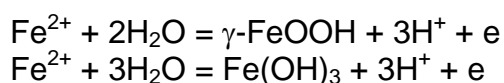


Fig.5.1 Electrolytic cell for recording Mössbauer spectra from samples in electrolytes (from [5.14]).

for its being hermetically sealed, the gases to be supplied and discharged, the electrode spaces to be separated, the electrolyte solutions to be changed and samples of the solution to be taken for analysis during the experiment.

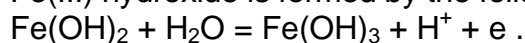
Electrodeposition of iron onto the  $\alpha$ - $^{56}\text{Fe}$  electrode was carried out from a sulphate solution containing 0.05 - 0.1 M Fe(II) ( $a = 94\%$   $^{57}\text{Fe}$ ). pH of 2.5 - 3.5 was adjusted with an ammonia solution. The process was conducted in an argon atmosphere at a current density 500 - 100 A/m<sup>2</sup>; ascorbic acid was added to the electrolyte before the electrodeposition to prevent Fe(II)  $\rightarrow$  Fe(III) oxidation.

In contrast to the use of a multilayer sample in [5.12], this technique makes use of both sides of the working electrode on electrodeposition and subsequent passivation which allows the signal-to-noise ratio to be enhanced by a factor of 2. It should be noted that in  $^{56}\text{Fe}$  foils 5 mm thick which were used in [5.14] the amount of  $^{57}\text{Fe}$  was equivalent to a layer 2.5 nm thick, i.e. approximately to the same amount which was supposed to be present in the passivating layer. In order to increase the useful signal fraction, the authors of [5.14-16] suggested the use of nickel foils as substrates and also of specimens with a well developed surface which were prepared by selecting, in particular, the proper conditions of iron electrodeposition. This technique was successfully employed for analysis of passivating films on an iron electrode in alkaline solutions [5.15] and also for studies of the effect of pH on anodic oxidation of Fe(II) in sulphate solutions, and for phase analysis of the oxide films formed [5.16]. Mössbauer spectra of these oxide layers are a doublet or a superposition of doublets and do not show a magnetic hyperfine interaction at room temperature. The quadrupole splittings vary in a wide range. In sulphate solutions when pH changes from 7.5 to 8.0, a distinct change of the phase composition of the oxide film occurs. From the hyperfine splitting parameters at pH < 8, it follows that of the two alternative reactions:



it is the first that probably occurs.

At pH  $\geq$  8.0 hydrate formation takes place and Fe(OH)<sub>2</sub> precipitates. Ferrous hydroxide participates in the precipitation of the oxide films directly on the anode surface. As pH increases, the precipitate structure, in the author's opinion, changes and the quadrupole splitting in Mössbauer spectra increases. From analysis of the experimental data it may be concluded that at pH ranging from 8 to 11, an amorphous Fe(III) hydroxide is formed by the following reaction:



At pH < 11, as is inferred from electrochemical data, the anode reaction should produce  $\gamma\text{-Fe}_2\text{O}_3$ , but the thickness of the passivating layer should be sharply diminished; the sensitivity of the technique [5.16] was not high enough to verify the statement.

Experience with an electrochemical cell that had been used in Mössbauer studies revealed that the current distribution at the working electrode, as a result of the electrode arrangement, may be very non-uniform. It is really critical to have a good parallel plate electrode configuration at the time of the potential step. ELDRIDGE and HOFFMAN designed a new cell [5.17] in which the working electrode ( $^{57}\text{Fe}$  film) and the counter-electrode were positioned in a parallel plate fashion. The solution thickness contributes only to 50 % absorption of  $\gamma$ -rays. The success of this new design was reflected in the reproducibility of multiple passivations, as opposed to the relative growth of the passive film signal characteristic of a slow passivation seen with an earlier cell.

The passive film thickness and structure depend on the passivation potential. The lack of measurable metallic iron signal loss after multiple potential step cycling indicates that cathodic reduction at  $\sim 400$  mV results in most of the iron ions in the passive film being reduced back to the metal. When stepped in the anodic direction (see Fig.5.2), the passive film

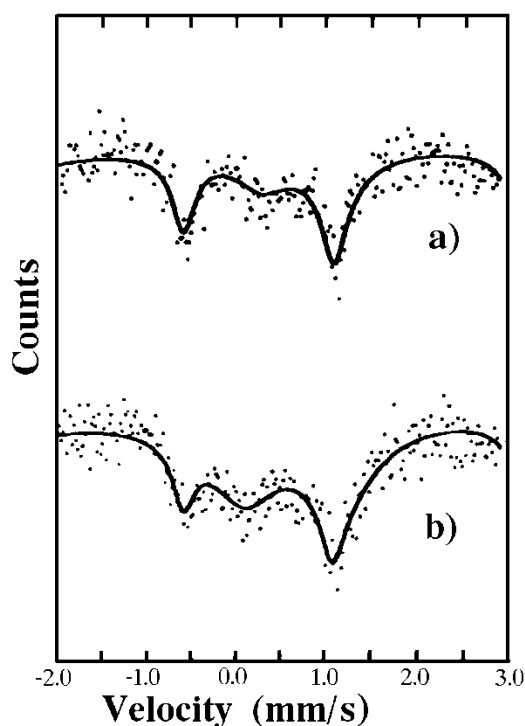


Fig.5.2 In situ transmission spectra of 10 nm  $^{57}\text{Fe}$  film passivated at different potentials in anodic direction: a - +350 mV and b - +1300 mV (from [5.17]).

grew about 250 % from +350 mV to 1300 mV. The spectrum a) is characterized by the following parameters:  $\delta = 0.72 \text{ mm/s}^{-1}$  relative to SNP,  $\Delta = 0.83 \text{ mm/s}^{-1}$  and  $F = 0.13$ , where  $F$  is a fraction of the total Mössbauer spectrum area due to the passive layer doublet, assuming the  $\alpha$ -Fe sextet to have a 3:4:1 amplitude ratio with equal peak widths; for spectrum b) -  $\delta = 0.63 \text{ mm/s}^{-1}$ ,  $\Delta = 1.07 \text{ mm/s}^{-1}$ ,  $F = 0.32$ .

A rough estimate of the passive film thickness at +1300 mV was 2.8 nm equivalent of  $^{57}\text{Fe}$ . The isomer shift decreases and quadrupole splitting increases with higher potential, suggesting a change in the film structure. These changes with increasing potential are consistent with a decrease in oxide water content in a partly hydrated ferric oxide or an oxyhydroxide.

Apart from in situ transmission mode studies of passivation processes some authors have used CEMS [5.13, 18-21] for this purpose. The reasons for that varied from a desire to use the equipment which is well proven in other electrochemical studies, to the enhancement in sensitivity of the technique. CEMS spectra can be obtained through the thin electrolyte layers present on immersed electrodes [1.18], however, current distribution problems may be severe. In [5.19] ex situ CEMS spectra were obtained, but relative absorptions at different potentials could not be unambiguously applied to monitor in situ changes in the passive film with potential.

The use of such physical methods of analysis of passive layers as ESCA or AES leads only to ex situ studies. For example, as described elsewhere [5.20, 21], the combination of CEMS and AES allows a complete qualitative as well as quantitative phase analysis of layers formed on the lower-lying layer. Very often it has been discussed whether such surface methods as CEMS may reflect the in situ status of the passive layer. Contact with air during the sample transfer may result in an oxidation of components of the layer, e.g. of  $\text{Fe}^{2+}$  to  $\text{Fe}^{3+}$ . In a layer which is loosely packed like rust, oxygen may have sufficient access to those species.

Some situations have been analyzed in [5.17, 22-24]. The in situ measurement capability with proper electrode placement allowed a clear comparison of in situ and ex situ spectra in order to detect changes in the passive film upon drying [5.17]. With the exception of very low passivating potentials, there is no significant loss of structurally bound water from the passive film upon drying, nor is there any phase change. It is possible that the films formed at +350 mV undergo further oxide growth upon air exposure and that spectral changes reflect this further oxidation and are not entirely the result of dehydration. From the fact that the ferrophosphate layer contains  $\text{Fe}^{2+}$  even after long exposure to air [5.24] it follows that the absence of  $\text{Fe}^{2+}$  in lower-lying layer is not due to an oxidation of  $\text{Fe}^{2+}$  to  $\text{Fe}^{3+}$  under ex situ conditions.

From the results of many investigations one has to conclude that the passivating effect cannot be due to the whole oxidic layer. One may assume that the passivation is due to a layer as thin as only 1-6 monolayers of close-packed oxygen ions, formed immediately on the metallic surface. The properties of such a layer on the metallic substrate would be amazing. The structure of  $\alpha\text{-Fe}$  would favour the formation of the oxides of the spinel type. However, the passivating layer does not contain remarkable amounts of  $\text{Fe}^{2+}$  nor magnetically ordered oxides like  $\text{Fe}_2\text{O}_3$  and  $\text{Fe}_3\text{O}_4$ . Their contribution, if any, is clearly less than 0.8 nm. The phase composition of the layers

formed by passivation does not fully agree with the composition stated in many publications, where  $\text{Fe}_3\text{O}_4$ ,  $\alpha$ -,  $\gamma$ - $\text{Fe}_2\text{O}_3$  are assumed. In accordance with [5.24] the layer consists most likely of (distorted)- $\gamma$ - $\text{FeOOH}$ . Thus, it is seen that transmission Mössbauer spectroscopy and CEMS may be effective tools of electrochemical studies. Both techniques have shown no magnetite to be present in the passive layer.

Smallest amounts of substance can be studied by emission Mössbauer spectroscopy, which allows the bulk samples to be investigated. The minimal amount to be investigated is determined by the half-life of the parent nuclide and by the measuring time. If Co or cobalt-containing substances are to be investigated, doping the sample with  $^{57}\text{Co}$ , which is the parent nuclide for  $^{57}\text{Fe}$ , allows emission spectra to be recorded from 1  $\mu\text{Ci}$ , i.e.  $1.25 \cdot 10^{12}$  atoms, in a relatively short period of time. For a cobalt foil this would be equivalent to 1/1000-th of the number of atoms making up a monolayer with an area of 1  $\text{cm}^2$ . The large difference in chemical properties of Fe and Co, and also the post-effects of the nuclear transformation, impose a complication on the use of  $^{57}\text{Co}$  as a probe atom to provide information on corrosion processes. At the same time for the in situ studies of cathodic and anodic behaviour of cobalt and its alloys [5.25-27] and also of its corrosion, emission Mössbauer spectroscopy may be the most efficient method [5.28,29]. Thus, in [5.28] the polarization of cobalt coatings was successfully studied in buffered borate solutions ( $\text{pH} = 8.5$ ) as a function of anodic potentials, the Mössbauer spectra being recorded in situ.  $^{57}\text{Co}$  was electrodeposited onto a metal cobalt surface. The required thickness of the layers was produced by addition of  $\text{CoCl}_2$ . To study the process at low passivating potentials, relatively thin layers were produced (20 - 30 Å). For higher-potential studies, up to an active-to-passive transition, the layer thickness was increased from 50 Å to 200 Å. The corrosion rate was always sufficiently low for the spectra to be recorded before the  $^{57}\text{Co}$ -containing active surface region was dissolved. This allowed the processes on the cobalt surface and its structure under "real" electrochemical conditions to be examined by Mössbauer spectroscopy. The oxide films that may have been formed during sample preparation, appeared to be reduced under conditions of cathodic polarization (-1.1 V).

Whereas corrosion studies by both transmission Mössbauer spectroscopy and emission Mössbauer spectroscopy are important, more widely used is Mössbauer spectroscopy in a backscattering geometry. One of the first works in this field [2.60] was related to corrosion. BONCHEV [3.28], when developing DCEMS, demonstrated this possibility studying the oxidation of  $\beta$ -Sn (see Fig.3.21). HUFFMAN [2.2] examined

the oxidation products of iron and tin to illustrate the theory of CEMS in the approximation of the exponential attenuation of electrons. More specialized papers [5.18-24,30-39] on the investigation of the oxidation of iron and steels by CEMS have shown its use for studies of kinetics and phase analysis of surface layers. There are several problems concerned with the analysis of the results of corrosion studies.

1. The absence of data banks for Mössbauer spectra of all the compounds which could be encountered during the studies is a problem. For quantitative determinations the importance of the  $f'$  parameter should be specially emphasized. An attempt to systematize the  $f'$  values is described in [5.40, 41].

2. The absence of a rigorous technique for obtaining information on the state of the substance e.g. crystallized, amorphous, or fine particles.

3. The absence of a detailed and experimentally verified technique of a layer-by-layer analysis.

4. The absence of a widely used technique for determining the thickness and continuity of the analyzed layers.

Sophisticated methods like DCEMS can be especially used for investigating thinnest overlayers. An example is the study of a passive layer which is present on iron kept in a dry atmosphere [3.88,5.42]. To obtain a higher sensitivity of the method,  $^{57}\text{Fe}$  foils  $\sim 30\ \mu\text{m}$  thick were used ( $a = 90\ \% \ ^{57}\text{Fe}$ ). The foils were cold-rolled from a 2 mm thick iron plate with an intermediate and final thermal treatment. The surface of original foils exposed to air for several months has not shown any apparent signs of corrosion, though it could be supposed to have been covered with a passive layer of a natural origin; it was interesting to investigate it by Mössbauer spectroscopy.

Some results of these investigations were considered above (see Sect.3.6 and Fig.3.42). DCEM spectra were recorded with a special care and were not inferior in their quality to the best DCEM spectra reported up to the present. The spectra were recorded with a  $\beta$ -spectrometer adjusted to detect electrons with an energy which is both slightly less and more than 7.3 KeV, with very low and high velocities to estimate both possible disturbing spectral effects: relaxation and geometry. From both DCEMS and ESCA data BELOZERSKII et al. [3.88,5.42] found that the oxide layer on the foil surface consisted of a very hydrous ferric oxide with a structure similar to liquid crystals.

The absence of a detectable Mössbauer signal from oxides or hydroxides at room temperature is caused, in the author's opinion, not only by the fact that the spectrum may be a smeared out relaxation pattern (see Fig.3.42). If, for example, relaxation exists, the  $f'$  factor value will not exceed 20 % of the typical  $f'$  value for the bulk Fe oxides and hydroxides. Such a layer prevents the pure iron surface from oxidation and allows the foil to be in a dry atmosphere for several months without acquiring the reddish or brown tint characteristic of oxidized materials. The low  $f'$  factor value for a series of oxides and hydroxides was reported elsewhere [5.43, 44]. According to these reports, freshly precipitated  $\text{Fe}(\text{OH})$  does not show a Mössbauer spectrum at 298 K. The reason for this is a low probability for recoilless scattering of a  $\gamma$ -quantum, as the ions of the gel-like  $\text{Fe}(\text{OH})_2$  are only loosely bound to the crystal lattice. The similar situation was observed for other hydroxides [5.44].

The scientific interest for passivation studies, to say nothing about the applications, stimulated the research in this field. An unexpected result of BELOZERSKII et al. that the passive layer thickness derived from DCEMS data (no more than 10 FeÅ) differs substantially from that obtained by ESCA, made a further contribution to the problem. The idea of the authors of the first series of works [3.183, 5.45] is in a sensitivity enhancement of the technique to the signal from the surface due to the different isotopic abundance of the surface and the backing (but not the bulk). Unfortunately, practically nearly no attention has been paid by the authors to comparing corrosion properties of the sample under investigation with those of real samples.

Within this approach, SHINJO et al. [5.45] produced samples which consisted of a very thin layer of the non-resonant isotopes on which a still thinner layer of the resonant isotope was deposited. On a 210 Å thick  $^{56}\text{Fe}$  film a  $^{57}\text{Fe}$  20 Å layer was deposited. Twenty such duplex films were made and investigated in transmission geometry. The Mössbauer spectrum from the sample contained the signal from ferric oxide (60 % of the total area). However, the authors had not considered that the similarity between the hyperfine interaction parameters of their samples and those of the bulk iron could not guarantee reproducible corrosion resistance and oxidation of their samples and the bulk iron or the well thermally treated foil. This may be due to a different surface activity, structural characteristics or the number of defects and dislocations in a unit volume. Indeed, it has been shown that on depositing layers even thicker than 200 Å, the oxidation processes are not the same as in the bulk sample [5.30, 46]. In order for both the physical properties and geometrical structure of such a sample as well as its corrosion resistance to be similar to those of the bulk, a special thermal treatment is needed. However, the treatment would have led to a complete "mixing" of the iron isotopes in the samples used e.g. in [5.45, 47], and this has therefore not been performed.

On using layers about 20 Å thick it should be taken into account that oxidation may occur directly on depositing such layers due to the residual oxygen and sometimes to the high temperature of the backing. If this is the case, spectra which are similar to those presented in [5.45] convey information on the hyperfine interaction parameters in a multilayer sophisticated structure, but no information about passive layers. The conclusion that similar oxidation may really take place was arrived at by STANIEK et al [3.183] who tried to check the validity of the hypothesis of BELOZERSKI et al [5.42] using a similar DCEM spectrometer, but the samples similar to [5.45]. Mössbauer spectra presented in [3.183] have rather poor quality and it is only due a hypothesis,



which is formulated beforehand that one can state that an oxide subspectrum is present in the spectrum. Moreover, since an additional layer was deposited in a relatively bad vacuum the overlayer of  $^{57}\text{Fe}$  was expected to be contaminated or eventually oxidized. Thus, on the surface of such a sample, no passive layer can be formed contrary to the surface of the bulk sample under investigation in [5.42].

It is clearly of fundamental interest that the Mössbauer signal from thin oxide layers and the bulk is variable and not directly related to the concentration of iron atoms in the environments. This variability, if exists, would be disastrous for some applications in surface analysis and nondestructive depth profiling. To check it, STADNIK et al.[3.67] used a DCEMS spectrometer in which the electrons analyzed have low take-off angles with respect to the surface. Such spectrometer has the highest surface selectivity. For a mean take-off angle of about  $20^\circ$ , the mean inelastic escape depth was less than  $20\text{\AA}$ . The crucial factor in the choice of an electron analyzer for such Mössbauer experiment is in fact the high transmission of the spectrometer. The quality of spectra obtained was high and the results were similar to those of BELOZERSKII et al.. Moreover, Stadnik et al. observed no enhancement of the surface oxide contribution when the Mössbauer effect was monitored using the low-energy LXY Auger electrons.

Studies of the passive layer are aimed, to a great extent, at a search for a subspectrum to be associated with the layer. Searching for the subspectrum the shape of which is not known, it is necessary to avoid any unambiguity connected with the experimental technique and especially with mathematical treatment of the results. The result of such treatment to a certain extent is predetermined by the hypothesis used and the data-processing program applied. A classical example is the analysis of spectral distortions due to geometry of the experimental set-up. Usually, a correction of spectra is carried out (see Sect.4). However, the accuracy of this procedure is limited, and an overcorrection or undercorrection takes place. KLINGELHÖFER and MEISEL [5.48] studied the surface of  $\alpha\text{-Fe}$  foils by DCEMS, where the distance from a source to the sample was about 10 mm. The cosine effect was corrected using one of the appropriate distribution functions, but other possible effects of spectrum distortion were not taken into account neither was the accuracy of the cosine correction evaluated. To decide only on the basis of this procedure about the presence of subspectra with unusual line shape and then to identify it as an oxide signal is doubtful. In order to solve problems of analysis of the passive layer of a natural origin on bulk samples, measurements should be conducted at temperatures near to liquid helium temperatures, since the small factor  $f'$  values cannot be supposed and relaxation effects cannot be present. Unfortunately, these experiments are complicated and have not been reported. Evaluations of the thickness

of the passive layer [3.67,5.42] formed on the iron surface under natural conditions agree with the evaluations obtained later [5.17,22] for a similar layer formed in electrochemical cells.

Apart from CEMS, studies of the oxidation of metals and alloys by Mössbauer scattering spectroscopy, with  $\gamma$ -quanta or K-X-rays being detected can also be performed. In [2.60] the detection of K-X-rays has enabled rust formed on a steel surface as a result of its exposure to an HCl-saturated atmosphere to be investigated. Detecting  $\gamma$ -quanta allows an investigation of rather thick corrosion deposits on the iron surface in an atmosphere of 100 % relative humidity. The studies of the phase composition of the rust layers more than 1  $\mu\text{m}$  thick were popular in first applications of Mössbauer spectroscopy in corrosion studies because it does have certain advantages. Firstly, in situ studies of corrosion the relatively strongly penetrating  $\gamma$ - and X-rays together with the enrichment of the sample surface in the resonant isotope are useful. Thus, for iron-based alloys at  $a = 90\%$   $^{57}\text{Fe}$ , it is relatively easy to separate out the signal from the surface layer 20 - 40 nm thick on a bulk sample. Secondly, the use of the layer-by-layer analysis is important of which there are three possible varieties. One is a simultaneous or separate detection of electrons or  $\gamma$ -quanta and recording their spectra and using the different penetration of these radiations. In [5.32], such a technique has been used to study the oxidation of iron in air at 490°C to 800°C. The layer-by-layer analysis can be accomplished by the variation of the angle of incidence and scattering (see Sect.2.6) and the use of destructive analysis, e.g. etching.

Hence, various Mössbauer techniques can be used to study corrosion and these are listed in Table 5.1.

When the process under study is to be interrupted to analyze the corrosion products, it is necessary to be sure of the validity of the results and to know the inaccuracy introduced by the measurement itself. On studying iron oxidation at elevated temperatures in dry air or pure oxygen there are no such problems, and the power of Mössbauer spectroscopy for studies of structure, phase composition and chemical properties of surface layers is achieved. It is no surprise that many research groups have concentrated their efforts in this direction. Some results of atmospheric corrosion studies, which are classical applications of Mössbauer spectroscopy, will be considered below.

Among reports where transmission geometry has been used, are the studies of oxidation of iron foils (99.9 % Fe) 10  $\mu\text{m}$  thick in  $\text{O}_2$  at 1 atm and in the temperature range 500°C- 700°C. The studies were aimed at obtaining information on iron diffusion through magnetite and oxygen diffusion through haematite [5.49-51]. The growth rate studies of haematite from magnetite on an oxidized iron foil with a magnetite/haematite ratio of 2:1, showed that the growth of haematite followed a parabolic law. In [5.52] CEMS was used to study the initial stages of high-purity (99.99 %) iron oxidation at 240 °C and

Table 5.1  
Corrosion studies by Mössbauer spectroscopy

Processes under study	Corrosive environments, objects, applications
Passivation	Solutions and electrode surfaces in solutions at various potentials. Properties and structure of passive films in solutions, in gases or in vacuum.
Corrosion in water and in aqueous solutions	Distilled water. The effect of oxygen. The effect of other admixtures in water. The temperature effect in aqueous media. Water vapor corrosion. Corrosion in power plants.
Corrosion in gases	Pure oxygen or dry air. Atmospheric and water vapor corrosion. Aggressive gases. Combined action of both gas media and solutions.
Corrosion in aggressive environments	Acids. Alkalis. Organic and natural media. Corrosion in tubing and autoclaves. Applications in agriculture.
Specific corrosion processes	Stress corrosion. Corrosion beneath lake and polymeric coatings. Transformations of corrosion products to enhance the protective properties and to identify the corrosion products.
Inhibition and passivation	The effect of special inhibiting or passivating admixtures on the on the composition and growth rate of protective films.
Corrosion of amorphous alloys	Materials science. A check on the theory used to describe corrosion of amorphous alloys.
Internal oxidation	Material science.

350°C and under an oxygen pressure of  $5 \cdot 10^{-3}$  Torr. Magnetite was formed on the iron surface with a layer thickness (d) in the range 260 Å to 4500 Å depending on the temperature and the sample treatment. An empiric relation was obtained

$$d(\text{\AA}) = -1.95 \cdot 10^3 \ln(1 - 0.01 \eta), \quad (5.1)$$

where  $\eta$  is the percentage contribution by the oxide to the total spectrum area. The oxygen uptake was measured for the samples [2.2, 3.32] but due to the insufficiently reliable roughness factor the oxide layer thickness was overestimated.

A detailed study of the structure of oxide layers and their transformations was made possible by CEMS and by detecting the scattered  $\gamma$ -quanta. By this method the oxidation behaviour of high-purity iron (99.99 %) and carbon steels (0.04 at % C) was investigated [5.32]. Short oxidation times even at about 500°C allowed the initial stages of oxidation to be investigated and the layers of  $\alpha$ -Fe<sub>2</sub>O<sub>3</sub> and Fe<sub>3</sub>O<sub>4</sub> to be detected. Under these conditions the oxide layer growth rate obeyed the parabolic law with the rate constant  $k = (6 \pm 3) \cdot 10^{-12} \text{ cm}^2 \text{ sec}^{-1}$ . It is interesting that a texture in iron oxide layers on iron has been observed. Haematite or magnetite layers up to 2000 Å thick on the surface of polycrystalline pure iron appear to have a preferential orientation of the magnetization vector in the plane of the layer. At oxidation temperatures above 500°C the Mössbauer spectra show that wustite is the main component in the oxide layers with the inner wustite layer and the outer magnetite layer being in equilibrium with each other. On increasing the length of the oxidation time the magnetite transformed into haematite.

The use of materials enriched in the Mössbauer isotope leads to an enhancement in sensitivity and improved accuracy of the method. The oxidation of iron foils has been investigated [5.46]. One foil with  $a = 70 \%$  <sup>57</sup>Fe, and two foils (99.99 and 99.94 % pure) with  $a = 2.14 \%$  <sup>57</sup>Fe were examined. The enriched foils were pretreated at different temperatures to prepare the surface. The oxidation was conducted in pure oxygen ( $p_{\text{O}_2}$

**Ошибка! Не указан аргумент ключа.** ~10 Torr) at temperatures from 250°C to 500°C. At 250°C the oxygen uptake followed the parabolic law and at 500°C it became significantly large and was associated with the growth of haematite whiskers.

Typical CEMS spectra are given in Fig.5.3 of two oxidized iron samples. The oxidation was conducted to give nearly equal weight-gains per unit geometrical area. The pretreatment of the enriched sample gave a spectrum with a similar line shape. The enrichment leads to a significantly larger observed effect and thereby to a higher sensitivity. An analysis of the accuracy of determining the thicknesses of the haematite layer  $d_h$  and magnetite layer  $d_m$  allowed the authors to suggest a method to calculate the roughness factor for the oxidized surface. The ratio of the weight-gain  $W$  to the sample area  $S$  may be written [5.46] as:

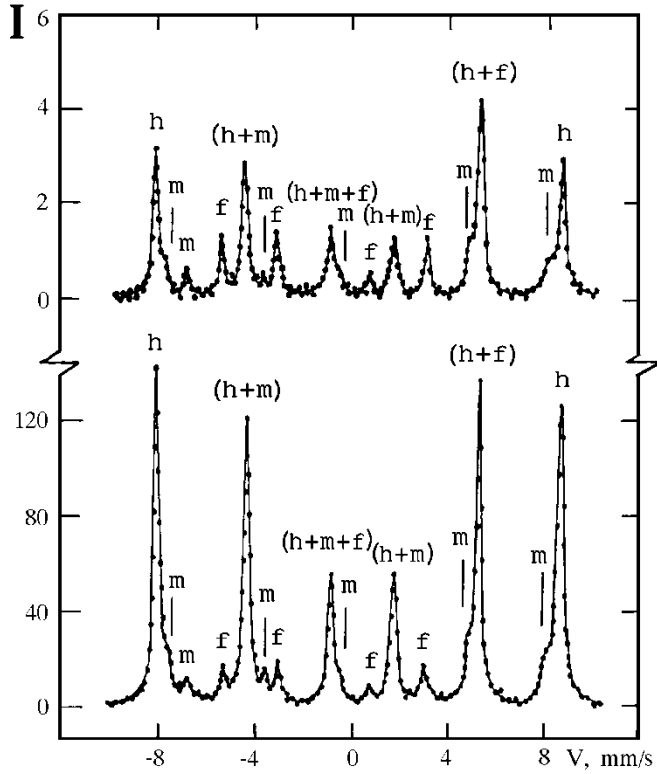


Fig.5.3 CEMS spectra from iron foils oxidized in an oxygen atmosphere (10 Torr): a - natural iron (99.99 %), 2 hrs at 400° C, b -  $\alpha$ - $^{57}\text{Fe}$  ( $a = 90\%$ ), successive heat treatments for 2 hrs at 250°C, 2 hrs at 150°C and 2 hrs at 400°C; f - iron; h - haematite; m - magnetite (from [5.46]).

$$W/S = (3N_h d_h + 4N_m d_m) r W_0, \quad (5.2)$$

where  $N_h$  and  $N_m$  are the number of haematite and magnetite "molecules" per unit volume of the oxide,  $r$  is the surface roughness factor, and  $W_0$  is the weight of an oxygen atom. Inserting the corresponding values into (5.2) we obtain

$$W/S = (1.562 d_h + 1.413 d_m), \quad (5.3)$$

where  $W/S$  is in  $\text{g/cm}^2$ , and  $d_h$  and  $d_m$  are in cm. At first the  $r$ -value for the most lightly oxidized sample is very large ( $r \approx 5.5$ ), but it then decreases rapidly to a nearly constant value of about 1.8 before increasing fairly slowly. This shows that the oxide coatings are not uniform and that the thickness as determined by CEMS is the average thickness of the oxide layers. The surface pits and scratches in which oxide particles

are formed may account for the large  $r$  factor values. The nearly constant  $r$  factor value of  $\approx 1.8$  is believed to characterize a good metallic iron surface. By using this technique layers of only two or three monolayers thick may be studied.

To significantly enhance the sensitivity one can use a "duplex" scatterer. An example is high purity iron with a 500 nm  $^{57}\text{Fe}$  layer deposited on it [5.30]. Preliminary experiments showed that due to defects, stresses and admixtures with carbon and other elements the layer structure is imperfect and a special treatment is required to compare the data with results recorded from ordinary samples. It was found that the oxidation carried out at 225°C under 1 atm of oxygen led to the formation of a cation deficient magnetite with the thickness following a logarithmic time dependence. Haematite appeared at 350°C. Oxidation at 450°C produced mainly  $\text{Fe}_3\text{O}_4$  which was nearly stoichiometric. The  $\text{Fe}_3\text{O}_4$  was not formed at lower temperatures since the magnetite layer was thick enough to hold the cation flux below the level favouring magnetite formation [5.30]. After treatment at 450°C for 10 min the flux increased and the  $\text{Fe}_3\text{O}_4$  became nearly stoichiometric. Thus, the technique can be used to enhance the analytical sensitivity to small amounts of newly formed phases on the sample surface. But it is desirable that the enrichment should be followed by thermal treatments. Preparing thinner layers causes the sensitivity to be further enhanced, but it excludes the thermal treatment and limits the applications of the technique.

Magnetite and the oxide with a very similar crystal structure - maghemite often occur in the rust and in the protective layers, especially under atmospheric and aqueous corrosion and after annealing. They give nearly identical X-ray diffraction patterns and this technique alone does not allow to distinguish them. As a rule, attempts to use electron diffraction fail since diffraction spectra of magnetite and maghemite are also very similar and the imperfection of their structure means that they cannot be differentiated. Due to the importance of identification of these oxides in corrosion studies the problem should be considered in more detail. Although Mössbauer spectroscopy allows very thin layers and fine particles to be investigated, there are some problems encountered on conducting the phase analysis.

The hyperfine interactions parameters are different for both oxides and on this basis it is possible to distinguish them. The spectrum of the "standard" magnetite displays two sextets at room temperature (see Fig.5.4a) due to two sites, A and B. The sextet with a greater magnetic field represents  $\text{Fe}^{3+}$  ions in tetrahedral sites (A sites), the other one with lower magnetic field corresponds to  $\text{Fe}^{3+}$  and  $\text{Fe}^{2+}$  ions in octahedral positions (B sites). The relative abundance of site occupancy must be 33% for A-sites and 66% for B-sites. But it was reported [5.53], that the Mössbauer line area ratio of the B-site to the A-site in stoichiometric magnetite was 1.85.

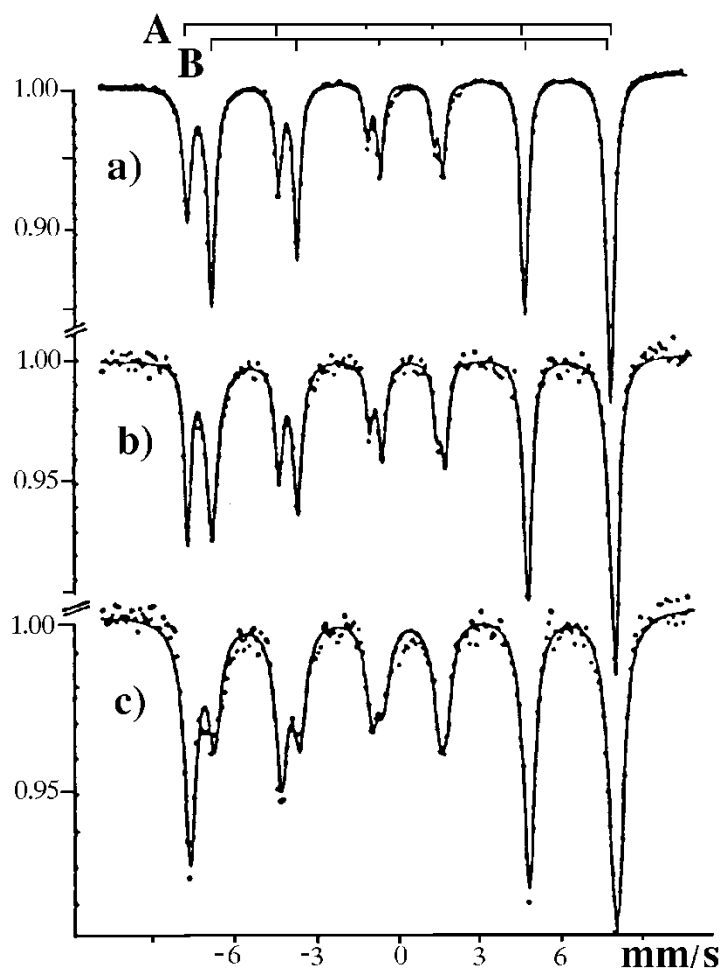


Fig.5.4 Spectra of magnetite samples at room temperature: a - standard sample; b - sample prepared under basic conditions:  $[\text{Cl}^-]/[\text{OH}^-] = 0.975$ ; c - sample prepared under acidic conditions:  $[\text{Cl}^-]/[\text{OH}^-] = 1.025$  (from [5.54]).

The experimental spectra are usually said to correspond to non-stoichiometric magnetite with vacancies in the B positions or with these positions occupied by ions other than  $\text{Fe}^{2+}$ . However, the spectra may be due to maghemite or mixture of maghemite and magnetite. At room temperature the maghemite sextet coincides sufficiently accurately with the sextet of ferric ions in A positions of magnetite and to distinguish them additional measurements are required. The high sensitivity of Mössbauer spectra to the stoichiometry of the magnetite is demonstrated in Fig.5.4 b and c, which correspond to the end products of oxidation in chloride medium for basic and acidic conditions, i.e.  $[\text{Cl}^-]/[\text{OH}^-] = 0.975$  and 1.025 respectively [5.54]. Parameters of the Mössbauer spectra are given in Table 5.2. The hyperfine interaction parameters of magnetite may change in a wide range, e.g. at room temperature for  $H_A$  from 49.8 to 47.5 Tesla and for  $H_B$  from 46.4 to 43.5 Tesla. The subspectrum due to B-sites

sometimes is practically not resolved from more intensive sub-spectrum – A, e.g. [5.55]. Moreover it is known [5.56, 57] that under superparamagnetism both sextets which are characteristic of  $\text{Fe}_3\text{O}_4$  collapse into one. Upon decreasing the particle size the sextets transform into a doublet similar to the  $\text{Fe(III)}$  doublet. Further decrease of the particle size results in the doublet transforming into a singlet.

Table 5.2

Mössbauer parameters of three magnetite  $\text{Fe}_{3-x}\text{O}_4$  samples [5.54] at room temperature. Isomer shifts are relative to metallic iron. a - standard sample; b - sample prepared in basic conditions:  $[\text{Cl}^-]/[\text{OH}^-] = 0.975$ ; c - sample prepared in acidic conditions:  $[\text{Cl}^-]/[\text{OH}^-] = 1.025$

	$H_A$ Tesla	$\delta$ mm/s	$H_B$ Tesla	$\delta$ mm/s	x
a	49.5	0.266	46.4	0.675	0
b	48.7	0.291	45.5	0.654	0.09
c	49.1	0.300	45.5	0.620	0.18

If the oxides making up the film are in a superparamagnetic state, the spectra should be obtained at temperatures lower than the blocking temperature, i.e. when superparamagnetism is not observed [5.58]. That is why, when at room temperature a spectrum is observed similar to a maghemite spectrum or  $\text{Fe(III)}$  doublet additional measurements must be performed at other temperatures. This may be time-consuming, but till now it is only Mössbauer spectroscopy that can identify and distinguish bulk non-stoichiometric magnetite and maghemite or identify high dispersed non-stoichiometric magnetite.

A thorough investigation of oxidation of an iron sample has been described [5.47]. The samples were (110) and (100) natural iron single crystals on the surface of which a 100 Å thick  $^{57}\text{Fe}$  layer was deposited by evaporation. Oxidation was performed under oxygen pressures  $2 \cdot 10^{-4}$  to  $8 \cdot 10^{-3}$  Torr at  $255^\circ\text{C}$ . The thickness of the oxide layers was measured between 10 and 100 Å, i.e. where other methods could not be easily used. The growth rate of the iron oxides on the (100) face turned out to be 10 times higher than on the (110) face. At early stages of oxidation, that is for oxide layer thicknesses of less than 80 Å, a logarithmic rate law  $d \sim \ln t$  was observed, which then became a parabolic rate law. The Mössbauer spectrum corresponded to magnetite. Haematite began to form after longer oxygen exposure, having been initially beneath the magnetite layer, and then having covered it. The result seemed unexpected, as well as the changes in the hyperfine interaction parameters within the 15 Å thick layer of the oxides. A question arises as to whether this is connected with the process of surface layer formation. The technique developed in [5.47] allows a signal from an oxide layer about 3 FeÅ thick for the Zeeman split spectrum, and from a layer about 1 FeÅ thick for the doublet to be detected. It should be repeated, that it is desirable to have a proof of the fact that the properties of the deposited layer are the same as those of the



substrate.

An important problem in science and technology is corrosion control in steel equipment used to generate steam, especially in atomic power plants. One of the first works using Mössbauer spectroscopy for corrosion studies was connected with this problem [5.4]. Iron corrosion kinetics was studied in deoxygenated water in an autoclave at temperatures of 180°C to 290°C for various lengths of time. The rate of the magnetite film growth was established. By the temperature dependence the Arrhenius activation energy was found to be  $(65.3 \pm 2.1)$  kJ which is comparable with the activation energy for the decomposition of the ferrous hydroxide formed at the surface. Results of the investigation of corrosion products which were removed from mild steels used in a high temperature water circuit in a nuclear reactor are also given in [5.4]. It was shown that the conversion of  $\text{Fe}(\text{OH})_2$  into  $\text{Fe}_3\text{O}_4$  was an important reaction which determined the nature of the corrosion products at the initial stage of the power plant operation. At later stages, larger  $\text{Fe}_3\text{O}_4$  particles were formed which inhibit the corrosion process. Corrosion processes in power plants are also influenced by ionizing radiations. For example, in [5.59,60] oxide layers were described as being formed on the low-carbon steel (0.1 % C) surface in distilled de-ionized water at 473 K and 100 atm. This steel construction was studied both under high intensity ionizing radiation (5.5 MeV electrons) and without it. The effect of the ionizing radiation on the low-carbon steel in an autoclave was not limited by the change of the corrosion rate, but was followed, at least in the early stages, by the formation of a specific oxide film.

Up to the beginning of the 1970's, special alloys and steels with a high concentration of alloying elements were used in nearly all power plants. These materials were the natural choice for Mössbauer studies. Thus, the kinetics of the initial growth stage and the composition of protective oxide films on special alloyed steels with a high concentration of alloying elements: martensite Fe-Cr steels and austenite Fe-Ni-Cr steels used in steam generation equipment, were studied [5.61], and corrosion processes in zirconium alloys were studied in [5.62]. To analyze the protective films on alloyed steels, Ensling et al. [5.61] used a special boiler, which simulated the conditions of power plant operation. The boiler was filled with deoxygenated water at 295°C and 142 Torr. A pH of ca 9 - 10 was maintained by adding LiOH. Typical Mössbauer spectra are given in Fig.5.5.

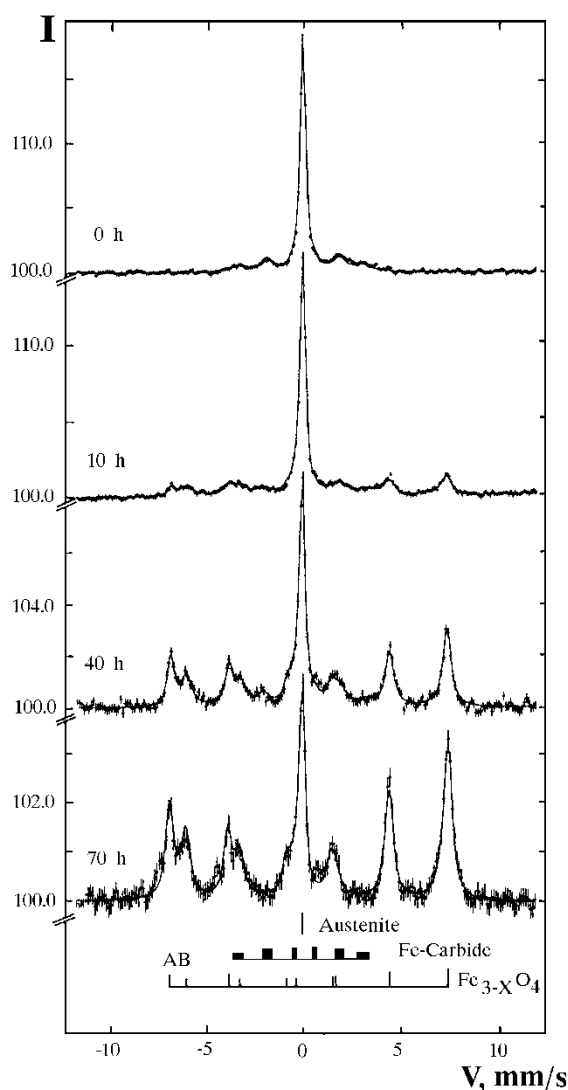


Fig.5.5 CEMS spectra of austenite steel 1.4550 (66 - 70 % Fe, 9 - 11 % Ni, 19 - 23 % Cr) oxidized in water at 295°C and 142 bar (from [5.61]).

The protective layer consists of non-stoichiometric magnetite with hyperfine interaction parameters similar to those of bulk samples. The magnetic stoichiometry changed with increasing exposure. For a higher Ni content in alloyed steels the protective layer appeared to consist of mainly nickel ferrite with the composition being close to  $\text{Ni}_{0.8}\text{Fe}_{2.2}\text{O}_4$ . Kinetic studies of the oxide growth rate show (Fig.5.6) that the oxidation rate of the alloys in the time intervals studied is most likely determined by diffusion through the oxide layer along the grain boundaries, dislocations and pores. A logarithmic rate law was considered to be most probable [5.61]. As Ni content decreases the corrosion rate becomes higher. Ensling et al. [5.63] investigated also oxide layers on tubes

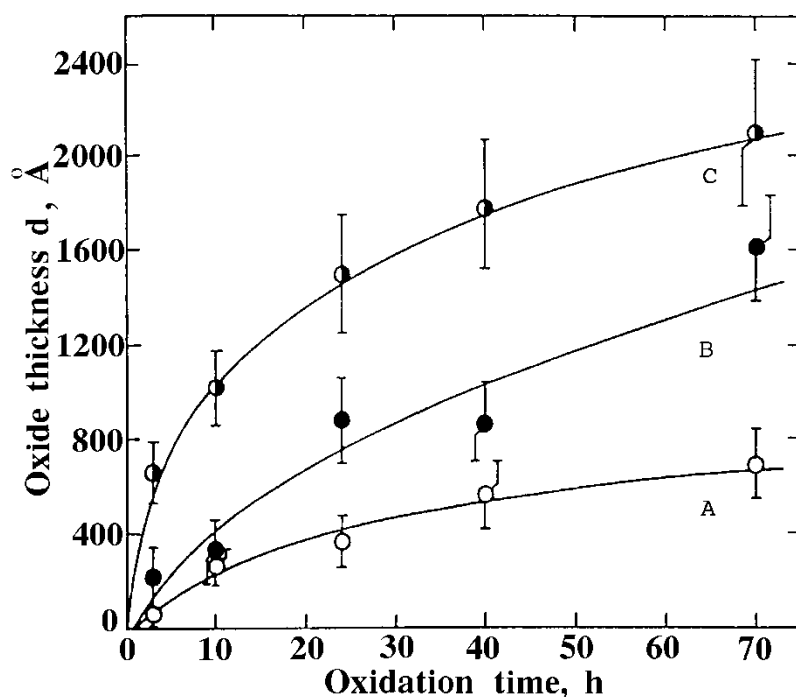


Fig.5.6 Oxide thickness  $d$  of stainless steels (from [5.35]) A - INCOLOY 800 (40-49 % Fe, 30-35 % Ni, 19-23 % Cr), B - 1.4550 (see Fig.5.5), C - 1.4122 (80 % Fe, 16,5 % Cr) (from [5.61]).

in steam generators by  $^{57}\text{Fe}$  Mössbauer spectroscopy in transmission and backscattering mode. The authors have shown that the protective oxide layers contained mainly  $\text{Fe}_{3-x}\text{O}_4$  ( $x \leq 0.03$ ) partly in microcrystalline form ( $< 50 \text{ nm}$ ). In addition to magnetite, hematite was also detected in one of the samples.

The use of construction austenite steels in atomic power plants has shown these steels to be susceptible to stress corrosion cracking. Thus, these materials turned out to be less reliable than anticipated. Furthermore, the cost of alloying elements needed to produce the steels is constantly increasing. Hence, since the mid 1970's the carbon steels have been of considerable interest for research and technology. It has been shown that it is possible to lower the total corrosion rate of perlitic steels to that of austenite steels by promoting the formation of thin (about  $100 \text{ Å}$ ) protective oxide layers. For this purpose neutral water is used in the circuits with controlled amounts of oxidizers (oxygen or hydrogen peroxide) to produce the protective oxide layers.

To substantiate the choice of oxygen or hydrogen peroxide the oxide film formation in the presence of oxidizers must be understood. These studies have been conducted by CEMS on real objects [5.64]. It was shown that in the system "perlite steel - aqueous  $\text{H}_2\text{O}_2$ " hydrogen peroxide played the most important role at the first stages of the oxide film formation on the steel surface (it stimulated the passage of ferrous ions into solution). In the solution hydrogen peroxide promotes the oxidation of ferrous iron to ferric iron. Relatively stable aqua-peroxo-hydroxo-complexes are formed by the Fe(III) hydrolysis products and hydrogen peroxide. Being adsorbed on the steel surface, the complexes form a phase which gives a quadrupole split Mössbauer spectrum corresponding to Fe(III). This is either magnetite in a superparamagnetic state, or a phase forming magnetite "seeds" on its interaction with the metal surface. Further magnetite growth may proceed without hydrogen peroxide participation. Increasing the temperature up to  $80^\circ\text{C}$  enhanced the formation of magnetite seeds on the steel surface in contact with  $\text{H}_2\text{O}_2$  solutions by a factor of 5 - 10 (as compared with that at room temperature).

The similarity of the chemical properties of perlite steels and  $\alpha\text{-Fe}$  leads to an assumption that by studying the corrosion of  $\alpha\text{-Fe}$  in  $\text{H}_2\text{O}_2$ -containing water one could obtain information on the corrosion products of perlite steels in the same solution (see the discussion about the natural passive layer). Iron corrosion in solutions of hydrogen peroxide is a convenient process to be studied by DCEMS [5.42]. Solutions were taken, containing 0.006 and 0.012 %  $\text{H}_2\text{O}_2$ , which are close in the composition to those used in water circuits of atomic power plants. For comparison experiments were made with higher concentration  $\text{H}_2\text{O}_2$  solutions (from 6.8 % to 13.6 %) at  $25^\circ\text{C}$  and  $85^\circ\text{C}$ . Samples from a solution were mounted in the  $\beta$ -spectrometer, brought to a vacuum of less than  $10^{-5}$  Torr. In Fig.5.7 Mössbauer spectra are given of a sample exposed for 22 hrs at  $25^\circ\text{C}$  in a 0.012 %  $\text{H}_2\text{O}_2$  solution. The results are given of DCEMS investigations on iron corrosion in low concentration hydrogen peroxide solutions in Table 5.3.

Corrosion in solutions of low concentration  $\text{H}_2\text{O}_2$  at room temperature leads to the appearance in the Mössbauer spectra of a single line presumably due to magnetite in a superparamagnetic state. For corrosion in 0.006 %  $\text{H}_2\text{O}_2$  the DCEMS data are in a good agreement with the oxide layer model with an average thickness of the layer  $d_{av} \approx 6 \text{ Fe}\text{\AA}$  covering the entire surface of the sample. At a hydrogen peroxide concentration of 0.012 % the oxide is about 220  $\text{Fe}\text{\AA}$  thick, covering only about 8 % of the sample surface. The shape of the Mössbauer spectra recorded from the samples corroded at  $85^\circ\text{C}$  become more complicated. To study the oxide films and the transformations of fine oxide particles on the surface, all samples were annealed in the  $\beta$ -spectrometer. The DCEMS spectra of the products are also given in Fig.5.7. Hence, it has been shown that low concentration of hydrogen peroxide suppresses the corrosion processes. The oxide layer grows during the exposure, but it is not easy to decide whether it is magnetite or maghemite. At elevated temperatures  $\gamma\text{-FeOOH}$  is also formed. Corrosion at high  $\text{H}_2\text{O}_2$  concentrations up to 16.8 % is nearly almost suppressed and leads only to the growth of the protective layer.

Table 5.3

Characteristics of  $\alpha$ -Fe samples after corrosion in solutions of low concentration  $H_2O_2$ 

Mössbauer parameters of se- parate phases	Average layer thickness $d(\text{\AA})$ of a given phase and its area, K(%) of the total sample area					
	Immediately after corrosion		After annealing at 200°C		After annealing at 400°C	
	d	K	d	K	d	K
Solution of 0.006 % $H_2O_2$ at room temperature						
Unsplit line	6	100				
Magnetite, $H_{\text{eff}} = 46.4$			13 $\pm$ 2	100		
Magnetite, $H_{\text{eff}} = 48.0$					150 $\pm$ 30	21 $\pm$ 4
Solution of 0.012 % $H_2O_2$ at room temperature						
Unsplit line	220 $\pm$ 30	8 $\pm$ 1				
Unsplit line and tra- ces of magnetite			180 $\pm$ 50	17 $\pm$ 4	20 $\pm$ 5	75
Magnetite, $H_{\text{eff}} = 48.0$					550 $\pm$ 200	6
Wustite					1000 $\pm$ 400	10
Solution of 0.006 % $H_2O_2$ at 85°C						
Relaxation spectrum	280 $\pm$ 40	63 $\pm$ 4				
Hydroxide + magnetite (relaxation spectrum), $H_{\text{eff}} = 44.8$			100 $\pm$ 20	100		
Magnetite, $H_{\text{eff}} = 44.8$					500	80

Note: Mössbauer parameters: for hydroxide  $\delta = 0.32$ ,  $\Delta = 0.80$ , for wustite  $\delta = 0.86$ ,  $\Delta = 0.75$  are in  $\text{mm}\cdot\text{s}^{-1}$ ,  $H_{\text{eff}}$  is in Tesla.

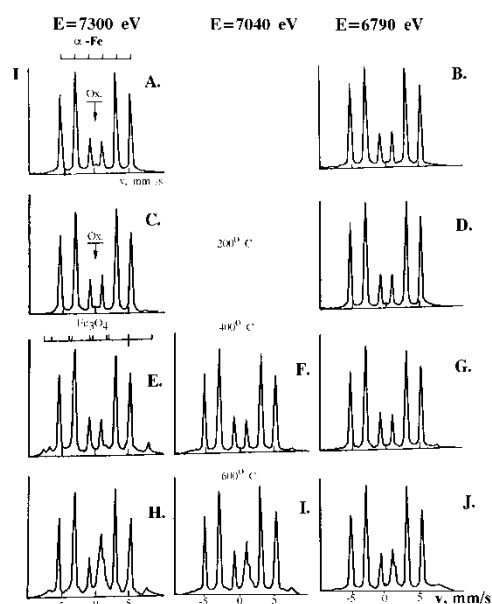


Fig.5.7 Some spectra obtained at different electron spectrometer settings (7300 eV, 7040 eV, 6790 eV, arranged in columns) for the sample immediately after corrosion at 25°C in a 0.012 %  $\text{H}_2\text{O}_2$  solution (A and B) and spectra obtained after subsequent annealings at 200°C (C and D), 400°C (E - G) and 600°C (H - J) (from [5.42]).

At intermediate  $\text{H}_2\text{O}_2$  concentrations  $\gamma\text{-FeOOH}$  is detected in the oxide layers.

Since DCEMS is rather complicated method, it is ordinary CEMS that has found practical applications for phase analysis of samples obtained from different parts of nuclear power plants. For example, LIPKA et al. [5.65] tried to evaluate the problem of decontamination and find an optimal process for the removal of rust. The authors found that the corrosion products contain iron at least in three forms:  $\text{Fe}_{3-x}\text{M}_x\text{O}_4$  where M represents substituents (e.g. Cu, Zn) and x is the degree of substitution;  $\gamma\text{-FeOOH}$  and in some cases a small amount of  $\alpha\text{-Fe}_2\text{O}_3$ . The relative amount of those components and the degree of substitution - x varies in a wide range ( $x = 0$  to  $0.8$ ). No superparamagnetic particles were observed in the samples under investigation. JAGGI et al. [5.66] investigated corrosion of carbon steel in water under the typical operating conditions of a pressurized water nuclear reactor (at  $310^\circ\text{C}$  and  $\text{pH} = 10.5$ ). At a low content of dissolved oxygen (less than  $0.05$  ppm) nonstoichiometric magnetite was first formed. After a prolonged corrosion the thicker rust layer was again magnetite but much closer to the stoichiometric composition.

In addition to and alongside with passivation, various protective coatings are used to protect metals and alloys from corrosion. Also of no less importance are works connected with studies of properties and transformations of corrosion-product layers in view of stopping the process of corrosion. Among these works are studies of the effect of rust transformers. One of the assets of Mössbauer spectroscopy is the possibility of *in situ* studies of corrosion taking place beneath protective coatings [5.25, 29, 67-75]. Nowadays many metal constructions are protected by various coatings. The rate of corrosion at the metal-coating interface is difficult to determine especially for a non-transparent coating. Emission Mössbauer spectroscopy was first used in this problem. Cobalt doped with  $^{57}\text{Co}$  was electrodeposited onto a Co metal surface. The mass of the deposit was equivalent to a layer  $50 \text{ \AA}$  thick [5.69,70]. The surface was then coated with polybutadiene to a thickness of  $0.01 \text{ mm}$ . It has been shown that after corrosion in  $3 \%$  NaCl solution for  $84 \text{ hrs}$  the amount of the oxide phase on the protected sample was two times less than that on the unprotected sample. LEIDHEISER et al. found that for polybutadiene coating [5.70] the contact between the cobalt metal and the polybutadiene is through an oxide or hydrous oxide at the interface; the oxide on cobalt does not thicken during the baking process and the reduction process cannot be a consequence of the reaction  $2\text{Co}^{3+} + \text{Co} \rightarrow 3\text{Co}^{2+}$ , during baking of the coating because the relative amount of unoxidized metal remains approximately constant before and after baking. The same technique was used by VERTES et al. [5.71] to study the interface between a cobalt substrate and a polyimide coating.

Electrochemical measurements and studies of cathodic delamination [5.72,73] encouraged emission Mössbauer spectroscopy and nuclear magnetic resonance spectroscopy to be applied in an effort to understand better the nature of cations when present within a polymeric coating. Ions of tin, cobalt and iron were electrochemically injected into polymer coatings. When a coated metal containing a defect is polarized cathodically while immersed in an electrolyte, the coating delaminates from the metal radially from the defect. The rate controlling step in the process is the rate at which cations are transported through the coating under the influence of the applied potential.

LEIDHEISER, VERTES et al. [5.72,73] found that ions can migrate through organic coatings under an applied cathodic potential. In the cobalt/polyimide interface the polyamic acid reacts with the cobalt substrate with the formation of additional divalent species at the expense of both the elemental and trivalent species. The isomer shift and the quadrupole splitting value for the divalent species are indicative of a cobaltcarboxyl interaction. The metal/coating interface is dynamic and the properties of the interface change with time.

Mössbauer spectroscopy shows an opportunity for studying the chemistry of the interfacial region in a nondestructive way as a function of time after formation of the interface. The chemical reactivity of the interface is exhibited by the change in the relative amounts of the divalent and trivalent species between the time of formation and after 3 months of storage.

Phase transformations in oxide layers below protective coating have been investigated [5.67,74] by in situ Mössbauer spectroscopy. Very important studies were done by BROOKS and THORPE [5.74]. They developed a technique to observe the onset of corrosion as it occurs beneath such protective layers, as paints, varnishes, greases and oils that are applied to metal surfaces to give short-term protection from corrosion. The technique was used to evaluate the effectiveness of various temporary protectives in different environments, without the need to remove the protective layer thus eliminating the possibility of any chemical changes or loss of corrosion products occurring as a result of removal. The temporary protective layers are typically 25  $\mu\text{m}$  for paints and 15  $\mu\text{m}$  per layer for varnishes.

To enhance the surface sensitivity of the backscattered X-rays technique Brooks and Thorpe deposited an approximate 20 nm  $^{57}\text{Fe}$  layer onto mild steel samples. The surface enriched samples were then annealed to allow the  $^{57}\text{Fe}$  to diffuse into the near surface region of the mild steel substrate. It was the first experiment in Mössbauer scattering spectroscopy in which the surface enrichment was accompanied by subsequent annealing. A diffusion model was developed to predict the surface distribution of  $^{57}\text{Fe}$  as a function of annealing parameters. It was essential that the annealing conditions did not result in any surface oxidation, and did result in a surface that was characteristic of the mild steel. Mössbauer spectroscopy and dynamic secondary ion mass spectrometry was used to monitor the phase composition, enrichment and diffusion process.

It was found that even the standard annealing processes could not be used since they resulted in detectable surface oxidation. A successful annealing procedure was finally achieved when the underside of the substrate was recleaned before annealing in a glass phial under 1 atm of argon in the presence of a freshly polished piece of titanium metal which acted as an oxygen scavenger and preferentially oxidized. The samples annealed by this procedure revealed no oxidation doublet in their Mössbauer spectra.

By Mössbauer spectroscopy it was shown for the first time that  $^{57}\text{Fe}$  evaporation and



the annealing procedure can produce well characterized samples with near-surface enrichment in the Mössbauer isotope to a depth of some 90 nm [5.74]. It was taken into account that the original substrates are not ideal surfaces and will include the normal surface roughness of rolled metal. Hence the average enrichment achieved improves the surface sensitivity of the technique as required and to uniquely identify the corrosion products it is necessary to perform variable temperature studies.

It is known that in the course of environmental exposure water, oxygen and salts diffuse through the paint film and cause corrosion of the metal resulting in the precipitation of corrosion products between the paint film and the metal. The structure of these corrosion products affects the adhesion of the film which in some time gets detached from the surface leading to increased corrosion. The effect of pigments on the development of corrosion products between the painting system and metal surface when exposed to marine environments has been investigated [5.67]. The pigments studied were: red mud zinc chromate, zinc chromate, red oxide zinc phosphate, manganese phosphate, barium chromate and basic lead silico-chromate. Mild steel specimens 150 x 100 x 1 mm were polished and degreased with sulphur-free toluene and then dried. These were painted with two coats of anticorrosive primer paint and two coats of finishing paint. The painted specimens were exposed at a marine site facing sea at an angle of 45° to vertical for 18 months.

The upper rust layer in all the cases consisted of  $\gamma\text{-Fe}_2\text{O}_3$ ,  $\gamma\text{-FeOOH}$  and  $\alpha\text{-FeOOH}$  due to the limited supply of oxygen and water and the pH is nearly neutral in the initial stages [5.67]. Under these conditions a few layers of  $\gamma\text{-Fe}_2\text{O}_3$  are formed a part of which gradually changes to  $\gamma\text{-FeOOH}$  and  $\alpha\text{-FeOOH}$ . As the exposure time increases more water and oxygen diffuses to the metal surface and due to cathodic reduction of oxygen ( $1/2\text{O}_2 + \text{H}_2\text{O} + 2\text{e} \rightarrow 2\text{OH}$ ) the pH becomes very high in 'this region which results in the delamination of the paint film which also detaches corrosion products at the metal surface. This area becomes more prone to corrosion due to easy availability of water, oxygen and salts.

When the area is wet, the primer diffuses out of the paint film and a competition between corrosion and inhibition takes place resulting in the formation of  $\gamma\text{-FeOOH}$  with highly distorted structure of the type  $\text{FeO}_x(\text{OH})_{3-2x}$  which adheres to the metal surface providing limited protection. Probably the degree of asymmetry of the central doublet of low rust layer can help in assessing the effectiveness of the primers because in the case of an unpainted panel, the corrosion rate is very high and high and the central doublet due to  $\gamma\text{-FeOOH}$  is completely symmetrical. Thereafter [5.67], the nature of the corrosion products between metal and paint seemed to be a critical parameter in the selection of primers for their improved performance.

The effectiveness of the coating strongly depends on the pretreatment of the steel surface. HOFFMAN and STRATMAN [5.75] investigated the fact that if the preoxidized iron surfaces are covered by organic coatings, then the polymer film doesn't adhere for

a long time to the metal substrate. The mechanism of this loss of adhesion is not well understood yet. The authors found that iron could corrode below an organic coating, the reduction of the rust scale being the cathodic reaction of this process. After wetting a dry polymer coated metal surface the oxygen reduction is not a necessary cathodic reaction. The reactive rust component is  $\gamma$ -FeOOH, which can be reduced to  $\text{Fe}(\text{OH})_2$  and spinel. The formation of spinel changes the rust morphology and causes the adhesion loss of the organic coating. The phase transformations in oxide layers below organic coating can be inhibited by removing the reactive  $\gamma$ -FeOOH from the rust layer or by modification of the surface of  $\gamma$ -FeOOH. The following modification techniques proved to inhibit the rate of rust reduction significantly: i - transformation of  $\gamma$ -FeOOH into the very stable  $\alpha$ -FeOOH, ii - precipitation of insoluble phosphates on the surface of  $\gamma$ -FeOOH, iii - modification of the surface of  $\gamma$ -FeOOH by organosilanes or organophosphates.

Corrosion conditions may change periodically, e.g. during wetting and drying of surfaces which are exposed to the atmosphere, during immersion and emersion of a corroded surface in the splash-zone of sea water and during a change between flowing conditions and times of stagnation of aerated water in pipes. The corrosion potential changes also periodically with time and the composition of a rust layer will change periodically, too, from an oxidized one to a  $\text{Fe}^{2+}$  enriched reduced state. These reactions are electrochemical in nature and allow a further corrosion of the metal phase just by reduction of  $\text{Fe}^{3+}$  ions to  $\text{Fe}^{2+}$  within the rust film. STRATMAN and HOFFMANN [5.43] investigated electrochemically induced phase transformations of isolated rust layers in situ by transmission Mössbauer spectroscopy. It has been found that oxidized rust films can be reduced in several stages. After re-oxidation the reduced FeOOH phases are oxidized reversibly, whereas  $\text{Fe}_3\text{O}_4$  can only be oxidized within the spinel structure to  $\text{Fe}_{3-x}\text{O}_4$ . Simultaneously to these redox reactions extremely small ( $d < 100$  Å)  $\alpha$ -FeOOH crystals are transformed into larger crystals, and to a certain extent  $\gamma$ -FeOOH is transformed into the lattice of  $\alpha$ -FeOOH.

So, despite the fact that no further corrosion is possible, the phases change slowly with time since the less stable phases are transformed into the more stable ones. The importance of the effect of aging on the electrochemical properties of rust layers is demonstrated in Fig.5.8. One can see that after the sample had been held for several months in a humid atmosphere the layers contain nearly no superparamagnetic  $\alpha$ -FeOOH and  $\gamma$ -FeOOH is partly transformed into the thermodynamically more stable phase  $\alpha$ -FeOOH. The rate of this reaction is much lower than the rate for the dissolution of the small  $\alpha$ -FeOOH crystals.  $\gamma$ -FeOOH may transform then into one of highly nonstoichiometric and probably highly hydrated magnetites. The oxidation is partly reversible, but magnetite

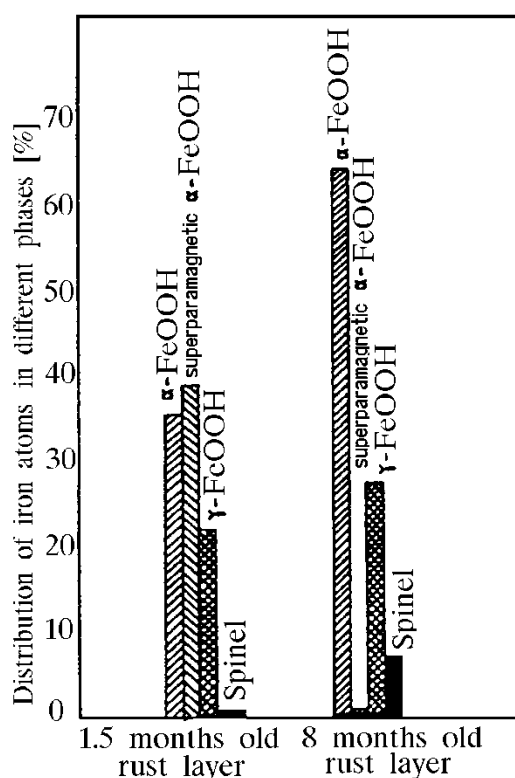


Fig.5.8 Phase composition of isolated rust layers as a function of the time storage in a humid atmosphere (from [5.47]).

cannot be oxidized back to  $\gamma$ -FeOOH. One example of such a reduction/oxidation cycle is atmospheric corrosion.

Problems connected with the pretreatment of metallic surfaces before painting and processes in rust layers due to rust converters were also intensively studied. ESCA and CEMS techniques were used by GUETLICH et al. [5.76,77] in studies of the formation of oxidic layers on steel in water of well defined hardness and chloride concentration with particular emphasis on the influence of added organic inhibitors. The layers contained a remarkable amount of constituent ions from the solution and fragments of the inhibitors which were decomposed by the corrosive medium. The authors assumed that the whole organic molecule determined the kind of transportation of the inhibitor to the iron metal, but the inhibition itself was due to functional groups only.

Phase transformations aimed at transforming the rust into more stable inert products are the goal in using rust converters. Most of them consist mainly of concentrated phosphoric acid. MEISEL et. al. [5.78, 79] studied the influence of phosphoric acid on the rust components and its application in the careful removal of radioactive corrosion products from the internal surface of vessels and tubes. The transformations of the rust by eight commercial rust converters produced in Germany were also investigated. Some

results of the quantitative evaluation of Mössbauer spectra of corroded specimens before and after application of the rust transformers are given in Fig.5.9. MEISEL et al. found, that in no case had either the pure phosphoric acid or any of the applied commercial rust transformer converted rust or some rust components into wustite, magnetite or maghemite, which are able to form a closed protective layer inhibiting further corrosion. The same results were reported by GRANCEDO et al. [5.80] in a study of application of nine commercial converters produced in Spain. Besides the transformation of corrosion products, the treatment of corroded samples may result in the formation of a protective phosphate layer on the surface metal. The layer may be very thin as compared with the covering layer and cannot be detected without a removal of the covering products [5.79].

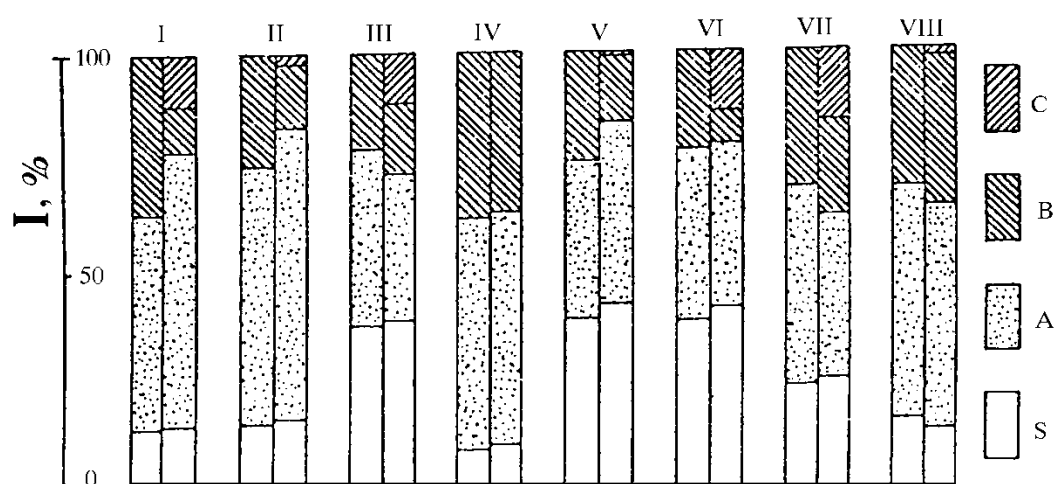


Fig.5.9 Results of the quantitative evaluation of dissipation spectra of corroded specimens before (left hand column) and after (right hand column) application of various rust converters. S: substrate (metallic iron); A:  $\beta$ -FeOOH (with additions of  $\gamma$ -FeOOH and B); B: highly dispersed (superparamagnetic)  $\gamma$ -Fe<sub>2</sub>O<sub>3</sub>/Fe<sub>3</sub>O<sub>4</sub>; C: ferrous phosphates (from [5.77]).

Corrosion studies of metals under lacquer or paint coatings were conducted also on objects of practical importance (e.g. cars). To do this, backscattered X-rays or  $\gamma$ -quanta were detected. It was shown that the first stages of car body corrosion involved a mixture of  $\beta$ - and  $\gamma$ -oxyhydroxides. The maximum amount and the growth rate of the oxides depend only on the type and quality of the coating. In some time the hydroxides convert into a mixture of goethite and haematite. The time of the conversion is determined by the corrosion conditions and is nearly independent of the coating quality.

Thus, Mössbauer spectroscopy allows the qualitative and quantitative study of corrosion products, often in situ and apart from reports mentioned above there are many others, e.g. [5.81 - 89]. It is possible to evaluate the average particle size of corrosion deposits, to study the stoichiometry and defect structure of oxides, to obtain information on the kinetics of corrosion passivation and inhibition. One of the most

complex, and at the same time the most important, problems in corrosion studies is the study of passive or protective films formed on the surface at an early stage of corrosion when the layer thickness is less than 100 Å and, in addition to the reports reviewed, [5.90-95] should be mentioned. Using  $^{57}\text{Fe}$  Mössbauer spectroscopy to characterize the rust products one ignores those phases which does not contain iron. In some respect this point may be very important since there are many products which are irrelevant to the corrosion process but can be mixed with the sample of rust.

## 5.2 Applications in Metal Physics

Mössbauer spectroscopy has developed into one of the most efficient research methods in metal physics and metallurgy [5.1,96-104]. The Mössbauer active isotopes include those of iron, tin, gold, rare earths and some other metals. The progress in Mössbauer spectroscopy has been followed by its use in wider applications in new problems of metal physics and, simultaneously, it has stimulated further developments of the technique. Thus, the need to quantitatively analyze the complex Mössbauer spectra observed for amorphous materials, alloyed steels and invar alloys has led to the development of spectra interpretation techniques. The need to perform in situ studies in a nondestructive manner has stimulated the use of scattering Mössbauer spectroscopy.

The use of CEMS is efficient in metal physics as well as in corrosion studies. At the same time there are fields where scattering techniques are most effectively pursued by photon detection. An example is the distribution of alloying elements in solid solutions (steels and alloys). At first the experimental studies were conducted in transmission geometry. The samples were foils made of the material under investigation. For many alloys the preparation of foils 10 - 50 µm thick is a difficult problem. Furthermore, the evaporation of alloying elements during the thermal treatment sometimes resulted in the phase composition of such thin foils being not the same as of the bulk under the same treatment conditions. The detection of the scattered photon allowed more correct experimental studies to be conducted on the distribution and redistribution of atoms in alloys. As a rule, studies of this kind are laborous, requiring advanced theories and extensive software for the computer treatment of experimental data (e.g., [4.25, 26]).

Typical studies in transmission geometry involve investigations of atomic redistribution in interstitial and substitutional solid solutions after thermal treatments [5.105-109] or steel tempering [5.110 -112]. Thus, on studies of secondaryhardening processes in a molybdenum-containing steel on foil samples it has been shown that the nucleation of special carbides does not precede the ordering of Mo atoms. Hence the

secondary hardening is not connected with such nucleation. Molybdenum atoms appear to migrate to dislocations to form "seeds" of the special carbides and are coherently bonded to the austenite lattice. On conducting the experiments special measures were undertaken to ensure the same chemical composition and identical processes in foils and in the bulk material.

These studies were continued on bulk samples and the backscattered K - X-rays were detected. A steel of similar composition (0.6 % C, 0.8 % Mo, 0.4 % Cr, 5 % Ni) was used. The dependences of hardness and the content  $C_C$  of carbide-forming elements in the initial solid solutions (Fig.5.10a and b) turned out to coincide for both transmission and scattering geometry. Tempering of the bulk samples resulted in lower  $C_C$  values

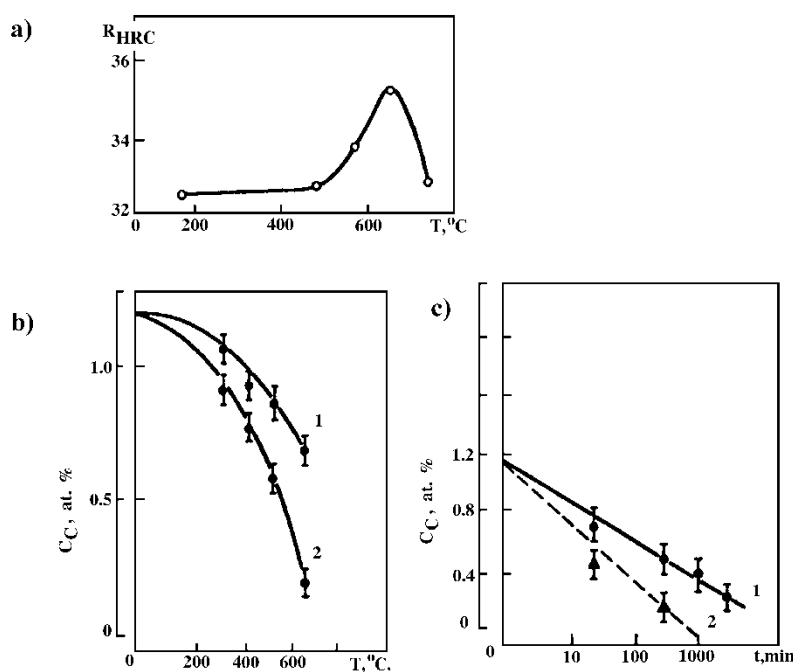


Fig.5.10 Some characteristics of secondary-hardening processes in molybdenum-containing steels. a - Temperature dependence of the hardness HRC, b - Temperature dependence of the content  $C_C$  of the carbide-forming elements, c - annealing time dependence at 600 $^{\circ}C$  of  $C_C$ ; 1 - transmission experiments with a foil (0.9 % C, 1.2 % Mo, 5 % Ni), 2 - scattering experiments (0.6 % C, 0.8 % Mo, 0.4 % Cr, 5 % Ni).

(cf. dependences 1 and 2 in Fig.5.10b). A more detailed study showed that chromium (0.4 %) and a small amount of Mo (0.2 %) were left in the solid solution. This means that the appearance of the secondary-hardening peak above 500 $^{\circ}C$  is due to only

molybdenum that has left the solid solution. To suppress the secondary-hardening peak, 0.6 % Mo is sufficient, whilst all the chromium is left in the solid solution. The lower content of alloying elements in the foil (i.e. in the solid solution) compared with that in the bulk sample subjected to the same thermal treatment is connected with differences between their structures. The withdrawal rate for the alloying elements from the solid solution in the foil is also higher (see Fig.5.10c), but the processes in the foil and bulk are essentially the same.

There are a number of studies of phase transformation in metals and alloys by transmission Mössbauer spectroscopy. However, the use of scattering Mössbauer spectroscopy has made it possible to perform the phase analysis in situ [5.113-117]. By combination of different techniques, larger amount of information can be obtained. Thus, to study bimetallic foils, both CEMS and transmission Mössbauer spectroscopy have been used [5.118,119]. Bimetallic plates and duplex metal foils are widely used in various fields of physics and technology, since layers with different magnetic properties can be produced within a sample. The magnetic properties within a layer may be changed due to external effects whereas those of the other layer are left unchanged. For the total foil thickness of the order of 10  $\mu\text{m}$  it is extremely difficult to measure the saturation magnetization; the presence of texture and a high level of internal stresses hinder the use of X-ray methods to determine the structure and phase composition of the foil. The efficiency of Mössbauer spectroscopy in this field was demonstrated by the study of a bimetallic foil of composition (19 % Cr, 2 % Mo, 10 % Ni, 69 % Fe) - layer I, and (19 % Cr, 2 % Mo, 13 % Ni, 66 % Fe) - layer II [5.118]. It proved that a greater Ni content in layer II completely suppresses the  $\gamma$ - $\alpha$  transformation in the layer.

CEMS in combination with etching has been used in metallurgical science for depth selective phase analysis. By this method the effect of cold rolling has been studied on the phase composition of alloys 5 % Mo, 21 % Ni, 74 % Fe and 5 % Mo, 26 % Ni, 69 % Fe [4.51]. It was found that different deformations of the sample during cold rolling on two sides lead to different amounts of martensite formation. Etching allowed the  $\alpha$ -phase depth distribution in the sample to be obtained [4.51, 52].

The above mentioned studies were performed on flat, sometimes polished, samples. Studies of metals with a complex shape such as: wires, spheres, fractures and ruptures have also been performed. Scattering Mössbauer spectroscopy can be used for this purpose. Thus, by CEMS and X-ray detection the phase composition and structure of austenite stainless steel wires have been investigated after electroplastic drawing [5.120, 121]. The investigations were aimed at elucidating the effect of the electric current on the metal drawing and applying electroplasticity in steel wire production. It has been shown that the  $\gamma$ - $\alpha$  transformation takes place during drawing and that the ratio of the two phases is dependent on the drawing method. For a given drawing

method the ratio depends on the distance from the wire surface. A high-density electric current partially suppresses the transformation. After the electroplastic drawing the amount of  $\alpha$ -phase is minimal compared with other drawing methods, the phase being non-uniformly distributed and mainly in the surface layer. After usual cold drawing  $\alpha$ -phase is uniformly distributed over the entire wire volume, and the amount of the phase is significantly larger than after electroplastic drawing. The diminished  $\alpha$ -phase content in the wire, especially in its volume after electroplastic drawing, is of practical importance for wire production from metastable austenite steels, since larger elongations can be reached without intermediate thermal treatments.

Mössbauer scattering spectroscopy also finds applications in studies of fracture toughness in metal physics, especially in phase analysis of bulk materials and finished products where other methods fail. For example, rough surfaces and mechanical deformations not only broaden X-ray lines but often make X-ray analysis difficult. One investigation of this type is a study of the dynamic effects in plates of a Fe-based alloy (9 % Ni, 0.1 % C, 0.45 % Mn, 0.22 % Si) where the fracture toughness was attributed to the amount of the retained austenite [5.122]. On mechanical deformation the austenite in the initially undeformed material gradually transforms into martensite and the energy dissipates into the phase transformation. The transformation was found to occur in a layer about 300  $\mu\text{m}$  deep.

Scattering Mössbauer spectroscopy using proportional counters allowed the rough surfaces and also fractures and ruptures (Fig.5.11) to be studied. From a 8 mm fracture fairly good CEMS spectra were taken, allowing the investigation of transformations occurring in steels with the initial  $\gamma + \epsilon$  structure [5.123]. The phase composition of the metal microvolumes which are the sites for the propagation of fractures were determined. The samples were rods  $\sim 10$  mm in diameter made from commercially available 25 mm thick sheets. The thermal treatments included annealing at 1050°C for 6 hrs, followed by cooling in air. The samples were tested under the following conditions: low-cycled fatigue, fatigue tests at 600 cycles/min on cylindrical specimens, and impact tests on notched specimens.

The Mössbauer spectrum of the original sample consisted of a single line (Fig.5.12). The slightly broadened line corresponds to Fe atoms both in the  $\gamma$  - and in  $\epsilon$ -phase. The spectra obtained from the fracture surfaces after various cyclic loadings are a superposition of a sextet with a single line in the centre. The central line is identical to that of the original sample, the sextet lines being broadened. Thus, the width of line I(VI) is 1.28 mm/sec. Such line broadening in Mössbauer spectra may be attributed to different local environments of Fe atoms, or to significant local lattice distortions, or to both. The two effects are difficult to discern.

The results of the phase analysis of the surface fractures in a steel are given in Table 5.4. To obtain the results, the  $f'$  factors for different phases were assumed to be equal. Necessary corrections were made to allow for both re-scattering effects in CEMS and saturation effects in the area dependence



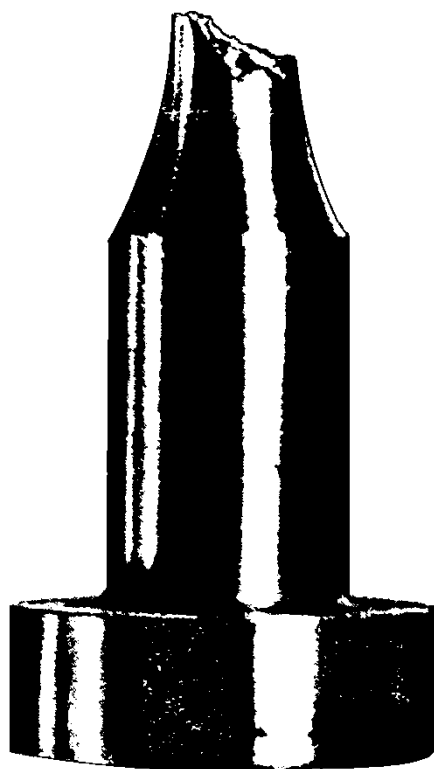


Fig.5.11 Steel fracture from which a CEMS spectrum has been obtained.

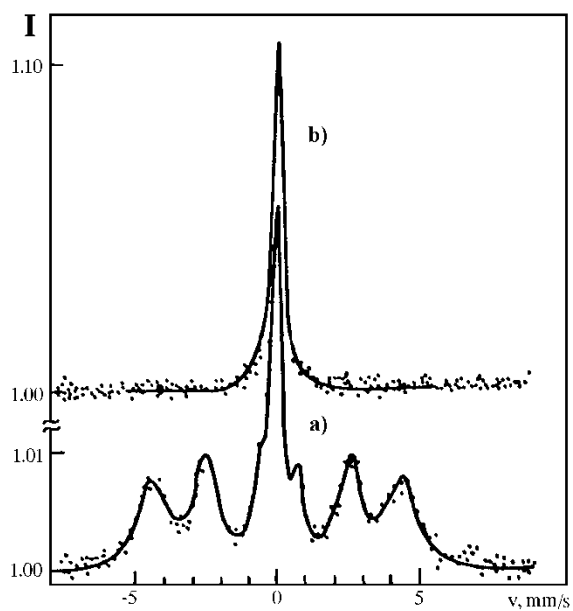


Fig.5.12 CEM spectra of steel (19.2 % Mn, 1.67 % Si, 0.9 % Ti, 0.07 % C): a - spectrum from the fracture surface shown in Fig.5.11, b - after annealing.(From [5.123]).

of the hyperfine splitting for detected X-rays. It follows from Table 5.4 that on increasing the loading rate the surface layer of the fracture is enriched in martensite. The appearance of the  $\alpha$ -phase in the site of destruction and its predominance there explain the contradiction between the intercrystallite character of the steel destruction and the high energy which is required. Martensite in the fracture layer is formed in front of a crack to be nucleated and propagated. The predominance of martensite in the fracture layers testifies to the large number of cracks in this area and to a significant stress relaxation preceding the formation and development of the cracks. This is the reason for the high energy of destruction of steels with the initial ( $\gamma + \epsilon$ ) structure. The processes mentioned above could proceed with equal probability within the grains and on their boundaries. A comparison of the CEMS and X-ray detection data shows that the processes responsible for the destruction of steels with the  $\gamma + \epsilon$  structure are localized in a zone with a width less than 5  $\mu\text{m}$ . On static loading tests the width increases up to 10  $\mu\text{m}$ .

Fatigue fractures in a Ni-alloyed carbon steel initially with an austenite-martensite structure have been investigated in [5.124]. It has been shown that after fatigue fracture the surface layer down to the depth of 0.1  $\mu\text{m}$  consists only of martensite, and the high stability of these steels to dynamic loading was associated with the martensite transformations following fatigue fractures.

Results of various non-destructive mechanical effects on metals, leading only to a change of their properties, have been studied by Mössbauer spectroscopy. The most fully investigated is plastic deformation in metals, often studied by transmission Mössbauer spectroscopy. However, the information on phase composition appears to be averaged over the entire foil volume. Scattering Mössbauer spectroscopy allows the phase transformation on each of the two sides of the sample and at a different depth to be studied [5.124]. An example is the study of the martensitic phases in cold-worked Fe-Mn alloys, which are characterized by the co-existence of  $\gamma$ -,  $\epsilon$ - and  $\alpha$ -phases. In an alloy of a given composition the phases transform as a result of thermal or mechanical treatments. Thus, for the alloys with 16 % to 30 % Mn the cold working leads to a partial or complete transformation of  $\gamma$ -phase into  $\epsilon$ - or  $\alpha$ -phase, and the  $\epsilon$ -phase into the  $\alpha$ -phase [5.125]. Phase diagrams were obtained for the alloys as a function of deformation, and also the depth distribution of the phases at different deformations and the manganese atom distribution in the bcc lattice.

NASU et al. [5.126] used different modes of Mössbauer spectroscopy to analyze Fe states on the surface of Hadfield steel deformed by sand-blast and/or shot-peening treatments. Hadfield steel is one of the high-manganese steels containing 12 - 14 wt.% Mn and 0.8 - 1.2 wt. % C having a fcc structure (austenite steel). It is used as an abrasion-resistant steel because of its remarkable work hardening. Two Hadfield steel specimens A and H3 having the compositions: 12 wt.% Mn and 1.1 wt.% C (specimen A) and 13.25 wt.% Mn and 0.82 wt.% C (specimen H3) were investigated. Thickness of these specimens were 0.5 mm for

A and 11 mm for H3. Thin foil specimens were cut from H3 and used for transmission  $^{57}\text{Fe}$  Mössbauer measurements at 20 K.

Table 5.4

Results of the phase analysis of iron-based alloy (19.2% Mn, 1.67% Si, 0.9% Ti, 0.07% C)

Loading	Detected radiation	Parameters of the $\gamma + \epsilon$ phases		Parameters of the magnetic phase			Phase composition (saturation effect and re-scattering are accounted for)	
		$\delta_{\gamma+\epsilon}$	$\eta_{\gamma+\epsilon}$	$\langle H_{\text{eff}} \rangle$	$\delta_{\alpha}$	$\eta_{\alpha}$	$C_{\gamma+\epsilon}$	$C_{\alpha}$
Low-cycled fatigue	electrons	-0.12	28	27.3	-0.01	72	27.6	72.3
	X-rays	-0.14	29	27.5	-0.04	71	35	65
Fatigue tests at 600 cycles/min	electrons	-0.12	10	27.5	-0.01	90	8.8	91.2
	X-rays	-0.14	26	27.5	-0.01	74	31.9	68.1
Impact tests	electrons	-0.12	23	28.0	-0.01	77	21.4	78.6
	X-rays	-0.15	46	28.1	-0.05	54	53.2	46.8

$\langle H_{\text{eff}} \rangle$  is the average effective magnetic field at a  $^{57}\text{Fe}$  nucleus in the  $\alpha$ -phase,  $\Delta\delta = \pm 0.01 \text{ mm}\cdot\text{s}^{-1}$ ,  $\eta_i$  are the relative areas (%) under the spectrum ( $i = \alpha, \gamma + \epsilon$ ),  $C_i$  is the relative content of  $i$ -th phase (%),  $\Delta\eta = \pm 5 \%$ ,  $C_{\alpha} = \eta_{\alpha}/(\eta_{\alpha} + 1.43\eta_{\gamma})$ .  $H_{\text{eff}}$  values are given in Tesla, isomer shifts are in  $\text{mm}\cdot\text{s}^{-1}$ .

Room temperature CEM spectra are shown in Fig.5.13 and X- ray backscattering spectra in Fig.5.14. The velocity scale is relative to  $\alpha$ -Fe at room temperature. Notation as "original" means the spectrum obtained from non-deformed surface. The lower spectra in Figs. were obtained from the deformed surface just after sand-blast treatment. Essential features of pattern are the same for all spectra. This implies that any carbide formation does not occur significantly by the deformation of the surface.

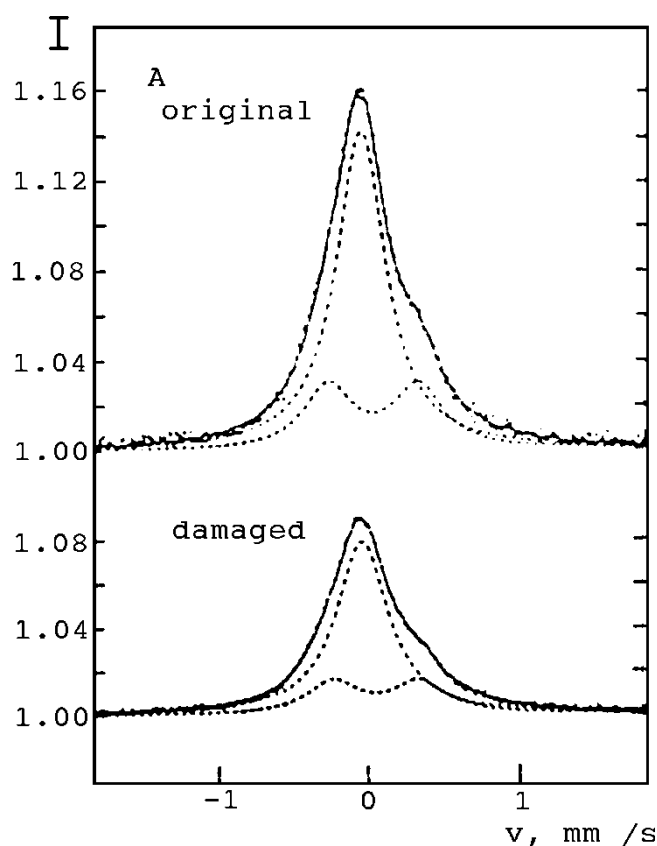


Fig.5.13.  $^{57}\text{Fe}$  CEM spectra of Hadfield steel, A, at room temperature. The upper spectrum is obtained from non-deformed specimen and the lower one is just after a sand-blast treatment of the surface. The velocity scale is relative to  $\alpha$ -Fe at room temperature [5.125].

The spectra of non-deformed and deformed surface consist of a singlet and a doublet attributed to the Fe atoms non-perturbed and perturbed by interstitial C atoms. No existence of the 6-line component is again evident and no appreciable change occurred by the deformation. However the area intensities of the doublets are determined, using a thin foil approximation, to be  $55 \pm 5\%$  and much larger than  $28 \pm 3\%$  of CEM spectra as shown in Fig.5.13. This implies that the concentration of carbon at the surface is less than the value in the bulk and the decarbonization occurred at the surface even before mechanical working.

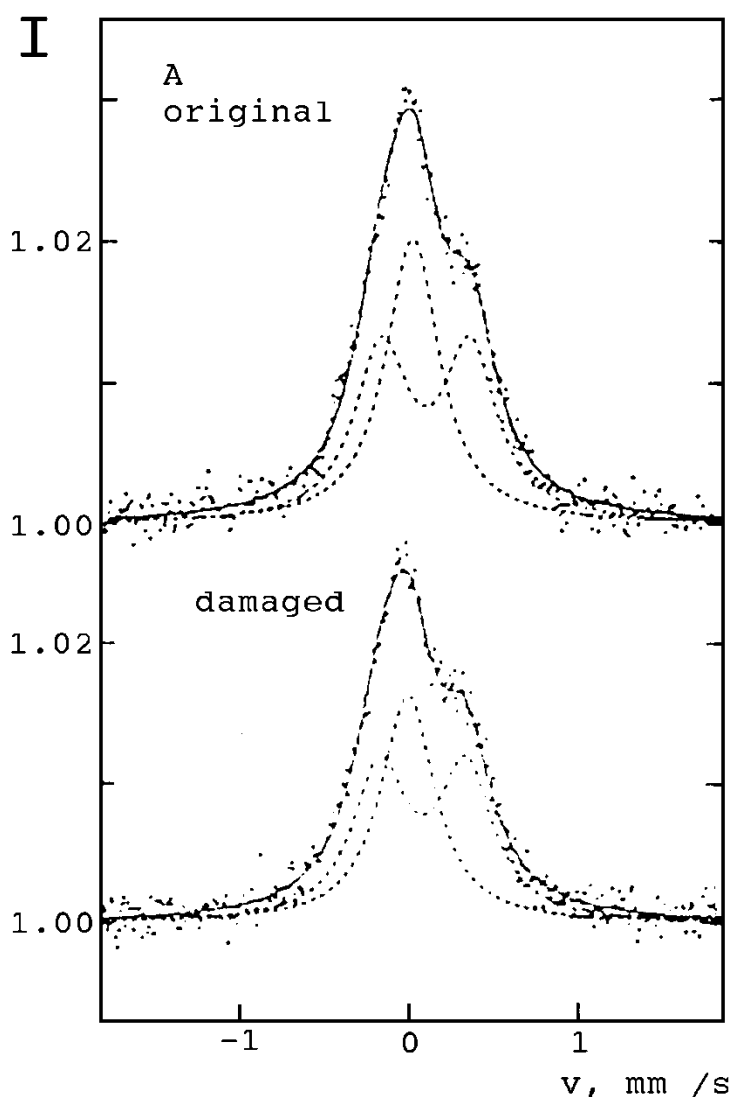


Fig.5.14. Mössbauer spectra by back-scattered X-rays of Hadfield steel, A, at room temperature. The same specimens were used as those for CEMS measurements. The velocity scale is relative to  $\alpha$ -Fe at room temperature [5.125].

In order to understand the change in magnetic properties by the deformation, transmission  $^{57}\text{Fe}$  Mössbauer spectra were measured at room temperature and at 20 K using a specimen H3. The spectra at 20 K for deformed specimens show the existence of the  $\epsilon$  martensite which could be related to the work hardening of Hadfield steel. Nasu et al. concluded that the work hardening of Hadfield steel could be related to the existence of  $\epsilon$  martensite whose formation is enhanced by decarbonization at the surface.

One widely used method of mechanical treatment is polishing. Thus, on polishing carbon steels austenite may be formed on the surface. The phenomenon has been studied by a combined use of several Mössbauer techniques involving the detection of  $\gamma$ -quanta, X-rays and electrons [5.127,128]. A ferrite matrix with spheroidal iron carbide

particles of volume about 16 % was studied [5.127]. Polishing caused an austenite layer about 70 nm thick to be formed on the surface. The layer was detected by either X-ray diffraction at glancing angles using the Cr  $K_{\alpha}$ -radiation or conventional metallography. Only Mössbauer spectroscopy allowed a reliable identification of the layer.

Surface changes occurring upon friction may be also examined by CEMS. An example is the study of scoring and scuffing on lubricated sliding surfaces and the breakdown of the lubricant [5.129]. Some iron-containing phases were identified on the surface together with a considerable amount of cementite on the scored surfaces; a mixture of highly deformed martensite and austenite was formed on the scuffed surfaces.

The lifetime of many metal objects depends on residual stress. Since the stress is maximal on the surface, CEMS have proved to be an appropriate technique to measure stresses [5.130]. Investigations have been carried out of residual stresses on different sides of bands made of amorphous alloys and also magneto-elastic effects due to surface crystallization [5.131-138].

The Mössbauer effect allows to check the homogeneity of disordered alloys versus the sample thickness. KRETTEK et al. [5.139] investigated the homogeneity of a ferromagnetic  $(\text{Fe}_{0.65}\text{Ni}_{0.35})_{1-x}\text{Mn}_x$  ( $x = 0.026$ ) alloy, prepared by diffusion of Mn into a  $\text{Fe}_{0.65}\text{Ni}_{0.35}$  foil, as a function of the sample thickness. The surface of the alloy was eroded step by step using  $\text{HNO}_3$  acid. The mean thickness of the removed layer was determined to be about 1  $\mu\text{m}$  for both sides of the foil using a sensitive weighing balance. A CEMS spectrum was recorded after each erosion step. Inhomogeneities in the Mn-concentration are revealed by differences in the hyperfine field splitting. The authors conclude that all  $(\text{Fe}_{0.65}\text{Ni}_{0.35})_{1-x}\text{Mn}_x$  samples prepared by diffusion of the Mn on the FeNi foils (1300 K, 120 h) are homogeneous in Mn-concentration.

Because of the homogeneity of the  $(\text{Fe}_{0.65}\text{Ni}_{0.35})_{1-x}\text{Mn}_x$  alloys these samples can be used as reference standards relating the mean hyperfine field and it is possible to determine the Mn-concentration in each layer of the homogeneously and inhomogeneously prepared alloys. The diffusion coefficient  $D$  of Mn in the FeNi foil at a temperature of about 1300 K was also evaluated ( $D = 10^{-11} \text{ cm}^2/\text{s}$ ).

The comparative investigation of thin films and bulk materials of an alloy of the same composition is very fruitful field for applications of Mössbauer backscattering spectroscopy [5.140, 141]. Magnetic  $\text{Fe}_{60}\text{Al}_{40}$  films were investigated by FNIDIKI and EYMERY [5.141]. The films were prepared by coevaporation at the starting pressure  $10^{-8}$  Torr. (The deposition rate of each element was typically 0,2 - 0.3 nm/s). The magnetic properties of the film at room temperature were nearly the same as those of bulk material chemically disordered either by cold working or by ion-implantation. At higher temperature (in the 573-773 K range), the films show a tendency towards new iron-rich phase precipitation instead of  $\text{L}_{20}$  ordering as expected from the bulk behaviour.

Mössbauer spectroscopy has made possible a detailed study of the processes occurring on diffusion saturation of alloy surfaces with various elements which causes the structure and the chemical composition of the surface layer to change. This has

contributed to a better understanding of thermochemical treatments and allowed quantitative methods of quality control in production [5.102, 142, 143] to be developed. Many thermochemical diffusion processes have been investigated, such as carburizing [5.143, 144], nitriding [5.143, 145-149], boriding [5.150-158], cyaniding and sulfiding. The results of such investigations is the phase composition of the coating obtained and the phase distribution within the coating. Mössbauer data obtained for different chemical compositions of the reacting media and at different temperatures, together with the mechanical test data, are of considerable value for practical purposes in choosing the proper composition of the reacting media and its temperature. Due to the increased surface hardness and reduced friction of these materials, expensive special alloys can be sometimes replaced by borided steels if a high mechanical strength is not required in the substrate.

The Fe - B system is one of the important systems in metal physics, e.g. well known are the amorphous alloys based on the system as well as the corresponding interstitial alloys. Boride coatings grown on iron and its alloys are widely used in industry due to the hardness and wear-resistance of iron borides. Boriding is used in production of gears, mills, and crankshafts. Activated powder mixtures of  $B_4C$  are used as a source of boron for boriding. Mössbauer spectroscopy can be used in studies of borided surface layers on Armco iron, which is (together with high-purity iron) often used as a reference material. The boriding process for these reference materials has been studied in [5.150], though the layers produced do not possess the needed mechanical properties and are often mechanically unstable and tend to descale. To study the early stages of the boriding of Armco iron, the diffusion treatments were performed using a powder mixture with crystalline boron added to slow down the process.

The thin borided layers were studied by CEMS, which is the most appropriate technique for the study. The annealed sheets of Armco iron were treated by a special diffusion treatment procedure in vacuum at  $850^\circ\text{C}$  for up to 24 hr. The Mössbauer spectra are shown in Fig.5.15. It is seen that the CEMS spectra are similar to the initial material. The solubility of boron in bcc iron at  $850^\circ\text{C}$  is very low (about  $10^{-3}\%$ ), and if some changes do occur in the surface layer they are in such a thin layer that its signal is not discernible ( $d \leq 300 \text{ \AA}$ ) [5.150].

For comparison, spectra are given in Fig.5.15 of the same sample, but boronized at  $1000^\circ\text{C}$  when iron has the fcc lattice. After boriding at this temperature for 15 hrs the layer is thick (about  $15 \mu\text{m}$ ) and easily detached from the sample. The scaled material is readily powdered and the corresponding transmission spectra are shown in Fig.5.15. It follows from the Mössbauer data that the inner layer formed on the substrate of solid solution of boron in the bcc iron lattice is the thickest (about  $10 \mu\text{m}$ ) and consists of mainly  $\text{Fe}_2\text{B}$  (spectrum  $\beta$  in Fig.5.15).

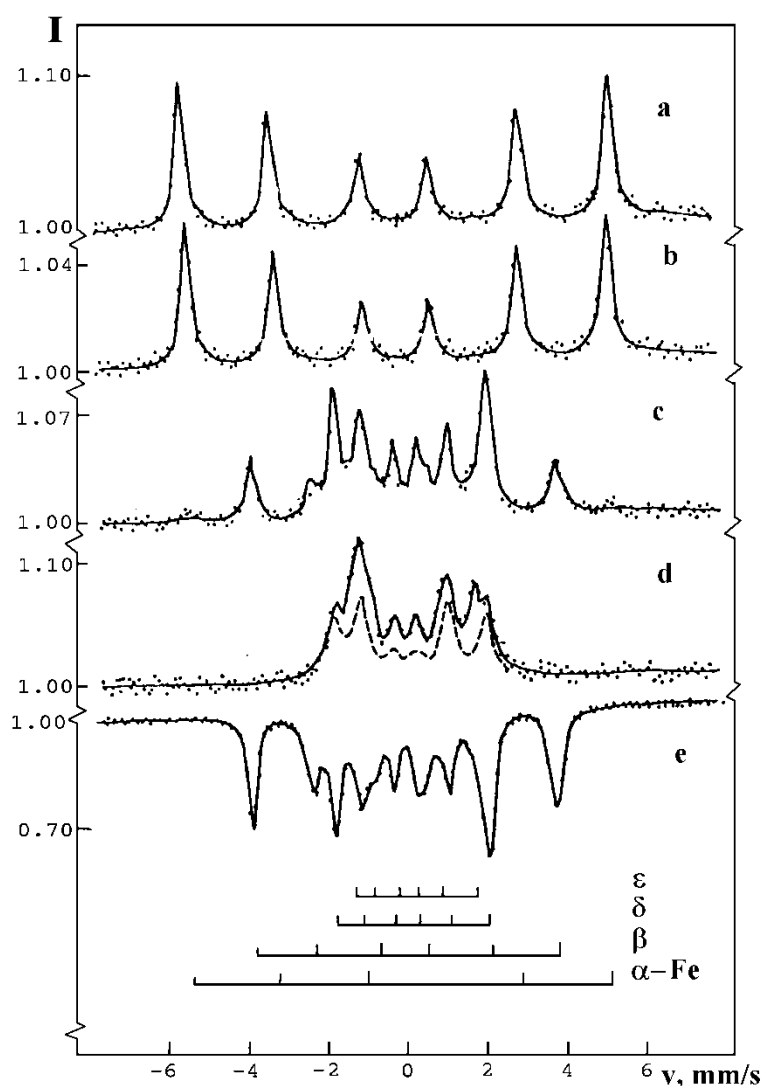


Fig.5.15 Room temperature Mössbauer spectra for: a - Armco iron before boronizing (X-ray detection); b - Armco iron boronized for 24 hrs at 850°C (CEMS); c - Armco iron boronized for 15 hrs at 1000°C (X-ray detection); d - the same as c, but 6 to 7.3 keV electrons are detected; e - detached surface film from iron borided at 1000°C for 15 hrs (transmission) (from [5.150]).

The next layer is FeB about 5  $\mu\text{m}$  thick (spectrum  $\delta$ ). There is one more (CEMS) spectrum characterized by a smaller splitting than the FeB spectrum; it can be attributed to a  $\text{FeB}_x$  compound with  $x > 1$ . It may be  $\text{FeB}_2$  or a solid solution of Fe in boron with a layer thickness of approximately 30 nm. For a more detailed study of this layer Armco iron boriding was conducted at the same temperature but in a more active solid medium ( $\text{B}_4\text{C}$  powder with 20 % SiC, activated with 2.5 %  $\text{KBF}_4$ ). The layers produced were thicker and the x value did not exceed unity [5.154]. Besides, the very thin upper



layer was a solid solution of boron in iron. The solid solution is amorphous or highly dispersed. A similar structure of the layer formed on boronizing, has also been observed for binary and ternary alloys.

The next step in the studies was to record experimental evidence for a gaseous phase contribution to the reactivity in the iron-boron system by components of the reacting mixture used for boriding [5.154]. The process was carried out at 850°C for 15 hrs in contact with a powder mixture of B<sub>4</sub>C (20 % by weight) and KBF<sub>4</sub> (10 %). Apart from Mössbauer spectroscopy, X-ray diffraction and electron scanning microscopy were used to analyze the treated samples. The coatings obtained by treating the same material with the same boriding medium in air and under vacuum were different in composition. The authors explained this in terms of the active participation of the gas phase at atmospheric pressure in the boriding process, and the high availability of reactive boron to form reaction products rich in boron, including a thin boron layer with dissolved iron atoms. The Mössbauer spectrum of this solid solution is a superposition of a doublet and a singlet. Under vacuum the effect of the gas phase is strongly reduced. The coating now consists of only the Fe<sub>2</sub>B phase formed due to solid and/or liquid state reactions with the powder components. To determine the contribution of each of the components, the iron samples were treated under vacuum at 850°C with either B<sub>4</sub>C, or with 10 % KBF<sub>4</sub> - SiC powders. The Mössbauer spectrum for a sample treated with B<sub>4</sub>C showed the absence of reaction products. The Fe<sub>2</sub>B phase formation in vacuum was associated with the solid phase reaction of KBF<sub>4</sub> whose melting point is 530°C. For solid boriding media the amount of reactive boron was determined by the formation of intermediate gaseous compounds. The mechanical properties of the boride coatings for the same metal can be changed by modifying the amount of reactive boron produced in the boriding media; for a given boriding medium it is achieved by changing the composition of the base metal [5.154].

The effect of the alloying element and its amount on the phase composition and the structure of boride coatings can be exemplified by studies of chromium-containing alloys. Significant variations in the properties of the boride coatings, formed on chromium-, manganese- and nickel-containing Fe-C ternary alloys, are well known. Unlike Ni, chromium and manganese preferentially enter the boride coatings thereby depleting the underlying alloy. Moreover, chromium entering iron borides as a substitutional admixture changes the structure and the properties of the coating [5.155]. As the chromium content increases in the alloys, the amount of reaction products richer in boron than Fe<sub>2</sub>B increases in the coating, and the coating depth is decreased. The

interfaces between the boride coating and the substrate appear to be relatively flat as compared with those observed for Armco iron. The Mössbauer parameters of the boride phases are changed appreciably due to the penetration of chromium. Hence, Mössbauer spectroscopy combined with other techniques (especially diffraction) is an efficient tool for studies of the formation of coatings providing the required mechanical properties and wear resistance.

Sometimes cheaper and simpler methods of surface modification of materials than thermochemical diffusion processes are needed. Reactions induced by field-generated plasma at liquid/solid interfaces is one such simple method to synthesis a metastable form of iron oxide and to modify material surfaces. The resulting chemical and microstructural changes on the surface of iron were studied by GHASAS et al. [5.159] using CEMS. By using the Fe/H<sub>2</sub>O system as a vehicle for experimentation it has been demonstrated that a change in the polarity of the processing voltage results in a change in the nature of the modification.

The storage of hydrogen is an urgent problem in the metal physics. Many metals and alloys were tested for this purpose. The use of FeTi as an effective material for solid-state storage of hydrogen is hindered by decomposition of the surface during cycling as well as by the need to activate the alloy after exposure to air. SANDERS and TATARCHUK [5.160] applied CEMS to determine mechanistic details about reactions occurring in thin-films of FeTi during initial activation and cyclic deactivation. They investigated 10 nm FeTi thin-film samples to qualify and quantify the surface reactions responsible for these various deactivation schemes. FeTi samples were prepared by evaporation of successive 1 nm layers of Ti (99.9 + %) and <sup>57</sup>Fe (93%) on precleaned quartz discs. Hydride cycles were performed near ambient temperature in H<sub>2</sub> at pressures up to 6500 kPa.

Sanders and Tatarchuk determined mechanisms for cyclic deactivation and activation of FeTi alloys. For cyclic deactivation of FeTi, trace impurities of O<sub>2</sub>/H<sub>2</sub>O in the H<sub>2</sub> charging gas react to form Fe<sup>0</sup>, TiO<sub>2</sub> and exposed FeTi. For activation of oxidized FeTi surfaces, Fe oxide overlayers were reduced by subsurface FeTi to form Fe<sup>0</sup>, TiO<sub>2</sub> and exposed FeTi. Elimination of oxygen impurities in the H<sub>2</sub> charging gas using a Pd overlayer as a filter substantiated the above noted mechanism proposed for cyclic deactivation. CEMS provides valuable qualitative and quantitative information for obtaining reaction pathways and is able to probe the buried Pd/FeTi interface.

Very often industrial applications of Mössbauer spectroscopy are mentioned e.g. [5.1]. In metallurgy there are three areas in which Mössbauer spectroscopy could make contributions to industry: i) as a research tool, ii) in quality control, iii) for in-service evaluation [5.161]. As a rule Mössbauer spectroscopy is not suited for routine in quality control or for in-service evaluation in industry because of the long sample turnaround times, relatively sophisticated nature of the technique and its interpretation. Till now

there are a few examples of a Mössbauer instrument in use for quality control, and no for in-service evaluation of materials or surfaces.

In practical applications the power of Mössbauer spectroscopy was demonstrated by CRANSHAW [5.161] in an investigation of nitride layers on iron and was connected with discrimination between the martensite, the austenite and the nitride layers. Carbonitriding an iron component requires the immersion of the component in a molten salt bath containing, for example, cyanides. The thickness of the layer depends on the combination of the time of immersion of the component and the temperature. It appears that this cannot always be relied on to give a desired thickness of the layer, and it is common practice to extract a few components from a batch, to cut them up and mount them and make a metallographic inspection with a microscope. This is quite a costly procedure.

In the nitrided layer the concentration of nitrogen or carbon falls off and between the outer nitrided layer and the iron base, there is a layer of carbon or nitrogen austenite, as shown in Fig.5.16. Fig.5.17 shows Mössbauer spectra taken by detecting

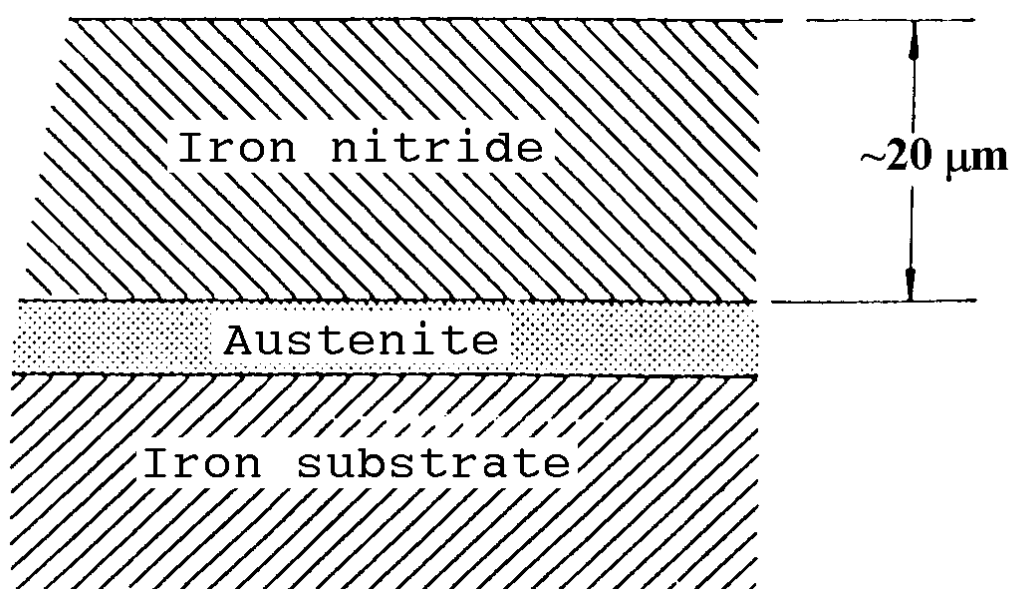


Fig.5.16 According to Cranshaw [5.161], a representation of the layers on a nitrided iron component.

back-scattered X-rays, of the surfaces of components treated by immersion in a commercial salt mixture for times between 2 and 30 minutes. In the top spectrum, a trace of martensite or ferrite from the underlying steel is visible. The central peak near zero velocity comes from the layer of nitrogen austenite between the nitrided layer and the underlying steel. The remainder of the spectrum comes from the hexagonal epsilon nitride,  $\epsilon\text{Fe}_2\text{N}_{1-x}$  with  $x$  ca. 0.3. As the immersion time is increased, the martensite component disappears, and then after it, the austenite peak does, until only the  $\epsilon$ -nitride is seen. The signal from the austenite layer is attenuated by the iron nitride

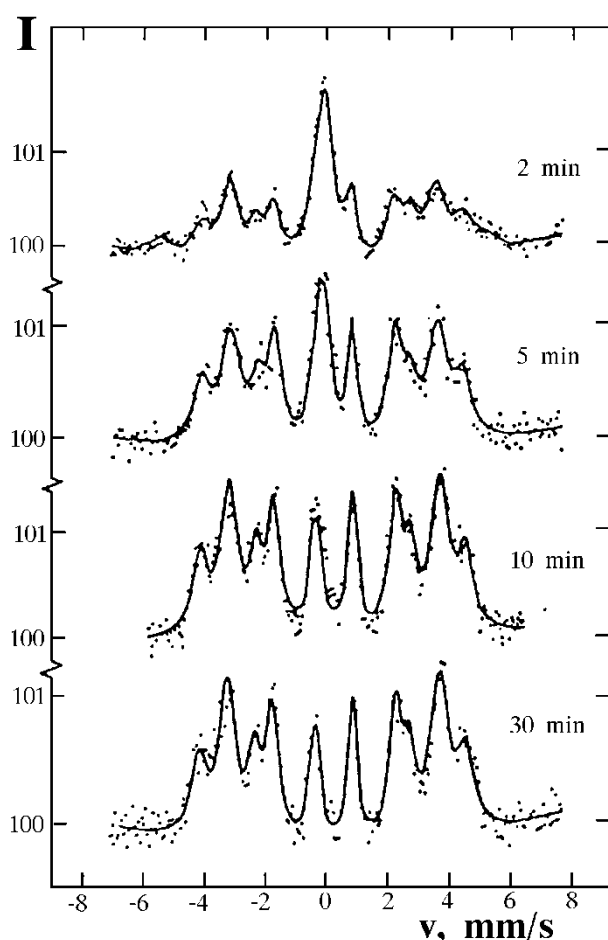


Fig.5.17 Mössbauer spectra by back-scattered X-rays of an iron component treated for different times in a commercial nitriding salt bath [5.161].

above it, and it only remains to make a calibration of the intensity of the austenitic line relative to the nitride spectrum to be able to measure the thickness of the nitride layer.

Because quality-control applications need to involve repetitive determinations of the same quantity, the full power of the technique is generally not necessary. As a result, simpler and more rapid Mössbauer techniques have been proposed and developed by HUGGINS et al. [5.162] for such applications. The technique for the specific industrial applications is the "on-off" resonance method. Basically, this method reduces the conventional Mössbauer spectrum of typically many data points to two data points.

The austenite determination in the backscattering geometry based on the detection of X-rays is the best example of quality control. If a source is in resonance with austenite line and a source strength is of about 40 mCi, an austenite determination can be made in about 5 minutes with a precision of  $\pm 2$  percent. The magnitude of the difference in the X-ray count rate between the source at rest and the source in rapid oscillation ( $v_{\max} > 10$  mm/s) is directly proportional to the percentage of iron in the form of austenite in the

top of the low alloy steel. This value has been shown to be a close approximation to the volume fraction of austenite measured by X-ray diffraction or metallography. For high alloy steels, however, because of the presence of significant amounts of chromium, nickel, manganese, etc., the resonant signal from the iron is effectively diminished and it is more precise to equate the resonant signal [5.162].

This monograph contains insufficient space to discuss all the applications of the Mössbauer effect to the surface studies of metals and alloys. Nevertheless, it is clear that the technique allows fundamental research in metal physics: an assessment of the distribution and redistribution of alloying elements, the detection of new metastable phases, the identification of microstructural and point defects, dislocations and interstitial impurities. Of no less importance are the numerous applications connected with the monitoring of surface quality which is influenced by various treatments, such as mechanical deformation, thermal and chemical treatment.

### 5.3 Ion Implantation and Laser Treatment of Metals

Despite great progress in chemistry, metals, usually in the form of alloys, remain the widely used materials for construction and manufacturing purposes. The degradation of metallic components often takes place at, or else is initiated at the surface and resulting metallic wear and corrosion annually account for tens of billions dollar losses and wastage. For the complex and costly machines and equipment e.g. in aerospace, it is very important to be able to protect critical metallic components.

There are hundreds of methods available for treating or coating metals by physical and chemical means. Some of them were considered in previous sections. The use of directed, energetic ion beams in vacuum in order to modify materials commenced about 25 years ago with emphasis on introducing electrically active species into silicon. This turned out to be a remarkably successful process, due to its precision and versatility. After this achievement, ion implantation has been extended successfully to the entire range of solid materials. This most sophisticated and versatile technique for improving resistance to wear or corrosion of metals and alloys found the greatest industrial application outside microelectronics also [5.163].

Ion implantation often removes the constraints imposed by the phase diagram thermodynamics on the formation of some alloys. Intense localized energy deposition creates effective temperatures of several thousand Kelvin, followed by quenching at around  $10^{12}$  K/s. As a result, high-temperature phases can be quenched in place.

Sometimes the effects of irradiation are more readily explained in terms of binary interactions between atoms. In all these instances ion implantation can lead to the formation of interesting metastable structures with unusual properties.

All modes of Mössbauer spectroscopy have been widely used in this area. Different spectrometer setups may be used in the measurements of ion beam modified metals, e.g. [5.164, 165]. The spectrometers as a rule are coupled directly to the ion implanter. During ion bombardment the sample may be cooled to liquid nitrogen temperature or heated. Mössbauer measurements have to be taken directly after ion beam modification at different temperatures. In Fig.5.18 a schematic view of the CEM spectrometer is shown [5.165]. Fig.18a shows a schematic diagram of the vacuum chamber. The work chamber has an inner diameter of 250 mm and a height of 255 mm. The sample is loaded from the top. To eliminate any vibrations from the pumping system, a damping flange is inserted between the turbomolecular pump and the chamber. In the lower part of the vacuum chamber a continuous-flow cryostat and a heater are mounted.

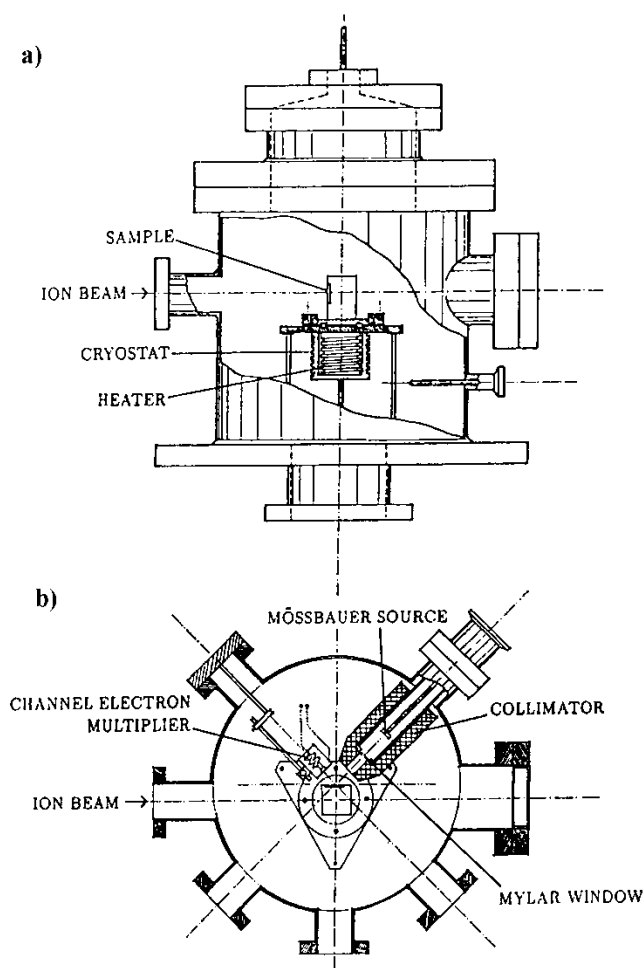


Fig.5.18 Schematic view of the CEMS chamber for in situ studies of the iron beam modification of metals. An elevation of the chamber is shown above (a), and a section through the target plane below (b) [5.165].

The Mössbauer spectrometer is placed in the upper part of the chamber. Fig. 5.18b shows a section through this part of the vacuum chamber. The sample is fixed to a copper block mounted on ball bearings on the top of the cryostat and the heater. Thus the sample can be rotated around its vertical axis by means of a linear-rotary motion feed through fitted to the top of the vacuum chamber. This makes possible CEMS measurements directly after the ion bombardment. The Mössbauer source and drive are separated from the vacuum chamber by a mylar window on the end of a tube which collimates the gamma ray beam on the sample surface. In this way a final pressure of about  $10^{-7}$  mbar at room temperature could be obtained in the chamber. To increase the collection efficiency for electrons emitted from the sample, the input of the channel electron multiplier was held at a positive potential with respect to the grounded sample.

Mössbauer spectroscopy allows the implantation process itself to be studied. Resonant scattering is a relatively slow process (its characteristic time is  $10^{-8}$  -  $10^{-6}$  s), hence it is impossible to directly observe the cascades following the penetration of the implanted ion in the solid, but the final states of the implanted ions can be studied in detail. Thus, studies are possible (specially by using of the coincidence measurement or a pulsed beam) on the trapping point defects on the formation of defects in the vicinity of a stopped Mössbauer atom, as well as clustering and nucleation of new phases, see H.De Waard and L. Niesen - p.p.1-87, vol.2 in [1.6] and [5.166- 171]. The sensitivity of the method greatly depends on the type of atoms implanted (either Mössbauer or their parent). The lowest doses of implanted ions are given in Table 5.5 [5.172]. The data show that in emission Mössbauer spectroscopy one can work with  $10^{-6}$  -  $10^{-4}$  at.% concentrations of the implanted ions. This is of special importance in studies of defects.

Implantation at low temperatures and subsequent isochronal thermal treatments allow the point defect migration in metals and trapping of vacancies to be investigated [5.173-177].

Table 5.5

The least doses of implanted ions used for Mössbauer studies

Nuclide	Dose, atoms/cm <sup>2</sup>	Nuclide	Dose, atoms/cm <sup>2</sup>
<sup>57</sup> Co	$5 \cdot 10^{10}$	<sup>125m</sup> Te	$2 \cdot 10^{15}$
<sup>83</sup> Kr	$1 \cdot 10^{14}$	<sup>129m</sup> Te	$2 \cdot 10^{12}$
<sup>119</sup> Te	$1 \cdot 10^{11}$	<sup>129m</sup> Xe	$5 \cdot 10^{11}$
<sup>119</sup> Sb	$1 \cdot 10^{11}$	<sup>133</sup> Xe	$5 \cdot 10^{12}$
<sup>119</sup> In	$1 \cdot 10^{10}$	The rare-earths	
<sup>125</sup> Sb	$5 \cdot 10^{13}$	( <sup>153</sup> Sm, <sup>161</sup> Tb, <sup>169</sup> Er)	$2 \cdot 10^{13}$

from [5.119]

An example is the study by Mössbauer effect on <sup>133</sup>Cs of implanted <sup>133</sup>Xe at 100 K in

iron and in some bcc metals. On implantation of Xe into platinum about 40 % of the xenon atoms enter the lattice, and the rest occupy the sites attracted by vacancies. Each of the sites is characterized by its own isomer shift and quadrupole splitting. On annealing (at 260 - 400 K for Pt) the vacancies become very mobile and are concentrated around the relatively large Xe atoms. Similar investigations have been carried out for  $^{119}\text{Sn}$  (or its parent nuclides  $^{119}\text{Sb}$  and  $^{119}\text{Xe}$ ) implantation into various metals [5.1|6].

Apart from studies of defects, Mössbauer spectroscopy allows the trapping by the implanted ion (atom) of small atoms such as H, He, N or O and the formation of specific clusters (which are sometimes treated as molecules in the metal lattice) to be examined. The trapping of He atoms by vacancies surrounding the implanted admixture has been investigated in detail [5.166, 178, 179]. A metal can be doped with suitable radioactive atoms and then helium atoms can be implanted. Many of the helium atoms will be trapped by the vacancies created by the doping. Annealing at a sufficiently high temperature leads to the dissociation of the helium-vacancy pair. The two components of the pair are sufficiently mobile to consequently be trapped by admixture atoms. A competing process is the cluster formation of the helium atoms.

An unusual feature of the trapping of helium atoms by admixtures is the existence of only one or two stable configurations with the well defined hyperfine interaction parameters. Thus, on implantation into Ni of In or Sb ions the latter trap only two or three helium atoms. To study these clusters quantitatively, the depth profile and the dose (i.e. the number) of helium atoms implanted into the lattice under investigation should be known. For this purpose low-energy nuclear reactions are usually used where the yield is known. For example, the known yield of the reaction  $^3\text{He}(d,p)^4\text{He}$  enables the dose of helium atoms left in the metal after implantation to be determined. The deuteron energy is 500 keV to 2000 keV, the energy of helium atoms produced by the nuclear reaction is sufficient for the helium atoms to reach the surface. The study of the energy distribution of these atoms allows the dose of helium atoms left in the sample and also their distribution profile to be determined. An example is the study of implantation into tungsten of  $^{119}\text{Sb}$  ions and helium. "Molecules" have been observed in which the helium atoms are near the  $^{119}\text{Sn}$  atoms. The bond energy of Sn and He atoms in this molecule is greater than that of helium atoms combined in a helium cluster in the metal. Another interesting phenomenon is the internal oxidation of ions implanted into a metal, e.g. Fe into copper, or  $^{119}\text{Sb}$  ions implanted into silver [5.166, 180]. Emission Mössbauer spectroscopy has been used in this problem and the number of ions implanted may be very small (see Table 5.5). (Hence the agglomeration probability of the implanted atoms is low.) After annealing at temperatures above 400 K lines corresponding to  $\text{SnO}_2$  appear in the Mössbauer spectrum.



Dilute substitutional alloys (which are otherwise impossible to produce) have been observed by low temperature implantation of rare-earth ions into fcc metals. In one of the first works in this field,  $^{161}\text{Tb}$  implantation has been investigated into Al, Ni, Cu, Ag and Au [5.166]. Such studies are of special importance for the development of a theory of magnetism, since they allow the behaviour of the rare earth ions to be investigated as a function of the crystal field.

Metals and alloys implanted with Fe or  $^{57}\text{Co}$  have been intensively investigated [5.181-186]. In the first investigations the recoil effect at the Coulomb excitation of  $^{57}\text{Fe}$  atoms was utilized. An advantage of experiments of this type is the possibility to observe the state of the atoms in a time interval of a few hundred ns after implantation, but the experiments are time- and labour-consuming. The next step was the use of isotope separators [5.183] to implant  $^{57}\text{Co}$  into certain metals to study after-effects and interactions with point defects [5.184,185].

The first investigations based on  $^{57}\text{Fe}$  implantation required doses of  $10^{16}$ - $10^{17}$  ions/cm<sup>2</sup> [5.186]. At present, spectra can be taken at doses of  $10^{13}$  ions/cm<sup>2</sup> and experimental data have been accumulated on studies of the effect of  $^{57}\text{Fe}$  implantation in Al, Si, Ge and 3d-, 4d- and 5d-metals. The final state of the implanted atoms is determined to a great extent by the ratio of the implanted atom size to the size of the matrix atoms. In matrices of Fe, Co, Ni, Rh, Os, Pt any aggregation of  $^{57}\text{Fe}$  atoms to form, for example, dimers, does not give rise to extra lines in the spectra. Conversely, in matrices of Al, Cu, Zn, Ag and Au an enhanced aggregation of Fe atoms is observed. Comparison of the different behaviour of Fe atoms gives a deeper insight into the laws governing alloy formation, especially in non-equilibrium systems. Iron atoms in substitutional and interstitial positions and clustering were studied by DE WAARD and ZHANG [5.164] and SIELEMANN et al. [5.187]. The low temperature solubility of iron in Al and Cu is nearly zero and in thermal equilibrium iron will always cluster or form intermetallic compounds. The first process only has been observed for Fe in Cu and both processes are found for Fe in Al. To obtain an appreciable substitutional fraction of isolated impurities in these metals implantation should be used [5.164].

The components of Mössbauer spectra not related to substitutional Fe monomers have been ascribed to small iron clusters for unannealed samples whereas annealing may lead to the formation of intermetallic compounds ( $\text{Fe}_x\text{Al}_y$ ) or  $\gamma$ -iron precipitates ( $\text{FeCu}$ ). It is well known that impurity clustering, if energetically favourable, is stimulated by implantation. The authors consider two effects of implantation that may lead to enhanced clustering . (i) If the defect cascades of two or more impurity atoms overlap,

one may expect impurity clustering. (ii) Isolated vacancies and vacancy clusters formed during implantation become mobile above characteristic annealing temperatures that correspond to well known recovery stages. It may also result in clustering. This effect is strongly temperature dependent.

To determine the contribution of these two effects to clustering, DE WAARD and ZHANG [5.164] carried out measurements at temperatures, where isolated vacancies are not mobile (around 220 K for Al and around 280 K for Cu). For  $^{57}\text{FeAl}$ , the substitutional fraction ( $f_s$ ) in samples implanted at 120 K is somewhat smaller than expected for a random impurity distribution but much larger than after room temperature implantation. For  $^{57}\text{FeCu}$ ,  $f_s$  for samples implanted at 120 K is less than 0.5 of the value expected for a random distribution and it falls to zero after annealing at 600 K, where extensive Fe clustering occurs. Vacancy trapping at the temperature where isolated vacancies become mobile does not contribute significantly to the observed defect sites.

SIELEMANN et al. [5.187] investigated Fe atoms in interstitial positions in metals which display little or vanishing solubility for the Fe atoms in thermal equilibrium. Production of interstitial sites for Fe atoms in various materials and the interstitial dynamics were stimulated by the method of in-beam Mössbauer spectroscopy combining recoil implantation and Coulomb excitation. Two strongly pronounced dynamical effects for the Fe-interstitial complex were observed: localized diffusion (cage motion) in several metals and in FeSc the onset of anomalously fast diffusion of Fe starting from interstitial sites.

There are a number of works devoted to copper, e.g. [5.188 -190]. The choice of copper results from the low solubility of the metals in the Cu-Fe system at room temperature, and by the absence of their intermetallic compounds. Ion implantation makes it possible to produce and study surface layers of metastable Cu-based alloys with more than 10 % Fe. Especially promising is ion-beam implantation with a high current density (more than 1 mA/cm<sup>2</sup>), since due to an intense mixing of the components in the alloy region, a more disordered distribution of iron atoms in the matrix takes place [5.190]. Fe-atoms in a copper matrix after implantation are: (i) isolated, that is, they have no other iron atoms as nearest neighbours; (ii) in clusters, from two to up to eleven Fe atoms; (iii)  $\gamma$ -Fe particles, or iron oxides. The surface layer of alloys so implanted are characterized by a vast number of structural defects. After high current density implantation the concentration of implanted iron does not exceed ~10 % with beam energies up to 100 keV. After annealing, the fraction of iron atoms in the form of  $\gamma$ -Fe particles initially increases, but then the  $\gamma \rightarrow \alpha$  transformation begins. The maximum iron concentration up to 25 at.% in Cu solid solution, was reached by laser processing. Apart from studies connected with the phase diagram of the metastable Cu-Fe system, information has been obtained on anomalies of the diffusion process and the effect of irradiation on diffusion.

The maximum iron concentration in Cu depends on the projectile energy and the stopping power but it is decisively determined by sputtering. The sputter yield has its maximum in an energy range of 50-200 keV and decreases for higher energies. MÖLLER et al. [5.191] calculated that at ion energies of about 1 MeV, layer thicknesses of a few hundred nm and ion concentrations of up to several tens at.% are obtainable, especially for element combinations not feasible with conventional metallurgical methods. A 20  $\mu\text{m}$  thick polycrystalline Cu (99.0%) foil was irradiated with an average dose of  $2 \cdot 10^{17}$  Fe/cm<sup>2</sup>. The sputter yield was calculated to be 5.1, corresponding to 19 at.% maximum concentration of implanted ions. According to calculations for this dose, a surface layer 130 nm thick has been removed by sputtering and thus the implantation profile reaches its maximum near the surface. In the conventional phase diagram the room temperature solubility of Fe in Cu is smaller than 0.26 wt. % Fe. The implanted area shows a silver coloured spot, indicating a high iron concentration. A concentration of  $\sim 16$  at. % was determined at the surface by AES, in agreement with calculations.

During implantation the driving force for phase transformations may arise primarily from the highest stress level caused by the aggregation of gas atoms and to dispersed atoms in the irradiated layer. On the other hand, atoms implanted to the matrix may induce the phase transformation due to compositional changes and alloying effects. SAKAMOTO et al. [5.192] have investigated the phase transformation in 17/7 stainless steel induced by irradiation with Fe ions, which are constituent element and the martensitic phase stabilizer of stainless steels. The measurements showed large difference in the fraction of the induced alpha phase between irradiations of stainless steel with <sup>56</sup>Fe ions and <sup>57</sup>Fe ions. In the case of <sup>57</sup>Fe ion irradiation, the projectile <sup>57</sup>Fe probe atoms "observe" the phase transformation which may be induced by them. It is most probable that CEMS in <sup>57</sup>Fe ion irradiation reflects the phase transformation due to compositional changes and alloying effects. It was the first observation of the projectile-isotope effect, which has a potentiality of a new technique to investigate non-equilibrium phase diagrams.

Let us consider some applied studies where CEMS has been used for analysis. Many investigations been aimed at the improvement of surface properties, such as hardness, friction, corrosion resistivity, fatigue behaviour and wear resistance [5.170, 179, 193-207]. In a number of reports this has been achieved by ion implantation with nitrogen. Other ions (boron, carbon, phosphorus and some metals) are also used to reach the desired effect, sometimes even using a substantially lower dose of implanted ions than with nitrogen [5.198,208-212]. When metal ions were used for surface modification, chromium was often selected. Thus, on implantation of a low-carbon steel with a dose of  $10^{17}$  Cr atoms/cm<sup>2</sup> and at an energy of 150 keV, electrochemical properties become practically the same as for stainless steel with 18 % Cr.

For ion implantation with nitrogen a special high current source of nitrogen ions is needed for industrial applications. Mössbauer spectroscopy combined with nuclear reaction analyses of the implanted isotopes is specially efficient to study the processes on the surface and to optimize the implantation procedure. Usually ion beams are used at energies of 20 - 200 keV and at current densities 10 - 30  $\mu\text{A}/\text{cm}^2$ , at doses of up to  $8 \cdot 10^{17}$  atoms/ $\text{cm}^2$  [5.194, 195]. The amount of nitrogen retained in the near-surface layer of an alloy is monitored by nuclear reaction analysis, e.g. by the  $^{14}\text{N}(\text{d},\text{p})^{15}\text{N}$ ,  $^{14}\text{N}(\text{d},\alpha)^{12}\text{C}$  or  $^{15}\text{N}(\text{p},\alpha\gamma)^{12}\text{C}$  reaction. The last has a narrow resonance ( $\Gamma \approx 0.9$  keV) at 429 keV and is especially efficient for monitoring the nitrogen content. The amount of oxygen in the layer in question can be measured by the  $^{16}\text{O}(\text{d},\text{p})^{17}\text{O}$  reaction.

As the ion current density increases, the relative amount of nitrogen retained in the near-surface layer decreases. This amount may also depend on the matrix composition. Thus, in carbon steels the amount is less in the quenched samples than in the annealed ones [5.195]. The sample temperature also influences the nitrogen retention. At temperatures above  $100^\circ\text{C}$ , the nitrogen begins to diffuse in the near-surface layers of pure iron and tool steel, but in stainless steel its amount does not change at temperatures up to  $320^\circ\text{C}$ . The total amount of nitrogen in the layer is not affected by oxide growth during implantation. Usually about 50 % of the implanted nitrogen is retained in the sub-surface layer, but sometimes the value approaches 100 %. The nitrogen content may reach 34 % [5.194].

Surface modification is due to the formation of nitride and carbonitride precipitates. Their composition and properties are determined by the composition and initial structure of the sample as well as by the implantation conditions. A significant role may be played by local self-heating of the sample and the related diffusion of nitrogen [5.195]. This means that nitrogen implantation of quenched steels should be carried out at low current densities to prevent the tempering effect. At the same time, the self-heating at high ion current densities may be useful when an increase in the modified layer thickness is desired. The implantation of annealed steels produces no change in the bulk properties, and the thickness of the modified layer can be controlled by the ion current density which improves the fatigue lifetime of the steel.

It looks expedient to search by means of Mössbauer spectroscopy for the correlation between the mechanical and tribological properties of the near surface layer and the phase compositions of the implanted layers [5.213-216]. WAGNER et al.[5.213] investigated a nitrogen implanted X10CrNiTi18.9 steel. In the case of the austenitic stainless steel X10CrNiTi18.9 the wear resistance and hardness increased as a function of the implantation dose and temperature. For that purpose the surfaces of the samples

were electrolytically and mechanically polished to change the ( $\gamma/\alpha'$ )-ratio of the untreated material in a wide range. The formation of iron nitrides started at doses between 2 and  $6 \cdot 10^{17} \text{ N}^+/\text{cm}^2$  depending on the surface treatment. First the nucleation of magnetic nitrides takes place, then at higher doses the nitrogen richer paramagnetic  $\text{Fe}_2\text{N}$ -nitrides are favoured. In the case of mechanically polished surfaces the ( $\gamma/\alpha'$ )-ratio in the near surface region changed in both directions.

The depth distribution of martensite in xenon-implanted stainless steels was investigated by JOHANSEN et al. [5.216]. Martensite was found to be induced only in steels with the lowest austenite stability (304 and 316 commercial steels) while the austenitic matrix phase is fully retained in the high-austenite steels (310 commercial steel). The martensite transformation originates at the surface and is gradually driven to larger depths with increasing ion fluence. At saturation, the thickness of the transformed layer depends on the composition of particular steels and on the implantation conditions, ranging from  $\sim 25 \text{ nm}$  in the 316 steel implanted at 100 keV to 100-150 nm in the 17/7 and 17/13 steels implanted at 200-300 keV.

It is possible to modify the properties of metal surfaces by post-ion irradiation of the implanted layer. The effect is due to radiation-induced phase transformations and also to radiation enhanced precipitation diffusion and segregation [5.179, 217-219]. To investigate these effects, foils e. g. of pure iron [5.179] or 1020 low carbon steel (0.2 wt.% C, 0.9 wt.% Mn) [5.217, 218] have been implanted with  $\text{N}_2^+$  ions in the energy interval between 30 and 150 keV. Such energies of the impinging ions provide for a homogeneous distribution in a layer  $\sim 100 \text{ nm}$  thick with N - concentration  $\sim 40 \%$ . Implanted samples (some annealed at  $400^\circ\text{C}$ ) have then been bombarded with 10 to 30 keV  $\alpha$ -particles that become homogeneously distributed within the same  $\sim 100 \text{ nm}$  thick layer, with a concentration  $\sim 1 \%$ . The composition and properties of the surface layer turned out to be changed after irradiation at  $\alpha$ -particles fluences of  $\sim 10^{15} \text{ cm}^{-2}$ . In iron foils the diffusion of nitrogen after irradiation is suppressed and nitrides are still present in the surface layer even after annealing at  $500^\circ\text{C}$ . In low carbon steels nitrogen diffusion depends on the type of carbonitride precipitates and the matrix that contains these precipitates. RAMOUS et al. [5.217, 218] found that the precipitates produced by  $\text{N}_2^+$  implantation were affected in the following ways: The  $\epsilon\text{-Fe}_{3.2}(\text{CN})$  precipitates are highly unstable and dissolve at rather low implantation dose;  $\epsilon\text{-Fe}_2(\text{CN})$  is very stable. The presence of He in the  $\text{N}_2^+$  implanted region modifies the thermal behavior of the carbonitrides. This is attributed to  $\text{He}_m - \text{V}_m$  complexes that agglomerate at the grain boundaries of the precipitates, inhibiting nitrogen diffusion. The trapping efficiency strongly depends on the kinds of precipitates formed.

The effect of ion implantation was augmented by several other generally related methods suitable for metals. In each of these procedures ion bombardment is combined with the application of a coating, e.g. by thermal evaporation or sputter deposition. The purpose of the ion bombardment is to enhance the performance of the coating by alteration of its composition, microstructure or adhesion to the substrate, or to induce interdiffusion between the coating and its substrate. This technique is called ion beam mixing. It is a descriptive term for the process whereby a thin coating is deposited onto a metal, and then caused to mix completely with the substrate under the influence of energetic ion bombardment [5.21].

Ion-beam mixing has greatly expanded the potential uses of ion beams to modify materials properties. Perhaps no other process is as efficient as ion-beam mixing for introducing large, nonequilibrium concentrations of alloying elements into a wide variety of hosts under carefully controlled conditions. The list of potential technological applications for ion-beam mixing has expanded further with the more recent development of ion-assisted deposition. By combining ion-beam mixing with simultaneous deposition, ion-assisted deposition removes the limitation on the altered layer thickness imposed by finite ion ranges. This innovation has stimulated renewed interest in understanding fundamental aspects of the ion-beam mixing process.

There are characteristic differences between radiation-enhanced diffusion, that is mass transport at high temperatures due to freely-migrating vacancy and interstitial defects, and the enhanced ion-beam mixing that is observed in many materials at intermediate temperatures. The high mixing efficiencies achieved during heavy-ion bombardment are a direct result of enhanced mass transport during the "cooling phase" of energetic displacement cascades. The observed correlations demonstrate that the mixing process is dominated by low-energy ( $\sim 1$  eV) atomic recoils, and not by higher energy ( $> 25$  eV) "ballistic" events. The available data on ion-beam mixing at intermediate temperatures differ substantially from measurements of known radiation-enhanced diffusion effects in larger-grained crystal line specimens.

To study the ion mixing mechanisms and the ion-induced reactions in the mixed region, a variety of modern analytical techniques have been used, such as Rutherford back-scattering spectrometry (RBS), X-ray diffraction, scanning electron microscopy (SEM) and many others. Among them CEMS is the most efficient if Mössbauer nuclei are involved. To localize the implanted atoms and to study the implanted atom-vacancy complex, electron and positron channeling [5.221, 222] has often been used along with CEMS.

Ion beam mixing induced by irradiation of the Fe/SiO<sub>2</sub> interface with 100 keV Ar<sup>+</sup> ions has been studied in [5.223]. In the mixed region,  $\sim 30$  nm thick, several iron-containing phases were identified. These included small clusters of metallic iron, an oxide phase, and a silicate phase. The phase composition depends on the Fe-ion fluence and the temperature. Similar studies of iron-beam mixing effects on metal/insulator systems are reported in a number of other papers [5.224]. Ion-beam mixing induced chemical reactions between tin [5.225], niobium [5.226] and iron oxides, iron and aluminium oxide [5.227] have been reported.

CEMS reveals the formation at the metal/metal interface of a variety of intermetallic phases due to ion-beam mixing. These phases seem to be insensitive to prolonged (several months) room temperature ageing. Thin metallic bilayers are popular objects for ion-beam mixing studies. Kr- and Xe-ion beam induced reactions of  $\alpha$ -Fe with deposited Ni- or Cr-layers [5.228], reactions in the iron-tin system (very popular among the Mössbauer spectroscopists) [5.229], and in Fe-Pd bilayers evaporated onto SiO<sub>2</sub> substrates [5.230] were investigated. Phase determination and spatial distribution of an ion-beam mixed internal interface: Fe/Sn was studied in [5.231].

To achieve a depth selectivity in studies of ion beam mixing in Fe-Pd bilayers, GUPTA et al. [5.230] evaporated a 5 nm thick <sup>57</sup>Fe layer at either the Pd-Fe interface or the Fe-substrate interface. Two sets of Fe-Pd bilayers, with Pd on top, were prepared by sequential evaporation of various constituents on oxidized Si substrates: 1- 40 nm natural Fe, 5 nm <sup>57</sup>Fe, 30 nm Pd and 2- 5 nm <sup>57</sup>Fe, 40 nm natural Fe, 30 nm Pd. To avoid sputtering effects during the ion bombardment, a 5 nm thick layer of C was also evaporated on top of the samples. Since <sup>57</sup>Fe is the isotope responsible for the Mössbauer effect in iron, the two different positions of the <sup>57</sup>Fe marker layer in specimens of sets 1 and 2 allowed to selectively probe the interface regions between Fe and Pd and between Fe and the SiO<sub>2</sub> substrate, respectively. Ion-beam mixing was performed by irradiating the specimens with 200 keV Kr<sup>2+</sup> ions at a dose of  $2.5 \cdot 10^{16}$  ions/cm<sup>2</sup>.

Fig.5.19 gives the spectra and the hyperfine field distributions of "as evaporated" and irradiated specimens of set 1. The Mössbauer spectra of the "as evaporated" specimens consist of a well defined sextet with hyperfine field parameters corresponding to  $\alpha$ -Fe and of a weak and broad magnetic component. The relatively small area under this broad component indicates that both the Fe-Pd and Fe-substrate interfaces are rather sharp. The Mössbauer spectrum of the Kr<sup>2+</sup> irradiated specimen (see Fig.5.19b) was very different from that of the "as-evaporated" specimen (Fig.5.19a) due to a large mixing effect in the Fe-Pd interface region. The corresponding hyperfine field distribution shows a broad peak in the range 190-360 kG, suggesting the formation of Fe-Pd alloys over a range of composition in the mixed region. The maximum of the peak occurs at  $27.3 \pm 0.2$  Tesla, which corresponds to a disordered Fe<sub>1-x</sub>Pd<sub>x</sub> phase with an average  $x = 0.72$ . This supports the finding of the earlier studies that the predominant phase formed in the mixed region was FePd<sub>3</sub>.

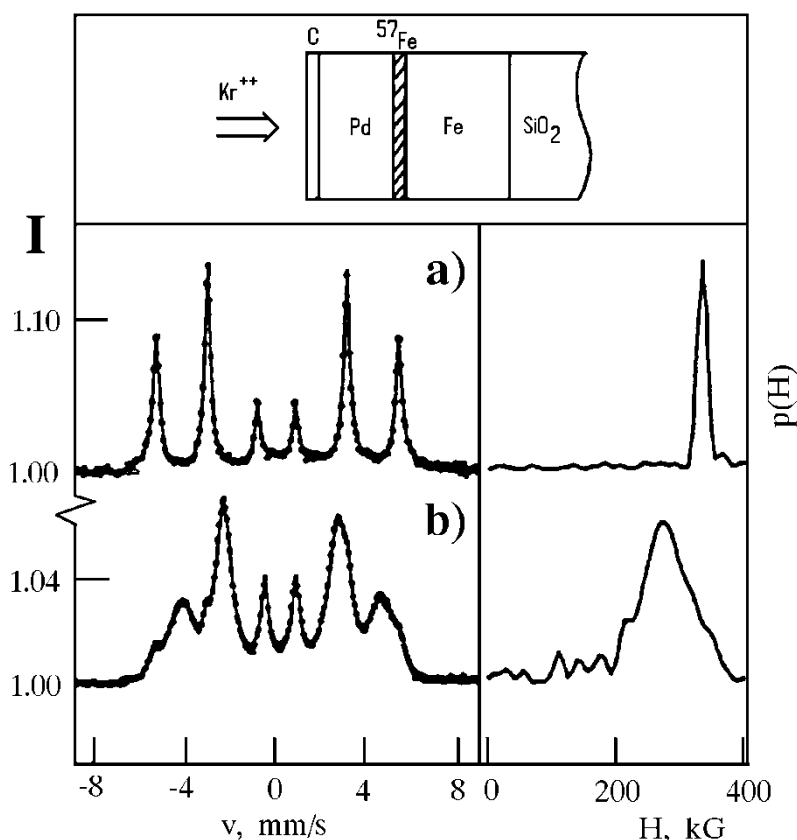


Fig.5.19 Mössbauer spectra (left) and corresponding magnetic hyperfine field distributions (right) of the "as evaporated" (a) and  $\text{Kr}^{++}$  irradiated (b) Fe-Pd samples having the  $^{57}\text{Fe}$  marker thin layer interfaced with Pd (set 1) (From [5.230]).

The small outer shoulders in the spectrum and the corresponding small hump in the field distribution around 33.0 Tesla indicate the presence of a weak  $\alpha$ -Fe component coming from the underlying region of the sample which remains unmixed. The authors conclude that: (i) a subsurface layer is formed in which Pd is completely mixed with Fe; (ii) iron is the dominant moving species responsible for the intermixing of the two metallic layers; (iii) in the mixed region  $\text{FePd}_3$  is the dominant phase; (iv) the unmixed Fe layer undergoes a possible transformation from  $\alpha$ - to  $\gamma$ -phase, which is metastable at room temperature.

Considerable interest in the implantation and the ion-beam mixing of metals has revolved around the production of metastable phases, particularly amorphous materials. Because high concentrations of a wide variety of elements can be alloyed, ion-beam mixing has been used to make various amorphous phases. Mössbauer spectroscopy is widely used in the area, e.g. [5.214, 232-241]. Apart from the studies of metal/metal



interfaces and amorphization, CEMS has been used in studies of adhesion of iron layers on glass and silica and the effect of proton bombardment on adhesive properties [5.242]. As an example, an improvement of the adhesion of thin metal films to substrates is discussed. This phenomenon can be found at relatively low doses e.g. in the case of metal films on teflon substrates. In a CEMS study of ion-irradiated Fe-teflon interfaces, a considerable amount of the iron films was found to be converted from  $\alpha$ -Fe into non-magnetic compounds resulting from chemical reactions with atoms from the underlying substrate.

INGEMARSSON et al. [5.243] examined whether similar reactions might take place when bombarding thin iron films deposited onto polyvinyl chloride. This system was found to exhibit radiation effects which were even more pronounced and new chemical, structural, electrical and optical features were observed as a result of the ion bombardment. No chemical cleaning was performed as it was found that this does not significantly affect the Mössbauer spectra of "as-deposited" Fe films. Films of  $^{57}\text{Fe}$  (~97 %) were thermally evaporated to thicknesses of 5 nm and 10 nm at a pressure below  $5 \times 10^{-6}$  Torr.

The formation of species upon ion bombardment is accompanied by considerable radiation damage in the proximity of the interface. Three general features were noticed: the relative amount of metallic iron decreases with decreasing film thickness, with increasing stopping power of penetrating ions and with increasing ion dose. Irradiation of thin Fe- polyvinylchloride film structures with energetic ions leads to the formation of iron-chlorine and iron-carbon compounds. An enrichment of chlorine in the interface region is evident at increasing ion doses and is further accompanied by alterations in the Mössbauer spectra in which components indicative of Fe-Cl and Fe-C compounds appear at the expense of metallic iron.

Mössbauer spectroscopy and especially CEMS have been widely used to study the effect of radiation on metals and alloys. This work includes alloys irradiated with energetic heavy ions [5.244], radiation damage resulting from proton and neutron irradiation of refractory metals and materials [5.245, 246], phase transitions in stainless steels influenced by plastic deformation and proton irradiation [5.247-250]. The success of CEMS in studies on surface modification of iron and its alloys is due to the fact that the mean projected range of the 50 keV  $\text{B}^+$  and  $\text{C}^+$  ions in iron is approximately equal to the thickness of the analyzed layer. Since the implantation range of hydrogen ions of 10 keV plasma is of the same magnitude, and the sensitivity of CEMS is as high as  $\sim 10^{14} - 10^{16}$  at/cm<sup>2</sup>, the technique has proved to be convenient in materials studies, in plasma physics and thermonuclear fusion [5.249, 250].

The structural modifications of iron and its alloys under neutron and ion bombardment, and particularly in a hydrogen plasma, are of crucial importance in fusion studies. Austenite stainless steels are common first-wall materials in existing experimental devices, and are likely to be used in future fusion power reactors.

Martensitic transformations can be induced in austenitic stainless steels also in a variety of processes: by cooling below the martensite start temperature, by heavy cold-work such as rolling or drawing, or by charging with hydrogen. In connection with the application of stainless steels in radiation environments it is of particular interest to notice that martensitic transformations can also be induced by ion implantation. The primary contribution to the driving force for ion implantation-induced martensitic transformation is due to accumulation of high stress levels in the implantation zone, whilst primary radiation damage and changes in composition only give minor contributions [5.250].

Phase transformations in stainless steel have been studied by CEMS after irradiation with neutrons, protons [5.178, 245, 249-251], deuterons [5.250, 252, 253],  $\alpha$ -particles [5.178, 253-255] and heavy ions [5.244, 256, 257]. Apart from the phase analysis of stainless steels, CEMS has been used to study iron impurities and their redeposition in tokamak, iron hydride formation during ion bombardment, and the interaction of tritium breeding lithium blanket materials with structural components.

Two studies of type 304 stainless steel should be mentioned. The steel is considered, to be used as a material for the first wall of thermonuclear reactors. HAYASHI et al. [5.253] observed the  $\gamma(\text{fcc}) \rightarrow \alpha(\text{bcc})$  phase transformation in the steel after irradiation of  $\text{He}^+$  and  $\text{H}^+$  ions up to fluence levels of  $10^{17}$  and  $10^{19}$  ions/cm<sup>2</sup>, respectively. Depth selective conversion Mössbauer spectroscopy and surface-sensitive X-ray diffractometry were employed to study the effect of irradiation. It was shown that the amount of the ion induced phase was highly sensitive to the fluence, the ion species and depth from the surface. The results make clear that the amount of the transformation strongly depends on the depth from the surface and ion species. JOHNSON et al. [5.250] studied martensitic transformations in the steels implanted with 8 keV helium, hydrogen and deuterium. The distribution of martensite in the implantation zone has been analysed as a function of depth. Transformation of the implanted layer occurs after implantation with  $10^{21}\text{m}^{-2}$   $\text{He}^+$  ions while 100 times higher fluence is required for the implanted layer to be transformed after hydrogen or deuterium implantation. This difference is due to the ability of helium to form high pressure gas bubbles, whilst implanted hydrogen is continuously lost by back diffusion to the surface.

At present a novel technique in ion implantation is developed using MeV-ion implanters for large area applications [5.258, 259]. The process of an interaction of concentrated pulsed energy flow into a substance includes a large variety of processes from heating to gas-dynamical ones. The thickness of the modified layer may exceed the projected ion range by more than an order of magnitude. According to [5.259] the total modified layer may be conventionally divided into three regions which differ in types of defects. When a proton beam is used to heat iron and iron-based alloys to the melting temperature, the beam must have a power density of  $10^7$  to  $10^8$  W/cm<sup>2</sup> and a particle energy of some hundred keV. HALLEN et al. [5.258] describe an irradiation facility capable of providing MeV ion irradiations (protons and alpha particles) at homogeneous doses over large areas. The technique is essential for attaining deep ion implantation, or when the interest is focused on the electronic interactions associated

with high-energy ions. One example of the application of the technique was considered above (see [5.243]).

Another innovative method of modifying the surface layer of metals and alloys and producing metastable phases is laser treatment [5.260-268]. The method has become one of the busiest areas in laser material processing research. Laser hardening, laser remelting, laser alloying, laser cladding and improvement of the resistance against corrosion and wear may be mentioned. By laser alloying it is possible to achieve the material improvement without affecting the bulk material. Using high-power laser treatments very sharp thermal gradients can be produced which rapidly heat the surface layers well above the melting temperature and allow a rapid cooling of the remelted layers ( $\sim 10^7$  K/s). By this method both amorphized metal surfaces can be produced and alloying of the surface layer with pre-deposited alloying elements is made possible. The alloying may be carried out in a variety of ways which differ in the manner of delivering the alloy ingredients: vapour phase deposition, painting, powder blowing, wire evaporation, foil melting. Many of the properties obtained by ion implantation can also be realized by laser processing. However, the results may differ due to the difference in the physics of the processes.

Other applications of laser-surface melting have been directed at enhancing surface hardness of steel and cast iron. An example is the surface melting of grey cast iron to produce a layer of white cast iron. By changing the incident power density of the laser and laser-material interaction time, different thicknesses can be produced of the surface layer where melting or phase transformations occur. Mössbauer spectroscopy by X-ray detection (which supply information about more thicker layers) is most often used in such studies and CEMS is of lesser importance. In steel the depth of the melted zone depends on the carbon content. Subsequent solidification processes lead to polyphase structures made up of austenite and cementite. Under the melted zone there is a solid transformed zone which consists mainly of martensite with grains of different coarseness and with a small variable amount of retained austenite. The two zones are heterogeneous, hence large fluctuations in microhardness may occur [5.260,261,266].

One of the first studies of laser quenching of industrially important alloys was devoted to the investigation of phase composition changes in surface layers of cast-iron at two incident power densities of a high-power CO<sub>2</sub> laser [5.60]. Under surface melting conditions the laser power was 3 kW at a beam translation speed of 0.8 mm/s. The spectrum recorded by REYMAN et al. [5.260] from the untreated sample was a sextet with broadened lines from martensite and a line from austenite with an area of approximately 10 % of the total spectrum. After laser treatment cementite was predominant in a layer to about 5  $\mu$ m thickness (over 45 % of the total area). Martensite and austenite were present in approximately equal amounts. After layer-by-layer abrasion it was shown that the amount of cementite and austenite decreased with depth and at a depth of 200  $\mu$ m their relative amounts were 10 % each with martensite

constituting about 80 % of the total amount. Microhardness of the treated surface increased from an initial value of 150 - 220 kg f mm<sup>-2</sup> to 950 - 1050 kg f mm<sup>-2</sup>. The surface did not melt at a laser power of 1 kW and a beam translation speed of 1.2 mm/s. Cementite was formed only in a layer about 0.2 µm thick and the amount of austenite increased in the thicker layers.

Other examples [5.264, 265, 269] concern laser treatment of carbon- and low-alloy steels (0.4 wt % C and 0.38 wt % C-Ni- Cr-Mo). The incident power density was 2.1 and 2.6 kW/s, respectively. The corresponding laser-material interaction times were 1.2 s and 2 s. The samples were coated with graphite to decrease reflectivity. During the laser treatment a stream of helium gas was directed onto the irradiated zone to improve the flatness of the melt and to prevent oxidation of the steel. Surface oxidation occurred in a carbon steel at the large incident power density. This resulted in a decreased surface melting. This effect was not observed for the low-alloy steel. CARBUCICCHIO et al. [5.264, 265] have shown that a critical parameter for laser treatments is the gas phase composition. Laser treatment with a continuous-wave CO<sub>2</sub>-laser on samples of commercial mild steel (C45) containing 0.45 wt % C was studied by SCHAAF et al. [5.269]. The authors demonstrated that Mössbauer spectroscopy performed in the back-scattering mode is a helpful tool for phase analysis in surface engineering. Chromium-boride was added to the substrate surface by powder injection during laser surface melting with a high power cw CO<sub>2</sub>-laser. The laser spot with a diameter of 2 mm was moved with a constant velocity of 10 mm/s relative to the sample. The chromium-boride (CrB<sub>2</sub> commercial powder of 40-100µm) with a melting point of about 2000°C was added by powder blowing into the laser melted pool behind the laser spot. Argon was used as carrier and protective gas. The laser melted pool exceeded this temperature and in the melt there were concentration gradients around the boride particles which were frozen in by the rapid self quenching of the sample. After rapid self quenching martensite and retained austenite were mixed with about 45 % (Fe, Cr)<sub>3</sub>B, which together with the undissolved CrB<sub>2</sub> particles, increased the hardness three times in comparison to the unalloyed sample.

Laser treated steels containing significant amounts of alloying elements were also intensively studied by Mössbauer spectroscopy. The phase transformations which occur at the surface and at various depths of a commercial X210Cr12 cold forming tool steel were investigated by SCHAAF et al. [5.270, 271]. The steel was submitted to single-pass laser irradiation with two power levels, 2700 W and 3050 W. Backscattering Mössbauer spectra were taken at the treated surface and at various depths down to 2 mm and were discussed in connection with metallographic and Vickers hardness data.

In Chapter 4 it was shown that the hyperfine interaction parameter distribution could be a sensitive indication of even moderate changes in the short-range order on "as-received" and laser-melted surfaces of amorphous alloys, e. g. iron-boron alloys. The interpretation of Mössbauer spectra may be clearly facilitated by a comparison with equilibrium and metastable intermetallic compounds. The structure of nano-second-pulse laser-melted surfaces of different evaporated layers and bulk ingots has been studied by FETZER et al. [5.272, 273] in the iron-boron system between 17 and 56 at.% B content. Considerable decrease (~10 %) of the width of hyperfine field distribution was observed for the laser-melted surfaces compared with the evaporated layers, indicating an larger disorder in the latter.

In the composition range between 12 and 56 at.% B alloys were either rapidly quenched from the liquid state by melt spinning, which resulted in continuous ribbons. Also, two- source coevaporation of the elements onto aluminium substrates was used. The accuracy of the composition of the evaporated samples is better than  $\pm 2$  at. %. The typical thickness of these samples was ~650 nm. Some crystalline ingots, prepared by induction melting in cold crucibles under Ar atmosphere with the compositions  $\text{Fe}_{83}\text{B}_{17}$ ,  $\text{Fe}_2\text{B}$ , and  $\text{FeB}$  were also used. Assuming a laser pulse length of 16 ns, a pulse energy of 8 mJ, a spot diameter of 0.4 mm and an absorption coefficient of  $10^9 \text{ m}^{-1}$ , FETZER et al have calculated the variation of temperature as a function of time and distance from the surface. The average quenching rate was approximately  $3.6 \times 10^9 \text{ K/s}$ .

The obvious narrowing of the hyperfine field distribution of the laser-melted thin surface films indicates that the short-range order of amorphous structures produced by different methods could be significantly different. In contrast with this behaviour, no amorphous alloy was obtained by laser melting of an equiatomic  $\text{FeB}$  ingot or an evaporated amorphous  $\text{Fe}_{44}\text{B}_{56}$  film. In the latter case the laser melting resulted in the low- temperature crystalline  $\alpha\text{-FeB}$  modification, indicating the important role of surface nucleation.

Laser treated surfaces of the  $\text{Fe}_{83}\text{Si}_{17}$  alloy and of the coatings prepared on low-carbon steel by laser surface alloying with Ni and Al were investigated by SCHNEEWEISS et al.[5.274]. The short range order in the surface layer after irradiation by neodymium glass laser pulses was found to be similar to that before irradiation. The high quenching rate of a single melt pool after single pulse action seems to have been masked by annealing due to the heat produced by successive pulses covering the whole surface. However, seven different phases were found in the dependence on chemical composition of alloy coatings and on the traverse speed, i.e. the speed of a relative motion of the sample and the continuous wave  $\text{CO}_2$ -laser beam.

In this and the previous sections different procedures of surface modification due to the formation of nitride precipitates were discussed. To develop novel, simple, efficient and technology compatible ways to nitride material surfaces OGALE et al. [5.275]

investigated nitridation of iron by pulsed excimer laser. The treatment was done by using a pulsed XeCl excimer laser ( $\lambda = 308$  nm, pulse width  $\sim 25$  ns), at a maximum energy per pulse of  $\sim 500$  mJ and energy densities up to  $\sim 3$  J/cm<sup>2</sup>. Pure liquid ammonia, obtained by condensing ammonia vapour on a height limiting sample pool and held at a temperature of  $-60^\circ\text{C}$  during the experiment, was poured over the sample. As a result, interface reactions between metallic iron and liquid ammonia were induced and a significant degree of nitridation of iron was achieved. The as-treated foil contained only  $\gamma$ -Fe-N austenite, which transformed to the  $\gamma'$ -FeN<sub>4</sub> phase via solid-state reactions with  $\alpha$ -Fe upon a thermal annealing treatment.

Coatings composed of Ni- and Co- based alloys, prepared by surface alloying of steel substrates, were studied by SCHNEEWEISS et al. [5.276]. The samples were prepared by feeding a powder of the alloying material directly into the laser spot on the substrate where the surface was scanned by a continuous wave CO<sub>2</sub>-laser beam. In all cases the substrate material was a low carbon steel (DIN WUST. 12), 5 mm thick. The results, in addition to phase composition data, showed the effect of the thermal history of samples. The contribution of Mössbauer spectroscopy consists in revealing structural details that result from rapid cooling of the remelted surface layer.

Steels and alloys containing significant amounts of alloying elements were intensively studied in the context of the improvement of their corrosion resistance. KULKARNI et al. [5.277] investigated the corrosion behaviour of virgin and pulsed laser treated maraging steel 69Fe-18Ni-8Co-5Mo. Pulsed ruby laser irradiation was used ( $\lambda = 693$  nm, pulse width  $\approx 30$  ns) at an energy density of  $10.0$  J/cm<sup>2</sup>. Electrochemical corrosion was obtained in a sodium acetate buffer solution. After pulsed laser treatment an austenitic phase was retained in the upper layer practically without change in the chemical composition but a higher corrosion resistance was achieved due to elimination of near-surface stress. A martensitic to austenitic transformation occurs at the surface upon laser treatment, but no change is observed in the mechanical properties of the bulk.

Nd-Fe-B permanent magnets are known industrially for their high performance and used, e. g. in Mössbauer spectrometers, but thus have been found to be extremely susceptible to corrosion. In humid atmospheres the Nd-Fe-B alloy shows approximately four times the corrosion activity of mild steel. It was shown by ARMSTRONG et al. [5.2781], that surface melting using a KrF excimer laser, and subsequent self-quenching helps to protect the magnet. This effect was attributed to the formation of an amorphous surface layer  $\sim 1$   $\mu\text{m}$  on an Nd<sub>15</sub>Fe<sub>77</sub>B<sub>8</sub> ingot by melting with nanosecond UV laser pulses and by the subsequent rapid quench of the molten surface layer. It was shown that laser glazing could provide a direct method of corrosion protection without the need for metal or plastic coatings. The layer had better corrosion properties than these due to the lack of grain boundaries and the absence of galvanic effects normally arising from a multiphase structure.

#### 5.4. Spin Texture Studies of Surface Layers

The intensity (area) ratios of the Mössbauer spectral lines always differ from the theoretical values for random orientation. This is caused mainly by the Goldansky-Karyagin effect, saturation effects and by texture. Some times Mössbauer spectroscopy is the only method of such texture studies.

Texture may be envisaged as a preferred orientation of an ensemble. The ensemble may be made up of spins, atoms, domains, crystallites. The occurrence of texture is a general phenomenon in nature. Processes of growth, precipitation, crystallization, especially in magnetic or electric fields, and plastic deformation, all lead to the appearance of texture. Mössbauer spectroscopy conveys information on spin texture which, in turn, provides information on both magnetic anisotropy and the texture of the principal EFG axes which reflects crystallographic features of the solid state structure.

Texture studies by Mössbauer spectroscopy started with a development of the theory of the angular dependence of the line intensities. First experiments were performed on the interactions of polarized  $\gamma$ -radiation with matter [5.279-282]. To detect texture there is no need to use sources of polarized  $\gamma$ -radiation [5.283],

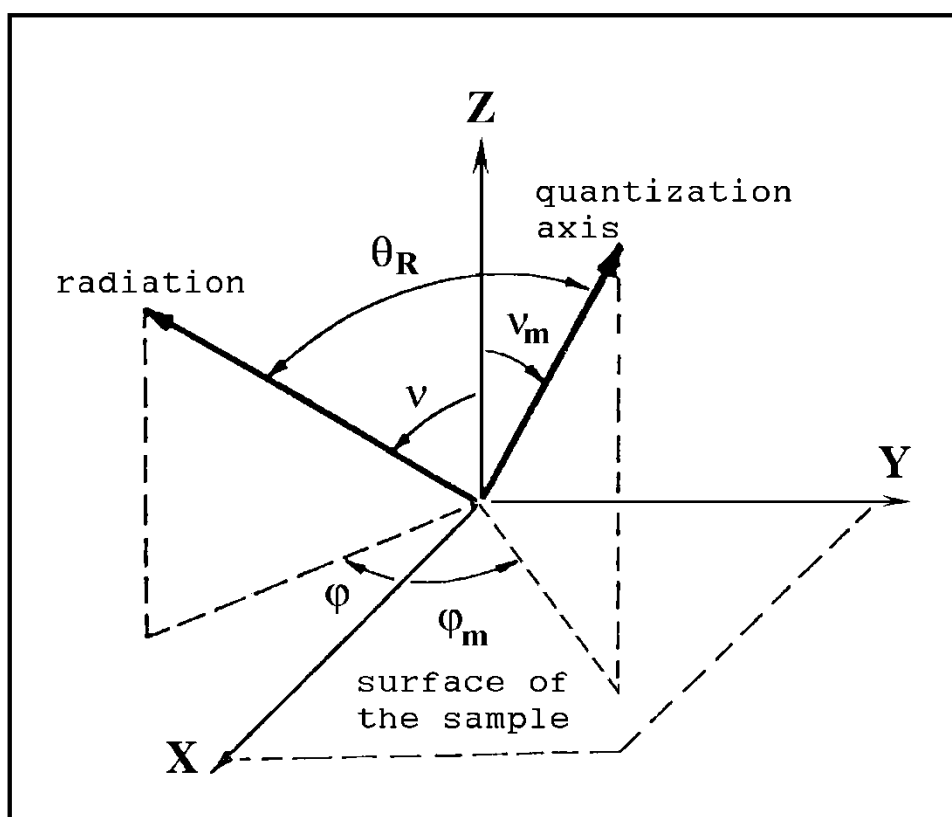


Fig.5.20 Coordinate system in texture studies.  $v$ ,  $\varphi$  and  $v_m$ ,  $\varphi_m$  are the angles specifying the direction of the incident radiation and quantization axis.

so in theoretical discussions and experimental techniques as well as in Mössbauer spectra interpretations we shall assume the use of unpolarized radiation.

Let us use a coordinate system related to the sample (Fig.5.20). The direction of Mössbauer quanta is specified by the angles  $\nu$  and  $\varphi$ , and the direction of the quantization axis is determined by the angles  $\nu_m$  and  $\varphi_m$ . Let us restrict ourselves to a pure dipole or electric quadrupole interactions (or  $H_{\text{eff}} \gg eqQ$  and  $H_{\text{eff}} \ll eqQ$ ), and assume an axial symmetry to be present. The observed spectrum will be determined by the mutual orientation of the two directions (i.e. by the  $\theta_R$  angle) of the radiation incident on the sample (or leaving it) and of the quantization axis in the layer under investigation. Let the sample be a thin single crystal with an isotropic  $f'$  factor, and the quantization axis be at angles  $\nu_m, \varphi_m$  to its surface. By an analysis of the experimental data, the ratio  $R'(\nu, \varphi, \nu_m, \varphi_m)$  of the areas under the lines of the Mössbauer spectra need to be found. For magnetic dipole interactions expression (1.31) is written in the form

$$R'_m(\nu, \varphi, \nu_m, \varphi_m) = \frac{A_{2,5}}{A_{3,4}} = \frac{4(1 - \cos^2 \theta_R)}{1 + \cos^2 \theta_R}, \quad (5.4)$$

where  $\cos \theta_R$  is determined by the equation:

$$\begin{aligned} \cos \theta_R(\nu, \varphi, \nu_m, \varphi_m) = & \sin \nu_m \sin \nu \cos \varphi_m \cos \varphi \\ & + \sin \nu_m \sin \nu \sin \varphi_m \sin \varphi + \cos \nu_m \cos \nu. \end{aligned}$$

In a polycrystalline sample with a random orientation of the crystallites and an isotropic  $f'$  factor the intensity ratios of the Mössbauer lines due to the averaging over all directions are  $R'_g = 1$  (see 1.30),  $R'_m = 2$ . The anisotropy of atomic vibrations in a solid may lead to  $R'_g \neq 1$ , or  $R'_m \neq 2$  even for a non-textured polycrystalline sample, consisting of randomly oriented crystallites - i.e., to the Goldansky- Karyagin effect (GKE). Thus, deviations of the  $R'_g$  values from unity, and  $R'_m$  values from two may be due to both texture of the sample and GKE.

For the GKE, the result of averaging is independent of the sample orientation with respect to the incident radiation. If on rotation of the polycrystalline sample relative to the  $\gamma$ -ray propagation the  $R'_g(R'_m)$  values change, then there is either a superposition of texture and the GKE, or texture only. To separate the contributions, measurements must be performed at different temperatures and different sample orientations.



The problem of texture determination by Mössbauer spectroscopy is to find a distribution function  $D(\vartheta_m, \varphi_m)$  which describes the distribution of the relative volumes wherein  $H_{\text{eff}}$  or the EFG are oriented along the  $(\vartheta_m, \varphi_m)$  direction in a unit solid angle (see Fig.5.20). In an ideal polycrystal the quantization axis directions are randomly distributed, hence the distribution function  $D(\vartheta_m, \varphi_m)$  should describe a sphere. For an ideal single crystal this function reduces to a set of  $\delta$ -functions, whose number does not exceed the number of anisotropy axes of the crystal. In real polycrystals (due to various reasons) directions of preferred orientation appear. Let us introduce a normalization condition for the  $D(\vartheta_m, \varphi_m)$  function:

$$\int_0^{2\pi} d\varphi_m \int_0^{\pi} D(\vartheta_m, \varphi_m) \sin \vartheta_m d\vartheta_m = 1 \quad (5.5)$$

and expand it into a series with respect to spherical harmonics

$$D(\vartheta_m, \varphi_m) = \sum_{l=0}^{\infty} \sum_{k=-l}^l D_{l,k} Y_{l,k}(\vartheta_m, \varphi_m) \quad (5.6)$$

where  $Y_{l,k}(\vartheta_m, \varphi_m)$  - is the real part of spherical harmonics and

$$D_{l,k} = \int_{\Omega} D(\vartheta_m, \varphi_m) Y_{l,k}(\vartheta_m, \varphi_m) d\Omega$$

where  $Y_{l,k}(\vartheta_m, \varphi_m)$  - is the real part of spherical harmonics and

- are the expansion coefficients. For a thin polycrystalline textured sample the ratios of areas under the Mössbauer lines are written in a more complicated expression than (5.4):

$$\begin{aligned} R_g(\vartheta, \varphi) &= \frac{1 + \langle \cos^2 \theta_R \rangle(\vartheta, \varphi)}{5/3 - \langle \cos^2 \theta_R \rangle(\vartheta, \varphi)} ; \\ R_m(\vartheta, \varphi) &= \frac{4 \left[ 1 + \langle \cos^2 \theta_R \rangle(\vartheta, \varphi) \right]}{1 + \langle \cos^2 \theta_R \rangle(\vartheta, \varphi)} ; \end{aligned} \quad (5.7)$$

where

$$\begin{aligned}
\langle \cos^2 \theta_R \rangle(\vartheta, \varphi) &= \int_0^{2\pi} d\varphi_m \int_0^\pi \cos^2 \theta_R(\vartheta, \varphi, \vartheta_m, \varphi_m) D(\vartheta_m, \varphi_m) \sin \vartheta_m d\vartheta_m \\
&= c_1 \sin^2 \vartheta \cos^2 \varphi + c_2 \sin^2 \vartheta \sin^2 \varphi + c_3 \cos^2 \vartheta \\
&\quad + c_4 \sin^2 \vartheta \cos \varphi \sin \varphi + c_5 \sin \vartheta \cos \vartheta \cos \varphi + c_6 \sin \vartheta \cos \vartheta \sin \varphi
\end{aligned}
\tag{5.8}$$

The  $c_i$  coefficients are obtained from the simultaneous linear equations (5.8) with

$$c_1 + c_2 + c_3 = 1. \tag{5.9}$$

Without any normalization the  $\langle \cos^2 \theta_R \rangle(\vartheta, \varphi)$  values and  $D_{l,k}$  coefficients have to be found from experimental data for five sample orientations  $\vartheta, \varphi$ . If (5.9) is satisfied, four sample orientation are needed.

Hence, an expression can be written for the  $D(\vartheta_m, \varphi_m)$  function which is often called the minimal texture  $D_{\min}(\vartheta_m, \varphi_m)$ . It contains the  $D_{l,k}$  coefficients with  $l = 0, 2$  and  $k = 0, 1, 2$ . Taking the above into consideration, instead of (5.6) we can use a simpler expression for  $D(\vartheta_m, \varphi_m)$ :

$$D_{\min}(\vartheta_m, \varphi_m) = \frac{1}{4\pi} + \sum_{k=-2}^{k=2} D_{2,k} Y_{2,k}(\vartheta_m, \varphi_m)$$

The idea is that it is necessary and sufficient to leave only six terms in the expansion series to describe the experimental Mössbauer data, since only the spin projections onto the  $\gamma$ -ray propagation direction may be determined. The minimal texture so determined may sometimes become negative for  $\vartheta_m, \varphi_m$  values, however this is physically impossible because  $D_{\min}(\vartheta_m, \varphi_m) > 0$ . In this case it can be made positive by a proper choice of the corresponding expansion coefficients  $D_{l,k}$ , so as to have  $D_{\min}(\vartheta_m, \varphi_m) \geq 0$  at any  $\vartheta_m$  and  $\varphi_m$  values.

Hence, to obtain a function of texture in the general case, Mössbauer spectra need to be recorded at five sets of angles  $\vartheta, \varphi$ . Different experimental geometries are presented in Figs.5.21 and 5.22. The conventional transmission geometry is shown in Fig.5.21 which allows texture in thin films and foils to be determined. To study the

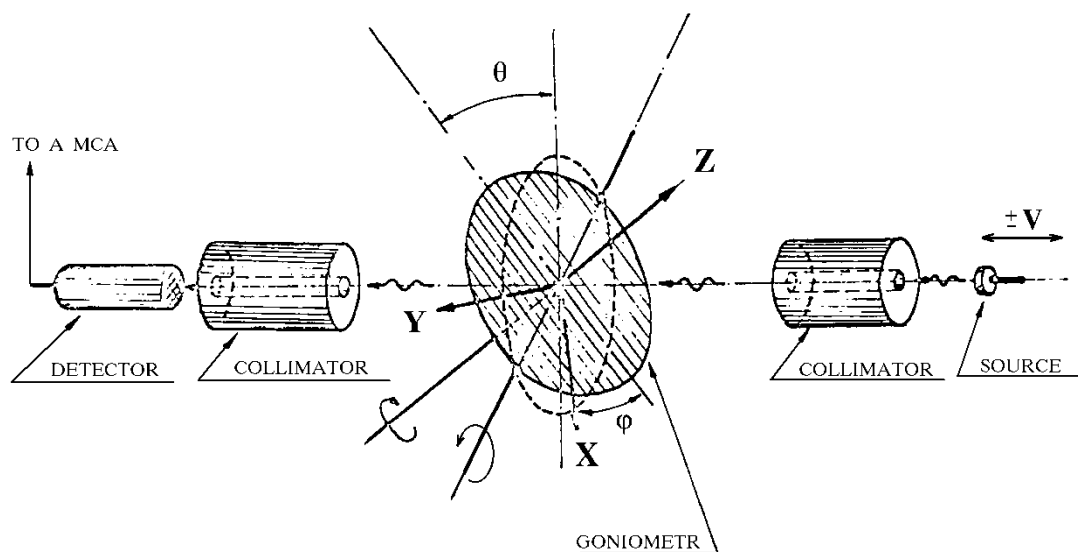


Fig.5.21 Experimental arrangement for texture studies in a transmission geometry.

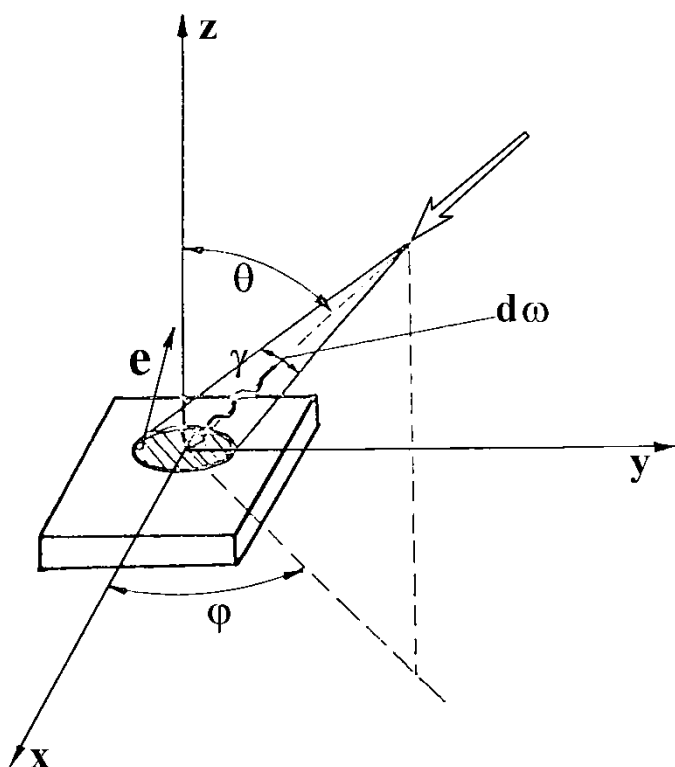


Fig.5.22a Experimental arrangement for texture studies in a scattering geometry for any angle of incidence. The surface of the sample is in the XY plane.

surface layer texture in bulk substances the geometry illustrated by Fig.5.22 should be used. Directions of the incident radiation are denoted by A,B,C,D. For the series of

spectra obtained, areas under the lines should be determined and the ratios calculated from (5.4) are used to calculate the  $\langle \cos^2 \theta_R \rangle(\nu, \varphi)$  values. The simultaneous equations (5.8) can be solved and the  $c_i$  coefficients may be found.

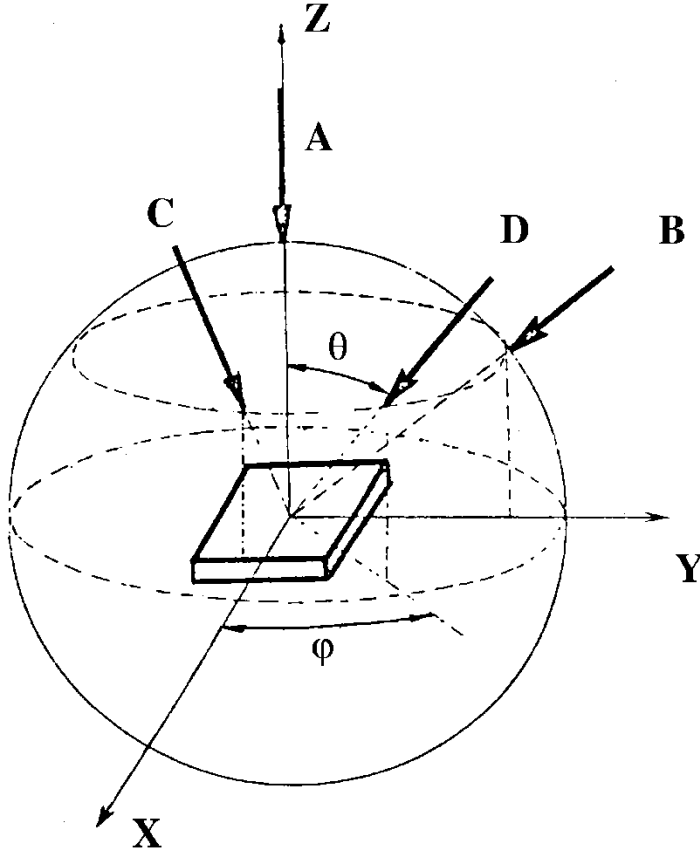


Fig.5.22b A typical complete set of directions for the determination of spin texture.

The technique of determining  $D_{\min}(\nu_m, \varphi_m)$  can be simplified if the texture principal axes system is known. There are many objects for which it may be known from the preparation conditions (amorphous alloy bands, thin foil, forged samples, etc.). Let us use the coordinate system, where the direction of the incident Mössbauer quanta and the directions of the quantization axes are specified by the angles  $\theta$  and  $\Phi$ , and  $\theta_m$  and  $\varphi_m$ , respectively. Equation (5.8) reduces substantially:

$$\langle \cos^2 \theta_R \rangle(\theta, \varphi) = C_1 \sin^2 \theta \cos^2 \varphi + C_2 \sin^2 \theta \sin^2 \varphi + C_3 \cos^2 \theta, \quad (5.10)$$

where

$$C_1 = \langle \sin^2 \theta_m \cos^2 \varphi_m \rangle, \quad C_2 = \langle \sin^2 \theta_m \sin^2 \varphi_m \rangle,$$

$$C_3 = \langle \cos^2 \theta_m \rangle, \quad C_1, C_2, C_3 \geq 0$$

and the normalization condition still holds. Thus, only two  $C_i$  parameters remain

independent, and the number of measurements for their determination reduces to two. The  $c_i$  coefficients in (5.8) should be distinguished from the  $C_i$  coefficients in (5.10). In the principal axes system the function of texture is written in the form

$$\begin{aligned}
 D_{\min}(\theta_m, \phi_m) &= \frac{1}{4\pi} + D_{2,0} Y_{2,0}(\theta_m, \phi_m) + D_{2,2} Y_{2,2}(\theta_m, \phi_m) \\
 &= \frac{1}{4\pi} \left[ 1 + \frac{15}{4} \left[ c_3 - \frac{1}{3} \right] (3 \cos^2 \theta_m - 1) \right. \\
 &\quad \left. + \frac{15}{2} (c_1 - c_2) \sin^2 \theta_m \cos 2\phi_m \right]. \quad (5.11)
 \end{aligned}$$

Studies of samples with a known principal axes system using Mössbauer spectroscopy involve a simpler discrete method of texture description. The function  $D_{\min}(\theta_m, \phi_m)$  which is a monotonous function of angles, is represented by a vector, whose orientations lie in one quadrant which is determined by the positive direction of the coordinate axes. In practice it is not the vector that is used, but a function which is represented by a superposition of three orthogonal  $\delta$ -functions directed along the principal axes

$$D_{\min}(\theta_m, \phi_m) = \frac{1}{4\pi} \left[ N_x \frac{\delta(\sin \theta_m^x)}{\sin \theta_m^x} + N_y \frac{\delta(\sin \theta_m^y)}{\sin \theta_m^y} + N_z \frac{\delta(\sin \theta_m^z)}{\sin \theta_m^z} \right] \quad (5.12)$$

where  $\theta_m^{x,y,z}$  - are the angles between the hypothetical vector's direction and the coordinate axes. This discrete description is equivalent to the continuous one in the sense that the angular dependences of the line intensity ratios remain the same as in the description method based on the continuous texture distribution function. The values of  $N_x$ ,  $N_y$ ,  $N_z$  are interpreted as spin populations along the corresponding axes and are found from the following expression

$$\langle \cos^2 \theta_R \rangle(\theta, \varphi) = N_x \sin^2 \theta \cos^2 \varphi + N_y \sin^2 \theta \sin^2 \varphi + N_z \cos^2 \theta. \quad (5.13)$$

If there is hypothesis on the principal axes system or the axes are known, only two independent experiments are required to determine  $N_x$ ,  $N_y$  and  $N_z$ . However it is more convenient to make three measurements (see Fig.5.22). The choice of the A,B,C directions is based on the analysis of expression (5.13):

A ( $\theta = 0^\circ$ ,  $\varphi$  - any angle) ; B ( $\theta = 54^\circ$ ,  $\varphi = 90^\circ$ ) ;

C ( $\theta = 54^\circ$ ,  $\varphi = 0^\circ$ ) . For the direction chosen:

$$\langle \cos^2 \theta_R \rangle_B + \langle \cos^2 \theta_R \rangle_C = 2/3 . \quad (5.14)$$

The equation can be used to check the correctness of the area ratio determinations from the experimental spectra. Equation (5.14) is independent of the thickness of the analyzed layer since the effective path length for the Mössbauer radiation is the same.

The considerations outlined above make it possible for textured samples to give spectra which are free of texture effects. It is of prime importance for phase analysis, when, for example, line asymmetry of the spectra from a two-phase sample is attributed to an extra phase. To obtain the spectra, the following procedures can be suggested. If the principal axes are known, and the  $\gamma$ -radiation is incident in the direction D( $\theta = 54.7^\circ$ ,  $\varphi = 45^\circ$ ), the required spectrum is recorded. If only the principal axis z direction is known, the two spectra should be added recorded at the same  $\theta$  angle value of  $54.7^\circ$ . Any  $\varphi_1$  value may be taken, and the  $\varphi_2$  value is  $\varphi_1 + \pi/2$ . Generally, four spectra should be added, corresponding to  $\theta = 54.7^\circ$ , with any  $\varphi_1$  value, and

$$\varphi_2 = \varphi_1 + \pi/2 , \quad \varphi_3 = \varphi_1 + \pi , \quad \varphi_4 = \varphi_1 + 3\pi/2 .$$

The possibilities of the method may be illustrated by an example of studies on surface spin texture in  $\alpha$ -Fe foils and in an amorphous alloy  $\text{Fe}_{80}\text{B}_{20}$  [5.284]. In accordance with the foil preparation, assume that the z principal axis is perpendicular to the foil surface. Let the x-axis be along the band. The Mössbauer spectra of an  $\alpha$ -Fe foil obtained in transmission geometry and CEM spectra are given in Fig.5.23. The results of the treatment of the spectra are presented in Table 5.6. It is seen that the foil has a strong spin texture in the (x 0 y) plane. More than 80 % of the magnetic moments are oriented in this plane. Surface texture is more pronounced than bulk texture. This may be explained by two effects: external stresses that have originated from the preparation of the foil and are described by a stress tensor  $\sigma_{ik}$ ; and the tendency of the magnetic domains to be directed parallel to the sample surface to minimize the energy of demagnetization.

In the (x 0 y) plane the spin populations along the x axis are higher than along the y axis, both for the surface and for the bulk, which is explained by the induced magnetic anisotropy spreaded over the entire foil volume. If there are such inhomogeneities as swells, draws, inclusions in the surface layer, then the appearance of magnetic dissipation fields increasing the z-component of the spin orientation results. This allows the use of CEMS for quality monitoring of the surface of ferromagnetics.

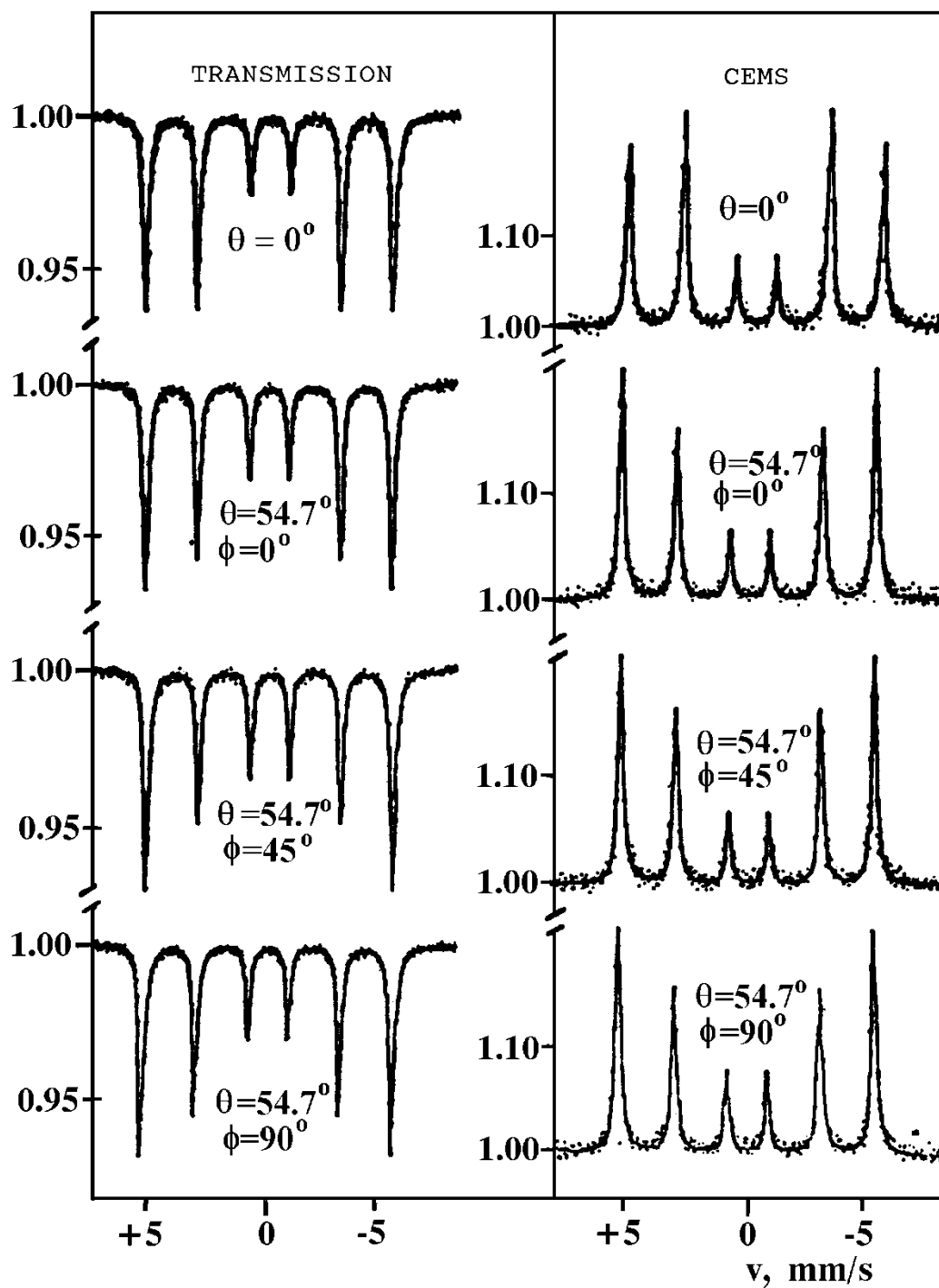


Fig.5.23 Mössbauer spectra from an  $\alpha$ -Fe foil 2  $\mu$ m thick.

It is known that spin texture in metglasses ribbon is extremely sensitive to strains and stresses [5.283]. Partly this is consistent with the very low of crystalline anisotropy in these materials. The observed volume spin texture depends upon the width of the ribbons and varies from the center to the edges [5.283].

The results of a study of the classical amorphous alloy  $\text{Fe}_{80}\text{B}_{20}$  are presented in Fig.5.24 and in Table 5.6. The study enabled BELOZERSKI and SEMENOV [5.284] to compare the results for the contact with the quenching support and non-contact surfaces of the band. These differences in magnetic properties of the surfaces are due to the different cooling conditions during the band production. A mathematical evaluation of the Mössbauer spectra of the band has revealed a strong uniaxial anisotropy along the y-axis (the y-axis is perpendicular to the rolling direction). This is explained by the compressive stresses along the band, the stresses on the non-contact surface of the band being much higher. Similar internal mechanical stresses occur in most amorphous alloys (especially upon quenching from the melt) and greatly affect the surface layer (Fig.5.24). To remove the anisotropy, the alloy was annealed under vacuum at 300°C for 2 hrs. Mössbauer spectra of the alloy after the annealing show the absence of anisotropy in the plane of the band ( $N_x = N_y$ ).

Table 5.6  
Parameters characterizing the discrete method of texture description

Sample	$\theta,$	$\phi,$	$\langle \cos^2 \Theta_R \rangle$	Spin populations along the principal axes		
				$N_x$	$N_y$	$N_z$
			$\pm 0.01$	$\pm 0.03$	$\pm 0.03$	$\pm 0.03$
$\alpha$ -Fe foil (surface)	0	—	0.070	0.501	0.420	0.070
	54.7	0	0.303			
	54.7	45	0.313			
$\alpha$ -Fe foil (trans-mission)	54.7	90	0.354	0.407	0.386	0.207
	0	—	0.207			
	54.7	0	0.313			
Noncontact surface	54.7	45	0.407	0.145	0.832	0.020
	54.7	90	0.327			
	0	—	0.020			
Contact surface	54.7	0	0.108	0.349	0.637	0.014
	54.7	45	0.363			
	54.7	90	0.538			
	0	—	0.014			
	54.7	0	0.271			
	54.7	45	0.349			
	54.7	90	0.384			



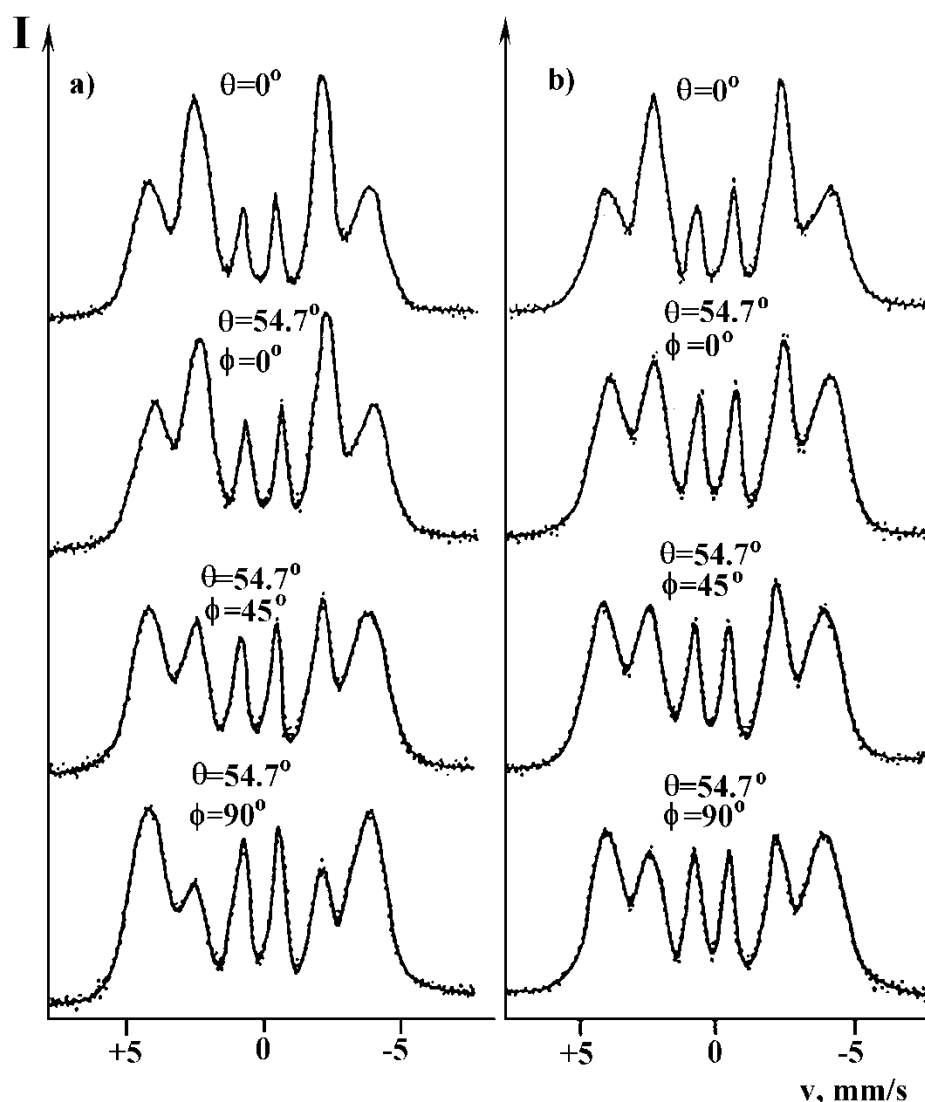


Fig.5.24 Mössbauer spectra from a band of an amorphous alloy: a - contact surface, b - non-contact surface.

Plots of the  $D(\theta_m, \varphi_m)$  functions are given in Fig.5.25 for the contact and non-contact surfaces of the band. A remarkable feature of these bands, in accordance with the plots above, is the strong magnetic anisotropy. Consideration of Fig.5.24 shows that the anisotropy is along the y-axis. Comparing the plots with those of the  $D(\theta_m, \varphi_m)$  function for the  $\alpha$ -Fe foil surface (Fig.5.25c), it is seen that the z-component of the spin population along the principal axes near the surface of amorphous alloys is several times less. Hence, the magnetic dissipation fields on the alloy surface are significantly weaker. This is indicative of the high magnetic quality of the surface of the  $\text{Fe}_{80}\text{B}_{20}$  alloy. The  $p(H_{\text{eff}})$  distributions (see Sect.4.6) coincide for the two surfaces of the amorphous alloy band. This means that the local environment of Fe atoms is the same for the two sides of the band, i.e., there is no difference in the concentrations of Fe

atoms and the metalloid atoms. BOURROUS and VARRET [5.285] studied the change of the out-of-plane spin population with annealing of a Fe-Cr-P-C amorphous ribbon. The progressive curvature and increasing perpendicular magnetic anisotropy of meltspun ribbons was observed during annealing. These results were explained by irreversible inhomogeneous structural relaxation in the Fe-Cr-P-C alloy.

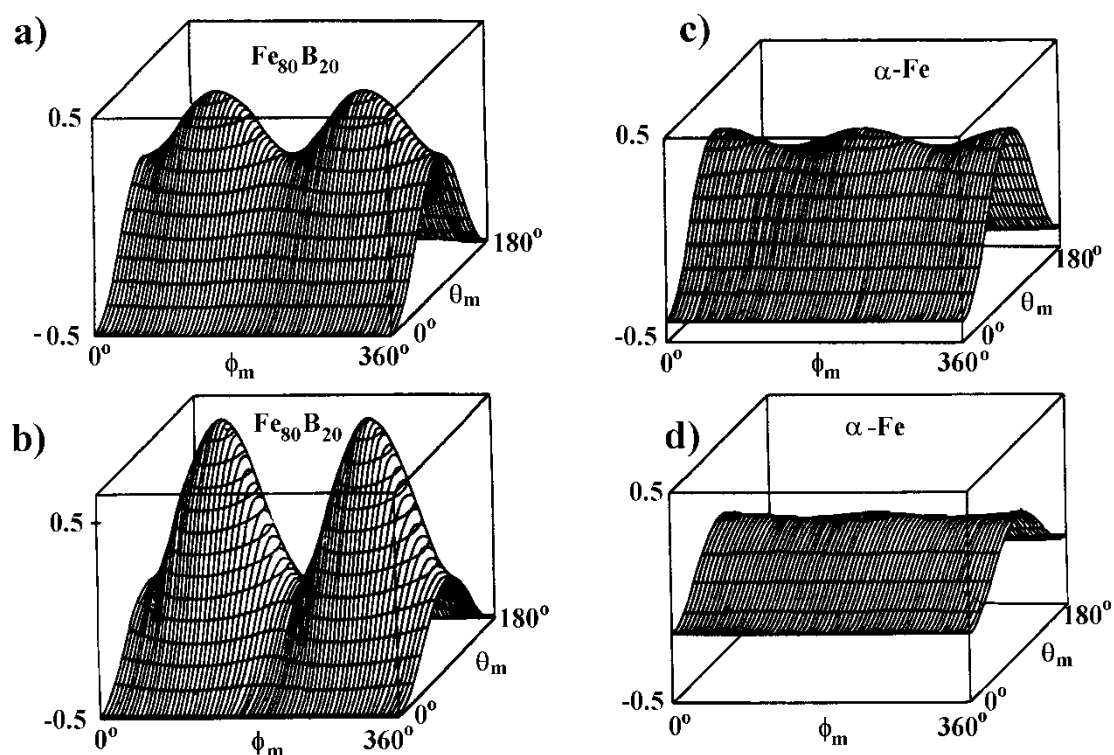


Fig.5.25 Texture distribution functions  $D(\theta_m, \Phi_m)$ . a,b - band of amorphous alloy  $\text{Fe}_{80}\text{B}_{20}$  (a - contact surface, b - non-contact surface); c,d -  $\alpha\text{-Fe}$  foil (c - surface (CEMS), d - transmission experiment).

The magnetic texture of a ribbon combines the influence of demagnetizing field and stresses due to the melt-spinning technique. Other techniques are used now for producing amorphous alloys. Sputtered samples is a simpler case since the low deposition rate, the clean atmosphere and substrate promote homogeneous quenching conditions, from which an axial magnetic texture may be expected [5.286]. However, in-plane magnetic texture has been detected in a sputtered sample of metallic glass  $\text{Fe}_{60}\text{B}_{40}$ . Another technique is electrochemical deposition. ZEMCIK et al. [5.287] investigated electrodeposited FeP amorphous system. The aim was to get information about the magnetic anisotropy of electrochemically made Fe-P and Fe-Ni-P amorphous alloys and about its correlation with the structure. The Fe-P foils exhibit lower magnetic anisotropy. In the samples are alloyed with Ni, the  $H_{\text{eff}}$  orientation is nearest to the normal.

Mössbauer effect on admixture  $^{57}\text{Fe}$  atoms may also be used to study the development of texture in some pure metal matrices. An example is the impurity effect on cube texture in pure aluminium foils reported in [5.288]. The samples containing ~ 0.0007 wt.% Fe were subjected to the same heat treatments as for texture observations in pure Al. The results suggest that the concentration of solute atoms in the matrix is the dominant factor of the suppression of the development of texture.

The implantation process itself may determine texture of samples. FAYEULLE et al. [5.289] investigated implantation in iron and steels of various crystallographic structures and compositions performed at 20°C with a fluence of  $2 \times 10^{17} \text{ N}^+ \text{ cm}^{-2}$ . Mössbauer spectra, showing texture developed after implantation, are presented in Fig.5.26. For nitride or carbonitride formed during the implantation at room temperature the c axis is preferentially oriented parallel to the surface plane. This texture appears on ferritic, martensitic as well as on austenitic steels. It is a very general phenomenon independent of the material and being determined only by implantation. The origin of texture generally observed in the case of nitrogen implantation at 20°C with a fluence of  $2 \times 10^{17} \text{ N}^+ \text{ cm}^{-2}$  could be compressive stresses that exist in planes parallel to the surface. These stresses could favour the nitride growth through the crystallographic relations identified from the initial matrix planes, these planes being correctly oriented in regard of strains [5.289].

A channeling mechanisms, if they exist may determine the preferential orientation of the sample after implantation. ASANO et al. [5.290] investigated magnetic anisotropy induced by ion-beam incidence in  $\text{Fe}_x\text{N}$  film and found that the low energy nitrogen ion bombardment with a large angle of incidence of the ion beam induced the magnetic anisotropy in the prepared  $\text{Fe}_x\text{N}$  films. The direction of appeared anisotropy is transverse to the incidence plane of the ion beam. The value of anisotropy may be compared to the magnetic anisotropy induced by the oblique incidence evaporation, whose easy axis was parallel to the incidence plane of iron vapour.

Thus, by Mössbauer spectroscopy it is possible to study surface spin texture in crystalline and amorphous samples of any thickness and to obtain the spatial spin orientation and re-orientation caused by external effects. The above techniques allow surface spin texture studies on direct mechanical stresses to be conducted. An important application of the technique is the determination of the easy magnetization axes and their re-orientation by thermal and mechanical effects.

If the hyperfine field spatial orientation obtained by Mössbauer spectroscopy possesses a mirror symmetry relative to the three principal planes, then two independent measurements are needed for its determination, if the orientation of the principal planes is known. Five measurements are required if the orientation is unknown. The result is not changed if a polarized  $\gamma$ -radiation is used. Therefore, only the averaged spatial orientation of the hyperfine field can be found. This amounts to the determination of the principal axes orientations and the spin populations along them and corresponds to the discrete model. However, in Mössbauer spectroscopy "continuous" models are considered as being more physical. Most widely used is the representation of the  $D(\theta_m, \phi_m)$  function as a sum of spherical harmonics.

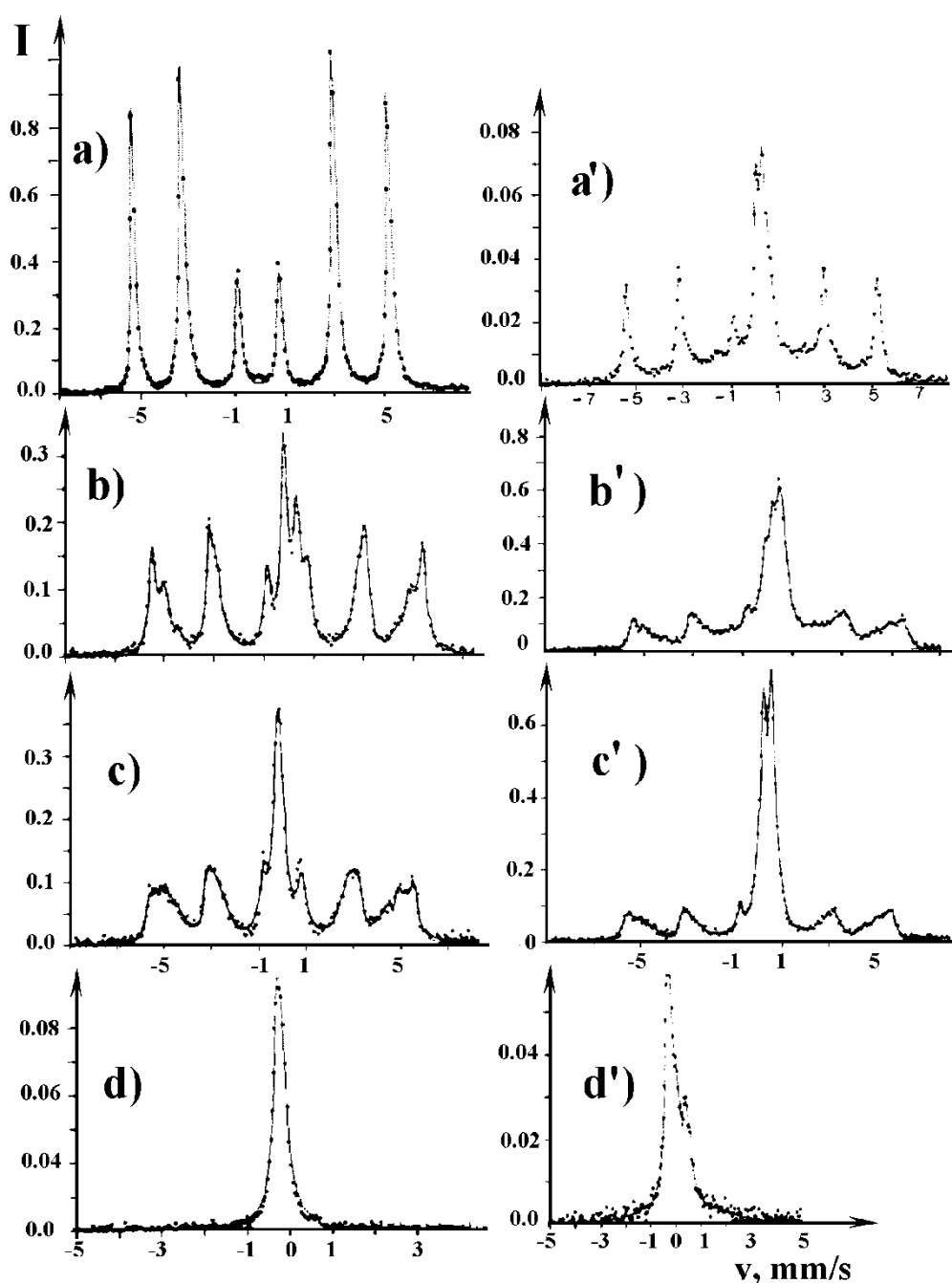


Fig.5.26. Mössbauer spectra of some non implanted specimens (a,b,c,d) and implanted (at 20°C with a fluence of  $2 \times 10^{17} \text{ N}^+ \text{ cm}^{-2}$ ) specimens (a',b',c',d') from [5.289]. a and a' are iron. b and b' - Z200C13 steel (tempered martensite, 2.1 C, 0.34 Si, 0.35 Mn, 11.1 Cr, 0.2 V). c and c' - 1841 steel (tempered martensite: 0.83 C, 0.36 Si, 0.3 Mn, 0.17 Ni, 4.1 Cr, 4.4 Co, 17.2 W, 1.3 V). d and d' - 1810 steel (austenite:  $1.5 \cdot 10^{-5}$  C, 10 Ni, 18 Cr). Chemical compositions are in wt.%.

## 5.5 Some Other Applications

The applications of Mössbauer spectroscopy in surface studies considered above do not exhaust all the resources of the technique. Some other applications should be mentioned. The essential result of the methodology development of Mössbauer spectroscopy, CEMS in particular, in the 1980's is the use of these techniques for studies in ultra high vacuum with a depth resolution of about one monolayer. The same depth selectivity can be achieved on analyzing samples placed in nearly any gas medium. Mössbauer spectroscopy allows solid/solid and liquid/solid interfaces, as well as clusters, monolayers and isolated atoms on internal surfaces of porous materials, to be studied. Various modifications of the method allow even the surface of fine particles placed on supports (e.g. porous zeolites, alumina or silica) to be investigated. Hence, when other fields of the Mössbauer effect applications are considered, the first one to be mentioned is the application in catalysis studies and ultra fine particles studies (with emphasis on superparamagnetism).

Catalysts play an important role in modern society since they are involved in the production of most chemicals. The use of catalysts is one of the important ways to reduce the environmental pollution caused by combustion of fossil fuels. Applications of Mössbauer spectroscopy in catalysis are limited mainly to catalyst characterization. If the catalyst contains a suitable Mössbauer isotope, the technique provides a wealth of useful and often unique information. It is fortunate that iron and cobalt are extremely important catalytic materials, with a much more complex chemistry than noble metal catalysts. Now Mössbauer spectroscopy has contributed significantly to the current understanding of catalysts used in ammonia synthesis, hydrotreating and CO hydrogenation. There are a number of reviews on the application of Mössbauer spectroscopy in the field [5.291-294].

Despite the importance of catalysis in general, very little has been known about the structural and chemical state of most heterogeneous catalysts under reaction conditions. Mössbauer spectroscopy gives us the information relevant to the active state of the catalyst. First of all, it allows *in situ* studies under realistic conditions since the structure of catalysts is in dynamic equilibrium with the reaction mixture. Secondly, the technique provides information on structures without limitation on the long-range order. It is important since many catalyst systems contain X-ray amorphous phases. Then, it is possible to separate signals from various phases and chemical states since catalysts are usually multiphasic in nature. The same situation was discussed in Sect.5.1. Finally, the method allows a simultaneous investigation of the catalytic activity and the bulk and surface structures of the catalyst.

The most catalysts studies were conducted with the use of  $^{57}\text{Fe}$  Mössbauer spectroscopy. For example, BERRY et.al. [5.295, 296] investigated iron-zirconium and iron-cerium oxide catalysts and also titania-supported iron, iron-ruthenium and iron-iridium catalysts, known to be catalytically active for the hydrogenation of carbon monoxide. In this studies unsupported iron-zirconium oxide catalysts have been prepared by the calcination in air of precipitates containing 15 mole % iron. The

Mössbauer spectra recorded *in situ* following the pretreatment of the solids in nitrogen, carbon monoxide and hydrogen showed that little change is induced in the catalysts under such conditions. The pretreated catalysts were unchanged by exposure to a 1 : 1 mixture of carbon monoxide and hydrogen at 270°C and 1 atmosphere pressure but were partially converted to iron carbide when used for the hydrogenation of carbon monoxide at 330°C and at 20 atmosphere pressure. The initial calcination of the precipitates in air during the formation of iron-cerium oxide catalysts induces phase segregation and the formation of small concentrations of large particle  $\alpha$ -iron (III) oxide in combination with cerium dioxide.

Titania-supported iron catalysts were prepared by the reduction in hydrogen of titania-supported iron oxide formed by impregnation and dehydration methods. Iron (III) in iron oxide supported on high surface area titania (240 m<sup>2</sup>/g) was found to be more resistant to reduction in hydrogen at a given temperature than the materials prepared on lower surface area titania. The results are related to the different dispersion of iron which can be attained on titania of differing surface area.

MAKSIMOV et al. [5.297] studied selective Fischer-Tropsch catalysts synthesized by the destruction of bimetallic carbonyl complexes on an activated  $\gamma$ -Al<sub>2</sub>O<sub>3</sub> support. The analysis of the mechanism of formation of surface-modifying metallic clusters allows at least three types of active surface centres to be distinguished: hydroxyl groups, oxygen vacancies and associates of vacancies. The problem of formation and stabilization of small metallic clusters for the production of active and selective Fischer-Tropsch catalysts was investigated in [5.298]. It was shown that the catalysts with 2 - 6 w.% of iron exhibited the best selectivity in alkylaromatic synthesis reaching 90 % of the total yield of hydrocarbons. At higher loading the process selectivity becomes much more poor. An addition to the catalyst of some amount of zirconium secures small iron clusters and promotes the process selectivity.

For the understanding of the state of a working catalyst one needs the information about the state of the system before reaction. In this connection the influence of promoters on the physical properties of iron zeolites catalysts was thoroughly investigated by a number of research groups. For example, SCHMIDT [5.299] showed that a correlation exists between the overall Sanderson electronegativity of a structural promoter and the stability of the bond strength between iron atoms in small clusters and carbon monoxide. The big advantage of Mössbauer spectroscopy as compared to the methods such as ESCA, AES is in the possibility of performing high pressure *in situ* measurements under technical relevant reaction conditions in the steady state of a working catalyst. Cation-exchanging zeolites may have all the cations located at the internal surfaces of the zeolites structure, and as such this may be an interesting model system for studies of chemisorption.

Mössbauer emission spectroscopy with its high sensitivity is an excellent *in situ* technique for investigating the composition and structure of catalysts. Hydrotreating catalysts are widely applied to remove heteroatoms from crude oil. Although these catalysts are only used in the sulfidic state, important information about their structure can be obtained from the study of the oxidic catalyst precursors. Therefore, both emission and transmission techniques have been applied to examine cobalt- and iron-containing hydrotreating catalyst precursors, respectively [5.300]. *In situ* Mössbauer emission spectroscopy has also been used [5.301] to study the type of phases present in sulfided activated carbon-supported Co and Co-Mo hydrodesulfurization catalysts.

Other Mössbauer isotopes were also used in catalysts studies. For example, the state of iridium and platinum in supported catalysts was investigated [5.302] by means of the 73 keV resonance in  $^{193}\text{Ir}$  and source experiments using the 77 keV resonance in  $^{197}\text{Au}$ .  $^{99}\text{Ru}$ ,  $^{119}\text{Sn}$ ,  $^{121}\text{Sb}$ , and  $^{151}\text{Eu}$  are also important Mössbauer isotopes for studies of catalysts and surfaces.

Mössbauer spectroscopy provides the following information on catalysts under realistic conditions [5.294]: phase identification, determination of oxidation state structure information, particle size determination, kinetics of bulk transformations. However, Mössbauer spectroscopy has one limitation in common with other *in situ* techniques: the most desirable information from a fundamental point of view, namely the atomic composition and structure of the catalytically active surface, cannot be obtained.

Combined XAFS and Mössbauer spectroscopy can give unique structural and chemical insight into the active state of many heterogeneous catalysts. It is clear that the application of such *in situ* techniques in the future is going to play an important role in transforming catalyst development to a science based on molecular and atomic insight [5.293].

Studies on small particles, especially if a significant number of the atoms are surface atoms, is a very efficient tool for examining surface phenomena. On the surface of a spherical particle with a diameter of less than about 10 nm, more than 10 % of the atoms will be at the surface. In such studies, all types of Mössbauer spectroscopy can be used. Sometimes the application of magnetic fields to the sample during the Mössbauer spectrum recording yields valuable information about the magnetic moment of the magnetic species (atoms or particles). The magnetic moment of the particles can be determined from the field dependence of the spectra and, if the magnetization of the particles is known, the particle size can be estimated. Studies of ultra fine particles enable us to get basic solid state information: how many atoms or molecules must be in a particle so that a separate phase is formed and how many atoms or molecules must be there for the particle properties to be the same as in the bulk. In practice the structure and the electronic properties of small particles are often different from those of the bulk. In many cases this is due to interactions with the support, but intrinsic surface and interface effects may also be present. Structural and electronic information is mainly obtained from the isomer shift and the quadrupole splitting of Mössbauer spectra.

Surface information on small particles may also be obtained by enriching the surface in the Mössbauer isotope. Unfortunately detailed information about surface structures of such particles is not easily obtained since their surface structure may be complex and the situation more complicated than in studies of passive layers (see Sect.5.1).

Apart from catalysts studies two main direction in small particles studies should be mentioned: magnetism (including superparamagnetism) and surface modification of particles (including solid/solid and solid/gas interactions). It is known that the size range near or below the critical size for the formation of singledomain particles in which superior magnetic properties, unattainable in bulk solids, are realized is the size range from a few to a few tens of nanometers. The particles must be prevented from coalescing into large aggregates, and in the case of metal particles, from oxidizing. For the smallest iron particles, the magnetic anisotropy energy barrier, estimated from the superparamagnetic relaxation of the Mössbauer spectra, was much greater than that expected for magnetocrystalline anisotropy [5.303].

A dramatically enhanced magnetic coercivity as high as 2500 Oe was achieved for a magnetic granular system Fe-(SiO<sub>2</sub>) where the ultra fine Fe particles were embedded in an amorphous SiO<sub>2</sub> matrix [5.304]. Average iron granule sizes were 17-70 Å, depending on the procedure of sample preparation. These approximately equiaxial granules exist in a magnetic single-domain form because their size is smaller than the critical size for single-domain Fe particles (~200 Å). The samples coercivity was about 50 times higher than that of the bulk Fe.

Most of the studies were conducted with different iron oxides particles. The magnetic moment of the small oxide particle sample was found to be smaller than that expected from the bulk. These results were interpreted in terms of a noncollinear spin arrangement near the surface of the small particles. In the study by MORRISH et al. [5.305] Mössbauer spectra of  $\gamma$ -Fe<sub>2</sub>O<sub>3</sub> particles enriched in <sup>57</sup>Fe at the surface were obtained and a significant intensity of lines 2 and 5 in large external fields parallel to the  $\gamma$ -ray direction was found for these samples. This result unambiguously shows that the noncollinearity is a surface phenomenon. It is likely that the effect can be explained by the symmetry of the surface atoms which may favour specific spin orientations for the various types of surface sites. It has been shown that the particle morphology or a boundary surface layer of the crystallites that make up a particle is an important factor influencing the noncollinear magnetic structure in fine particles [5.306]. Mössbauer spectra of CoFe<sub>2</sub>O<sub>4</sub> particles (10-100 nm size range and up) obtained with a longitudinal magnetic applied field unambiguously establish that a noncolinear structure exists that is most pronounced for the smallest particles.



A large fraction of the atoms in ultra fine particles are exposed to the gaseous environment over the sample and the possible effects of chemisorption on surface magnetism may be estimated. Such particles are usually present on a support, and solid-solid interface effects may be important for the systems. Unfortunately in the studies of such particle systems it may often be difficult to separate surface effects from size effects.

A noncolinear spin arrangement of the iron atoms near the surface of the particles of  $\text{NiFe}_2\text{O}_4$  coated with organic molecules such as oleic acid was found by BERKOWITZ et al. [5.307]. The pinning of the surface spins is similar to that observed in  $\gamma\text{-Fe}_2\text{O}_3$  particles. It may be regarded as a strong magnetic anisotropy that is induced by the chemisorbed molecules. This pinning may also affect the total magnetic anisotropy energy constant of the particles. MORUP et al. [5.308] found that the superparamagnetic relaxation time depends on the organic species covering the surface of 6.0 nm  $\text{Fe}_3\text{O}_4$  particles exposed to acetone, oleic acid, and stearic acid. This is due to a change in the magnetic anisotropy energy constant.

The properties, composition and size of metallic and oxide particles depend on the interaction with the support. The metal salt used in the impregnation for the preparation of particles plays an important role. MEISEL and HOBERT [5.309] found that silica impregnated with  $\text{FeCl}_3$  gave large antiferromagnetic  $\alpha\text{-Fe}_2\text{O}_3$  crystals after calcination, whereas in silica impregnated with  $\text{Fe}(\text{NO}_3)_3$  or  $\text{Fe}(\text{CO})_5$  in absolute ether RUBASKOV et al. [5.310] found that after similar calcination the sample showed a paramagnetic doublet. Thorough investigation of the parameters of the Mössbauer spectra of iron oxides produced in silica gel pores by impregnation with  $\text{Fe}(\text{NO}_3)_3$  solution of different concentration was reported by BELOZERSKI and KAZAKOV [5.311]. The phase composition of supported oxides depends on the type of silica, iron concentration in solution, pretreatment and subsequent calcination.

The peculiarity of the Mössbauer spectra of fine particles is the dependence of parameters such as the recoil-free fraction, isomer shift, quadrupole splitting, and especially magnetic hyperfine field on the particle size. The problem is that the quantitative dependence of the Mössbauer parameters on the particle size is rather complex and in most cases not yet established. Atoms at the surface of small particles are in a less symmetric environment than atoms in the bulk. Therefore, the Mössbauer atoms at surfaces are expected to show quadrupole splittings different from those of the bulk.

One of the interesting phenomena determining the shape of Mössbauer spectra is superparamagnetism [5.303, 312, 313]. The particle size of magnetically ordered particles was directly determined by Morup and Topsoe [5.314] from the dependence of the spectra on the strength of the applied magnetic field at temperatures above the superparamagnetic blocking temperature. The particles size distribution may determine the shape of Mössbauer spectra of such particles [5.58].

It has been shown that the isomer shift of supported fine particles on silica was changed by the adsorption of metallic potassium. Such changes may occur upon chemisorption on the very small metallic clusters. Measurements of absolute  $f'$  factors as a function of temperature allow the motion of atoms on the inequivalent surface and inner-core sites to be examined. SMIT et al.[5.315] suggested a model of the thermal motion of atoms in fine particles where both inter- and intra- particle vibrations were taken into account. Assuming massless spring that connects the gold nearest neighbors, the intra- particle vibrations have been calculated numerically by solving the coupled equations of motion, yielding the normal mode energies and degeneracies.

Mössbauer studies of particles have found a number of applications. Redox phenomena in the iron oxide colloids induced by adsorption were studied in [5.316]. The reactivity of spinel iron oxide colloids towards adsorption has been investigated by photometry, electron microscopy, X-ray diffraction and Mössbauer spectroscopy. It is known that particles with very broad size distribution from 0.01  $\mu\text{m}$  to 50  $\mu\text{m}$  are formed during corrosion in water. Dispersed products of corrosion in a high temperature water circuit in a nuclear reactor were collected on a special filter placed in the water stream [5.317]. The phase analysis of the products allowed the optimal water characteristics to be determined in the circuits with controlled amounts of oxidizers to produce the protective oxide layers under the typical operating conditions of a water nuclear reactor.

Multilayer specimens are useful for various fundamental studies, especially of interfaces. This also allows new magnetic materials to be developed for technical applications. Due to the recent progress in thin-film fabrication techniques, such as molecular beam epitaxy, significant development has been achieved in experiments on surfaces and interfaces. One of the most up-to-date subjects in the field of magnetism concerns artificially structured multilayers [5.318].

The magnetic behaviour of the near surface or interface may differ in many aspects from that of the interior [5.319]. Mössbauer spectroscopy is quite suitable to gain depth- dependent information about a magnetic order in thin films. In general, it can be said that ground-state magnetic moments at ferromagnetic Fe surfaces and interfaces are much less different from the bulk value than found in early studies like the once famous "dead layer" model. The proposal of the dead- layer model had contributed significantly to activating the discussion of surface magnetic moments. Mössbauer spectroscopy is a technique to check the popular "dead layer" concept. Experimental results on vacuum surfaces have indicated that the top surface layers are also ferromagnetic. From Mössbauer spectra SHINJO et al. [5.320] found that even on electrodeposited surfaces dead layers were absent.

In the 1980's a considerable progress was made in studies of overlayers with a monolayer thickness and also of artificially structured multilayers. In such experiments, metallic monolayers are deposited in ultra-high vacuum on well defined non-magnetic substrates (as a rule, single crystals) and the magnetic properties are studied by applying various techniques. Mössbauer spectra have revealed that the temperature dependence of the magnetization at a surface region is different from that of the interior in various cases. In many Mössbauer studies of magnetic excitation it was assumed that the temperature dependence of the magnetic hyperfine field  $H_{\text{eff}}(T)$  was the same as of the spontaneous magnetization  $M_S(T)$ . For example, in bulk  $\alpha$ -Fe the deviation from proportionality between  $H_{\text{eff}}(T)$  and  $M_S(T)$  is smaller than 0.5 % between 0 K and 300 K. However, it is not a priori clear that relation is also valid at surfaces. CEMS and SQUID magnetometer measurements on the same 4 monolayers Fe(110) film on Ag(111) by LUGERT and BAYREUTHER [5.321] have shown that the relation indeed holds for each individual atomic layer within the experimental error of  $\pm 1$  %. It can therefore be concluded that the variation of the hyperfine field indeed measures the spin deviation at surfaces and in ultra-thin films.

KIANKA et al. [5.322] used the technique with the resolution of their measurement quite enough to catch any anomaly of the hyperfine field even if it exists only at the topmost atomic layer. The spectra for a vacuum surface of Fe(100) single crystal at low temperatures were measured. However, their results do not exhibit any significant surface anomaly as predicted by some theoretical calculations. The conclusion was that the hyperfine field at the topmost surface layer of Fe(100) in vacuum was not greatly different from the bulk. Now both CEMS and DCEMS are used to investigate epitaxially grown ultra-thin Fe layers with metastable crystalline structures. Using CEMS, a monolayer resolution was achieved by PRZYBYLSKI and GRADMANN [5.323] in observing the hyperfine field of Fe- overlayers deposited on a W single crystal (110) substrate.

As the next field of application of Mössbauer spectroscopy for surface studies, geochemistry should be mentioned. The surface sensitivity of CEMS makes this technique valuable for mineral weathering studies. For example, such oxidation product on siderite surfaces as  $\alpha$ -FeOOH was identified. In a similar study, the oxidation mechanism of biotite has been investigated. An interesting application of CEMS was in lunar samples study. A component in the Mössbauer spectra that could be attributed to superparamagnetic iron particles was found. The results were used to explore the hypothesis that the surface of these samples contained metallic iron particles produced by the exposure to the solar wind.

Mössbauer spectroscopy surface studies were also carried out with resonant atoms present in adsorbed chemical species. These experiments give information on the vibrational motion of the Mössbauer atoms in the adsorbed molecules. If surface

diffusion takes place, this motion is reflected in the Mössbauer spectra as a line broadening, which increases as the diffusion constant increases. Very rapid liquid-like diffusion results in the disappearance of the Mössbauer signal and this problem was discussed in Sect.5.1. When the surrounding of surface atoms is changed by chemisorption, the spectral components due to these atoms are expected to be altered. To observe these effects in adsorbents, it is required, of course, that a large fraction of the Mössbauer atoms be present on the surface.

Chemical reactions on solid/solid and solid/gas interfaces may be very effectively studied by means of Mössbauer spectroscopy. Often subsurface interactions take place at depths beyond the sampling perspective of techniques such as XPS and AES. Sputter-etching may be used to expose buried interfaces, but this often destroys the chemistry and crystal structure of interest. The insensitivity of Rutherford backscattering spectroscopy to chemical changes makes the techniques inappropriate for analyzing the above noted interface. The short survey of applications of the Mössbauer effect to studies of near surface layers will be concluded by discussing two of the reactions above. As an example of solid/gas interaction the formation of iron fluoride hydrate may be considered occurring during the exposure of an  $\alpha$ - $^{57}\text{Fe}$  foil to the vapour of a 40 % hydrogen fluoride solution in the presence of atmospheric oxygen [5.324]. Other instances are an investigation of a solid lubricant  $\text{MoS}_2$  and its interaction with transition metals [5.325, 326].

In the gaseous phase water forms a strong 1:1 complex with hydrogen fluoride and it can therefore be expected to be a major contaminant in the production of HF. Thus the influence of water on the reaction between HF and the surfaces of ferrous alloys is of great practical importance and was investigated by CROUSE and STANDER [5.324] by CEMS at very low  $\gamma$ -rays glancing angles. The glancing angles of 25-30, 12-15 and 8-10 mrad were used and a significant fraction of incident  $\gamma$ -quanta were attenuated within a surface film. As a result the signal from such a film is enhanced relative to the substrate as parallel incidence is approached. The initial reaction product was  $\text{FeF}_2 \cdot 4\text{H}_2\text{O}$ . The compound is stabilized by the reduction potential of the metallic iron substrate. Further oxidation occurs with increasing layer thickness to form a non-stoichiometric  $\text{Fe}_2\text{F}_{5+7x} \cdot 7\text{H}_2\text{O}$  reaction product. The Fe(II)/Fe(III) ratio within the fluoride layer was a function of distance from the iron substrate and the layer can be represented as  $\text{Fe}_2\text{F}_{5+x} \cdot (7-x)\text{H}_2\text{O}$  with  $-1 \leq x \leq +1$ . At the substrate/layer interface  $x = -1$  and the layer consists of  $\text{FeF}_2 \cdot 4\text{H}_2\text{O}$  only. At the layer-air interface  $x$  tends towards one and the layer composition tends towards the thermodynamically most stable iron fluoride hydrate ( $\text{FeF}_3 \cdot 3\text{H}_2\text{O}$ ). This is in accordance with a thermodynamic analysis of the reactions of metallic iron with gaseous HF,  $\text{H}_2\text{O}$  and  $\text{O}_2$ .

MoS<sub>2</sub> is a technologically important material and is used most effectively as a hydrodesulfurization catalyst and as a solid lubricant. When used as a solid lubricant, MoS<sub>2</sub> is most often applied to stainless steels or other Fe containing substrates. In addition, transition metals have been intentionally incorporated into the MoS<sub>2</sub> crystal structure to provide lower coefficients of friction and to extend the lubricant wearlife. The effectiveness of MoS<sub>2</sub> depends on its ability to adhere to metal surfaces yet to remain inert to the substrate-lubricant and vapor-lubricant reactions which may alter its composition and crystal structure.

ZABINSKI et al. [5.325, 326] investigated MoS<sub>2</sub>-Fe surface interactions, MoS<sub>2</sub>/Fe buried-interfaces, the interfacial chemistry occurring at the defected nonstoichiometric MoS<sub>2</sub>/Fe interface and suggested a model Fe-MoS<sub>2</sub> interface. On the iron side of the interface, the overlayer should be thin enough so that interfacial chemical phenomena can be distinguished from bulk chemical phenomena. For these reasons, a relatively contiguous iron films from 0.2 to 3.0 nm of 93.0 % <sup>57</sup>Fe thick were vacuum evaporated onto the surfaces of the basal plane of single crystals molybdenite. Nondestructive depth profiles of the near surface region were obtained using Low Energy Electron Mössbauer Spectroscopy (see Sect.3.10) and techniques described in [3.176]. Mössbauer spectra demonstrated that due to annealing in ultra high vacuum iron is agglomerated into discrete particles and sulfur is stripped from the MoS<sub>2</sub> surface by iron microcrystals and is adsorbed on them. Annealing at higher temperatures causes: further increases in the size of iron particles and sulfur desorption and/or migration back to the MoS<sub>2</sub> surface. Iron located at the bottom of the particles migrates between the sulfur layers in MoS<sub>2</sub> and reacts to form oriented layers of FeMo<sub>2</sub>S<sub>4</sub>. Annealing above the (Fe + 2MoS<sub>2</sub> → FeMo<sub>2</sub>S<sub>4</sub>) bulk reaction temperature of 1023 K does not cause further reaction. ZABINSKI et al. [5.326] decided "that Fe may titrate crystal defects forming FeMo<sub>2</sub>S<sub>4</sub>".

To study the influence of defects on interfacial chemistry the surfaces of molybdenite single crystals were damaged with energetic Ar<sup>+</sup> ions. MoS<sub>2</sub>-Fe interface was prepared by vacuum deposition of 3.0 nm of 95 % <sup>57</sup>Fe onto the damaged molybdenite basal plane at room temperature. CEM spectra recorded from specimens annealed by different temperatures are shown on Fig.5.27. Sputtering removes some of the surface sulfur and abandons the underlying by Mo. The second sextuplet in the CEM spectrum shown in Fig.5.27a is likely due to Fe-Mo interactions. The broad and concave baseline in Figs. 5.27a-c according to ZABINSKI et al. also suggests Fe-Mo interactions at the interface. Annealing the sputterdamaged specimen to 673 K for 0.5 h caused the Fe to agglomerate into particles and to form an FeMo<sub>2</sub>S<sub>4</sub>-like material as evidenced by the appearance of a broad Fe<sup>+2</sup> doublet with the isomer shift of 0.87 mm/s and quadrupole splitting of 1.53.

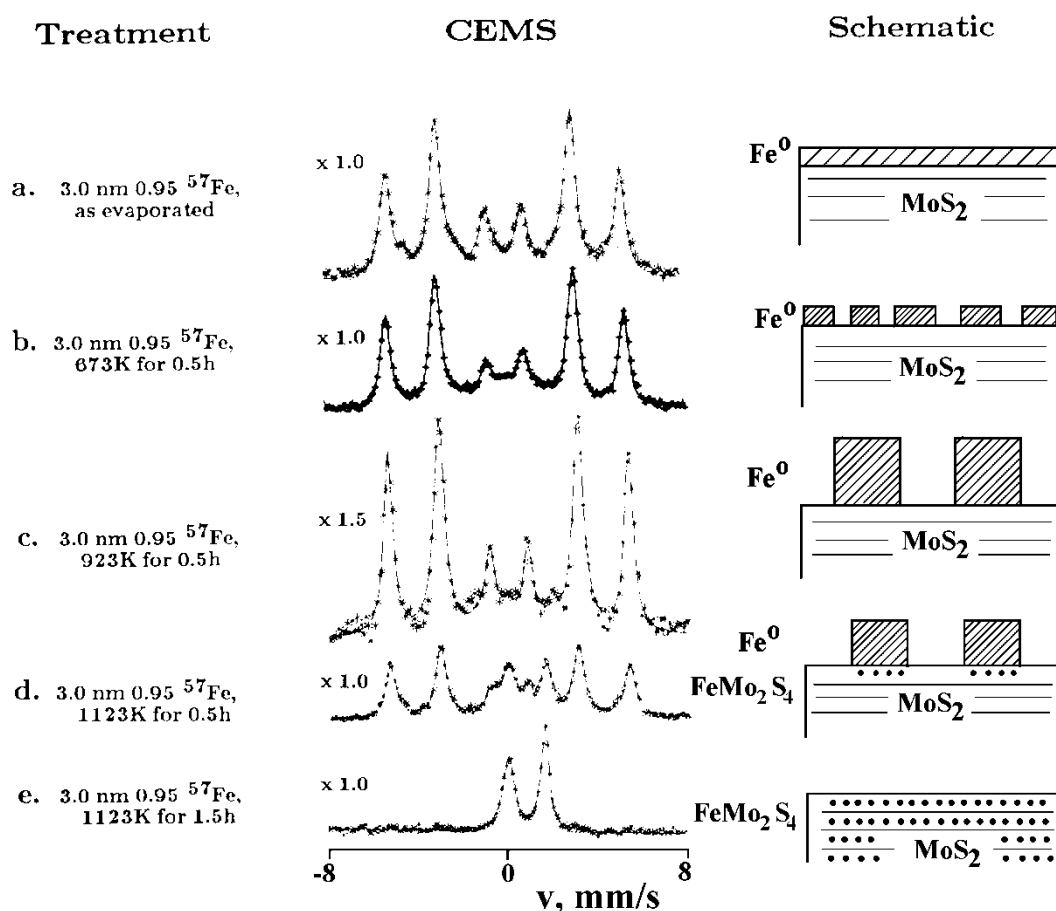


Fig.5.27 CEM spectra from the iron coated  $\text{MoS}_2$  single crystals. The specimen "as evaporated" is molybdenite single crystal damaged by  $2 \cdot 10^{15} \text{ Ar}^+/\text{cm}^2$  and then covered by 3 nm  $^{57}\text{Fe}$  layer (a = 95 %). b - annealed to 673 K for 0.5 h, c - annealed to 923 K for 0.5 h, d - annealed to 1123 K for 0.5 h, e - annealed to 1123 K for 1.5 h, (From [5.326])

Annealing to 923 K for 0.5 h permitted Fe to agglomerate into larger particles. The interfacial  $\text{Fe}^{+2}$  doublet remains broad and does not change significantly in its area. Iron apparently interacts with the reduced molybdenum on the surface and cannot form significant amounts of  $\text{FeMo}_2\text{S}_4$  at 923 K, as it did in the case of unspattered  $\text{MoS}_2$ -Fe interfaces. The subsequent annealing to 1123 K for 0.5 h permitted Fe to diffuse between the sulfur layers in  $\text{MoS}_2$  to form  $\text{FeMo}_2\text{S}_4$ . A singlet accounting for 7 % of the available iron is observed and likely arises from Fe-Mo interactions. The remaining iron is in the form of metallic crystallites.

The large reduction in the CEMS spectral area on annealing to 1123 K is unusual and probably is due to iron at the bottom of the particle diffusing into the  $\text{MoS}_2$  substrate. This phenomenon is illustrated in Figs. 5.27d and e as a simultaneous spreading of iron across molybdenite as  $\text{FeMo}_2\text{S}_4$  and sinking of iron into the substrate to form  $\text{FeMo}_2\text{S}_4$ . As illustrated in Fig.5.27d and e iron has formed  $\text{FeMo}_2\text{S}_4$  by spreading across and diffusing below the molybdenite surface. ZABINSKI et al. [5.326] concluded, that defects and the presence of excess sulfur in the  $\text{MoS}_2$  crystal structure

significantly affect reactions occurring at the  $\text{MoS}_2/\text{Fe}$  interface. Defects introduced in the  $\text{MoS}_2$  basal plane by sputtering, and also the presence of ultra fine particles provide pathways for the diffusion of iron within  $\text{MoS}_2$  where  $\text{FeMo}_2\text{S}_4$  is formed.

## References

- 5.1 G.J. Long and J.G. Stevens (eds.), Industrial Applications of the Mössbauer Effect, Plenum Press, New York, 1987.
- 5.2 I. Dezsi, A. Vertes and L. Kiss, J. Radioanal. Nucl. Chem., 2 (1968) 183-189.
- 5.3 D.D. Joye and R.C Axtmann, Anal. Chem., 40 (1968) 876-878.
- 5.4 A.M. Pritchard and C.M. Dobson, Nature, 224 (1969) 1295.
- 5.5 W. Meisel, Werkst. Korros., 21 (1970) 249.
- 5.6 W. Meisel and Ph. Gütlich, Werkst. Korros., 32 (1970) 296- 301.
- 5.7 W. Meisel, Trends in Mössb. Spectr., Proc. 2-nd Seeheim Workshop on Mössb. Spectr., ed. by P. Gütlich and G.M. Kalvius, Univ. Mainz, 1983, pp.15-26.
- 5.8 W. Meisel, Hyperfine Interactions, 46 (1989) 73-90.
- 5.9 A. Vertes and H. Czako-Nagy, Electrochem. Acta, 34(6) (1989) 721-58.
- 5.10 G.M. Bancroft, J. Mayne and P. Ridgway, Brit. Corros. J., 6 (1971) 119.
- 5.11 A. Volenic, J. Cirak and M. Seberini, Brit. Corros. J., 10 (1975) 196-200.
- 5.12 W.E. O'Grady, J. Electrochem. Soc., 127, No. 3 (1980) 555- 563.
- 5.13 Lin Mou Ching, R.G. Barnes and T.E.Furtak, Phys. Steel. Ind. Conf., APS/AISI, Bethlehem, Pa, 5-7 Oct. 1981, N.Y., 1982, p.202.

- 5.14 Y.Y. Esipenko and A.M. Sukhotin, *Zashch. Met.*, 23(6) (1987) 1053-58 / *Prot. Met. (Engl. Transl.)*, 23 (6) (1987) 781-84.
- 5.15 Y.Y. Esipenko and A.M. Sukhotin, *Zashch. Met.*, 24(3) (1988) 364-71 / *Prot. Met. (Engl. Transl.)*, 24(3) (1988) 285-91.
- 5.16 Y.Y. Esipenko, A.M. Sukhotin, N.V. Rasskazova and G.B. Alyushina, *Electrochim. Soc.*, 24 (1988) 1554-1558.
- 5.17 J. Eldridge and R.W. Hoffman, *J. Electrochem. Soc.*, 136(4) (1989) 955-61.
- 5.18 M.E. Kordes, J. Eldridge, D. Scherson and R.W. Hoffman, *J. Electroanal. Chem.*, 164, No. 2 (1984) 393-397.
- 5.19 M.E. Brett, K.M. Parkin and M.J. Graham, *J. Electrochem. Soc.*, 133 (1986) 2031-35.
- 5.20 U. Stumm, W. Meisel and P. Gütlich, *Hyperfine Interactions*, 28 (1986) 923-925.
- 5.21 W. Meisel, U. Stumm and P. Gütlich, *Fresenius Z. Anal. Chem.*, 329 (1987) 395-399.
- 5.22 W. Meisel, U. Stumm and P. Gütlich, *Fresenius Z. Anal. Chem.*, 333(4-5) (1989) 555-60.
- 5.23 U. Stumm, W. Meisel and P. Gütlich, *Hyperfine Interactions*, 57 (1990) 2115-19.
- 5.24 W. Meisel, U. Stumm and P. Gütlich, *SIA, Surf. Interface Anal.*, 12(1-12) (1988) 430.
- 5.25 A. Vertes, H. Mehner and S. Nagy, *J. Radioanal. Nucl. Chem.*, 111(2) (1987) 283-288.
- 5.26 A. Vertes, J. Jaen, L. Kiss and E.V. Shepeleva, *Hyperfine Interactions*, 28 (1986) 1079-1081.
- 5.27 H. Leidheiser Jr., *J. Electrochem. Soc.*, 135(1) (1988) 5- 11.
- 5.28 G.W. Simmons and H. Leidheiser Jr., in *Mössbauer Effect Methodology*, ed. by I.J. Gruverman and C.W. Seidel, Vol. 10, Plenum Press, New York, 1976, pp.215-225.
- 5.29 A. Vertes, H. Czako-Nagy, P. Deck and H. Leidheiser Jr., *J. Electrochem. Soc.*, 134(7) (1987) 1628-1632.
- 5.30 G.W. Simmons, E. Kellerman and H. Leidheiser Jr., *Corrosion-NACE*, 29, No. 6 (1973) 227-233.
- 5.31 H. Leidheiser Jr., G.W. Simmons and E. Kellerman, *Electrochem. Soc.*, 120 (1973) 1516-1518.
- 5.32 A. Sette Camara and W. Keune, *Corrosion Sci.*, 15 (1975) 441-453.
- 5.33 D.C. Cook, *Hyperfine Interactions*, 28 (1986) 891-894.
- 5.34 K. Nomura and Yu. Ujihira, *Hyperfine Interactions*, 29 (1986) 1467-1470.
- 5.35 M. Fujinami and Yu. Ujihira, *Hyperfine Interactions*, 29 (1986) 1475-1482.
- 5.36 M. Carbucicchio and G. Palombarini, *Hyperfine Interactions*, 41 (1988) 621-624.
- 5.37 J.R. Gancedo, M. Gracia, J.F. Marco and J. Placios, *Hyperfine Interactions*, 41 (1988) 637-640.
- 5.38 N.R. Bulakh, S.V. Ghaisas, S.A. Kulkarni, S.M. Kanetkar, S.B. Ogale and S.K. Date, *Hyperfine Interactions*, 41 (1988) 641-644.
- 5.39 K. Nomura, M. Tasaka and Yu. Ujihira, *Hyperfine Interactions*, 41 (1988) 681-684.
- 5.40 W. Meisel, *Proc. 5th Intern. Conf. Mössbauer Spectrosc.*, Bratislava, Czechoslovakia, ed. by M. Hucl and T. Zenev, 1973, p.200.



- 5.41 W. Meisel and G. Kreysa, *Z. Anorg. Allg. Chem.*, 395 (1973) 31-36.
- 5.42 G.N. Belozerskii, C. Bohm, T. Ekdahl and D. Liljequist, *Corros. Sci.*, 22, No. 9 (1982) 831 - 844.
- 5.43 M. Stratman and K. Hoffmann, *Corros. Sci.*, 29(11/12) (1989) 1329-52.
- 5.44 A.M. Pritchard and B.T.Mould, *Corros.Sci.*, 11 (1971) 9.
- 5.45 T. Shinjo, T. Shigematsu, N. Hosoi, T. Iwasaki and T. Takada, *Jap. J. Appl. Phys.*, 21 (1982) L220 - L222.
- 5.46 G.P. Huffman and H.H. Podgurski, *Oxid. Metals*, 10, No. 6 (1976) 377-401.
- 5.47 M. Domke and B. Kyvelos, *Corros Sci.*, 23, No. 8 (1983) 921-930.
- 5.48 G. Klingelhöfer and W. Meisel, *Hyperfine Interactions*, 57 (1990) 1911-18.
- 5.49 D.A. Channing and M.J. Graham, *Electrochem. Soc.*, 117 (1970) 389-391.
- 5.50 D.A. Channing and M.J. Graham, *Corrosion Sci.*, 12 (1972) 271-274.
- 5.51 D.A. Channing, S.M. Dickerson and M.J. Graham, *Corrosion Sci.*, 13 (1973) 833-838.
- 5.52 M.J. Graham, D.F. Mitchell and D.A. Channing, *Oxid. Metals*, 12, No. 3 (1978) 247-256.
- 5.53 G.A. Sawatzky, F.van der Woude and A.H. Morrish, *Phys. Rev.*, 183 (1969) 383.
- 5.54 A.A. Olowe, D. Rezel and J.M.R. Genin, *Hyperfine Interactions*, 46 (1989) 429-436.
- 5.55 G. Haley, J.G. Mullen and J.M. Honig, *Solid State Comm.*, 69, No. 3 (1989) 285-287.
- 5.56 S. Moerup, *J. Phys. Colloq.*, 37, C6 (1976) 287-290.
- 5.57 S. Moerup, *Proc. Intern. Conf. Mössbauer Spectrosc.*, Bucharest, Romania, 1977, ed. by D.Barb and D. Tarina, 1 (1978) 229-230.
- 5.58 G.N. Belozerskii, *Phys. Stat. Sol. A*46 (1978) 131-140.
- 5.59 B.G. Ershov, N.I. Kartashov, A.I. Milaev, P.Ya. Glazunov and Yu.V. Baldokhin, *DAN SSSR*, 274, No. 5 (1984) 1120- 1123.
- 5.60 Yu.V. Baldokhin, Yu.V. Maksimov, B.G. Ershov and N.I. Kartashov, in *Applications of the Mössbauer Effect*, ed. by Yu.M. Kagan and I.S. Lybutin, Vol. 3, Gordon and Breach Scie. Publ., Amsterdam, 1985, pp. 1063-1066.
- 5.61 J. Ensling, J. Fleisch, R. Grimm, J. Gruber and P. Gütlich, *Corros. Sci.*, 18 (1978) 797-808.
- 5.62 Yu. F. Babikova, P.L. Gruzin, A.V. Ivanov and V.P. Filippov, *Atomnaya Energiya*, 38 (3) (1975) 138-142.
- 5.63 J. Ensling, P. Gütlich and R. Ries, *Werkstoffe Korros.*, 29 (1978) 250.
- 5.64 L.N. Moskvina, G.N. Belozerskii, A.A. Efimov, S.B. Tomilov, V.F. Teterin and E.P. Bredikhina, *Teploenergetika*, No. 3 (1981) 52-55.
- 5.65 J. Lipka, J. Blazek, D.Majersky, M. Miglierini and M. Seberini, *Hyperfine Interactions*, 57 (1990) 1969-74.

- 5.66 N.K. Jaggi, K.R.P.M. Ras, Y.D. Dande, P.K.Chauhan and H.S. Gadityar, Proc. Intern. Conf. Appl. of the Mössb. Effect, Jaipur, India, December 1981, New Dehli, 1982, pp 313-315.
- 5.67 R.K. Nigam, B.P. Hajela, S. Sengupta, B.C. Srivastava and K.N. Gupta, Hyperfine Interactions, 28 (1986) 935-939.
- 5.68 A. Vertes, I. Czako-Nagy, P. Deck and H. Leidheiser Jr., Hyperfine Interactions, 41 (1988) 729-732.
- 5.69 H. Leidheiser Jr., G.W. Simmons and E. Kellerman, J. Electrochem. Soc., 120, No. 11 (1973) 1516-1518.
- 5.70 H. Leidheiser Jr., S. Music and G.W. Simmons, Nature, 297 (1982) 667.
- 5.71 A. Vertes, I. Czako-Nagy, P. Deck and H. Leidheiser Jr., J. Electrochem. Soc., 134 (1987) 1628.
- 5.72 A. Vertes, A. Czirak, H. Czako-Nagy and H. Leidheiser Jr., J. Electrochem. Soc., 135 (1988) 2143-2146.
- 5.73 H. Leidheiser Jr., A. Vertes, J. E. Roberts and R. Turoscy, Hyperfine Interactions, 57 (1990) 1955-1962.
- 5.74 J.S. Brooks and S. Thorpe, Hyperfine Interactions, 47-48 (1-4) (1989) 159-178.
- 5.75 K. Hoffman and M. Stratman, Ber. Bunsen-Ges. Phys. Chem., 93 (11) (1989) 1389-95.
- 5.76 P. Gütlich, W. Meisel and E. Mohs, Werkst. Korros., 33 (1982) 35-39.
- 5.77 W. Meisel and P. Gütlich, Werkst. Korros., 32 (1981) 296-301.
- 5.78 W. Meisel, E. Mohs, H.-J. Guttmann and Ph. Gütlich, Corros.Sci., 23 (1983) 465-471.
- 5.79 W. Meisel, H.-J. Guttmann and P. Gütlich, Corros.Sci., 23 (1983) 1373 -1379.
- 5.80 J.R. Gancedo, M. Gracia, W. Francisco, M. Morcillo and S. Feliu, Hyperfine Interactions, 46 (1989) 461-465.
- 5.81 D.D. Joye and R.C. Axmann, Analytical Chem., 40, No. 6 (1968) 876-878.
- 5.82 P.C. Bhat, M.P. Sathyavathiamma, N.G. Puttaswamy and R.M. Mallya, Proc. Intern. Conf. Appl. of the Mössb. Effect, Jaipur, India, December 1981, New Dehli, 1982, pp. 435- 437.
- 5.83 Y. Ujihira, Rev. Anal. Chem., 8 (1985) 125-177.
- 5.84 A.K. Singh, T. Ericsson, L. Haggstrom and J. Gullman, Corros. Sci., 25 (1985) 931-945.
- 5.85 Z. Jinshan, N. Mulin, D. Gang, L. Shuyuan, Z. Huimin, Z. Qiang, C. Kegin and Y. Xuegen, Hyperfine Interactions, 29 (1986) 1457-1461.
- 5.86 Mössbauer Handbook "Corrosion Studies", Mössbauer effect Data Center, Asheville, USA, 1985.
- 5.87 K. Nomura and Y.Ujihira, Hyperfine Interactions, 57 (1990) 2023-2028.
- 5.88 T. Kobayashi, K. Fukumura, Y. Isozumi and R. Katano, Hyperfine Interactions, 57 (1990) 1923-1928.
- 5.89 N.R. Furet, C. Haces, F. Corvo and C. Diaz, Hyperfine Interactions, 57 (1990) 1833-1838.
- 5.90 A.M. Pritchard, Chem. Phys. Lett., 23, No. 4 (1973) 514- 515.
- 5.91 M.J. Graham, Proc. Electrochem. Soc., 86 (1986) 228-233.

- 5.92 A. Abras, A.A.G. Campos, A.V. De Carvalho and L.O. Ladiera, *Appl. Phys.*, A41 (1986) 185-189.
- 5.93 H.A. Ahmed, R.P. Underhill, W.W. Smeltzer, M.E. Brett and M.J. Graham, *Oxid. Met.*, 28(5-6) (1987) 347-351.
- 5.94 W. Meisel, U. Stumm, C. Thilmann, R. Gancedo and P. Gütlich, *Hyperfine Interactions*, 41 (1988) 669-672.
- 5.95 S. Rezaie-Serej and D.C. Cook, *Hyperfine Interactions*, 41 (1988) 701-704.
- 5.96 V.V. Chekin, *Messbauerovskaja Spectroscopia Splavov Zsheleza, Zolota i Olova*, Energoatomizdat, Moskva, 1981.
- 5.97 L.H. Schwartz, in *Applications of Mössbauer Spectroscopy*, ed. by R.L. Cohen, Vol. 1, Acad. Press, New York, 1976, pp. 85-128.
- 5.98 G.P. Huffman and F.E. Huggius, *Applications of Mössbauer Spectroscopy in Steel Industry*, in *Mössbauer Spectroscopy and its Chemical Applications*, ed. by J.G. Stevens and G.K. Shenoy, *Adv. in Chemistry*, ser. 194, Washington D.C., 1981, pp. 265-304.
- 5.99 T.E. Cranshaw, *Studies in Physical and Theoretical Chemistry*, in *Advances in Mössbauer Spectroscopy, Applications to Physics, Chemistry and Biology*, ed. by B.V. Thosar, P.K. Iengar, J.K. Srivastava and S.C. Bharagava, Vol. 25, *Els. Sci. Publ. Comp.*, Amsterdam, 1983, pp. 217-246.
- 5.100 F.E. Fujita, *Proc. Intern. Conf. Appl. of the Mössb. Effect*, Jaipur, India, December 1981, New Dehli, 1982, pp. 45-52.
- 5.101 U. Gonser, *Mössbauer Spectroscopy*, in *Microscopic Methods in Metals*, ed. by U. Gonser, *Topics Curr. Phys.*, Vol.40, Springer, Berlin, 1986, pp. 409-448.
- 5.102 P.A. Montano, *Hyperfine Interactions*, 27 (1986) 147-159.
- 5.103 M. Maurer and J.M. Friedt, *Hyperfine Interactions*, 27 (1986) 135-146.
- 5.104 B.T. Fultz and H.H. Hamdeh, *Hyperfine Interactions*, 45(1-4) (1989) 55-72.
- 5.105 P.L. Gruzin, Yu.A. Rodionov and Yu.D. Jarov, *Dokl. Akad. Nauk SSSR*, 202, No. 3 (1972) 316-319.
- 5.106 L.V. Mironov, A.P. Khomskiy, V.V. Ovchinnikov, V.A. Makarov and G.A. Dorofeyev, *Fiz. Met. Metalloved.*, 60(3) (1985) 551-524 / *Sov. Phys. - Fiz. Met. Metallography* (English transl.), 60(3) (1985) 95-99.
- 5.107 S. Nasu, H. Takano, F.E. Fujita, K. Takanashi, H. Yasuoka and H. Adachi, *J. Magn. Mater.*, 54-57 (1986) 943-944.
- 5.108 J. Foct and P. Rochegude, *Hyperfine Interactions*, 28 (1986) 1075-1078.
- 5.109 J.M.R. Genin, O.N.C. Uwakweh, J. Schanen and Ph. Bauer, *Hyperfine Interactions*, 41 (1988) 575-578.
- 5.110 G.N. Belozerskii, V.M. Yerkin, V.A. Malyshevskii, O.G. Sokolov, E.M. Sosenushkin and Yu.P. Khimich, *Fiz. Met. Metalloved.*, 43(1) (1977) 145-151.
- 5.111 S.M. Dubiel and G. Inden, *Z. Metallk.*, 78(8) (1987) 544-549.
- 5.112 J. Foct, P. Rochegude and A. Hendry, *Acta Metall.*, 36(3) (1988) 501-505.
- 5.113 B.T. Fultz, J.I. Kim, Y.H. Kim and J.M. Morris Jr., *Metallurg. Trans.*, 17A(6) (1986) 967-972.

- 5.114 S. Skrzypek, E. Kolawa, J.A. Sawicki and T. Tyliczszak, *Mater. Sci. Eng.*, 66 (1984) 145-149.
- 5.115 B.K. Das, K. Chowdhury, D.L. Bhattacharya and A.K. Tewari, *Phys. Stat. Sol.*, A93 (1986) K29-31.
- 5.116 D.C. Cook, *Metalurg. Trans.*, 18A (1987) 201-210.
- 5.117 J. Li and B.X. Liu, *Phys. Stat. Sol.*, A99 (1987) K31-34.
- 5.118 G.N. Belozerskii, V.M. Yerkina, S.M. Irkaev, V.G. Semenov and S.A. Khazanov, *Fiz. Met. Metalloved.*, 44(3) (1977) 511-516 / *Sov. Phys. - Fiz. Met. Metallography* (Engl. Transl.), 44(3) (1978) 48-53.
- 5.119 M.A.Z. Vasconcellos, S.R. Teixeira, F.L. Freire Jr., M.C.S. Nobrega, P.H. Dionisio, W.H. Schreiner and I.J.R. Baumvol, *Mater. Sci. Eng.*, A104 (1988) 169-79.
- 5.120 V.I. Spitzin, V.I. Goldanskii, O.A. Troitzkii, G.N. Belozerskii, N.E. Kirjanichev and Yu.V. Baldokhin, *Dokl. Akad. Nauk SSSR*, 268, No. 4 (1983) 871-874.
- 5.121 G.N. Belozerskii, A.A. Gavrish, V.V. Dodoladov, N.E. Kirjanichev, V.P. Moiseev, V.G. Ryjkov and O.A. Troitzkii, *Izv. Akad. Nauk SSSR, Metally*, No. 5 (1983) 234-238.
- 5.122 K.J. Kim and L.H. Schwartz, *J. Physique Colloque*, C6, 37, No 12 (1976) 405-408.
- 5.123 G.N. Belozerskii, V.N. Gitzovich, E.M. Sosenushkin, O.G. Sokolov and S.A. Chekashova, *Fiz. Met. Metalloved.*, 55(4) (1983) 788-791.
- 5.124 Yu.V. Baldokhin, N.F. Shukin and I.Ya. Georgiva, in *Applications of the Mössbauer Effect*, ed. by Yu.M. Kagan and I.S. Lybutin, Vol. 1, Gordon and Breach Scie. Publ., Amsterdam, 1985, pp. 311.
- 5.125 F. Gauzzi, B. Verдини and G. Principi, *J. Mater. Sci.*, 18 (1983) 3661-3670.
- 5.126 S. Nasu, H. Tanimoto and F.E. Fujita, *Hyperfine Interactions*, 57 (1990) 2009-2014.
- 5.127 L.J. Swartzendruber and L.H. Bennett, *Scr. Metal.*, 6 (1972) 737-742.
- 5.128 O.V. Misevich, A.L. Kholmetskii, V.A. Chudakov and G.P. Shpen'kov, *Dokl. Akad. Nauk BSSR*, 32(6) (1988) 518-21.
- 5.129 T.E. Cranshaw and R.C. Campany, *J. de Physique Colloque* C2, 40, No. 3 (1979) 14-16.
- 5.130 R.L. Collins, R.A. Mazak and C.M. Yagnik, in *Mössbauer Effect Methodology*, ed. by I.J. Gruverman and C.W. Seidel, Vol. 8, Plenum Press, New York, 1973, pp. 191- 210.
- 5.131 N.Saegusa and A.H. Morrish, *Phys. Rev. B*, 26 (1982) 6547- 6553.
- 5.132 Yu. Baldokhin, O.S. Kozlova, V.A. Makarov and V.P. Ovcharov, *Fiz. Met. Metalloved.*, 53(5) (1982) 1027-1029.
- 5.133 G.N. Belozerskii, V.G. Semenov and S.A. Chekashova, *Fiz. Met. Metalloved.*, 55(5) (1983) 923-930.
- 5.134 U. Gonser, M. Ackermann and H.G. Wagner, *J. Magn. Magn. Mater.*, 31-34 (1983) 1605-1607.
- 5.135 M. Fujinami and Y. Ujihira, *Hyperfine Interactions*, 27 (1986) 301-304.
- 5.136 E. Bauer-Grosse and G. Le Caer, *Pilos. Mag.*, 56(4) (1987) 485-500.

- 5.137 E. Galvao da Silva, R.B. Scorzelli, F. Sanchez-Sinencio, F. Octevio Alvarez and J.G. Mendoza-Alvarez, *Solid State Commun.*, 72(11) (1989) 1059-63.
- 5.138 J. Pavlovsky and T. Zemcik, *Phys. Stat. Sol. A* 112 (1989) K1-6.
- 5.139 G. Krettek, B. Huck and J. Hesse, *Hyperfine Interactions*, 57 (1990) 1935-1940.
- 5.140 M.A.Z. Vasconcellos, S.R. Teixeira, P.H. Dionisio, W.H. Schreiner and I.J.R. Baumvol, *Nucl. Instrum. Methods Phys. Res.*, A280(2-3) (1989) 557-63.
- 5.141 A. Fnidiki and J.P. Eymery, *J. Phys. Colloq.* 49 (12) (1988) 1735-1736.
- 5.142 P.L. Gruzin and Yu. V. Petrikin, *Zavodskaja Laboratorja*, No. 9 (1975) 984.
- 5.143 V.K. Sedunov, T.Ya. Menshikova, K.P. Mitrofanov, S.I. Reyman and N.I. Rokhlov, *Metalloved. Termich. Obrabotka Metallov*, 9 (1977) 13-15.
- 5.144 A. Handa, Y. Ujihira and I. Okabe, *J. Mater. Sci.*, 16 (1981) 1999-2002.
- 5.145 Y. Ujihira and A. Handa, *J. Physique C2*, 40, No. 3 (1979) 586-588.
- 5.146 F. Berry, M.E. Brett, P. Bowen and W. Jones, *J. Chem. Soc. Dalton Trans.*, 11 (1981) 1-6.
- 5.147 D. Firrao, M. Rosso, G. Principi and J. Frattini, *J. Mater. Sci.*, 17 (1982) 1773-1788.
- 5.148 K. Umeda, E. Kita and A. Tasaki, *IEEE Trans. Magn.*, 22(5) (1986) 591-593.
- 5.149 K. Gonzalez, R. Iraldi and F. Gonzalez-Jimenez, *Hyperfine Interactions*, 28 (1986) 619-622.
- 5.150 M. Carbucicchio, L. Bardani and G. Palombarini, *J. Mater. Sci.*, 15 (1980) 711-719.
- 5.151 M. Carbucicchio, G. Palombarini and G. Sambogna, in *Applications of the Mössbauer Effect*, ed. by Yu. M. Kagan and I.S. Lybutin, Vol. 2, Gordon and Breach Scie. Publ., Amsterdam, 1985, p.483.
- 5.152 M. Carbucicchio, G. Meazza and G. Palombarini, *J. Mater. Sci.*, 17 (1982) 3123-3128.
- 5.153 G. Palombarini and M. Carbucicchio, *J. Mater. Sci. Let.*, 4 (1985) 170-172.
- 5.154 M. Carbucicchio and G. Palombarini, *J. Mater. Sci. Letters*, 4 (1985) 483-486.
- 5.155 M. Carbucicchio and G. Sambogna, *Thin Solid Films*, 126 (1985) 299-305.
- 5.156 M. Carbucicchio, G. Palombarini and G. Sambogna, *Hyperfine Interactions*, 41 (1988) 617-620.
- 5.157 A. Handa and Y. Ujihira, *Proc. Intern. Conf. Appl. of the Mössb. Effect*, Jaipur, India, December 1981, New Dehli, 1982, pp.306-309.
- 5.158 A. Handa and Y. Ujihira, *J. Mater. Sci.*, 18 (1983) 1887- 1894.
- 5.159 S.V. Ghaisas, N.R. Bulakh, S.A. Kulkarni, S.M. Kanetkar, S.B. Ogale, S.K. Date and A. Mitra, *J. Phys. D, Appl. Phys.*, 22(2) (1989) 364-367.

- 5.160 J. H. Sanders and B.J. Tatarchuk, *Hyperfine Interactions*, 57 (1990) 2083-2088.
- 5.161 T.E. Cranshaw, in *Industrial Applications of the Mössbauer Effect*, ed. by G.J. Long and J.G. Stevens, Plenum Press, New York, 1987, pp.7-23.
- 5.162 F.E. Huggins, G.P. Huffman and G.R. Dunmyre, in *Industrial Applications of the Mössbauer Effect*, ed. by G.J. Long and J.G. Stevens, Plenum Press, New York, 1987, pp.137-151.
- 5.163 G. Dearnaley, *Nucl. Instr. Meth. Phys. Res.*, B50 (1990) 358-367.
- 5.164 H.De Waard and G.L. Zhang, *Hyperfine Interactions*, 56 (1990) 1569-1576.
- 5.165 M. Hans and G.K. Wolf, *Hyperfine Interactions*, 56 (1990) 1593-1598.
- 5.166 L. Niesen, *Hyperfine Interactions*, 35 (1987) 587-600.
- 5.167 G. Weyer, *Hyperfine Interactions*, 27 (1986) 249-262.
- 5.168 H. de Waard, *Hyperfine Interactions*, 40 (1988) 31-48.
- 5.169 G. Weyer, *Hyperfine Interactions*, 43 (1988) 187-204.
- 5.170 J.P. Eymery and A. Fnidiki, *Diffus. Defect Data*, 57-8 (1988) 229-240.
- 5.171 G. Langouche, *Hyperfine Interactions*, 68 (1991) 95-111.
- 5.172 I. Dezsi, *Proc. Intern. Conf. Appl. of the Mössb. Effect*, Jaipur, India, December 1981, New Dehli, 1982, pp 141- 142.
- 5.173 G. Weyer, F.T. Pedersen, H. Grann and K.B. Nielsen, *Hyperfine Interactions*, 29 (1986) 1233-1236.
- 5.174 H. Grann, F.T. Pedersen and G. Weyer, *Hyperfine Interactions*, 29 (1986) 1237-1240.
- 5.175 F.T. Pedersen, H. Grann and G. Weyer, *Hyperfine Interactions*, 29 (1986) 1241-1244.
- 5.176 H.R. Weerkamp, H. Andreassen and L. Niesen, *Hyperfine Interactions*, 29 (1986) 1267-1270.
- 5.177 A. Bhagawat, K.G. Prasad and R.P. Sharma, *Hyperfine Interactions*, 42 (1988) 977-980.
- 5.178 N. Hayashi, I. Sakamoto, E. Johnson, L. Graabak, P. Borgesen and B.M.U. Scherzer, *Hyperfine Interactions*, 42 (1988) 989-992.
- 5.179 M. Behar, P.J. Viccaro, M.T.X. Silva, A. Vasquez, C.A. dos Santos and F.C. Zawislak, *Nucl. Instr. Meth. Phys. Res.*, B19-20(1) (1987) 132-135.
- 5.180 W. Segeth, H. Andreassen, D.O. Boerma and L. Niesen, *Hyperfine Interactions*, 29 (1986) 1271-1274.
- 5.181 G.D. Sprouse, G.M. Kalvius and S.S. Hanna, *Phys. Rev. Lett.*, 18 (1965) 1041-1043.
- 5.182 S. Laubach, P. Schwalbach, M. Hartick, E. Kankleit, B. Keck and R. Sielemann, *Hyperfine Interactions*, 53 (1990) 75-92.
- 5.183 F.S. De Barros, D. Hafemeister and P.J. Viccaro, *J. Chem. Phys.*, 52 (1970) 2865-2869.
- 5.184 I. Dezsi, R. Coussement, S. Feher, G. Langouche and Cs. Fetzer, *Hyperfine Interactions*, 29 (1986) 1275-1278.
- 5.185 K.G. Prasad, *Hyperfine Interactions*, 34 (1987) 197-200.

- 5.186 B.D. Sawicka and J.A. Sawicki, *Phys. Stat. Sol.*, A18 (1973) K85-87.
- 5.187 R.Sielemann, M. Menningen, B. Keck, G. Vogl and Y. Yoshida, *Hyperfine Interactions*, 56 (1990) 1643-1648.
- 5.188 H. Andreassen, S. Damgaard, J.W. Petersen and G. Weyer, *Phys. Lett.*, A90 (1982) 89-92.
- 5.189 T. Shigematsu, S. Stanick, W. Keune, R.H. Nussbaum, H.D. Pfannes, D. Liljequist and G. Longworth, in *Applications of the Mössbauer Effect*, ed. by Yu.M. Kagan and I.S. Lybutin, Vol. 2, Gordon and Breach Scie. Publ., Amsterdam, 1985, p. 469.
- 5.190 I.I. Ali-Zade, K.G. Binnatov, P.L. Gruzin, V.N. Nevolin and Yu.V. Petrikin, *Izv. Akad. Nauk SSSR, ser. Fiz.*, 50, No. 12 (1986) 2304-2309.
- 5.191 G. Möller, G. Klingelhöfer, P. Schwalbac and E. Kankeleit, *Hyperfine Interactions*, 56 (1990) 1627-1636.
- 5.192 I. Sakamoto, N. Hayashi, B. Furubayashi and H. Tanoue, *Hyperfine Interactions*, 42 (1988) 1005-1008.
- 5.193 M. Carbucicchio and L. Bardani, *J. Appl. Phys.*, 52(7) (1981) 4589-4592.
- 5.194 G. Marest, C. Skoutarides, Th. Barnavon and J. Tousset, *Nucl. Instr. Meth.*, 209-210 (1983) 259-265.
- 5.195 E. Ramous, G. Principi, L. Giordano, S. Lo Russo and C. Tosello, *Thin Solid Films*, 102 (1983) 97-106.
- 5.196 N. Monocoffre, G. Hollinger, H. Jaffrezic, G. Marest and J. Tousset, *Nucl. Instr. Meth. Phys. Res.*, B7/8 (1985) 177-183.
- 5.197 N. Monocoffre, G. Marest, S. Hiadsi and J. Tousset, *Nucl. Instr. Meth. Phys. Res.*, B15 (1986) 620-624.
- 5.198 H. Reuther, *Phys. Stat. Sol.*, A93 (1986) 201-205.
- 5.199 Y.S. Dorik, S.M. Chaudhari, S.V. Ghaisas, S.B. Ogale and V.G. Bhide, *J. Appl. Phys.*, 60 (1986) 2959-2965.
- 5.200 G. Wagner, R. Leutenecker, T. Louis and U. Gonser, *Hyperfine Interactions*, 42 (1988) 1017-1020.
- 5.201 F.M. Kustas, M.S. Misra and D.L. Williamson, *Nucl. Instr. Meth. Phys. Res.*, B31 (1988) 393-401.
- 5.202 G. Terwagne, M. Piette, P. Bertrand and F. Bodart, *Mater. Sci. Eng.*, B2(1-3) (1989) 195-201.
- 5.203 G. Terwagne, G. Van Tendeloo and S.E. Donnelly, *J. Appl. Phys.*, 65(11) (1989) 4225-29.
- 5.204 V.A. Tsurin, A.M. Sorkin, V.A. Pavlov and A.P. Stepanov, *Poverkhnost*, 11 (1988) 131-5.
- 5.205 G. Wagner, R. Leutenecker and U. Gonser, *Hyperfine Interactions*, 56 (1990) 1653-1656.
- 5.206 D.L. Williamson, Y. Qu, R.H. Wei, W.S. Sampath and P.J. Wilbur, *Mater. Res. Soc. Symp. Proc.*, 128 (1989) 409-414.
- 5.207 G. Marset, *Diffus. Defect Data*, 57-8 (1988) 273-326.
- 5.208 M. Fujinami, Y. Ujihira, H. Reuther and E. Richter, *Hyperfine Interactions*, 42 (1988) 985-988.
- 5.209 D.L. Williamson, F.M. Kustas, Yi Qu and S.R. Smith, *Hyperfine Interactions*, 42 (1988) 1029-1032.
- 5.210 H. Reuther, *Nucl. Instr. Meth. Phys. Res.*, B30 (1988) 61- 66.

- 5.211 M.A. El Khakani, H. Jaffrezic, G. Marest, N. Moncoffre and J. Tousset, *Mater. Sci. Eng.*, A115 (1989) 37-42.
- 5.212 Y. Zhang, S. Bi, L.M. Mei and Z.H. Lei, *J. Phys. Colloq.*, 49(12) (1988) 1749-50.
- 5.213 G. Wagner, T. Luis, R. Leutenecker and U. Gonser, *Hyperfine Interactions*, 46 (1989) 501-508.
- 5.214 G. Marest, S. Hiadsi, J. Tousset, P. Guiraldenq and Nguyen Du, *Hyperfine Interactions*, 46 (1989) 491-499.
- 5.215 H. Reuther, E. Richer and I.S. Szucs, *Phys. Stat. Sol.*, A118 (1990) 409-413.
- 5.216 A. Johansen, E. Johnson, L. Sarholt-Kristensen, S. Steenstrup, E. Gerritsen, C.J.M. Denissen, H. Keetels, J. Politiek, N. Hayashi and I. Sakamoto, *Nucl. Instr. Meth. Phys. Res.*, B50(1-4) (1990) 119-26.
- 5.217 S.M.M. Ramos, L. Amaral, M. Behar, G. Marest, A. Vasquez and F.C. Zawislak, *Hyperfine Interactions*, 46 (1989) 483- 489.
- 5.218 S.M.M. Ramos, L. Amaral, M. Behar, G. Marest, A. Vasquez and F.C. Zawislak, *J. Phys., Condens. Matter.*, 1(45) (1989) 8799-808.
- 5.219 A. Santaniello, J. Roth and F.E. Wagner, *Nucl. Instr. Meth. Phys. Res.*, B48(1-4) (1990) 499-503.
- 5.220 L.E. Rehn and P.R. Okamoto, *Nucl. Instr. Meth. Phys. Res.*, B39 (1989) 104-113.
- 5.221 H. Hofsass, G. Lindner, S. Winter, B. Besold, E. Recknagel and G. Weyer, *Nucl. Instr. Meth. Phys. Res.*, B13 (1986) 71-75.
- 5.222 B. Besold, E. Danielsen, H. Hofsaess, G. Lindner, J.W. Petersen, E. Recknagel, M. Sondergaard, G. Weyer and S. Winter, *Mater. Sci. Forum*, 15-18 (1987) 665-668.
- 5.223 P.Q. Zhang, G. Principi, P. Paccaghella, S. Lo Russo and G. Battaglin, *Nucl. Instr. Meth. Phys. Res.*, B28 (1987) 561-566; *J. Mater. Sci. Lett.*, 7 (1988) 484-486.
- 5.224 A.J. Burggaaf, D. Scholten and B.A. van Hassel, *Nucl. Instr. Meth. Phys. Res.*, B32 (1988) 32-36.
- 5.225 J. Li, B.X. Liu, H.D. Li and Zhang Xiufang, *Hyperfine Interactions*, 42 (1988) 997-1000.
- 5.226 J. Li and B.X. Liu, *Nucl. Instr. Meth. Phys. Res.*, B31 (1988) 407-411.
- 5.227 S.B. Ogale, D.M. Phase, S.M. Chaudhari, S.V. Ghaisas, S.M. Kanetkar, P.P. Patil and V.G. Bhide, *Phys. Rev. B, Condens. Mater.*, 35 (1987) 1593-1601.
- 5.228 A.Vertes, E. Kuzmann, G. Vertes, Z. Szokefalvy-Nagy, E. Kotay and G. Mezey, *Hyperfine Interactions*, 42 (1988) 1013-1016.
- 5.229 S. Moncher, G. Principi, L.M. Gratton, C. Tosello, I. Czako-Nagy and A. Vertes, *Hyperfine Interactions*, 46 (1989) 535-540.
- 5.230 A. Gupta, G. Principi, G. Battaglin, S. LO Russo and Q. Zhang, *Hyperfine Interactions*, 56 (1990) 1587-1592.
- 5.231 J.H. Sanders, D.L. Edwards, J.R. Williams and B.J. Tatarchuk, *J. Appl. Phys.*, 67(6) (1990) 3121-31.
- 5.232 A. Bhagawat, M.B. Kurup, K.G. Prasad and R.P. Sharma, *Hyperfine Interactions*, 29 (1986) 1167-1173.
- 5.233 E. Kuzmann and I.N. Spirov, *Hyperfine Interactions*, 29 (1986) 1175-1178.



- 5.234 Li Shi, Xu Yingting, Li Guodong, Li Dexin, Xu Peiguang and Xiong Zhaokui, *Hyperfine Interactions*, 42 (1988) 1001-1004.
- 5.235 Q. Wang, Zhang Xiufang, Gao Naifei and Guo Youjiang, *Hyperfine Interactions*, 42 (1988) 1021-1024.
- 5.236 M. Kopcewicz, D.L. Williamson and F.E. Cecil, *Hyperfine Interactions*, 56 (1990) 1599-1604.
- 5.237 N. Hayashi, I. Sakamoto, H. Tanoue and T. Toriyama, *Radiat. Eff.*, 106(4) (1988) 265-70.
- 5.238 L.M. Gratton, A. Gupta, W. Keune, S. Lo Russo, J. Parellada, G. Principi and C. Tosello, *Mater. Sci. Eng.*, A115 (1989) 161-64.
- 5.239 N. Hayashi, I. Sakamoto, A. Nakai and N. Kobayashi, *Trans. Jpn. Inst. Met.*, 29 (1988) 77-80.
- 5.240 N. Hayashi, T. Toriyama, I. Sakamoto and K. Hisatake, *J. Phys., Condens. Mater.*, 1(24) (1989) 3849-58.
- 5.241 N. Hayashi, I. Sakamoto and H. Kobayashi, *Nucl. Instr. Meth. Phys. Res.*, B39(1-4) (1989) 587-90.
- 5.242 M. Carbucicchio, A. Valenti, G. Battaglin, P. Mazzoldi and R. dal Maschio, *Hyperfine Interactions*, 29 (1986) 1213-1216.
- 5.243 P.A. Ingemarsson, T. Ericsson, G. Possnert and R. Woppling, *Hyperfine Interactions*, 46 (1989) 549-556.
- 5.244 E. Kuzmann, I.N. Spirov, A. Vertes and E. Kovacs- Csetenyi, *Mater. Sci. Forum*, 13-14 (1987) 325-330.
- 5.245 A.K. Zhetbaev, N.N. Zinchenko, Sh. Sh. Ibragimov and A.N. Ozernoi, in *Applications of the Mössbauer Effect*, ed. by Yu.M. Kagan and I.S. Lybutin, Vol. 4, Gordon and Breach Sci. Publ., Amsterdam, 1985, pp 1471-1474.
- 5.246 M. Miglierini and J. Sitek, *Key Engineering Materials*, 40-41 (1990) 281-285.
- 5.247 Sh. Sh. Ibragimov, M.F. Vereshchak and T.M. Zhantikin, *Hyperfine Interactions*, 29 (1986) 1293-1296.
- 5.248 H. Kuwano and Y. Hamaguchi, *J. Nucl. Mater.*, 155-7 (1988) 1071-1074.
- 5.249 J.A. Sawicki and B.D. Sawicka, *Nucl. Instr. Meth. Phys. Res.*, B23 (1987) 482-486.
- 5.250 E. Johnson, L. Grabaek, A. Johansen, L. Sarholt-Kristensen, P. Borgesen, B.M. U. Scherzer, N. Hayashi and I. Sakamoto, *Nucl. Instr. Meth. Phys. Res.*, B39(1-4) (1989) 567-72.
- 5.251 V.A. Tsurin, A.M. Sarkin, V.A. Pavlov and A.P. Stepanov, *Poverkhnost*, No. 11 (1988) 131-135.
- 5.252 B.D. Sawicka, J.A. Sawicki, F.E. Wagner, W. Möller, P. Borgesen and R. Wordel, *Hyperfine Interactions*, 29 (1986) 1205-1208.
- 5.253 N. Hayashi, I. Sakamoto, E. Johnson, L. Graabak, P. Borgesen and B.M.U. Scherzer, *Hyperfine Interactions*, 42 (1988) 989-992.
- 5.254 H. De Waard, F. Pleiter, L. Niesen and D.W. Hafemeister, *Hyperfine Interactions*, 10 (1981) 643-650.
- 5.255 S. Nasu and F.E. Fujita, *Hyperfine Interactions*, 29 (1986) 1279-1282.

- 5.256 H. Roy-Poulsen, E. Johnson, A. Johansen, L. Sarholt-Kristensen and H. Hayashi, *Hyperfine Interactions*, 29 (1986) 1201-1204.
- 5.257 F. Studer, N. Nguyen, G. Fuchs and M. Toulemonde, *Hyperfine Interactions*, 29 (1986) 1287-1292.
- 5.258 A. Hallen, P.A. Ingemarsson, P. Hakansson, B.U.R. Sundqvist and G. Possnerts, *Nucl. Instr. Meth. Phys. Res.*, B36(3) (1989) 345-349.
- 5.259 A.D. Pogrebnyak, G.E. Remnev, I.B. Kurakin and A.E. Ligachev, *Nucl. Instr. Meth. Phys. Res.*, B36(3) (1989) 286-305.
- 5.260 S.I. Reyman, V.S. Schpinel and V.P. Gor'kov, in *Prikladnaya Yadernaya Spectroscopiya*, Energoizdat, Moskva, 1982, pp. 205-211.
- 5.261 E. Ramous, L. Giordano, G. Principi and A. Tiziani, *J. Physique, Colloque C5*, 44, No. 10 (1983) 501-505.
- 5.262 M. Carbucicchio and G. Sambogna, *Thin Solid Films*, 126 (1985) 299-305.
- 5.263 P. Matteazzi, L. Lanotte and V. Tagliaferri, in *Rapidly Quenched Metals*, Proc. 5th Intern. Conf., Wurzburg 1984, ed. by S. Steeb and H. Warlimont, Vol.2, Elsev. Sci. Publ. BV, Amsterdam, 1985, pp 1199-1202.
- 5.264 M. Carbucicchio, G. Sambogna and G. Palombarini, *Hyperfine Interactions*, 28 (1986) 1021-1024.
- 5.265 M. Carbucicchio and G. Palombarini, *J. Mater. Sci.*, 21 (1986) 75-82.
- 5.266 E.V. Yakshtas, Yu.I. Reksnis, R.V. Kanapenas and A.P. Amulyavichus, *Fiz. Met. Metalloved.*, 66(4) (1988) 821-823.
- 5.267 S.M. Kanetkar, P.P. Patil, S.V. Ghaisas, S.B. Ogale and V.G. Bhide, *Hyperfine Interactions*, 40 (1988) 587-590.
- 5.268 S. Joshi, D.M. Phase, S.M. Kanetkar, S.V. Ghaisas, S.B. Ogale and V.G. Bhide, *Hyperfine Interactions*, 41 (1988) 689-692.
- 5.269 P. Schaaf, V. Biehl, U. Gonser, M. Bamberger, M. Langohr and F. Maisenhalder, *Hyperfine Interactions*, 57 (1990) 2095-2100.
- 5.270 P. Schaaf, Ph. Bauer and U. Gonser, *Hyperfine Interactions*, 46 (1989) 541-548.
- 5.271 P. Schaaf, Ph. Bauer and U. Gonser, *Z. Metallk.*, 80(2) (1989) 77-82.
- 5.272 Cs. Fetzer, L. Grönösy, T. Kemény, E. Kotai, M. Tegze, I. Vincze, W. Hoving and F. van der Woude, *Phys. Rev.*, 42(1) (1990) 548-554.
- 5.273 Cs. Fetzer, L. Grönösy, T. Kemény, M. Tegze and I. Vincze, *J. Non-Cryst. Solids*, 117-118 (1990) 160-163.
- 5.274 O. Schneeweiss, K. Volenic, S. Libovicky and A. Sedlacek, *Hyperfine Interactions*, 57 (1990) 2105-2108.
- 5.275 S.B. Ogale, P.P. Patil, S. Roorda and F.W. Saris, *Appl. Phys. Lett.*, 50(25) (1987) 1802-04.
- 5.276 O. Schneeweiss and K. Volenic, *Hyperfine Interactions*, 46 (1989) 527-534.
- 5.277 A.V. Kulkarni, R. Lal, S.M. Kanetkar, S.M. Chaudhari and S.V. Ghaisas, *Radiat. Eff.*, 107(264) (1989) 139-45.
- 5.278 J.V. Armstrong, J.M.D. Coey, J.G. Lunney and M.E.G. Lyons, *Hyperfine Interactions*, 46 (1989) 467-471.

- 5.279 S.V. Kar'agin, Dokl. Akad. Nauk SSSR, 148 (1963) 1102- 1107.
- 5.280 U. Gonser, M. Ron, H. Ruppertsbery, W. Keune and A. Trautwein, Phys. Stat. Sol., A10 (1972) 493-501.
- 5.281 U. Gonser and G. Fischer, in Mössb. Spectrosc. II, ed. by U. Gonser, Topics Curr. Phys., Springer, 1981, pp. 125-172.
- 5.282 H.D. Pfannes and M. Fischer, Appl. Phys., 13 (1977) 313.
- 5.283 J.M. Greneche, M.H. Hery and F. Varret, J. Magn. Magn. Mater., 26 (1982) 153.
- 5.284 G.N. Belozerskii and V.G. Semenov, Fiz. Tverd. Tela, 27 (1985) 1818-1823 / Sov. Phys.- Solid State (Engl. Transl.), 27 (1985) 1090-1093.
- 5.285 M. Bourrous and F. Varret, J. Magn. Magn. Mater., 66 (1987) 229-235.
- 5.286 F. Varret, J.C. Walker and C.L. Chien, J. Magn. Magn. Mater., 66 (1987) 225-228.
- 5.287 T. Zemcik, E. Kuzmann, S. Vitkova and G. Raichewskii, Hyperfine Interactions, 55 (1990) 1107-1112.
- 5.288 T. Suzuki, K. Arai, M. Shiga and Y. Nakamura, Metall Trans., A16 (1985) 27-36.
- 5.289 S. Fayeulle, G. Marest, N. Moncoffreand and J.Tousset, Applied Surface Science, 32 (1988) 141-155.
- 5.290 M. Asano, K. Umeda, E. Kita and A. Tasaki, IEEE Trans. Magn., 24(6) (1988) 2997-99.
- 5.291 H. Topsoe, J.A. Dumesic and S. Moerup, in Application of Mössbauer Spectroscopy, ed. by R.L. Cohen, Vol. 2, Academic Press, New York, 1980, p. 55.
- 5.292 A.M. van der Kraan and J.W. Niemantsverdriet, in Industrial Applications of the Mössbauer Effects, ed. by G.J. Long and J.G. Stevens, Plenum Press, New York, 1987, p.609-634.
- 5.293 B. S. Clausen and H. Topsoe, Hyperfine Interactions, 47 (1989) 203-217.
- 5.294 J.W. Niemantsverdriet, Hyperfine Interactions, 53 (1990) 93-96.
- 5.295 F.J. Berry, S. Jobsen and M.R.Smith, Hyperfine Interactions, 46 (1989) 607-618.
- 5.296 F.J. Berry and H. Du , Hyperfine Interactions, 57 (1990) 1747-1759.
- 5.297 Y.V. Maksimov, V.V. Matveev, I.P. Suzdalev, T.I. Khomenko and A.A. Kadushin, Hyperfine Interactions, 57 (1990) 1987-1991.
- 5.298 Y.V. Maksimov, V.V. Matveev, I.P. Suzdalev, M.V. Tsodikov and O.G. Ellert, Hyperfine Interactions, 57 (1990) 1983-1987.
- 5.299 F. Schmidt, in Industrial Applications of the Mössbauer Effects, ed. by G.J. Long and J.G. Stevens, Plenum Press, New York, 1987, p.667-681.
- 5.300 M.W.J. Craje, R.H. Hadders, W.L.T.M. Ramselaar, E. Gerkema, V.H.J. de Beer and A.M. van der Kraan, Hyperfine Interactions, 57 (1990) 1801-1809.
- 5.301 A.M. Van der Kraan, M.W.J. Craje, E. Gerkema, W.L.T.M. Ramselaar and V.H.J. De Beer, Hyperfine Interactions, 46 567-574 (1989).
- 5.302 H.V. Brandis, F.E. Wagner, J.A. Sawicki and J.H. Rolston, Hyperfine Interactions, 46 (1989) 575-582; Hyperfine Interactions 57 (1990) 2127-2132.

- 5.303 S. Moerup, J.A. Dumesic and H. Topsoe in Application of Mössbauer Spectroscopy, ed. by R.L. Cohen, Vol.2, Academic Press, New York, 1980, p.1.
- 5.304 G. Xiao and C.L. Chien, J. Appl.Phys., 63(8) (1988) 4252- 54.
- 5.305 A.H. Morrish, K. Haneda and P.J. Schurer, J. Phys. Colloq., 37 (1976) C6-301.
- 5.306 K. Haneda and A.H. Morrish, J. Appl. Phys., 63(8) (1988) 4258-60.
- 5.307 A.E. Berkowitz, J.A. Lahut, I.S. Jacobs, I.M. Levinson and D.W. Forester, Phys. Rev. Lett., 34 (1975) 594.
- 5.308 S. Mørup and H. Topsoe, Appl. Phys., 11 (1976) 63.
- 5.309 W. Meisel and H. Hobert, Exp. Tech. Phys., 16 (1968) 237.
- 5.310 A.M. Rubaskov, P.B. Fabrichny, B.V. Strakhov and A.M. Babishkin, Russ. J. Phys. Chem., 46 (1972) 765.
- 5.311 G.N. Belozerskii and M.I. Kazakov, Vestnik Leningradskogo Universiteta, 22 (1982) 67-73.
- 5.312 G.N. Belozerskii and B.S. Pavlov, Phys. Tverdogo Tela, 25 (1983) 1690-1697.
- 5.313 D.H. Jones, Hyperfine Interactions, 47-48 (1989) 289-310.
- 5.314 S. Mørup and H. Topsoe, Proc. Intern. Conf. Mössbauer Spectrosc., Bucharest, Romania, ed. by D. Barb and D. Tarina, 1 (1977) 229.
- 5.315 H.H.A.Smit, R.C. Thiel and L.J. De Jongh, Hyperfine Interactions, 47-48 (1989) 519.
- 5.316 E. Tronc, J.P. Jolivet, P. Belleville and J. Livage, Hyperfine Interactions, 46 (1989) 637-643.
- 5.317 A. Efimov, L.N. Moskvina, G.N. Belozerskii, M.I. Kazakov, B.A. Gusev and A.V. Semanov, Atomnaya Energiya, 67, No.6 (1989) 389-392.
- 5.318 T.Shinjo, Interface Magnetism, Surface Science Reports, Vol. 12, No. 2 (1991) 49-98.
- 5.319 G. Bayreuther, Hyperfine Interactions, 47 (1989) 237-249.
- 5.320 T.S. Shinjo, T. Matsuzawa, T. Takada, S. Nasu and Y. Murakami, J. Phys. Soc. Jpn., 35 (1973) 1032.
- 5.321 G. Lugert and G. Bayreuther, Phys. Rev., B38 (1988) 11068.
- 5.322 W. Kianka, K. Debusmann, W. Keune, R.A. Brand and N. Hosiotou, Solid State Commun., 58 (1986) 641.
- 5.323 M. Przybylski and V. Gradmann, Phys. Rev. Lett., 59 (1987) 1152.
- 5.324 P.L. Crouse and C.M. Stander, J. Phys. Chem. Solids, 49(10) (1988) 1145-1151.
- 5.325 J.S. Zabinski and B.J. Tatarchuk, Surface Science, 241 (1991) 157-170.
- 5.326 J.S. Zabinski, T. George and B.J. Tatarchuk, Surface Science, 241 (1991) 171-189.



**Variables and abbreviations** (in the alphabetical order)

Symbol		Page on which symbol first appears
A	mass number	46
A	the amplitudes (parameters of surface roughness)	169
$A(t_a)$	the area under the spectrum	44
$A_{kk}$	coefficients	76
A	the area	105
APK	Almost Pure K-conversion	167
$A_{S,B}$	the area under the spectrum from a S(B) phase	173
$A_{e,v}$	the area under the spectrum	208
A,B,C,D	directions of the incident radiation	400
$a = k^2(z^2 - x^2)$		21
a	isotopic abundance	34
$a_r$	a constant	86
$a_R$	a constant	87
$a(E)$	the $\mu_a(E)/v$ ratio a	109
$B_k m_g, m_e, m_e')$	coefficients	64
$B_{j-1}$	a parameter	153
$B(a(E), v_L d)$	the function	288
$b = v d_a$	effective thickness of the sample for the detected radiation	83
$b' = (v_1 - v_2) d_1$		118
c	the velocity of light	3
CEMS	Conversion Electron Mossbauer Spectroscopy	28
C	a constant	38
$c_1, c_2, c_3$	constants	61
$C_x$	the parameter	105
c	parameter	110
$C_K$	a parameter	110
c	a constant	176
$C_i$	the factors that determine an electron beam attenuation ( $i = 1...5$ )	178
C	a constant	212
C	the constant	214
$C_i'$	a parameter analogous to the weight factors but for the photoelectric effect	294

$c_i$	the weight factor	287
$c_1, c_2$	constants	316
$C_C$	the content of carbide-forming elements in the initial solid solution	363
$c_i$	the coefficients, $i = 1...6$	399
$C_i$	coefficient, $i = 1...3$	401
$d_a$	thickness of the sample (absorber, scatterer)	37
$D$	a special function	59
$D$	factor	81
$d$	parameter	110
$d_I, d_A$	thicknesses of the analyzed layers	116
$D_{i-1}, C_{i-1}$	parameters	153
DCEMS	Depth Selective Conversion Electron Mossbauer Spectroscopy	148
$d_s$	the source thickness	191
$d_i$	escape depth of electrons of an i-group	242
$D$	the symbol for an operator	319
$d/dy - \nu I$	the differential operation	326
$d_h, d_m$	the thickness of haematite and magnetite layers	346
$D(v_m, \varphi_m)$	a distribution function	398
$D_{l,k}$	the expansion coefficients	398
$D_{\min}(v_m, \varphi_m)$	the minimal texture function	399
$D_{\min}(v_m, \phi_m)$	the function of texture in the principal axes system	402
$D$	directions of the incident radiation	400
$E$	energy	1
$e$	excited state (index)	2
$E_0$	energy of an excited state	2
$E_R$	recoil energy	3
$\Delta E$	inaccuracy of energy determination	4
$E'$	energy of interaction of a nucleus with an electromagnetic field	5
$E$	electric field strength	5
$e$	electron charge	6
EFG	the electric field gradient	7
$E_s$	transition energy in the source	8
$E_a$	transition energy in the absorber	8
$E^\circ$	transition energy for $r^2 = 0$	8
$\delta E_g, \delta E_e$	value of the shift of a nuclear levels	7
eV	electron Volt	8
$eQ = \langle I, I   Q_{zz}   I, I \rangle$	the electric quadrupole moment	10

$E_Q^m$	the eigenvalues of the $H_Q'$ Hamiltonian	11
$E_M^m$	the shift of the levels due to magnetic interactions	13
$\varepsilon_n, \varepsilon_{n0}$	eigenenergies	2
EC	electron capture	33
$\varepsilon$	the energy given by the roots of the secular equation	17
$\varepsilon = E_S - E_S v/c$	energy parameter	37
$\varepsilon_{av}$	the average energy loss	146
$E_b$	minimum energy for the backscattered gamma-rays	51
$E'$	energy of the emitted photon	56
EL, ML	multipolarity of electric and magnetic transitions	60
$E_{ij}$	transition energy	84
$E_j^e$	energy of a j-sublevel of an excited state	84
$E_i^g$	energy of an i-sublevel of the ground state	84
$E_2(v_x x)$	a second order exponential Plachek function	108
$E_2(a(E), b)$	a special function	109
$E_2(a, \infty)$	the special function for a bulk sample	118
$E_0$	initial energy of a beam of electrons	142
$dE/ds$	the energy loss	139
$E_{av}$	average energy of the beam	165
$E_{dis}$	the dissociation energy	222
$E_2'(l, \infty)$	a derivative of the function $E_2(l, \infty)$	305
$f$ ( $f'$ )	the probability of recoilless emission (absorption), Lamb-Mossbauer factor	1
$F_L^M(\theta, \varphi)$	the angular functions	18
$f^*$	parameter analogous to the $f$ parameter	45
$F_r$	the elastic resonant scattering amplitude	58
$F_{coh}$	the coherent resonance scattering amplitude	59
$f_1, f_2$	probability amplitudes of the Mossbauer effect	59
$f_R$	the Debye-Waller factor	61
$F(E, S, x)$	a certain function	67
$F_R$	the elastic Rayleigh scattering amplitude	69



438

$F_L(\theta)$	angular distribution	75
$F'_r$	factor	81
$F_r, F_m$	functions	83
$F'_r, F'_m$	functions	86
$\mathcal{F}_{\text{coh}}(k_0=k_f)$	the coherent scattering amplitude	99
$f$	a positive function	167
$f_i, q_i$	parameters	168
$F(x, E)$	the function describing the experimental beta-spectrum	191
$F(x, p)$	the function analogous to the function $F(x, E)$	192
$F$	the Fano factor	222
$F'$	the variance of the gas multiplication factor	236
$F_i$	functions	283
$\mathcal{F}(\beta)$	the function	302
$f(E)$	a function	304
$F(\theta)$	atomic form factor	306
$F$	Fourier transform	321
$f_s$	the substitutional fraction	383
$g$	ground state (index)	2
$\langle g   a   e \rangle$	nuclear matrix element	2
$g_I$	gyromagnetic ratio	13
$g_1$	number of radioactive nuclei in a unit volume of the source	39
$G_{j-1}$	parameters	215
$G_{kk}(t)$	perturbation factor	76
GM	Geiger-Muller counter	188
GA DCEMS	the glancing-angle DCEMS	204
$G$	the parameter	105
$g(\gamma)$	extinction coefficient	241
$H$	energy operator	2
$H$	magnetic field strength	5
$H_{\text{eff}}$	effective magnetic field acting on the nucleus	13
$H_c$	the Fermi contact field	14
$H_L$	contribution to $H_{\text{eff}}$ from the orbital motion of valence electrons	15
$H_D$	spin-dipolar term	15
$H_o$	applied external field	15
$H_d$	the dipole field	15
$H_{mm'}$	the matrix element of the Hamiltonian $H$	17
$h(t_a)$	the function	41
$(hkl)$	a single plane or a set of parallel planes	67

$[hkl]$	direction	68
$H(s)$	a function	106
$H$	the function	155
$h_i$	parameters	327
$\mathcal{H}$	Hamiltonian	5
$\mathcal{H}_Q$	Hamiltonian for interaction with electrons	5
$\mathcal{H}_M$	Hamiltonian for interaction with the magnetic field	5
$\mathcal{H}_\delta, \mathcal{H}'_Q$	Hamiltonians	7
$\mathcal{H}_M$	Hamiltonian for the magnetic interaction	13
$I$	the nuclear spin	10
$I_k$	operator of the nuclear spin projection	10
$I_\pm = I_x \pm iI_y$	the shift operators	11
$ I_e m_e\rangle$	nuclear state	18
$\langle I_g    1    I_e \rangle$	the reduced matrix element	18
$\langle I_g m_g   M   I_e m_e \rangle$	the Clebsch-Gordan coefficient	18
$I_i(\theta)$	the angular distribution of the Mossbauer spectra component	19
$I(\infty)$	intensity off resonance	24
$I(v)$	intensity at any velocity $v$	28
$I(0)$	intensity on resonance for unsplit lines in both the source and absorber	28
$I(v, d_a)$	intensity of radiation transmitted (scattered) by the sample of the thickness $d_a$	38
$I_{\text{back}}$	intensity of the background	46
$I_r(v)$	intensity of gamma-rays scattered into the solid angle $d\omega$ due to the Mossbauer effect only	64
$I(S)$	intensity of detected radiations	63
$I_0$	integral intensity	79
$I_r(S)$	line shape due to elastic resonant scattering	83
$I_{rn}(S)$	the same as $I_r(S)$ , but due to inelastic resonant scattering	84
$I_R(S), I_{Rn}(S)$	the partial spectra due to Rayleigh scattering	86
$I_{Rn+C}(S), I_{R+C}$	the partial spectra due to electron scattering	91
$I(v, v_i)$	the Mossbauer spectrum in SEDMS	94
$I_x(v, x, \theta)$	the intensity of X-rays scattered as a result of the Mossbauer effect at an angle $\theta$ from the layer $dx$	105

440

$I_X(E, \infty)$	the spectrum from a bulk sample	119
$I$	the mean excitation energy	139
$I_{ph, j}$	the contribution into the background from the photoelectrons of a $j$ -layer	154
$I'(\infty)$	the total normalized beam of background electrons	154
$I'$	the beam of detected electrons	154
$I$	the ionization potential of the gas	222
$I_m$	the ionization potential of the main component of the gas filling	221
$I_q$	the ionization potential of the quench component	223
$I'(E, x)$	the line shape of a hypothetical transmission spectrum of a layer $dx$ at depth $x$	320
$I(p), I'(E)$	the functions	321
$I'[E(\infty)]$	the function	322
$I'(E, y)$	the response of a sample to monochromatic radiation	324
$I(E, q)$	the functions	328
$J(E)$	$\gamma$ -spectrum	1
$J_M(E), J'_R(E)$	components of $\gamma$ -spectrum	1
$J^a(E)$	the absorption line	24
$J(E)$	energy distribution of $\gamma$ -rays from the source	36
$J(E, v)$	energy distribution of $\gamma$ -rays	38
$J^S_M(E, v)$	energy distribution of Mossbauer $\gamma$ -rays from the source with self-absorption	40
$J_0$	the Bessel function	41
$J_M(E, v)$	energy distribution of Mossbauer $\gamma$ -rays	38
$J_M(E, v, u_n)$	energy distribution where noise is taken into account	45
$J_M(E, S, x)$	energy distribution at a depth $x$	79
$J'(E', v_i)$	the energy spectrum of the scattered $\gamma$ -quanta	93
$J_r(E', v_i), J_R(E', v_i)$	the partial spectra due to elastic scattering	93
$J(\gamma)$	the intensity of the field on the sample surface	243
$J(a(E))$	the function	288
$\hat{J}$	information matrix	310
$[\hat{J}]_{ta, ta}$	the information matrix element	311

$I(\mathcal{E})$	the function describing the line shape	315
$k$	wave vector	2
$k$	Boltzmann constant	3
$k_i$	partial intensity	47
$k_f, k_0$	wave vectors of incident and scattered $\gamma$ -quanta	58
$k^{\wedge}_0, k^{\wedge}_f$	coordinate systems	60
$k_m$	number	76
$K_{ai}, K_{\beta i}$	the transition type	102
$K = m_e - m_g$		59
$K_i(x)$	the function	212
$K(p - q)$	the function	328
$k$	the rate constant	345
$L$	total orbital momentum quantum number	15
LSIC's	large scale integrated circuits	27
$L_S(E)$	Lorentzian line for the source	36
$L_a(E)$	Lorentzian line for the sample	37
$l$	non-resonant absorption length	47
$\mathcal{L}$	the penetration depth for the radiation	100
$\mathcal{L}(E, \mathcal{E}, d_1, d_2)$	a factor	118
$\mathcal{L}(k, t_a/2)$	the function	156
$L$	topographic layer (see Fig.3.16)	169
$L$	the luminosity	180
$\mathcal{L}(x, E, \theta)$	the functions describing energy loss distribution of electrons	191
*	convolution	191
$\mathcal{L}'(x, p)$	a function analogous to the $L_{rukopis}(x, E)$ function	192
$L_j(V)$	the resonant profile of the $j$ -th phase	213
$\mathcal{L}$	field penetration into the sample	242
$\mathcal{L}T$	the LaPlace transform of the function $T$	322
$L_{ph}$	the thickness of a gas layer	222
$M$	matrix element of operator $H$	2
$M$	mass of a nucleus	3
$mm\ s^{-1}$	millimeter per second	8
$m$	the spin projection onto the quantization axes	11
$Ml$	magnetic dipole transition	13
MCA	multichannel analyzer	24
ml/s	millilitre/second	125
$M_j$	the formula weight of the compound	212
$M$	the gas multiplication factor	221
$M$	the mean gas multiplication factor	236
ML	multipolarity of magnetic transitions	60
$N$	channel number of a MCA	25
$N$	Avogadro number	46

neV	nanoelectron Volt	34
$n(x)$	number of radioactive nuclei in a unit volume at the depth $x$	35
$n_s$	number of Mossbauer atoms in a unit volume of the source number of resonant atoms in a unit	35
$n_a$	number of resonant atoms in a unit volume of the sample	37
$n = 1 - \sigma - i\beta$	the complex index of refraction	98
$N = nZx$	the number of electrons	140
$n_{\text{eff}}^i$	the effective density of Mossbauer atoms in a given phase	174
$N_J$	the number of iron atoms in the formula	212
$N$ with line	the average number of ion pairs produced by a particle or a quantum	236
$N_h, N_m$	the number of haematite and magnetite "molecules" per unit volume of the oxide	346
$N_x, N_y, N_z$	spin populations along the corresponding axes	402
$O((\mu_r/\mu_a)^2)$	a (negligible) contribution to the spectrum	305
$p$	vector of electric dipole moment	5
PFC	Potassium ferrocyanide	9
$P$	the probability of a nuclear transition	18
$p(t_a)$	the saturation function	41
$p(u_n, v)$	the probability	44
$p$	background parameter	46
$p$	factor	66
$P(m_e)$	relative populations	75
$P(s)$	the probability	138
$P_j(v, x)$	the fraction of the beam absorbed on the way to the sublayer $dx$ in a layer $j$	153
$P$	saturation vapour pressure (Fig.3.47)	226
$p = NM$	the average number of ion pairs produced in the active counter volume after gas multiplication	236
$P'_i(E)$	the probability of the scattered radiatic of an $i$ -type to escape the surface as a result of only resonant scattering of monochromatic $\gamma$ -rays	286
$P''_i(E)$	the quantity analogous to $P'_i(E)$ for resonant re-scattering	286
$P_i(E) = P'_i(E) + P''_i(E)$	the function	286
$\mathcal{P}_i(E)$	the probability of the appearance on the surface of radiation of an $i$ -type after photoelectric absorption of re-scattered $\gamma$ -quanta	299

$\mathcal{P}'_i(E)$	the function analogous to $\mathcal{P}_i(E)$ , but due to X-rays produced in first scattered event	299
$P_i$	the observed effect magnitude in an i-th channel of MCA	310
$p$	variables	328
$q = eZ$	nuclear charge	5
$\mu$	vector of magnetic dipole moment	5
$Q_{ik}$	tensor of the electric quadrupole moment	5
$Q$	parameter	83
$q_i$	parameter	168
$Q(\gamma, x)$	the wave field intensity at the depth $x$	240
$Q_i(E)$	the probability determining the total scattered intensity of radiation of an i-type	289
$q$	variables	328
$Q$	the operator	329
$Q'$	a differential operator of the $(N - 1)$ order with constant coefficients	329
$r$	radius-vector	2
$R$	energy resolution	4
$r_p$	radius-vector of the p-th proton	6
$r^2_g, r^2_e$	the mean-square radius	7
$R$	shielding factor	13
$R_m, R_g$	the line intensity ratios	19
$r(0), r(t)$	initial and final atom's positions	58
$R$	reflectivity	98
$R(x)$	reflection, ratio of the backscattered electrons to the incident ones	136
$r_B$	the Bethe range	145
$R_e$	the extrapolated range	142
$R_M$	the maximum range	142
$r_0$	a distance	147
$r_{eff}$	effective range	165
$R(\gamma)$	angular dependence of the reflected wave	240
$R_\gamma(E)$	the function determining the absolute value of the observed effect	290
$r$	the surface roughness factor	346
$S = E\gamma/c$	change in the $\gamma$ -quantum energy	8
$mm\ s^{-1}$	millimeter per secon	20
SS	stainless steel	9
SNP	Sodium nitroprusside	9

SEDMS	selective excitation double Mossbauer spectroscopy	94
sr	steradian	100
$S(v,x)$	the "volumetric source strength"	108
$S_x(v,x)$	the volumetric source strength of X-rays	108
s	a distance	138
S	stopping power	139
s	the total path length	147
$S_{K,j}(v,x)$	the volumetric source strength of the sublayer $dx$ in a j-layer	153
$S_{av}$	the average path length (see Fig.3.13)	165
S	surface (see Fig.3.16)	169
$S'(V,E)$	the spectrometer profile	176
s	the scattered area	179
s	the sample area	345
T	temperature	3
$t_a$	effective thickness of the sample	38
$t'$	effective thickness for the source	38
$t_s(E)$	total effective thickness of the sample	82
$T_M$	the Morin temperature	96
$t^e = \mu d a$	a parameter	106
$T(x)$	a function describing the passage of electrons through a substance (ratio of the transmitted electrons to the incident ones)	136
$T^{tot}(E,x,\cos\theta)$	the weight function for a plane surface for all groups of electron	160
$T^{tot}_{t,t}(x); T^e(x); T^A(x)$	the weight functions	160
$T^K_{t,t}(x); T^A_{t,t}(x); T^L_{t,t}(x)$	the weight functions	161
$T^K_{E,\cos\theta}(x)$	the probability	162
$T^K_E(\cos\theta)$	the angular distribution	162
$T^K_{x,\cos\theta}(E)$	the energy distribution	162
$[T(E_0,x\rho_x/\rho_{Fe})]_{Fe}$	the weight function for a substance X of density $\rho_x$	164
$T^i_{t,t}(0)$	the initial value of $T^i_{t,t}(x)$	164
$T(z_T)$	the topographic weight function	169
$T_{APK,t}(x)$	the weight function for K-conversion electrons in the APK interval	171
T	transmission	182
$T^K_{op}(K_i(x))$	an operator	213

$T_{U,\Delta U}(x)$	the weight functions analogous to the $T_V(x)$ functions	239
$T'(x_i)$	the weight functions specifying the shape and position of the i-layer	244
$T_i(x)$	experimentally obtained weight functions for i-energy intervals	244
$T_r(x,E)$	the weight function for elastically scattered $\gamma$ -rays	279
$T_n(x)$	the weight function for inelastically scattered $\gamma$ -rays	279
$T^\gamma(x,E)$	the probability for a $\gamma$ -quantum to escape the surface	281
$t = 1/\cos\theta$	a variable	281
$T_k^\gamma(x,E)$	the weight function for the case of (k-1) re-scattering being taken into account	282
$t = 1/\cos\theta - 1$	the variable	287
$u$	the displacement vector of an atom	21
$u_n$	the noise velocity	44
$U(x)$	the primitive functions to the $T(x)$	164
$U_{t,t}^i(\infty)$	a measure of the yield of electrons of the i-th group from a bulk	165
$U_q, U_p$	(operation) voltages of the counter	226
$\Delta U$	the voltage range	226
$U$	the position of the discriminator window	239
$V$	velocity	8
$V_{\max}$	velocity corresponding to the N-th channel of a MCA	25
$v(t)$	function	26
$V_0$	maximum velocity value	27
$v_i$	velocity corresponding to the i-th maxima	28
$V$	Volt	125
$v(m_g, m_e)$	Doppler velocity, corresponding to the $\gamma$ -transition $E_0(m_g, m_e)$	64
$v_e$	the electron velocity	139
$v(\theta)$	a function determining the angular distribution of $\gamma$ -rays due to Rayleigh scattering	306
$V = cE$	the spectrometer setting	176
$W_X, W_Z$	parameters	22
$W(\theta)$	the directional correlation function	75
$W_{ij}(\theta_i, \varphi_i)$	directional correlation functions for the transition energy $E_{ij}$	84



$W_{ij}(\theta)$	directional correlation functions	85
$w_x(v,b)$	the probability	109
$w(v,d)$	a function	109
$w$	the average energy for ion-pair formation	222
$W$	the wavelength (parameter of surface roughness)	169
$W_1(E,x)$	the probability of resonant scattering for monochromatic $\gamma$ -rays at a depth $x$	287
$W_2(E,x)$	the probability of a single resonant re-scattering	287
$W(E,x) = W_1(E,x) + W_2(E,x)$		287
$w(\theta)$	a function determining the angular distribution of $\gamma$ -rays due to Rayleigh scattering	306
$W$	the weight-gain	345
$W_O$	the weight of an oxygen atom	346
$x^1$	axis	6
$x_p^1$	projection of vector $r_p$ on the $x$ -axis	6
$x^2, y^2, z^2$	the mean square amplitudes	21
$x^2$	mean square displacement	2
$x = \mu_r / \mu_a$	parameter	82
$x_1$	the escape depth	174
$x_0$	the coordinate of the boundary between the first layer and the substrate	324
$Y_{l,k}(v_m, \varphi_m)$	the real part of spherical harmonics	398
$Z$	number of protons in the nucleus	6
$Z_{surf}$	the function describing the wavy surface shape	169
$Z_T$	the topographic depth	169
$z^\wedge, k_0^\wedge, k_f^\wedge$	coordinate systems	60
$\alpha$	total internal conversion coefficient	33
$\alpha_K$	the K-shell-conversion coefficient	105
$\alpha = r_B / \lambda_{tr}$	parameter	147
$\beta$	ratio of the $\gamma$ -quantum energy to the rest energy of the electron	51
$\beta_1, \beta_2$	angles specifying the orientation of $k_0$ and $k_f$	77
$\beta_r, \beta_{rn}$	parameters	83
$\beta$	$\mu_r / \nu$	109
$\beta = v_e/c$		139

$\beta$	parameter	152, 284
$\beta(E) = \mu_a(E)/\mu_{ph}$		302
$\beta'(E) = \mu_a(E)/\nu_{ph}$		302
$\Gamma_{nat}$	natural line width	1
$\Gamma$	full width at half maximum	2
$\Gamma_a$	absorber (scatterer) line width	37
$\Gamma_{exp}$	width of the experimental line	41
$\Gamma_\gamma$	partial width	58
$\gamma_\infty$	antishielding factor	13
$\gamma_1, \gamma_2$	angles for the incident and outgoing radiation	56
$\gamma_{cr}$	the angle of total reflection (the critical angle)	71
$\gamma_1$	a glancing angle	98
$\gamma$	$\mu_a/\nu$	109
$\Gamma = (A/A')_x/(A/A')_0$	the ratio	150
$\gamma$	parameter	152
$\delta_{ik}$	Kronecker symbol	6
$\delta$	isomer (chemical) shift	8
$\delta(E)$	delta-function	303
$\delta_e$	the relative standard deviation	312
$\delta(\sin\theta^i_m)$	delta-functions, $i = x, y, z$	402
$\Delta$	quadrupole splitting or constant of the quadrupole interaction	12
$\Delta(\theta)$	constant of the quadrupole interaction directly obtainable from the Mossbauer spectrum	17
$\Delta_i i'$	splitting of the ground state	84
$\Delta = [(\mu_a(E))_1 - (\mu_a(E))_2]d_1$		118
$\Delta\cos\theta$	the angular interval	180
$\Delta$	the deviation	312
$\Delta x$	the thickness of the stripped layer	327
$\varepsilon$	resonance effect magnitude	28
$\varepsilon_{exp}$	experimental resonance effect magnitude	46
$\epsilon_{tot}$	the probability of the photoelectric absorption in the $r_{eff}$ layer	222
$\epsilon(E, \cos\theta)$	an efficiency function	161
$\epsilon_{ph}$	the total probability of the absorption in the $r_{eff}$ layer	222
$\eta(d)$	the relative area under the partial spectrum of the total spectrum	129
$\eta$	parameter	155

$\eta^I(E_0) = \rho_I / (\rho_{Fe} r_B(E_0))$	a ratio	168
$\eta = (\varphi_{xx} - \varphi_{yy}) / \varphi_{zz}$	the asymmetry parameter	11
$\Theta$	Debye temperature	3
$\Theta_D$	characteristic temperature	21
$\theta$	polar angle, specifying $H_{eff}$ direction in the principal axes system of the EFG tensor	15
$\theta$	polar angle between z-axis ( $H_{eff}$ ) and the $\gamma$ -quantum direction	18
$\theta$	polar angle, specifying displacement vector	21
$\theta_0$	the angle in theory of Rayleigh scattering	51
$\theta_{hkl}$	a direction of Rayleigh coherent scattering	67
$\theta$	the angle between $k_0$ and $k_f$	77
$\theta_i$	polar angle	84
$\theta$	the average angle at which electrons enter the input slit of the spectrometer	177
$\theta_R$	angle between directions of $\gamma$ -quanta and the quantization axis	397
$\theta; \phi; \theta_m; \varphi_m$	angles	401
$\theta_m^{x,y,z}$	the angles between the hypothetical vectors direction and the coordinate axes	402
$\nu$	angle specifying the direction of $\gamma$ -quanta	397
$\nu_m$	angle specifying the direction of the quantization axes	397
$\kappa$	an effective linear extinction (absorption) coefficient	129
$\kappa$	parameter	155
$\kappa(\gamma)$	angular dependence of electrons	240
$\kappa$	the parameter	281
$\tilde{\lambda}$	the wavelength	36
$\lambda$	the mean free path between the interacti events	on 139
$\lambda_{tr}$	the transport mean free path	143
$\lambda_e$	the mean free path between elastic collisions	143
$\lambda_i$	the total inelastic mean free path	146
$\lambda_I$	the path length on which the electron loses energy I	200
$\lambda_r$	the parameter for elastically resonantly scattered $\gamma$ -rays	282

$\lambda_i$	the parameter analogous to $\lambda_r$	288
$\mu$	vector of magnetic dipole moment	5
$\mu_n$ with line	the nuclear magneton	13
$\mu_B$	the Bohr magneton	14
$\mu(E)$	total linear absorption coefficient	28
$\mu_s(E)$	total linear extinction coefficient in the source	36
$\mu_{rs}, \mu_s$	resonant and nonresonant linear coefficient in the source	36
$\mu_a$	linear absorption coefficient in the sample	37
$\mu_r(E)$	linear resonant coefficient in the sample	38
$\mu_r$	maximum $\mu_r(E)$ value	38
$\mu_r^i$	maximum $\mu_r(E)$ value at i-resonance	38
$\mu^m$	mass absorption coefficient	46
$\mu_{ph}$	linear coefficient for the photoeffect	48
$\mu_R$	linear coefficient for Rayleigh scattering	48
$\mu_C$	linear coefficient for Compton effect	48
$\mu'_a(E', v)$	the total linear scattering coefficient in the "analyzer" moving at a velocity $v$	94
$v$	linear absorption coefficient of the detected radiation	83
$v_X$	the total linear absorption coefficient for X-rays	105
$\xi = \mathcal{F}_r / \mathcal{F}_R$	parameter	69
$\xi$	$\mu_r / \mu_a$	286
$\xi$	the parameter	291
$\xi$ (Erukopis)	the noise	315
$\pi_g, \pi_e$	parties	60
$\rho_e = -e \psi(0) ^2$	the charge density at the centre of the nucleus	7
$\rho$	density	46
$\sigma_s(E)$	resonant cross section in the source	36
$\sigma_0$	maximum cross section of the resonant interaction	36
$\sigma_a(E), \sigma_r(E), \sigma_a$	cross sections in the sample (absorber)	37
$\sigma'_0$	the $cr_Q$ value in the sample with fluctuations in nearest environment	41
$\sigma_e$	atomic absorption cross section	46

$\sigma_R$	the Rayleigh scattering cross section	51
$d\sigma_M/d\omega$	differential cross section for Mossbauer scattering on resonance	54
$d\sigma_R/d\omega$	differential cross section for Rayleigh scattering	54
$\sigma_1, \sigma_2$	polarizations of $\gamma$ -rays in $k_0$ and $k_f$ directions	59
$\sigma_{coh}(E)$	the coherent resonant elastic scattering cross section	66
$\sigma_{tot}$	the total cross section for the 10-keV $\gamma$ -quanta	222
$\sigma_{ph}$	the photoelectric cross section for the 10 keV $\gamma$ -quanta	222
$\sigma_N, \sigma_M, \sigma_p$	the standard deviation of the quantities $N$ , $M$ and $p$	236
$\sigma_p / p$	accuracy of energy determination	236
$\sigma_\epsilon$	the standard deviation in evaluation of $\epsilon$	312
$\tau$	reciprocal lattice vector	69
$\tau$	a period	105
$\tau_s$ ( $\tau_a$ )	the measuring time in a scattering (transmission) experiment	107
$\varphi$	electrostatic potential	5
$\varphi_p(0)$	electric potential at the centre of the nucleus due to the $p$ -th proton	6
$\nabla^2\varphi = 4\pi\rho_e$	Poisson equation	7
$\varphi_{ik} = ( \partial^2\varphi_p / \partial x_p^i \partial x_p^k )_0$	$i,k$ -component of the EFG tensor	7
$mm\ s^{-1}$	millimeter per second	20
$\varphi_{zz}$	$z$ -component of the EFG tensor	10
$(\varphi_{zz})_{lat}$	component of the EFG caused by the surrounding ions	13
$(\varphi_{zz})_{val}$	component of the EFG due to own electron: of the unfilled shells	13
$\varphi$	azimuthal angle, specifying $H_{eff}$ direction in the principal axes system of the EFG tensor	15
$\varphi_m$	the wave-function	17
$\varphi$	azimuthal angle between $z$ -axis ( $H_{eff}$ ) and the $\gamma$ -quantum direction	18
$\varphi$	azimuthal angle, specifying displacement vector	21

$\varphi_i$	azimuthal angle	84
$\varphi = \arctg 4A/W$		206
$\varphi(E)$	a function describing the response of the sample to monochromatic radiation	315
$\varphi(E, \mathbf{x})$	the probability for monochromatic radiation to reach a depth $x$	324
$\varphi^{\wedge}(E, p); \varphi^{\wedge}(E, q)$	the functions	328
$\varphi$	angles specifying the direction of $\gamma$ -quanta	397
$\varphi_m$	angles specifying the direction of the quantization axes	397
$\phi$	the work function	223
$\phi$	angles	401
$\chi$	the exit angle of the $\beta$ -spectrometer	182
$\chi$	polarizability	241
$\psi_n, \psi_{n0}$	eigenstates	2
$ \psi^2(0) ^2$	the electron density at the nucleus	7
$d\omega, d\omega'$	solid angles (see Fig.2.9)	57
$\omega$	the fluorescence yield	101
$(\cos\theta)_{av}$	the average value	143
$\langle \cos^2 \theta_R \rangle (v, \varphi)$	the function	398
$\langle \cos^2 \theta_R \rangle (\theta, \varphi)$	the function	401
*	convolution	191
$[ \ ]_i$	the jumps of derivatives of the $I'(E, y)$ spectrum recalculated for monochromatic radiation	325



**Index**

Absorber line width,	37
Absorption probability $f$ of recoilless $\gamma$ -quanta,	1
Ammonia solution,	336
Amorphous ferric oxide,	335
Anisotropy of atomic vibrations,	22
Anodic oxidation,	336
Anodic potential,	339
Anode reaction,	336
Antishielding factor,	13
APK (Almost Pure K-conversion),	167
Asymmetry parameter,	11
Atomic absorption cross section,	46
Atomic form factor,	306
Average energy of the beam,	165
Avogadro number,	46
Bessel function,	41
Bethe range,	140
Boltzmann constant,	3
Bohr magneton,	14
Cathodic polarization,	339
CEMS (Conversion Electron Mossbauer Spectroscopy),	28
Centre of gravity of the spectrum,	11
Characteristic temperature,	21
Charge density at the nucleus,	8
Chemical isomer shift,	7
Clebsh-Gordan coefficients,	18
Coherent resonance scattering amplitude,	59
Complex index of refraction,	98
Corrosion,	333
Corrosion inhibition,	334
Critical angle,	71
Cross section in the absorber,	37
DCEMS (Depth Selective Conversion Electron Mossbauer Spectroscopy),	148
Debye-Waller factor,	61
Debye temperature of the crystal,	3
Dehydration,	338
Dipole field,	15
Directional correlation function,	75
Dissociation energy,	222
Effective linear extinction coefficient,	129
Effective magnetic field acting on the nucleus,	13
Effective range,	165
Effective thickness of the sample,	38
Effective thickness for the source,	38



EFG (Electric field gradient),	7
Eigenstates,	2
Elastic resonant scattering amplitude,	58
Electric field strength,	5
Electric quadrupole moment,	10
Electric quadrupole moment tensor,	5
Electrochemistry,	335
Electrolytic cell,	335
Electron capture,	33
Electron charge,	6
Electron density at the nucleus,	7
Electrostatic interaction,	7
Electrostatic potential,	5
Emission of $\gamma$ -radiation,	1
Emission probability $f$ of recoilless $\gamma$ -quanta,	1
Energy distribution of $\gamma$ -rays,	38
Energy loss distribution of electrons,	191
Energy of an excited state,	2
Energy operator,	2
Energy resolution,	4, 180
Energy shift of the nuclear levels,	8
Escape depth,	174
Exit angle of the $\beta$ -spectrometer,	182
Expansion coefficients,	398
Experimental line width,	41
Experimental resonance effect magnitude,	46
Fano factor,	222
Fermi contact field,	14
Ferrophosphate layer,	338
Ferrous hydroxide,	337
Fluorescence yield,	101
Fourier transform,	321
GA DCEMS (glancing-angle DCEMS),	204
Gas multiplication factor,	221
Geiger-Muller counter,	188
Glancing angle,	98
Gyromagnetic ratio,	13
Haematite,	345
Half-width being close to the natural one - $\Gamma_{\text{nat}}$ ,	1
Hamiltonian for the electrostatic interaction,	5
Hamiltonian for the magnetic interaction,	13
Hyperfine parameter distributions,	335

Inaccuracy of energy determination,	4
Information matrix,	310
Integral intensity,	79
Intensity of the background,	46
Intensity of detected radiations,	63
Ionization potential of the gas,	222
Isomer shift,	8
Isomer shift calibration,	9
Isomer shifts interpretation,	9
Isotopic abundance,	34
Kronecker symbol,	6
Lamb-Mossbauer factor,	1
Layer-by-layer analysis,	323
Linear scattering (absorption) coefficients,	46
Lorentzian form,	17
Luminosity of the DCEMS spectrometer,	180
Magnetic dipole moment vector,	5
Magnetic dipole transition,	13
Magnetic field strength,	5
Magnetite,	345
Mass number,	46
MCA (multichannel analyzer),	24
Mean square displacement of the Mossbauer atom,	2
Minimal texture function,	399
Morin temperature,	96
Mossbauer effect,	1
Mossbauer effect Data and Reference Journal	4
Mossbauer effect probability,	3
Mossbauer experiments,	8
Mossbauer spectroscopy,	4
Natural line width,	1
Noise velocity,	44
Nuclear charge,	5
Nuclear magneton,	13
Nuclear matrix element,	2
Nuclear spin,	10
Nuclear state,	18
Observed resonance effect magnitude,	28
Oxidation,	333
Oxide,	340
Partial width,	58

Passive layer,	334
Passivation,	334
Penetration depth for the radiation,	100
Perturbation factor,	76
PFC (Potassium ferrocyanide),	9
Phonon spectrum,	2
Polarizability,	241
Post-effect,	339
Precipitation,	337
Probability amplitudes of the Mossbauer effect,	59
Probability of "forward" re-scattering, 1 Probability of $\gamma$ -quantum resonant emission,	2
Quality parameter,	311
Quality of a spectrum,	310
Quantity of information,	310
Rayleigh scattering cross section,	51
Reciprocal lattice vector,	69
Recoil effects,	1
Recoil energy,	3
Reduced matrix element,	18
Relative populations,	75
Relaxation pattern,	340
Resonant cross section in the source,	36
Roughness factor,	345
Sample area,	345
Saturation function,	41
Saturation vapour pressure,	226
Scattered area,	179
Scattering of $\gamma$ -radiation,	1
SEDMS (selective excitation double Mossbauer spectroscopy),	94
Selectivity of Mossbauer spectroscopy,	IV
Sensitivity,	IV
Shielding factor,	13
Shift operators,	11
SNP (Sodium nitroprusside),	9
Spectrometer profile,	176
Spectrometer setting parameter,	176
Spin-dipolar term,	15
SS (stainless steel),	9
Standard deviation,	312
Sulphate solution,	336
Surface,	IV

Surface roughness factor,	346
Surface roughness parameters,	169
Texture,	21
Total linear absorption coefficient,	28
Transmission mode spectroscopy,	32
Transition energy,	1
Transition energy in the absorber,	8
Transition energy in the source,	8
Transmission,	182
Topographic depth,	169
Topographic layer thickness,	169
Topographic weight functions,	169
Total internal conversion coefficient,	33
Volumetric source strength,	108
Wave vector,	2
Weight functions,	160
Work function,	223